National University of Ireland Maynooth

NUI MAYNOOTH
Ollscoil na hÉireann Má Nuad

Non-linear Dynamic Transformer Modelling and Optimum Control Design of Switched-mode Power Supplies

Tue T. Vu

A thesis submitted in partial fulfillment for the degree of
Doctor of Philosophy

in the
Faculty of Science and Engineering
Electronic Engineering Department

Supervisor: Prof. John V. Ringwood
Head of Department: Dr. Ronan Farrell

August 2014

Declaration of Authorship

I, Tue T. Vu, declare that this thesis titled 'Non-linear Dynamic Transformer Modelling and Optimum Control Design of Switched-mode Power Supplies' and the work presented in it are my own. I confirm that:

- This work was done wholly or mainly while in candidature for a research degree at this University.
- Where any part of this thesis has previously been submitted for a degree or any other qualification at this University or any other institution, this has been clearly stated.
- Where I have consulted the published work of others, this is always clearly attributed.
- Where I have quoted from the work of others, the source is always given. With the exception of such quotations, this thesis is entirely my own work.
- I have acknowledged all main sources of help.
- Where the thesis is based on work done by myself jointly with others, I have made clear exactly what was done by others and what I have contributed myself.

Signed:

Date:

Abstract

With recent advances in semiconductor manufacturing and computational technology, digital control systems have grown to a relatively mature stage, and will soon become a viable replacement for their analogue counterparts in the design of isolated and non-isolated DC-to-DC converters in general, and flyback converters in particular. Inspired by this possibility, the thesis adopts the first-ever digital control design in the field for wide-operating range flyback converters, based on a low-cost microcontroller.

Accurate transformer modelling is a necessary exercise for the study of the flyback converters as well as for model-based controller design. Therefore, a non-linear dynamic model, which allows an accurate representation of both linear dynamics and non-linear core behaviour in a practical transformer, is proposed. The parameters of the proposed transformer model are obtained using time-domain system identification based on experimental data. In order to reduce the round-off error typically occurring in the collected time-domain data, a method which is based on adjusting the value of the current sensing resistor is also adopted.

To facilitate control design, a control-oriented model is developed based on the full converter model through a simplification step. As demonstrated in the thesis, the control-oriented model is able to preserve the bulk of the full converter model fidelity, critical for a control design step, while at the same time requiring a significantly shorter execution time for simulation when compared with the full converter model. For the purpose of implementing isolated-feedback control within a low-cost microcontroller, a magnetic sensing principle, which can operates in both continuous and discontinuous conduction modes of the flyback converter, is developed. The proposed sensing principle is also based on the bias winding voltage of the flyback transformer to estimate the converter output voltage; however, the sampling instant is chosen at the point where the secondary current is known, instead of the knee point where the secondary current is zero. The implementation of the proposed sensing technique, based on analogue circuitry and a microcontroller, is also studied.

Finally, optimum digital control for a wide-operating range flyback converter is developed and implemented. The control architecture is purposely designed to perform a variety of tasks, including efficiency optimisation, magnetic sensing, and valley switching operation, in addition to the main task of regulating the output voltage. Three different methods for synthesizing optimum compensators, based on mixed-sensitivity H_∞ robust control theory, gain-adaptive predictive functional control (GAPFC) theory, and gain-adaptive quantitative feedback theory (GAQFT), are also studied. In order to improve the performance of the robust controllers, parametric variations of the flyback converter models are minimized before applying the robust control. Two possibilities for reducing converter parametric model uncertainty, based on adapting the converter open-loop gain and varying the sampling rate of the digital controller, are also demonstrated.

Acknowledgements

I wish to express my sincere gratitude to my PhD. supervisor, Prof. John V. Ringwood, who has provided great support and taught me many lessons over the past four years. It has been a great honour to work with him and to be his student. I appreciate all his patience, guidance and encouragement which has made the completion of this thesis possible.

I am grateful to Semiconductor Research Cooperation (SRC), Texas Instruments, and National University of Ireland - Maynooth (NUIM) for the academic and financial support which allowed me to pursuit my education.

I would like to extend my thanks to Seamus O'Driscoll who has provided many invaluable ideas and helpful discussions for my research.

Thanks to all of the administrative, technical and academic staff in the Electronic Engineering Department, NUI Maynooth, for their support, and to other NUIM colleagues in the Electronic Engineering Department, Josh Davidson, Andrej Roessling, Simon Giorgi, Paul Mc Namara, Iain Keaney, Tom Kelly, Francesco Paparella, Davide Padeletti, and Paula Garcia Rosa, for sharing many exciting stories and after-lunch walks.

Finally, I sincerely thank my wife, Thao Bui, and my parents for their invaluable support, encouragement and belief throughout my graduate career and every other aspect of my life.

Contents

Acronyms

Notation	**Description**
ABM	analogue behavioural modelling.
AC	alternating current.
AIC	Akaike's information theoretic criterion.
BSS	bias-side sensing.
CCM	continuous conduction mode.
DC	direct current.
DCM	discontinuous conduction mode.
EMI	electromagnetic interference.
EO	efficiency optimisation.
FEA	finite element analysis.
FFT	fast Fourier transform.
GM	gain margin.
iGSE	improved Generalized Steinmetz Equation.
IV	instrumental variable.
LMI	linear matrix inequality.
LS	least-squares.
LTI	linear time invariant.
MDL	Rissanen's minimum description length.
MOSFET	metal-oxide-semiconductor field-effect transistor.
MRAC	model reference adaptive control.
MS	magnetising sensing.

Notation	**Description**
OE	output error.
OEO	offline efficiency optimiser.
PCM	peak current mode.
PCMC	peak current mode control.
PFC	predictive functional control.
PFM	pulse-frequency modulation.
PM	phase margin.
PRBS	pseudo-random binary signal.
PSS	primary-side sensing.
PWM	pulse-width modulation.
QFT	quantitative feedback theory.
RBS	random binary signal.
SFL	switching frequency limiter.
SISO	single input single output.
SMPSs	switched mode power supplies.
SNR	signal-to-noise ratio.
SRIVC	simplified refined instrumental variable method for continuous time system identification.
STR	self-tuning regulators.
SVD	singular value decomposition.
VMC	voltage mode control.
VSM	valley switching modulator.
VSO	valley switching operation.

List of symbols

Notation	**Description**
T_{pwm}	Period of a PWM signal.
f_{pwm}	Frequency of a PWM signal.
$v_{in}(t)$	Instantaneous converter input voltage.
V_{in}	Steady state value of $v_{in}(t)$.
$\tilde{v}_{in}(t)$	Small signal AC variation of $v_{in}(t)$.
$i_m(t)$	Instantaneous magnetizing inductor current.
I_m	Steady state value of $i_m(t)$.
$\tilde{i}_m(t)$	Small signal AC variation of $i_m(t)$.
$v_c(t)$	Instantaneous output capacitance voltage.
V_c	Steady state value of $v_c(t)$.
$\tilde{v}_c(t)$	Small signal AC variation of $v_c(t)$.
$v_{out}(t)$	Instantaneous converter output voltage.
V_{out}	Steady state value of $v_{out}(t)$.
$\tilde{v}_{out}(t)$	Small signal AC variation of $v_{out}(t)$.
$d(t)$	Instantaneous duty ratio of a PWM signal.
D	Steady state value of $d(t)$.
$\tilde{d}(t)$	Small signal AC variation of $d(t)$.
$i_{out}(t)$	Instantaneous output current of the flyback converter.
$i_{in}(t)$	Instantaneous input current of the flyback converter.
L_m	Magnetizing inductor.
C	Output capacitor.
R	Output resistive load.
$i_{dyn}(t)$	Instantaneous dynamic load.
I_{dyn}	Steady state value of $i_{dyn}(t)$.
$\tilde{i}_{dyn}(t)$	Small signal AC variation of $i_{dyn}(t)$.
$\mathbf{x}(t)$	State variable vectors.
$\mathbf{y}(t)$	Output variable vectors.
$\mathbf{u}(t)$	Input variable vectors.
$Y_{in}(s)$	Input admittance.
$G_{idyn}(s)$	Output-current-to-input-current transfer function.

Notation	Description
$G_{id}(s)$	Control-signal-to-input-current transfer function.
$G_{vin}(s)$	Line-to-output-voltage transfer function.
$Z_{out}(s)$	Output impedance.
$G_{vd}(s)$	Control-signal-to-output-voltage transfer function.
$s_q(t)$	State variable of the switch Q.
$s_d(t)$	State variable of the diode D.
$q(t)$	General pulse-train control signal.
$q_{pwm}(t)$	PWM control signal.

List of Figures

List of Tables

Chapter 1

Introduction

1.1 Background

Nowadays, direct current (DC) voltage is commonly used in many applications ranging from personal devices, e.g. mobile phones, digital computers, to modern home appliances and state-of-the-art industrial instruments and implements, such as LED lighting, TV, and electric vehicles. These applications are generally powered either by alternating current (AC) voltage sources, mainly from electrical grids, or by unregulated DC voltage sources, e.g. batteries, solar panels; however, their internal circuits need a well regulated, ideally constant, DC voltage level to operate. The requirement for a constant DC voltage results in the introduction of a DC voltage regulator, also termed a DC power supply, whose main function is to transform any AC or DC voltages to a pre-defined DC voltage level.

In general, DC voltage regulators can be built based on either linear-circuit or switched-circuit principles. Compared with linear voltage regulators, switched mode power supplies (SMPSs) are preferable in modern applications due to their high energy conversion efficiency, which exceeds that obtained from the traditional linear approach. For example, a standard linear regulator containing a dissipative series resistor typically offers an efficiency of 30% which is much lower than the efficiency, ranging from 70% to 95%, of existing SMPSs [1, 2]. Furthermore, the utilization of high switching frequencies in SMPSs results in dramatic reduction in both size and weight of fundamental components, compared with linear regulators having the same power rating. Recent advances in digital control, semiconductor device, and magnetic components, make SMPSs even more compact and effective, properties which are attractive modern applications.

Depending on the nature of the input voltage, SMPSs can be classified as DC-to-DC or AC-to-DC applications, whose designs are quite similar and fundamentally based on DC-to-DC power converters except that AC-to-DC power supplies make use of a rectifier circuit to convert AC voltage to DC voltage, and an isolation transformer to ensure the safety of the users. In a large number of AC-to-DC applications, the transformer is incorporated into the DC-to-DC converter, which results in a class of converters, termed transformer isolated topologies, consisting of flyback converters, forward converters, push-pull transformer-isolated buck converters, full-bridge transformer-isolated buck converters, boost-derived isolated converters, and many others [3]. Flyback converters are commonly found in low-cost external power supplies, with output power ranging from a few watts to 120W, while other isolated topologies lend themselves to average and high power applications, typically from 100W to a couple of kilowatts.

Although each transformer-isolated topology has its own arrangement of circuit components and power-transfer scheme, its operating principle is similar to conventional DC-to-DC converters which rely on a switching semiconductor device (or devices) and energy-stored elements to control the amount of power transferred from the converter inputs to the outputs, subject to a constant output voltage. Taking a converter having only one switch and one inductor as an example, the energy from the converter input is firstly built up in the inductor when the switch is closed. The energy accumulated in the inductor is then delivered to the converter output when the switch is open. The total power transferred from input to output as well as the converter output voltage is determined by the ratio between the on- and off-time of the switch and the operating cycle, i.e. how fast the switch operates. Both the duty ratio and operating cycle are used as a control variable when designing controllers for SMPSs. In addition to the output voltage regulation, other control objectives, e.g. converter efficiency, electromagnetic interference (EMI) noises, acoustic noise, complexity, implementability, transient responses, are also important.

The focus of this thesis is on the design and implementation of low-cost digital controllers for external AC-to-DC SMPSs with the aim of maximizing the system efficiency, and providing fast transient responses with global stability. Although a conventional flyback converter, whose operation is discussed in detailed in Chapter 2, is adopted in this study as an example to theoretically and experimentally verify the effectiveness of the proposed control solution, some observations and theoretical results that emerged throughout the thesis can also be applied to other transformer-isolated converter topologies, which will be detailed in Chapter 9.

1.2 Motivation

According to the recent report in [4], the worldwide market share for external AC-to-DC SMPSs has shown a faster growing rate than other applications, and is expected to increase from about \$9.3 billion in 2011 to \$14.0 billion in 2016. The main contribution to such a rapid growth in the power supply market comes from low-power application segments such as mobile communications, computers, consumers, portable medical and LED lighting [4], which mainly rely on either single stage or two stage "flyback" converter topologies. The control solutions for commercial flyback converters are dominated by analogue designs but have been gradually evolved into digital implementation in recent years. The transition from analogue to digital control is due to the fact that analogue control can not keep up with stringent requirements of converter efficiency, and production costs and size, which have recently been imposed by new energy programs and market demands. Although digital control is more advantageous than its analogue counterpart in terms of functionality, programmability, i.e. ability to implement different control algorithms in the same hardware, susceptibility to ageing and environmental variations, and part counts, the application of digital control to flyback converters faces a serious challenge mostly because of limited control loop bandwidth and limited resolution of the signal measured. In addition to these inherent drawbacks, the cost-constraints imposed by the low-cost nature of flyback converters makes the challenge of digital control design even harder to handle.

Some attempts have been made in [5–8] to develop digital control prototypes for a flyback converter; however, these works focus on either the optimisation of converter efficiency or the development of sensing techniques rather than on controller design perspectives. Furthermore, the authors in [5–8] used high computational power processors for implementation which may not bring real benefit for low-cost applications. Therefore, in this thesis, the author tries to address the problem of designing fast and globally stable digital control using only low-performance microcontrollers.

Since the transformer is the most essential, and also the most complicated, part of the flyback converter, understanding and modelling its operation are necessary for the design of both the converter power stage and controller. In order to predict all responses of the flyback converter during start-up or over-load phases, both linear and non-linear characteristics of the transformer are important and need to be accurately modelled. Although transformer modelling has been intensively considered in power electronics, existing studies focus on either linear dynamic modelling [9–14] or non-linear core modelling [15–19] but not both. Therefore, an attempt is made in Chapter 5 towards the representation of both linear and non-linear behaviours using a unified transformer model and the identification of the model parameters using experimental data.

One important step in control design is to simulate the performance of the closed-loop flyback converter before prototyping. The converter model used for simulation should be as accurate as possible, which allows prediction of all potential instability occurring during a transition from one operating mode to another. A fully accurate converter model typically requires a significant execution time for simulation and produces an overwhelming amount of data, which makes the simulation infeasible. On the other hand, a simple converter model can be simulated in a much shorter time compared with that of the fully accurate model; however, the data generated is generally not accurate enough to draw any conclusion. For this reason, it is required to develop a converter model which can retain all essential dynamic characteristics of the flyback converter required by digital control, but offers a significantly reduced simulation time. Such is the main motivation for the research presented in Chapter 6.

For safety reasons, control for flyback converters requires isolation in the feedback path. Isolating control is conventionally implemented by an optical isolator and its drive circuit, but the optical solution has recently been replaced by magnetic sensing [5]. The main reason behind such a replacement is to improve the output voltage regulation and reduce the size and cost of the closed-loop system. Various magnetic sensing techniques have been proposed in the literature [5, 8, 20–27] with the main focus is on discontinuous conduction mode (DCM) flyback converters. Although several authors have tried to generalize their methods for both continuous and discontinuous conduction modes of the flyback converter [8, 21], they have not fully addressed the inherent issue of magnetic sensing in continuous conduction mode (CCM), i.e. the so-called cable voltage drop. Therefore, in Chapter 7, the author attempts to find a unified magnetic sensing solution which can operate seamlessly in both CCM and DCM and is capable of being implemented with a low performance microcontroller.

1.3 Main contributions

The main original contributions of this thesis are summarized as follows:

1. Chapter 2 develops a small signal model for both CCM and DCM flyback converters using a general load model that can represent both resistive and current-source-type loads. The efficacy of such a model is shown to be useful for the control design exercises in Chapters 7 and 8.

2. A non-linear dynamic transformer model and a systematic framework used to obtained model parameters from experimental time-domain data are proposed in Chapter 5. It is shown that the proposed model can accurately describe both frequency-dependent dynamics and non-linear core behaviours of a practical transformer and is valid for both small and large signals. As also demonstrated in Chapter 5, the time-domain identification approach may require a longer time to collect data, but it does need only simple measurement equipment and, most importantly, allows determination of transformer model parameters at least as accurate as those obtained with frequency-domain data. A method for reducing the round-off error occurring during data collection, based on varying the ranging resistor, is also demonstrated. Chapter 5 also shows that a unique mapping between the parameters of a continuous-time model and its Tustin equivalent discrete-time counterpart can be established by imposing a proper constraint on the discrete-time model. The possibility to improve the accuracy of the non-linear core model, by including the air gap length into the identification process, is also explored.

3. In Chapter 6, a control-oriented model is obtained through simplification of the full converter model in Chapter 5. It is shown that the control-oriented model allows significant reduction of the simulation execution time, by around 3 orders of magnitude, compared with the full model, while can retain adequate intra-cycle and inter-cycle dynamic fidelity of the flyback converter required by control design. An approach to the improvement of the execution speed of the simulation, based on algebraic loop removal and time-constant adjustment, is also demonstrated.

4. A unified CCM and DCM magnetic sensing principle, which relies on sampling the bias winding voltage at the point where the secondary current is known, is developed in Chapter 7. It is demonstrated that the unified sensing solution operates smoothly and accurately regardless of variations in operating modes of the flyback converter. Two approaches to the implementation of the unified magnetic sensing principle, based on analogue circuits and microcontrollers, are also explored.

5. In Chapter 8, an optimum digital control architecture for a flyback converter is proposed to satisfy a given set of specifications, e.g. system efficiency, performance, design complexity. Three different approaches to optimum controller synthesis, based on mixed-sensitivity H_∞ robust control theory, gain-adaptive predictive functional control (GAPFC) theory, and gain-adaptive quantitative feedback theory (GAQFT), are also developed. It is shown in Chapter 8 that :

   - For a flyback converter model with wide parametric variations, a H_∞ controller approach can ensure robust stability but cannot achieve the performance target as given by the design specifications.

- The GAPFC controller and the GAQFT controller can both provide stable and fast transient response performance even though global stability of only the GAQFT controller has been theoretically verified.

A new simple representation of the converter model, which is suitable for controller design, is also derived in Chapter 8.

Some contributions of this thesis have been published in a number of conferences and journals, as outlined below.

Journal articles

1. Vu, T. T. and O'Driscoll, S. and Ringwood, J. V., "Nonlinear dynamic transformer time-domain identification for power converter application", *IEEE Trans. on Power Electron.*, vol. 29, no. 1, pp. 318-327, Jan. 2014.
2. Vu, T. T. and O'Driscoll, S. and Ringwood, J. V., "Digital gain-adaptive robust control for variable-frequency, efficiency-optimized flyback converters", in preparation for submission to *IEEE Trans. on Power Electron.*.

Conference articles

1. Vu, T. T. and O'Driscoll, S. and Ringwood, J. V., "3-winding flyback transformer model extraction using time-domain system identification", *Proc. IEEE Int. Symp. on Power Electronics, Electrical Drives, Automation and Motion (SPEEDAM)*, Sorrento, Italy, pp. 458-463, June 2012.
2. Vu, T. T. and O'Driscoll, S. and Ringwood, J. V., "Primary-side sensing for a flyback converter in both continuous and discontinuous conduction mode", *Proc. Irish Signal and System (ISSC)*, Maynooth, Ireland, July 2012.
3. Vu, T. T. and O'Driscoll, S. and Ringwood, J. V., "Computationally efficient fixed parameter digital control of power converters", *Proc. IEEE Int. Symp. on Industrial Electronics (ISIE)*, Istanbul, Turkey, June 2014.
4. Vu, T. T. and O'Driscoll, S. and Ringwood, J. V., "A feasibility study into the robust control of a variable-frequency wide operating range flyback converter", *Proc. Irish Signal and System (ISSC)*, Limerick, Ireland, June 2014.
5. Vu, T. T. and O'Driscoll, S. and Ringwood, J. V., "Control-oriented modelling and simulation of a variable-frequency efficiency-optimized flyback converter", *Proc. IEEE Multi-Conf. on System and Control (MSC)*, Antibes, France, Oct. 2014

1.4 Thesis layout

The remainder of this thesis is organised as follows. The basic operation of the flyback converter and its switched model, averaged large- and small-signal models are introduced in Chapter 2. In the same chapter, the typical transfer functions of the voltage-mode controlled flyback converter and the peak current model controlled flyback converter are detailed. This is followed by a summary of the formulae for calculating total losses occurring inside the flyback converter and the offline efficiency optimisation procedure.

Chapter 3 presents an extensive review of power transformer modelling and simulation of DC-to-DC converters, while a review of the control methods proposed for handing wide variation range of DC-to-DC converter is discussed in Chapter 4.

Since the quality of a controller depends on the model and the control algorithm used, while the quality of control is influenced by the controller and the sensing network, the technical chapters in this thesis are separated into modelling, sensing network design, and controller design. In particular, a non-linear dynamic transformer model is proposed and identified from time-domain data in Chapter 5. The full-order flyback converter model resulting from the work in Chapter 5 is used as a basis for the development of the control-oriented model in Chapter 6. A unified magnetic sensing principle and its analogue and digital implementation are dealt with in Chapter 7. All the results developed in Chapters 2, 6, and 7 are employed during design and implementation of a low-cost optimum digital controller for the flyback converter proposed in Chapter 8. Finally, conclusions and suggested follow-on work are detailed in Chapter 9.

Chapter 2

Analysis of flyback DC-to-DC converters: Background

2.1 The flyback DC-to-DC converter

Compared to other transformer isolated topologies, the DC-to-DC flyback converter offers a number of distinctive advantages, such as simplicity, ease of design, and low cost, which make it one of the most prevalent choices for low-power AC-to-DC power supplies, typically below 200W. A typical example of such design, whose circuit diagram is illustrated in Fig. 2.1, is composed of three main stages: a rectifier, a power factor corrector, and a flyback DC-to-DC converter. The first stage rectifies the sinusoidal alternating current (AC) line voltage $v_{ac}(t)$ into the direct current (DC) signal $v_{rec}(t)$, which contains a large peak-to-peak ripple. The use of the rectifier circuit and capacitors can distort the input current $i_{ac}(t)$, drawn by the AC-to-DC power supply, and results in a low power factor. This is not acceptable for applications with input power exceeding 75W, according to IEC 6000-3-2 standard specifications [28]. Therefore, the power factor corrector is typically placed after the rectifier circuit, as shown in Fig. 2.1, to elevate the power factor of the system and also to provide the pre-regulated DC voltage $v_{in}(t)$ for the next stage. It should be noted that, for a power level less than 75W, the concern about the AC current distortion and harmonics is not important. Therefore, the power factor corrector is commonly replaced with a capacitor in many adapters/chargers to reduce the production cost. With or without the power factor corrector, the input DC voltage $v_{in}(t)$ is typically higher than the set point output voltage V_{out}, hence, the flyback DC-to-DC converter will perform a voltage step-down conversion and regulation to supply a constant DC level, as needed.

Basically, the flyback converter, as shown in Fig. 2.1, shares the operation principle with its buck-boost counterpart [3]. In particular, the transformer acts like two windings coupled through a magnetic core; one winding is used to store energy in the core while the other is used to remove it. When the metal-oxide-semiconductor field-effect transistor (MOSFET) Q_1 is on, the energy from the power factor corrector or input capacitor is accumulated within the transformer, and the secondary diode D_2 is reverse-biased. Turning Q_1 off will reverse the voltage on the secondary terminals of the transformer, which in turn forward-biases D_2 and forces the energy stored in the transformer to be transferred to the output load. By changing the ratio between the on- and off-cycle of the switch Q_1, we can manage the amount of energy transferring through the flyback

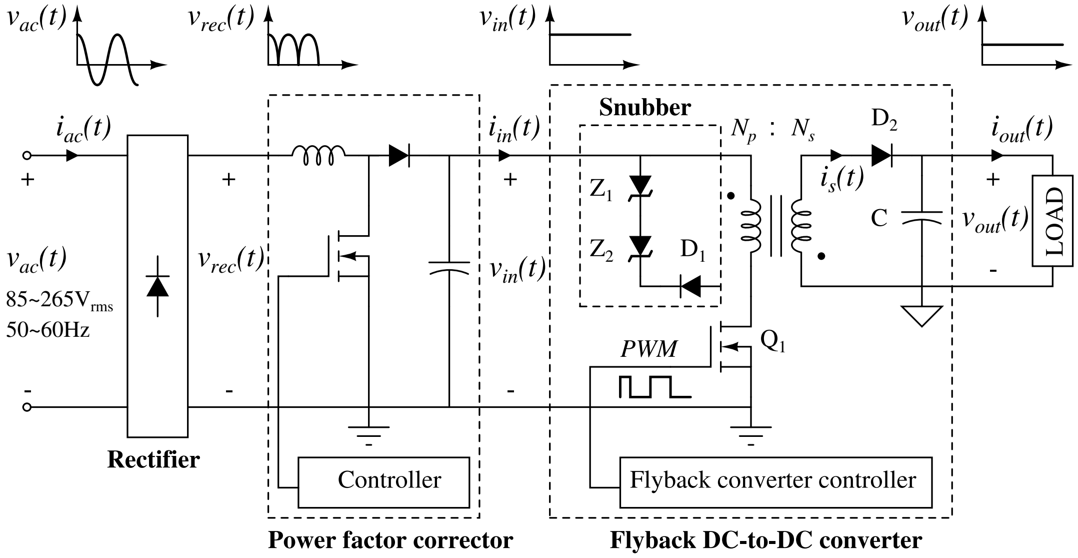

Figure 2.1: Circuit diagram of an external AC-to-DC power supply designed based on the DC-to-DC flyback topology

converter or, equivalently, the magnitude of $v_{out}(t)$. Since the flyback transformer is connected in an inverse polarisation manner, the input and output voltages of the converter have the same sign. This is one of the main differences between the buck-boost and flyback converters.

The detailed operation of the flyback converter and its mathematical model will be discussed in Sections 2.2 and 2.3, respectively. Given the small signal model of the flyback converter, Section 2.4 investigates two commonly used approaches, called voltage mode control (VMC) and peak current mode control (PCMC), to design a feedback loop for the output voltage regulation stage. In practice, the transition from Q_1 on to off can cause a large voltage spike across the drain and source of the MOSFET. This spike can easily pass the voltage rating and destroy the MOSFET if the snubber circuit, as can be seen in Fig. 2.1, is not utilized. Though the snubber circuit can prevent the switch Q_1 from being damaged, it dissipates the clamped energy into heat and, as a result, lowers the efficiency of the whole system. The power loss model for the flyback converter and efficiency improvement techniques are addressed in Sections 2.5 and 2.6, respectively.

2.2 Principle of operation

The behaviour of the flyback DC-to-DC converter can be adequately explained through its simple model, as presented in Fig. 2.2. D and Q are ideal switching devices while the flyback transformer is modelled by a magnetizing inductance L_m in parallel with an ideal transformer, whose transformation ratio n is defined by

$$n = \frac{N_s}{N_p}, \tag{2.1}$$

where N_p and N_s are a number of turns of the primary and secondary windings, respectively. It is noted that the inductor L_m is used in the transformer equivalent circuit to imitate the distinctive characteristic of the physical device, which is capable of storing energy. The load at the output of the flyback converter can be a constant resistance, or a current source with constant or unknown dynamic. In this thesis, we will consider a general load, including a resistor in parallel with a current source, as illustrated in Fig. 2.2, during the development of the converter model and control solution.

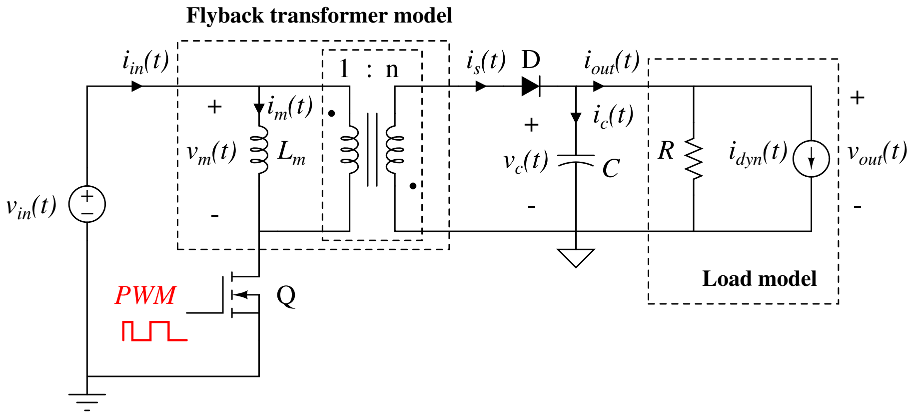

Figure 2.2: Simple model of the DC-to-DC flyback converter

Depending on the energy-transfer scheme, the operation of the DC-to-DC flyback converter can be divided into: (1) continuous conduction mode (CCM), in which only a part of the energy stored in the flyback transformer, when Q is on, is delivered to the output during the switch Q off-time, and (2) discontinuous conduction mode (DCM), in which all of the energy accumulated in the transformer, during the Q on-time, is transferred to the load by the end of the switching cycle.

2.2.1 Continuous conduction mode

As the energy stored in the transformer can be determined from the magnetizing inductor current i_m, the condition for the converter staying in CCM is equivalent to $i_m(t)$ never dropping to zero during the commutation cycle, as illustrated in Fig. 2.3. Although the waveform of $i_m(t)$ depends on the external excitation and pulse-width modulation (PWM) signal, it is typically the case that a heavy load and high switching frequency will impose the continuous mode of operation.

Since the converter circuit in Fig. 2.2 contains piecewise-linear elements, such as the diode D and switch Q, its operation can be formulated by breaking the commutation cycle into sub-intervals, in which the states of D and Q are fixed, and correspondingly solving the differential equations relating voltage and current signals for each configuration. Let us assume that the PWM signal has a switching period of T_{pwm} and duty ratio of d, as plotted in Fig. 2.3. The operation of the CCM flyback converter within a switching cycle can be decomposed as follows.

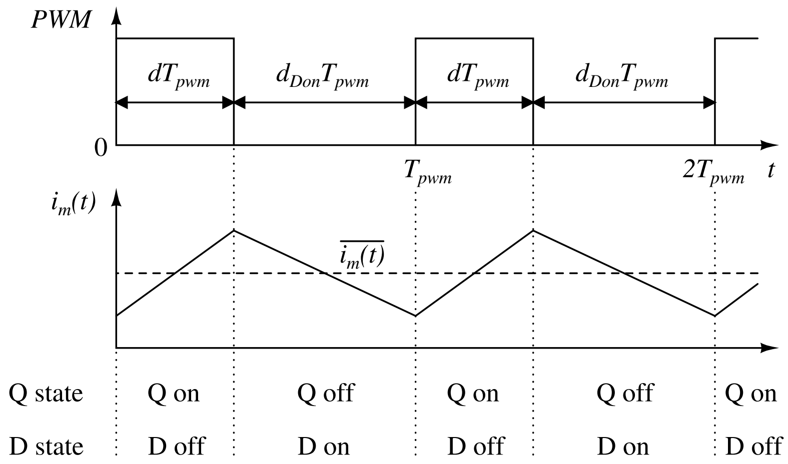

Figure 2.3: Magnetizing inductor current waveform of a PWM flyback converter in CCM

- For $0 \leq t \leq dT_{pwm}$: The switch Q is on and the diode D is off. The flyback converter in Fig. 2.2 reduces to a linear circuit whose branch voltages and currents can be established, based on the Kirchhoff's voltage and current laws, as

$$\begin{aligned} \frac{d}{dt}\mathbf{x}(t) &= \mathbf{A}_1\mathbf{x}(t) + \mathbf{B}_1\mathbf{u}(t), \\ \mathbf{y}(t) &= \mathbf{C}_1\mathbf{x}(t) + \mathbf{E}_1\mathbf{u}(t), \end{aligned} \tag{2.2}$$

where

$$\begin{aligned} \mathbf{A}_1 &= \begin{bmatrix} 0 & 0 \\ 0 & -\frac{1}{RC} \end{bmatrix}, \qquad \mathbf{B}_1 = \begin{bmatrix} \frac{1}{L_m} & 0 \\ 0 & -\frac{1}{C} \end{bmatrix}, \\ \mathbf{C}_1 &= \begin{bmatrix} 0 & 1 \end{bmatrix}, \qquad \mathbf{E}_1 = \begin{bmatrix} 0 & 0 \end{bmatrix} \end{aligned} \tag{2.3}$$

are state space matrices, while

$$\mathbf{x}(t) = \begin{bmatrix} i_m(t) \\ v_c(t) \end{bmatrix}, \quad \mathbf{u}(t) = \begin{bmatrix} v_{in}(t) \\ i_{dyn}(t) \end{bmatrix}, \quad \mathbf{y}(t) = [v_{out}(t)] \tag{2.4}$$

denote the state vector, input vector and output vector, respectively. It should be noted that the definition of the vectors $\mathbf{x}(t)$, $\mathbf{u}(t)$ and $\mathbf{y}(t)$ in Eq. (2.4) will be used throughout this chapter.

- For $dT_{pwm} \leq t \leq T_{pwm}$: The switch Q is off while the diode D is on. The state space equations describing the system in this mode are

$$\begin{aligned} \frac{d}{dt}\mathbf{x}(t) &= \mathbf{A}_2\mathbf{x}(t) + \mathbf{B}_2\mathbf{u}(t), \\ \mathbf{y}(t) &= \mathbf{C}_2\mathbf{x}(t) + \mathbf{E}_2\mathbf{u}(t), \end{aligned} \tag{2.5}$$

where

$$\begin{aligned}\mathbf{A}_2 &= \begin{bmatrix} 0 & -\frac{1}{nL_m} \\ \frac{1}{nC} & -\frac{1}{RC} \end{bmatrix}, \quad \mathbf{B}_2 = \begin{bmatrix} 0 & 0 \\ 0 & -\frac{1}{C} \end{bmatrix}, \\ \mathbf{C}_2 &= \begin{bmatrix} 0 & 1 \end{bmatrix}, \quad \mathbf{E}_2 = \begin{bmatrix} 0 & 0 \end{bmatrix}.\end{aligned} \tag{2.6}$$

2.2.2 Discontinuous conduction mode

Similarly, the discontinuous mode of operation can also be detected through examination of the current waveform across L_m. Specifically, if there exists a duration at the end of the commutation cycle where $i_m(t)$ is zero, as demonstrated in Fig. 2.4, the converter is said to be in DCM. In contrast to CCM, DCM typically occurs when the amount of energy gathered in L_m during the Q on-time is small, for example at light load conditions, or when the off-time of the operational cycle is long, i.e. low switching frequencies. The mathematical description of the flyback converter in DCM can be developed in a similar way as in Section 2.2.1. Specifically, the operation of the DCM flyback converter within a switching cycle can be separated into three parts, as demonstrated in Fig. 2.4. It should be noted that both DCM and CCM share most of the state space equations except for the configuration where both Q and D are off.

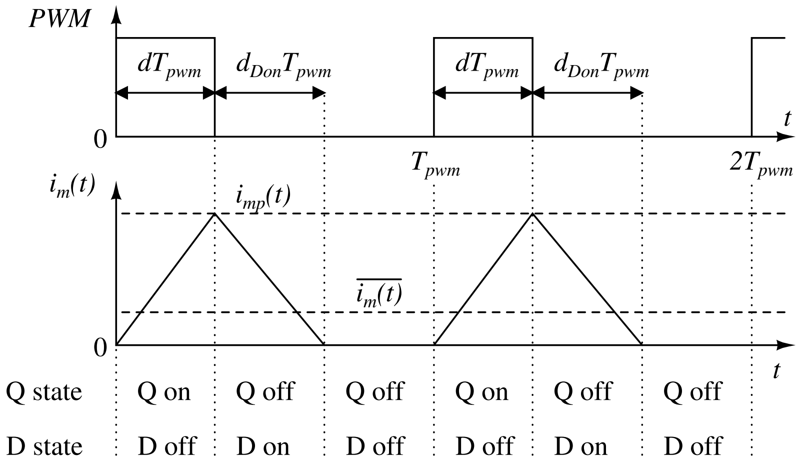

Figure 2.4: Magnetizing inductor current waveform of a PWM flyback converter in DCM

- For $0 \le t \le dT_{pwm}$: The switch Q is on and the diode D is off. Equation (2.2) can be used for this configuration.
- For $dT_{pwm} \le t \le (d + d_{Don})T_{pwm}$: The switch Q is off while the diode D is on. Equation (2.5) is employed.
- For $(d + d_{Don})T_{pwm} \le t \le T_{pwm}$: Both the switch Q and diode D are off. After simplifying

the circuit in Fig. 2.2, one can derive the following equations, as

$$\begin{aligned} \frac{d}{dt}\mathbf{x}(t) &= \mathbf{A}_3\mathbf{x}(t) + \mathbf{B}_3\mathbf{u}(t), \\ \mathbf{y}(t) &= \mathbf{C}_3\mathbf{x}(t) + \mathbf{E}_3\mathbf{u}(t), \end{aligned} \tag{2.7}$$

where

$$\begin{aligned} &\mathbf{A}_3 = \begin{bmatrix} 0 & 0 \\ 0 & -\frac{1}{RC} \end{bmatrix}, \qquad \mathbf{B}_3 = \begin{bmatrix} 0 & 0 \\ 0 & -\frac{1}{C} \end{bmatrix}, \\ &\mathbf{C}_3 = \begin{bmatrix} 0 & 1 \end{bmatrix}, \qquad \mathbf{E}_3 = \begin{bmatrix} 0 & 0 \end{bmatrix}. \end{aligned} \tag{2.8}$$

2.3 Modelling the power stage of the flyback converter

The switched model of the flyback converter, as discussed in Sections 2.2.1 and 2.2.2, can accurately describe both intra- and inter-cycle evolution of the state variable and output signals; however, such a model is too general to be used, particularly for DC analysis and control design. Sections 2.3.1 and 2.3.2 consider the application of the state space averaging technique [3,29,30] to develop large- and small-signal models for the flyback converter in CCM and DCM, respectively. The resulting state-space models from Sections 2.3.1 and 2.3.2 are then transformed to a set of transfer functions in Section 2.3.3.

2.3.1 Large- and small-signal state space models in CCM

2.3.1.1 Averaged large-signal model

If the PWM frequency is chosen to be considerably higher than the natural frequency of the flyback converter as well as the dynamic of the excitation signals, the averaged values of the state variables will not deviate much from their instantaneous values. In such a case, the inter-cycle behaviour of the converter can be modelled by averaging Eqs. (2.2) and (2.5) over one operational period as

$$\begin{aligned} \frac{d}{dt}\overline{\mathbf{x}(t)} &= \Big(d(t)\mathbf{A}_1 + \big(1-d(t)\big)\mathbf{A}_2\Big)\overline{\mathbf{x}(t)} + \Big(d(t)\mathbf{B}_1 + \big(1-d(t)\big)\mathbf{B}_2\Big)\overline{\mathbf{u}(t)}, \\ \overline{\mathbf{y}(t)} &= \Big(d(t)\mathbf{C}_1 + \big(1-d(t)\big)\mathbf{C}_2\Big)\overline{\mathbf{x}(t)} + \Big(d(t)\mathbf{E}_1 + \big(1-d(t)\big)\mathbf{E}_2\Big)\overline{\mathbf{u}(t)}, \end{aligned} \tag{2.9}$$

where $d(t)$ indicates the instantaneous duty ratio of the PWM signal. The over-line operator, denoting the local average over an interval of length T_{pwm}, is defined by

$$\overline{\mathbf{x}(t)} = \frac{1}{T_{pwm}} \int_t^{t+T_{pwm}} \mathbf{x}(\tau)d\tau. \tag{2.10}$$

The differential equation Eq. (2.9) is typically named the time-invariant large-signal state space model, which can be used directly to synthesize non-linear feedback controllers.

2.3.1.2 Steady state analysis

By keeping the duty ratio $d(t) = D$ fixed and imposing a constant input, i.e. $\overline{\mathbf{u}(t)} = \mathbf{U} = [V_{in} \quad I_{dyn}]^T$, the flyback converter will reach the steady state after all transients have subsided, i.e. $\overline{\mathbf{x}(t)} = \mathbf{X} = [I_m \quad V_c]^T$ and $\overline{\mathbf{y}(t)} = \mathbf{Y} = [V_{out}]$. The state space equation describing the converter in equilibrium can be derived by simplifying Eq. (2.9) to

$$\begin{aligned} 0 &= \big(D\mathbf{A}_1 + (1-D)\,\mathbf{A}_2\big)\mathbf{X} + \big(D\mathbf{B}_1 + (1-D)\,\mathbf{B}_2\big)\mathbf{U}, \\ \mathbf{Y} &= \big(D\mathbf{C}_1 + (1-D)\,\mathbf{C}_2\big)\mathbf{X} + \big(D\mathbf{E}_1 + (1-D)\,\mathbf{E}_2\big)\mathbf{U}. \end{aligned} \tag{2.11}$$

Substituting the expressions for $\mathbf{A}_1$, $\mathbf{A}_2$, $\mathbf{B}_1$, $\mathbf{B}_2$, $\mathbf{C}_1$, $\mathbf{C}_2$, $\mathbf{E}_1$ and $\mathbf{E}_2$ in Eqs. (2.3) and (2.6) into Eq. (2.11), we can solve for the quiescent values of the magnetizing inductor current, capacitor and output voltages as

$$\begin{aligned} I_m &= \frac{n}{1-D}\left(\frac{V_{out}}{R} + I_{dyn}\right), \\ V_c &= \frac{nD}{1-D}V_{in}, \\ V_{out} &= \frac{nD}{1-D}V_{in}. \end{aligned} \tag{2.12}$$

2.3.1.3 Small-signal model

To construct a small-signal model of Eq. (2.9), some further steps, consisting of perturbing the state variables around their nominal operating points and cancelling non-linear high-order terms, need to be conducted. For perturbation purposes, we introduce a small AC duty ratio variation and input variations, denoted by $\tilde{d}(t)$ and $\tilde{\mathbf{u}}(t) = \big[\tilde{v}_{in}(t) \quad \tilde{i}_{dyn}(t)\big]^T$, respectively, into the given quiescent values D and $\mathbf{U} = \big[V_{in} \quad I_{dyn}\big]$. This will result in

$$\begin{aligned} d(t) &= D + \tilde{d}(t), \\ \overline{\mathbf{u}(t)} &= \mathbf{U} + \tilde{\mathbf{u}}(t). \end{aligned} \tag{2.13}$$

In response to the variations in Eq. (2.13), the state variable and output vectors, $\overline{\mathbf{x}(t)}$ and $\overline{\mathbf{y}(t)}$, deviate from their equilibrium points $\mathbf{X} = \big[I_m \quad V_c\big]$ and $\mathbf{Y} = [V_{out}]$ by amounts $\tilde{\mathbf{x}}(t) = \big[\tilde{i}_m(t) \quad \tilde{v}_c(t)\big]^T$ and $\tilde{\mathbf{y}}(t) = \big[\tilde{v}_{out}(t)\big]$, respectively. Such deviations can be formalized by

$$\begin{aligned} \overline{\mathbf{x}(t)} &= \mathbf{X} + \tilde{\mathbf{x}}(t), \\ \overline{\mathbf{y}(t)} &= \mathbf{Y} + \tilde{\mathbf{y}}(t) \end{aligned} \tag{2.14}$$

Substituting the perturbed variables in Eqs. (2.13) and (2.14) into the non-linear large-signal model in Eq. (2.9) yields

$$\begin{aligned}\frac{d}{dt}\big(\mathbf{X}+\tilde{\mathbf{x}}(t)\big) &= (\mathbf{A}_1-\mathbf{A}_2)\big(D+\tilde{d}(t)\big)\big(\mathbf{X}+\tilde{\mathbf{x}}(t)\big)+(\mathbf{B}_1-\mathbf{B}_2)\big(D+\tilde{d}(t)\big)\big(\mathbf{U}+\tilde{\mathbf{u}}(t)\big)\\ &\quad+\mathbf{A}_2\big(\mathbf{X}+\tilde{\mathbf{x}}(t)\big)+\mathbf{B}_2\big(\mathbf{U}+\tilde{\mathbf{u}}(t)\big),\\ \mathbf{Y}+\tilde{\mathbf{y}}(t) &= (\mathbf{C}_1-\mathbf{C}_2)\big(D+\tilde{d}(t)\big)\big(\mathbf{X}+\tilde{\mathbf{x}}(t)\big)+(\mathbf{E}_1-\mathbf{E}_2)\big(D+\tilde{d}(t)\big)\big(\mathbf{U}+\tilde{\mathbf{u}}(t)\big)\\ &\quad+\mathbf{C}_2\big(\mathbf{X}+\tilde{\mathbf{x}}(t)\big)+\mathbf{E}_2\big(\mathbf{U}+\tilde{\mathbf{u}}(t)\big).\end{aligned} \tag{2.15}$$

By multiplying out Eq. (2.15) and eliminating the DC terms, based on Eq. (2.11), and products of small-signal AC quantities, such as $\tilde{d}(t)\tilde{\mathbf{x}}(t)$, one obtains the linear small-signal state space model, in CCM, as

$$\begin{aligned}\frac{d}{dt}\tilde{\mathbf{x}}(t) &= \big(D\mathbf{A}_1+(1-D)\mathbf{A}_2\big)\tilde{\mathbf{x}}(t)+\big(D\mathbf{B}_1+(1-D)\mathbf{B}_2\big)\tilde{\mathbf{u}}(t)\\ &\quad+\big((\mathbf{A}_1-\mathbf{A}_2)\,\mathbf{X}+(\mathbf{B}_1-\mathbf{B}_2)\,\mathbf{U}\big)\tilde{d}(t),\\ \tilde{\mathbf{y}}(t) &= \big(D\mathbf{C}_1+(1-D)\mathbf{C}_2\big)\tilde{\mathbf{x}}(t)+\big(D\mathbf{E}_1+(1-D)\mathbf{E}_2\big)\tilde{\mathbf{u}}(t)\\ &\quad+\big((\mathbf{C}_1-\mathbf{C}_2)\,\mathbf{X}+(\mathbf{E}_1-\mathbf{E}_2)\,\mathbf{U}\big)\tilde{d}(t).\end{aligned} \tag{2.16}$$

Using the expression of the state matrices in Eqs. (2.3) and (2.6), one can simplify Eq. (2.16) to

$$\begin{aligned}\frac{d}{dt}\tilde{\mathbf{x}}(t) &= \mathbf{A}_{ccm}\tilde{\mathbf{x}}(t)+\mathbf{B}_{ccm}\tilde{\mathbf{u}}(t)+\mathbf{F}_{ccm}\tilde{d}(t),\\ \tilde{\mathbf{y}}(t) &= \mathbf{C}_{ccm}\tilde{\mathbf{x}}(t)+\mathbf{E}_{ccm}\tilde{\mathbf{u}}(t)+\mathbf{K}_{ccm}\tilde{d}(t).\end{aligned} \tag{2.17}$$

where

$$\begin{aligned}&\mathbf{A}_{ccm}=\begin{bmatrix}0 & -\frac{1-D}{nL_m}\\ \frac{1-D}{nC} & -\frac{1}{RC}\end{bmatrix},\quad \mathbf{B}_{ccm}=\begin{bmatrix}\frac{D}{L_m} & 0\\ 0 & -\frac{1}{C}\end{bmatrix},\quad \mathbf{F}_{ccm}=\begin{bmatrix}\frac{V_{out}+nV_{in}}{nL_m}\\ -\frac{\frac{V_{out}}{R}+I_{dyn}}{(1-D)C}\end{bmatrix},\\ &\mathbf{C}_{ccm}=\begin{bmatrix}0 & 1\end{bmatrix},\quad \mathbf{E}_{ccm}=\begin{bmatrix}0 & 0\end{bmatrix},\quad \mathbf{K}_{ccm}=\begin{bmatrix}0\end{bmatrix}.\end{aligned} \tag{2.18}$$

2.3.2 Large- and small-signal state space models in DCM

2.3.2.1 Averaged large-signal model

The application of the state space averaging approach to switched-mode converters requires that the variations of the state variables within an operational cycle should be much smaller than their average values. Although such a small ripple condition can be easily satisfied in a CCM flyback converter, this is not the case in DCM where the inductor current $i_m(t)$, as demonstrated in Fig. 2.4, inherently possesses a large ripple in its waveform. Therefore, the original state-space averaging formulae in [30] need to be modified in order to correctly predict the inter-cycle behaviour in DCM [31]. Applying the modified procedure, as discussed in [31], to Eqs. (2.3), (2.6) and (2.8), one can obtain the following averaged model:

$$\begin{aligned}
\frac{d}{dt}\overline{\mathbf{x}(t)} &= \Big(d(t)\mathbf{A}_1 + d_{Don}(t)\mathbf{A}_2 + \big(1 - d(t) - d_{Don}(t)\big)\mathbf{A}_3\Big)\mathbf{M}\overline{\mathbf{x}(t)} \\
&\quad + \Big(d(t)\mathbf{B}_1 + d_{Don}(t)\mathbf{B}_2 + \big(1 - d(t) - d_{Don}(t)\big)\mathbf{B}_3\Big)\overline{\mathbf{u}(t)}, \\
\overline{\mathbf{y}(t)} &= \Big(d(t)\mathbf{C}_1 + d_{Don}(t)\mathbf{C}_2 + \big(1 - d(t) - d_{Don}(t)\big)\mathbf{C}_3\Big)\mathbf{M}\overline{\mathbf{x}(t)} \\
&\quad + \Big(d(t)\mathbf{E}_1 + d_{Don}(t)\mathbf{E}_2 + \big(1 - d(t) - d_{Don}(t)\big)\mathbf{E}_3\Big)\overline{\mathbf{u}(t)},
\end{aligned} \tag{2.19}$$

where

$$\mathbf{M} = \begin{bmatrix} \frac{1}{d(t)+d_{Don}(t)} & 0 \\ 0 & 1 \end{bmatrix} \tag{2.20}$$

indicates the modification matrix, and $d_{Don}(t) = \frac{T_{Don}}{T_{pwm}}$ is called the *diode conduction ratio* in this thesis, and T_{Don} is the diode conduction time. A close examination of $\mathbf{M}$ in Eq. (2.20) reveals that only a correction term $\frac{1}{d(t)+d_{Don}(t)}$, for the magnetizing inductor current, has been introduced in Eq. (2.19), and $\mathbf{M}$ reduces to an identity matrix of size 2 in the case of CCM, i.e. the approaches in [30] and [31] yield the same result in CCM.

Although the state matrices of the averaged DCM model, as described in Eq. (2.19), depend on two variables, $d(t)$ and $d_{Don}(t)$, they can be simplified to functions of $d(t)$ only. In order to perform such a simplification, it is important to note that the diode conduction ratio $d_{Don}(t)$ has an algebraic dependency on the instantaneous duty ratio $d(t)$ and the averaged state vector $\overline{\mathbf{x}(t)}$. Starting with the waveform of the inductor current shown in Fig. 2.4, the average of $i_m(t)$ over one switching cycle can be written as

$$\overline{i_m(t)} = \frac{i_{mp}(t)}{2}\big(d(t) + d_{Don}(t)\big). \tag{2.21}$$

During the interval $0 \leq t \leq d(t)T_{pwm}$, in which the switch Q is on, the inductor current $i_m(t)$ ramps up with a slope of $\frac{v_{in}(t)}{L_m}$, which is assumed to be constant. At the end of the Q on-time, $i_m(t)$ reaches its peak value which can be calculated by

$$i_{mp}(t) = \frac{v_{in}(t)}{L_m}d(t)T_{pwm}. \tag{2.22}$$

Substituting Eq. (2.22) into Eq. (2.21), and solving the resulting equation for $d_{Don}(t)$, yields

$$d_{Don}(t) = \frac{2L_m\overline{i_m(t)}}{\overline{v_{in}(t)}(t)d(t)T_{pwm}} - d(t). \tag{2.23}$$

By substituting Eqs. (2.3), (2.6), (2.8) and (2.23) into Eq. (2.19), and multiplying out the resulting equation, one can obtain

$$\begin{aligned}
\frac{d}{dt}\overline{i_m(t)} &= -\frac{2\overline{i_m(t)}\ \overline{v_c(t)}}{n\overline{v_{in}(t)}d(t)T_{pwm}} + \frac{d(t)\overline{v_c(t)}}{nLm} + \frac{d(t)\overline{v_{in}(t)}}{Lm},\\
\frac{d}{dt}\overline{v_c(t)} &= \frac{\overline{i_m(t)}}{nC} - \frac{\big(d(t)\big)^2 T_{pwm}\overline{v_{in}(t)}}{2nL_mC} - \frac{\overline{v_c(t)}}{RC} - \frac{\overline{i_{dyn}(t)}}{C},\\
\overline{v_{out}(t)} &= \overline{v_c(t)}.
\end{aligned} \tag{2.24}$$

2.3.2.2 Steady state analysis

The DC operating point of the flyback converter in DCM can be determined in a similar fashion to the situation for CCM, by imposing a constant duty ratio $d(t) = D$, input voltage $\overline{v_{in}(t)} = V_{in}$ and dynamic load $\overline{i_{dyn}(t)} = I_{dyn}$, and then solving Eq. (2.24) for the steady state values of the state variables and output voltage. Since the derivatives of $\overline{i_m(t)}$ and $\overline{v_c(t)}$ are zero at steady state, the differential equation Eq. (2.24) will be simplified to an algebraic relation, which is given by

$$\begin{aligned}
0 &= -\frac{2I_mV_c}{nV_{in}DT_{pwm}} + \frac{DV_c}{nLm} + \frac{DV_{in}}{Lm},\\
0 &= \frac{I_m}{nC} - \frac{D^2T_{pwm}V_{in}}{2nL_mC} - \frac{V_c}{RC} - \frac{I_{dyn}}{C},\\
V_{out} &= V_c.
\end{aligned} \tag{2.25}$$

Solving Eq. (2.25) for I_m, V_c, and V_{out} yields

$$\begin{aligned}
I_m &= \frac{D^2T_{pwm}V_{in}}{2L_m} + \frac{nV_c}{R} + nI_{dyn},\\
V_c &= -\frac{RI_{dyn}}{2} + \sqrt{\left(\frac{RI_{dyn}}{2}\right)^2 + \frac{D^2T_{pwm}RV_{in}^2}{2L_m}},\\
V_{out} &= V_c.
\end{aligned} \tag{2.26}$$

2.3.2.3 Small-signal model

By applying the linearisation procedure, as presented in Section 2.3.1, to the non-linear model in Eq. (2.24), one can derive a small signal model for a DCM flyback converter as

$$\begin{aligned}
\frac{d}{dt}\tilde{i}_m(t) &= -\frac{2M}{DT_{pwm}}\tilde{i}_m(t) - \left(\frac{2nM}{DT_{pwm}R} + \frac{2I_{dyn}}{DT_{pwm}V_{in}}\right)\tilde{v}_c(t)\\
&\quad + \frac{D(M+2)}{L_m}\tilde{v}_{in}(t) + \frac{2(M+1)V_{in}}{L_m}\tilde{d}(t),\\
\frac{d}{dt}\tilde{v}_c(t) &= \frac{1}{nC}\tilde{i}_m(t) - \frac{1}{RC}\tilde{v}_c(t) - \frac{D^2T_{pwm}}{2nL_mC}\tilde{v}_{in}(t) - \frac{1}{C}\tilde{i}_{dyn}(t) - \frac{DT_{pwm}V_{in}}{nL_mC}\tilde{d}(t),\\
\tilde{v}_{out}(t) &= \tilde{v}_c(t),
\end{aligned} \tag{2.27}$$

where the scalar variable $M = \frac{V_{out}}{nV_{in}}$ denotes the ratio between the output voltage and the input voltage referred to the secondary side of the transformer. In order to facilitate the mathematical derivation in Section 2.3.3, it is preferable to express the linear model in Eq. (2.27) in a matrix form as

$$\begin{aligned}\frac{d}{dt}\tilde{\mathbf{x}}(t) &= \mathbf{A}_{dcm}\tilde{\mathbf{x}}(t) + \mathbf{B}_{dcm}\tilde{\mathbf{u}}(t) + \mathbf{F}_{dcm}\tilde{d}(t),\\ \tilde{\mathbf{y}}(t) &= \mathbf{C}_{dcm}\tilde{\mathbf{x}}(t) + \mathbf{E}_{dcm}\tilde{\mathbf{u}}(t) + \mathbf{K}_{dcm}\tilde{d}(t).\end{aligned} \tag{2.28}$$

where

$$\begin{aligned}&\mathbf{A}_{dcm} = \begin{bmatrix} -\frac{2M}{DT_{pwm}} & -\frac{2nM}{DT_{pwm}R} - \frac{2I_{dyn}}{DT_{pwm}V_{in}} \\ \frac{1}{nC} & -\frac{1}{RC} \end{bmatrix}, \quad \mathbf{B}_{dcm} = \begin{bmatrix} \frac{D(M+2)}{L_m} & 0 \\ -\frac{D^2T_{pwm}}{2nL_mC} & -\frac{1}{C} \end{bmatrix},\\ &\mathbf{F}_{dcm} = s\begin{bmatrix} \frac{2(M+1)V_{in}}{L_m} \\ -\frac{DT_{pwm}V_{in}}{nL_mC} \end{bmatrix}, \quad \mathbf{C}_{dcm} = \begin{bmatrix} 0 & 1 \end{bmatrix}, \quad \mathbf{E}_{dcm} = \begin{bmatrix} 0 & 0 \end{bmatrix}, \quad \mathbf{K}_{dcm} = \begin{bmatrix} 0 \end{bmatrix}.\end{aligned} \tag{2.29}$$

2.3.3 Small signal models in the frequency domain

2.3.3.1 Transfer functions of the CCM flyback converter

The small-signal model of the CCM flyback converter, developed in Section 2.3.1.3, is represented in the state space (or time domain) format, which is not commonly used in control design and stability assessment of power converters. The reason is that the state space representation does not directly show how the output variable, i.e. the output voltage, is affected by disturbances in the input variables, i.e. the input voltage and load current, and control signal, i.e. duty ratio. Therefore, the small signal model of the flyback converter in the frequency domain is developed in this section. The state space equation in Eq. (2.18) can be converted to the frequency domain by Laplace transformation as follows:

$$\begin{aligned}s\tilde{\mathbf{x}}(s) &= \mathbf{A}_{ccm}\tilde{\mathbf{x}}(s) + \mathbf{B}_{ccm}\tilde{\mathbf{u}}(s) + \mathbf{F}_{ccm}\tilde{d}(s),\\ \tilde{\mathbf{y}}(s) &= \mathbf{C}_{ccm}\tilde{\mathbf{x}}(s) + \mathbf{E}_{ccm}\tilde{\mathbf{u}}(s) + \mathbf{K}_{ccm}\tilde{d}(s)\end{aligned} \tag{2.30}$$

where

$$\tilde{\mathbf{x}}(s) = \begin{bmatrix} \tilde{i}_m(s) \\ \tilde{v}_c(s) \end{bmatrix}, \quad \tilde{\mathbf{u}}(s) = \begin{bmatrix} \tilde{v}_{in}(s) \\ \tilde{i}_{dyn}(s) \end{bmatrix}, \quad \tilde{\mathbf{y}}(s) = \left[\tilde{v}_{out}(s)\right]. \tag{2.31}$$

Notice that the derivation of Eq. (2.30) is performed with zero initial conditions. Solving Eq. (2.30) for $\tilde{\mathbf{x}}(s)$ and $\tilde{\mathbf{y}}(s)$ leads to

$$\begin{aligned}\tilde{\mathbf{x}}(s) &= \big(s\mathbf{I} - \mathbf{A}_{ccm}\big)^{-1}\mathbf{B}_{ccm}\tilde{\mathbf{u}}(s) + \big(s\mathbf{I} - \mathbf{A}_{ccm}\big)^{-1}\mathbf{F}_{ccm}\tilde{d}(s),\\ \tilde{\mathbf{y}}(s) &= \Big(\mathbf{C}_{ccm}\big(s\mathbf{I} - \mathbf{A}_{ccm}\big)^{-1}\mathbf{B}_{ccm} + \mathbf{E}_{ccm}\Big)\tilde{\mathbf{u}}(s)\\ &\quad + \Big(\mathbf{C}_{ccm}\big(s\mathbf{I} - \mathbf{A}_{ccm}\big)^{-1}\mathbf{F}_{ccm} + \mathbf{K}_{ccm}\Big)\tilde{d}(s).\end{aligned} \tag{2.32}$$

Substituting Eq. (2.18) into Eq. (2.32) and simplifying the resulting equation to

$$\begin{aligned}\tilde{i}_m(s) &= Y_{in}(s)\tilde{v}_{in}(s) + G_{idyn}(s)\tilde{i}_{dyn}(s) + G_{id}(s)\tilde{d}(s),\\ \tilde{v}_{out}(s) &= G_{vin}(s)\tilde{v}_{in}(s) + Z_{out}(s)\tilde{i}_{dyn}(s) + G_{vd}(s)\tilde{d}(s)\end{aligned} \tag{2.33}$$

where

$$\begin{aligned}
Y_{in}(s) &= \frac{\tilde{i}_m(s)}{\tilde{v}_{in}(s)}\bigg|_{\tilde{i}_{dyn}(s),\tilde{d}(s)=0} = \frac{\frac{D}{RL_mC}\left(sRC+1\right)}{s^2+\frac{s}{RC}+\frac{(1-D)^2}{n^2L_mC}},\\
G_{idyn}(s) &= \frac{\tilde{i}_m(s)}{\tilde{i}_{dyn}(s)}\bigg|_{\tilde{v}_{in}(s),\tilde{d}(s)=0} = \frac{\frac{1-D}{nL_mC}}{s^2+\frac{s}{RC}+\frac{(1-D)^2}{n^2L_mC}},\\
G_{id}(s) &= \frac{\tilde{i}_m(s)}{\tilde{d}(s)}\bigg|_{\tilde{v}_{in}(s),\tilde{i}_{dyn}(s)=0} = \frac{s\frac{V_{in}}{(1-D)L_m}+\frac{(1+D)V_{in}}{(1-D)RL_mC}+\frac{I_{dyn}}{nL_mC}}{s^2+\frac{s}{RC}+\frac{(1-D)^2}{n^2L_mC}},\\
G_{vin}(s) &= \frac{\tilde{v}_{out}(s)}{\tilde{v}_{in}(s)}\bigg|_{\tilde{i}_{dyn}(s),\tilde{d}(s)=0} = \frac{\frac{D(1-D)}{nL_mC}}{s^2+\frac{s}{RC}+\frac{(1-D)^2}{n^2L_mC}},\\
Z_{out}(s) &= \frac{\tilde{v}_{out}(s)}{\tilde{i}_{dyn}(s)}\bigg|_{\tilde{v}_{in}(s),\tilde{d}(s)=0} = \frac{-s\frac{1}{C}}{s^2+\frac{s}{RC}+\frac{(1-D)^2}{n^2L_mC}},\\
G_{vd}(s) &= \frac{\tilde{v}_{out}(s)}{\tilde{d}(s)}\bigg|_{\tilde{v}_{in}(s),\tilde{i}_{dyn}(s)=0} = \frac{\frac{V_{in}}{nL_mC}\Big(-s\frac{nL_m}{(1-D)V_{in}}\left(\frac{V_{out}}{R}+I_{dyn}\right)+1\Big)}{s^2+\frac{s}{RC}+\frac{(1-D)^2}{n^2L_mC}}.
\end{aligned} \tag{2.34}$$

The transfer functions $Y_{in}(s)$, $G_{idyn}(s)$, $G_{id}(s)$, $G_{vin}(s)$, $Z_{out}(s)$ and $G_{vd}(s)$ are typically termed the input admittance, output-current-to-input-current transfer function, control-signal-to-input-current transfer function, line-to-output-voltage transfer function, output impedance and control-signal-to-output-voltage transfer function, respectively. Since $\tilde{v}_c(s) = \tilde{v}_{out}(s)$, the equation describing $\tilde{v}_c(s)$ as a function of $\tilde{v}_{in}(s)$, $\tilde{i}_{dyn}(s)$ and $\tilde{d}(s)$ has been omitted from Eq. (2.33) to avoid repetition.

2.3.3.2 Transfer functions of the DCM flyback converter

Similarly, the small signal model of the DCM flyback converter in the frequency domain, which is derived from Eq. (2.28), is governed by

$$\begin{aligned}\tilde{\mathbf{x}}(s) &= \left(s\mathbf{I}-\mathbf{A}_{dcm}\right)^{-1}\mathbf{B}_{dcm}\tilde{\mathbf{u}}(s) + \left(s\mathbf{I}-\mathbf{A}_{dcm}\right)^{-1}\mathbf{F}_{dcm}\tilde{d}(s),\\ \tilde{\mathbf{y}}(s) &= \Big(\mathbf{C}_{dcm}\left(s\mathbf{I}-\mathbf{A}_{dcm}\right)^{-1}\mathbf{B}_{dcm}+\mathbf{E}_{dcm}\Big)\tilde{\mathbf{u}}(s)\\ &\quad+\Big(\mathbf{C}_{ccm}\left(s\mathbf{I}-\mathbf{A}_{dcm}\right)^{-1}\mathbf{F}_{dcm}+\mathbf{K}_{dcm}\Big)\tilde{d}(s),\end{aligned} \tag{2.35}$$

Breaking the brackets in Eq. (2.35) and collecting like terms together gives

$$\begin{aligned}\tilde{i}_m(s) &= Y_{in}(s)\tilde{v}_{in}(s) + G_{idyn}(s)\tilde{i}_{dyn}(s) + G_{id}(s)\tilde{d}(s),\\ \tilde{v}_{out}(s) &= G_{vin}(s)\tilde{v}_{in}(s) + Z_{out}(s)\tilde{i}_{dyn}(s) + G_{vd}(s)\tilde{d}(s)\end{aligned} \tag{2.36}$$

where

$$
\begin{aligned}
Y_{in}(s) &= \left.\frac{\tilde{i}_m(s)}{\tilde{v}_{in}(s)}\right|_{\tilde{i}_{dyn}(s),\tilde{d}(s)=0} = \frac{s\frac{D(M+2)}{L_m} + \frac{2D(M+1)}{RL_mC} + \frac{DI_{dyn}}{nL_mCV_{in}}}{s^2 + s\left(\frac{2M}{DT_{pwm}} + \frac{1}{RC}\right) + \frac{4M}{DT_{pwm}RC} + \frac{2I_{dyn}}{nDT_{pwm}CV_{in}}},\\
G_{idyn}(s) &= \left.\frac{\tilde{i}_m(s)}{\tilde{i}_{dyn}(s)}\right|_{\tilde{v}_{in}(s),\tilde{d}(s)=0} = \frac{\frac{2nM}{DT_{pwm}DC} + \frac{2I_{dyn}}{DT_{pwm}CV_{in}}}{s^2 + s\left(\frac{2M}{DT_{pwm}} + \frac{1}{RC}\right) + \frac{4M}{DT_{pwm}RC} + \frac{2I_{dyn}}{nDT_{pwm}CV_{in}}},\\
G_{id}(s) &= \left.\frac{\tilde{i}_m(s)}{\tilde{d}(s)}\right|_{\tilde{v}_{in}(s),\tilde{i}_{dyn}(s)=0} = \frac{s\frac{2(M+1)V_{in}}{L_m} + \frac{2(2M+1)V_{in}}{RL_mC} + \frac{2I_{dyn}}{nL_mC}}{s^2 + s\left(\frac{2M}{DT_{pwm}} + \frac{1}{RC}\right) + \frac{4M}{DT_{pwm}RC} + \frac{2I_{dyn}}{nDT_{pwm}CV_{in}}},\\
G_{vin}(s) &= \left.\frac{\tilde{v}_{out}(s)}{\tilde{v}_{in}(s)}\right|_{\tilde{i}_{dyn}(s),\tilde{d}(s)=0} = \frac{\frac{2D}{nL_mC}\left(-s\frac{DT_{pwm}}{4} + 1\right)}{s^2 + s\left(\frac{2M}{DT_{pwm}} + \frac{1}{RC}\right) + \frac{4M}{DT_{pwm}RC} + \frac{2I_{dyn}}{nDT_{pwm}CV_{in}}},\\
Z_{out}(s) &= \left.\frac{\tilde{v}_{out}(s)}{\tilde{i}_{dyn}(s)}\right|_{\tilde{v}_{in}(s),\tilde{d}(s)=0} = \frac{-\frac{2M}{DT_{pwm}}\left(s\frac{DT_{pwm}}{2M} + 1\right)}{s^2 + s\left(\frac{2M}{DT_{pwm}} + \frac{1}{RC}\right) + \frac{4M}{DT_{pwm}RC} + \frac{2I_{dyn}}{nDT_{pwm}CV_{in}}},\\
G_{vd}(s) &= \left.\frac{\tilde{v}_{out}(s)}{\tilde{d}(s)}\right|_{\tilde{v}_{in}(s),\tilde{i}_{dyn}(s)=0} = \frac{\frac{2V_{in}}{nL_mC}\left(-s\frac{DT_{pwm}}{2} + 1\right)}{s^2 + s\left(\frac{2M}{DT_{pwm}} + \frac{1}{RC}\right) + \frac{4M}{DT_{pwm}RC} + \frac{2I_{dyn}}{nDT_{pwm}CV_{in}}}.
\end{aligned}
\tag{2.37}
$$

2.4 PWM control and modelling

In essence, the regulation of the flyback converter in Fig. 2.1 can be made by means of feedback control, in which the output voltage $v_{out}(t)$ is compared with a reference value to form an error voltage. This error is then utilized directly or indirectly to decide the on- and off-time of the MOSFET. Depending on the switching pattern, the control signal can be classified as pulse-width modulation (PWM), pulse-frequency modulation (PFM), delta-sigma modulation (DSM), and so on. The difference between them is explained in detail in Chapter 4. In this section, the focus is on PWM control techniques which utilize a fixed switching period, but adjust the duty cycle in order to regulate the output voltage. More precisely, two commonly used schemes, termed voltage mode control (VMC) and peak current mode control (PCMC), will be analysed, in Sections 2.4.1 and 2.4.2, respectively.

2.4.1 Voltage mode control

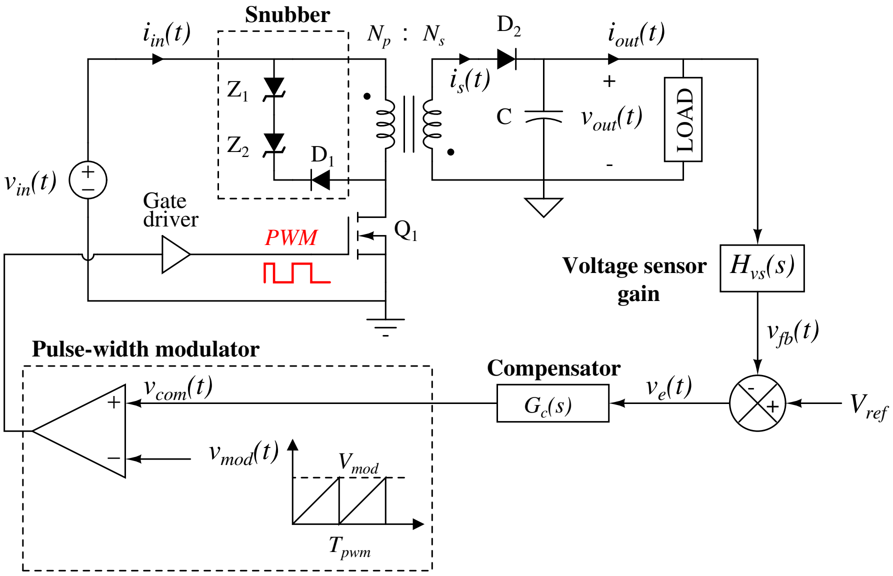

Figure 2.5: Output voltage regulation for the flyback converter based on VMC

The VMC scheme, whose block diagram is illustrated in Fig. 2.5, offers an intuitive and direct approach to the design of a feedback loop for the flyback converter. The output voltage $v_{out}(t)$ is firstly measured using a sensor having a gain of $H_{vs}(s)$. The feedback signal $v_{fb}(t)$ from the sensor circuit is then compared with the reference input V_{ref} to get the error voltage $v_e(t)$ and, accordingly, form the command signal $v_{com}(t)$. The duty ratio $d(t)$ of the PWM signal is controlled by $v_{com}(t)$ through a pulse-width modulator, which can be simply implemented by a comparator and the sawtooth voltage $v_{mod}(t)$ having a frequency of $f_{pwm} = \frac{1}{T_{pwm}}$ and a peak-to-peak amplitude of V_{mod}. One major characteristic of VMC, which can be discovered from Fig. 2.5, is that only a single feedback path is present in the design. As a consequence, VMC is simple to design and implement. However, the single feedback loop also causes a slow transient response of VMC. The reason is that any change in the input voltage or output load must be first sensed as an output change and then corrected by the feedback loop.

In an AC-to-DC application, galvanic isolation is required, for safety reasons, in both the power transfer and feedback paths. Therefore, the voltage sensor network, as shown in Fig. 2.5, is traditionally comprised of a voltage divider and an opto-isolator installed on the secondary side of the converter. Due to the low performance and high cost, the opto-coupler based solution is gradually being replaced by a new sensing technique in many new designs, termed magnetic sensing (MS). The investigation of the MS method and its application to the flyback converter is presented in Chapter 7.

For compensator design and closed-loop performance analysis, the linear model of the voltage mode controlled converter, as shown in Fig. 2.5, is required. Since the averaged small-signal description of the power stage was derived in Section 2.3, in the following sections, the focus is put on modelling the pulse-width modulator and presenting the feedback system in a form which is useful for the subsequent chapters.

2.4.1.1 Modelling the pulse-width modulator

As demonstrated in Fig. 2.6, the duty ratio is a direct result of the comparison of the compensator output $v_{com}(t)$ and a pre-defined sawtooth waveform $v_{mod}(t)$. Since $v_{mod}(t)$ has a minimum of zero and maximum of V_{mod}, the duty ratio $d(t)$ will be zero when $v_{com}(t) \leq 0$, and will be clamped at 1 for $v_{com}(t) \geq V_{mod}$. When $0 \leq v_{com}(t) \leq V_{mod}$, the relation between $d(t)$ and $v_{com}(t)$ is linear and can be described by

$$d(t) = \frac{v_{com}(t)}{V_{mod}}. \tag{2.38}$$

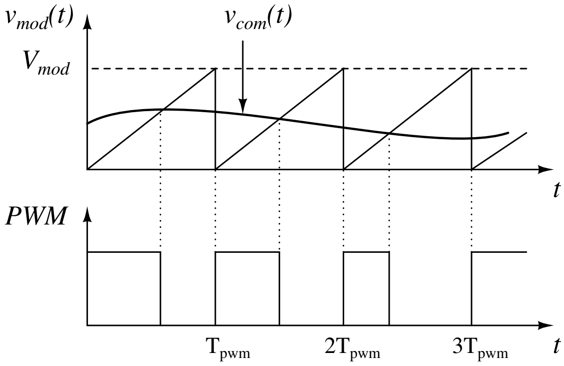

Figure 2.6: Timing diagram of the pulse-width modulator

Equation (2.38) describes the large signal characteristics of the VMC pulse-width modulator. For a linearised version of Eq. (2.38), the principle described in Section 2.3 can be reused, which results in

$$\tilde{d}(t) = \frac{\tilde{v}_{com}(t)}{V_{mod}}, \tag{2.39}$$

where $\tilde{d}(t)$ and $\tilde{v}_{com}(t)$ indicate the AC small-signal variations of $d(t)$ and $v_{com}(t)$. Since the operation of the pulse-width modulator is independent of that of the converter power stage, the large- and small-signal models, as given in Eqs. (2.38) and (2.39), respectively, are valid for any working condition of the converter.

2.4.1.2 Small-signal transfer functions in CCM

Given the transfer functions of the flyback converter in Eq. (2.33) and the pulse-width modulator in Eq. (2.39), the small-signal model of the feedback loop designed with VMC can be found as

$$\begin{aligned}\tilde{i}_m(s) &= Y_{in}(s)\tilde{v}_{in}(s) + G_{idyn}(s)\tilde{i}_{dyn}(s) + G_{id}(s)\tilde{d}(s),\\ \tilde{v}_{out}(s) &= G_{vin}(s)\tilde{v}_{in}(s) + Z_{out}(s)\tilde{i}_{dyn}(s) + G_{vd}(s)\tilde{d}(s),\\ \tilde{d}(s) &= \frac{\tilde{v}_{com}(s)}{V_{mod}}.\end{aligned} \tag{2.40}$$

For output voltage regulation, the description of the converter output voltage as a function of the control signal and input disturbances is of interest. Therefore, Eq. (2.40) can be reduced to

$$\tilde{v}_{out}(s) = G_{vin}(s)\tilde{v}_{in}(s) + Z_{out}(s)\tilde{i}_{dyn}(s) + G_{vd}(s)\frac{\tilde{v}_{com}(s)}{V_{mod}}, \tag{2.41}$$

where the transfer functions $G_{vin}(s)$, $Z_{out}(s)$ and $G_{vd}(s)$ are provided in Eq. (2.34). Given the small signal equivalent model of VMC in Eq. (2.41), the block diagram of the voltage regulation feedback loop can be constructed as in Fig. 2.7, where the input variables $\tilde{v}_{in}(s)$ and $\tilde{i}_{dyn}(s)$ are typically known as input disturbances.

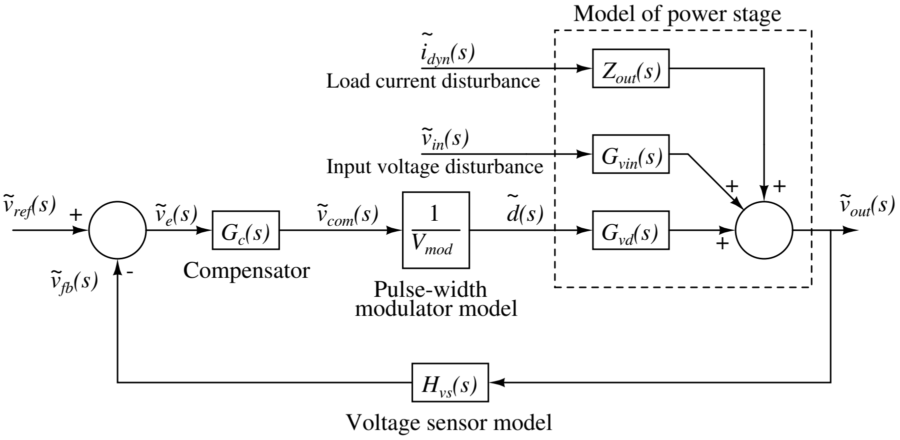

Figure 2.7: Small signal model of the voltage mode controlled flyback converter in CCM.

2.4.1.3 Small-signal transfer functions in DCM

Similarly, by inserting Eq. (2.39) into Eq. (2.36) and solving the resulting equation for $\tilde{v}(s)$, we can obtain the transfer functions of the voltage model controlled converter in DCM, which is similar to Eq. (2.41), except that the expressions of $G_{vin}(s)$, $Z_{out}(s)$ and $G_{vd}(s)$ are taken from Eq. (2.37). It should be noted that the graphical representation of VMC for a CCM converter, as presented in Fig. 2.7, is also applicable to the DCM scenario.

2.4.2 Peak current mode control

The limitations of the system performance using VMC prompts designers to seek other control topologies which are able to offer improvements over VMC. Peak current mode control (PCMC), which was first adopted in [32], was immediately seized upon as a superior approach to design controllers for power converters. The reason is that it offers several advantages over classical direct duty ratio control, such as an automatic over current protection, improved dynamic response, minimization of the effect of non-minimum phase, and many others. PCMC and its variants subsequently have been a subject of intensive research and many publications [33–41] for over two decades.

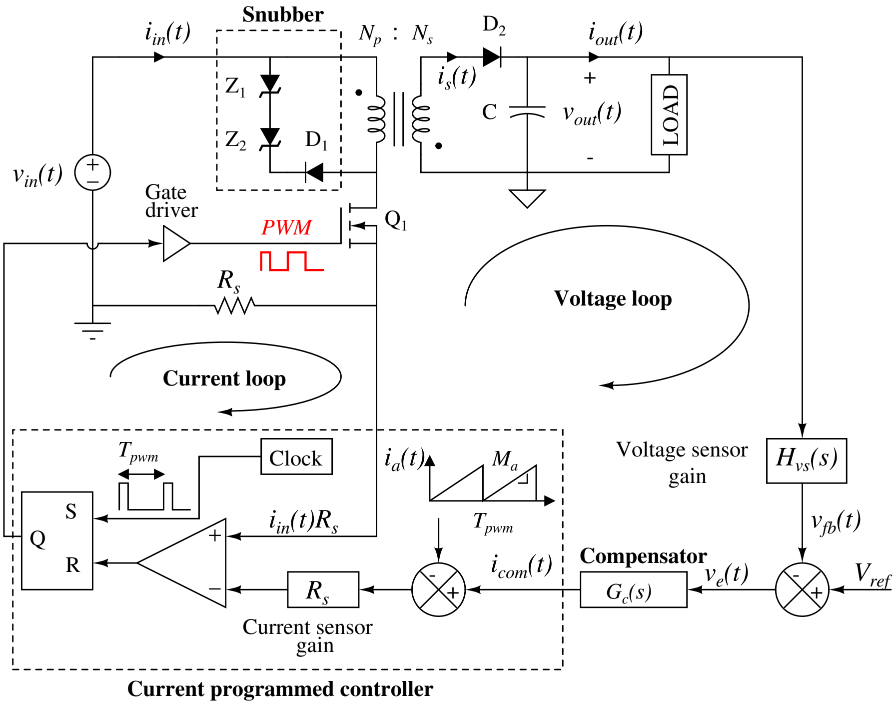

Figure 2.8: Output voltage regulation for the flyback converter based on PCMC

PCMC regulates the output voltage through control of the magnetizing inductor current rather than the duty ratio. By avoiding the direct duty ratio command, the controller is capable of handling fast input voltage and load variations during the operating time, and protecting the power circuit from hazardous conditions. In principle, PCMC has two loops, as can be seen in Fig. 2.8. The inner current loop is responsible for forcing the magnetizing inductor current to follow a reference level that is programmed by the outer voltage loop.

To generate the PWM signal, the current programmed controller, as depicted in Fig. 2.8, uses a fixed frequency clock to cyclically set the SR latch, while the comparator resets the SR latch whenever the sensed inductor current $i_m(t)$ reaches the current command $i_{com}(t) - i_a(t)$. In this way, the peak inductor current precisely follows the reference level which is yielded by the voltage control loop. Figures 2.9 and 2.11 demonstrate such a modulation procedure for the flyback converter in CCM and DCM, respectively. As the current command $i_{com}(t) - i_a(t)$ is related to the duty ratio of the PWM signal, the regulation of the converter output voltage can be achieved with a proper design of the compensator $G_c(s)$.

In practice, the magnetizing inductor current $i_m(t)$ is not a physical quantity, hence can not be measured directly. Fortunately, $i_m(t) = i_{in}(d)$ for the duration when the MOSFET is on. Therefore $i_{in}(t)$ presents an alternative to $i_m(t)$ in the implementation of PCMC. The artificial ramp $i_a(t)$ is required to stabilise the current mode controller when the flyback converter is in CCM and $d(t) \geq 0.5$.

The performance and stability of the system in Fig. 2.8 can only be characterised when its AC equivalent circuit model is available. For such a requirement, the operation of PCMC will be mathematically described in Sections 2.4.2.1 and 2.4.2.2.

2.4.2.1 Small-signal transfer functions in CCM

The control variable in PCMC is the instantaneous peak value of the inductor current, while the small signal AC equivalent model, developed in Section 2.3, predicts the converter behaviour in terms of variations in the duty ratio and average input voltage, and average dynamic load. Therefore, it is necessary to find the relationship between the current command $i_{com}(t)$, the duty ratio $d(t)$ and the other model variables.

For the inductor current waveform in Fig. 2.9, the average value of $i_m(t)$ over one switching period can be computed via

$$\overline{i_m(t)} = i_{com}(t) - M_a d(t) T_{pwm} - \frac{1}{2} m_1 \big(d(t)\big)^2 T_{pwm} - \frac{1}{2} m_2 \big(1 - d(t)\big)^2 T_{pwm}, \tag{2.42}$$

where M_a, m_1, and m_2 are the slope of $i_a(t)$, the slope of $i_m(t)$ during the switch on-time, and the slope of $i_m(t)$ during the switch off-time, respectively. The compensation slope M_a is normally unchanged during the operation, while the rising and falling inductor current slopes m_1 and m_2 are dependent on the input and output voltages via

$$\begin{aligned} m_1 &= \frac{\overline{v_{in}(t)}}{L_m}, \\ m_2 &= \frac{\overline{v_{out}(t)}}{n L_m}. \end{aligned} \tag{2.43}$$

In the derivation of Eq. (2.43), the voltage drops on the secondary diode D$_2$, MOSFET and parasitic resistance are assumed to be small and can be neglected, and $\overline{v_{in}(t)}$ and $\overline{v_{out}(t)}$ are assumed to be virtually constant within a switching cycle, for example the time interval from 0 to T_{pwm} as

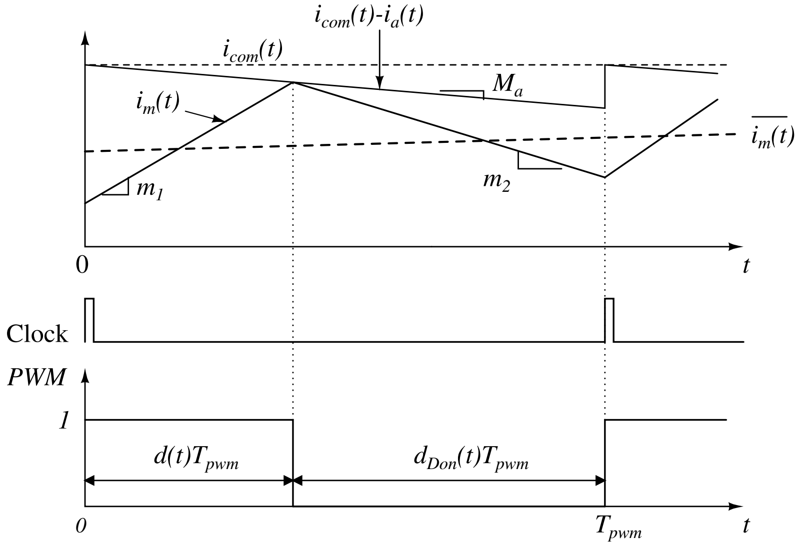

Figure 2.9: Operation of the current programmed controller with slope compensation in CCM

exemplified in Fig. 2.9. Substituting Eq. (2.43) into Eq. (2.42) yields

$$\overline{i_m(t)} = i_{com}(t) - M_a d(t)T_{pwm} - \frac{\overline{v_{in}(t)}\big(d(t)\big)^2 T_{pwm}}{2L_m} - \frac{\overline{v_{out}(t)}\big(1-d(t)\big)^2 T_{pwm}}{2nL_m}, \tag{2.44}$$

In order to find the small signal model of the current programmed controller, Eq. (2.44) is perturbed and linearised around a DC quiescent point. This leads to

$$\tilde{i}_m(t) = \tilde{i}_{com}(t) - M_a T_{pwm}\tilde{d}(t) - \frac{D^2 T_{pwm}}{2L_m}\tilde{v}_{in}(t) - \frac{\big(1-D\big)^2 T_{pwm}}{2nL_m}\tilde{v}_{out}(t). \tag{2.45}$$

Solving Eq. (2.45) for $\tilde{d}(t)$ yields

$$\tilde{d}(t) = F_m\big(\tilde{i}_{com}(t) - \tilde{i}_m(t) - F_{in}\tilde{v}_{in}(t) - F_v\tilde{v}_{out}(t)\big), \tag{2.46}$$

where F_m, F_{in} and F_{out} are typically referred as the modulator gain, input voltage feed-forward gain, and output voltage feed-forward gain, respectively. The expressions for F_m, F_{in} and F_{out} can be found as

$$F_m = \frac{1}{M_a T_{pwm}}, \quad F_{in} = \frac{D^2 T_{pwm}}{2L_m}, \quad F_v = \frac{\big(1-D\big)^2 T_{pwm}}{2nL_m}. \tag{2.47}$$

The Laplace transform of Eq. (2.46), with zero initial conditions, is

$$\tilde{d}(s) = F_m\big(\tilde{i}_{com}(s) - \tilde{i}_m(s) - F_{in}\tilde{v}_{in}(s) - F_v\tilde{v}_{out}(s)\big). \tag{2.48}$$

Combining Eqs. (2.48) and (2.33) results in the small signal transfer functions of PCMC, which is

$$\begin{aligned} \tilde{i}_m(s) &= Y_{in}(s)\tilde{v}_{in}(s) + G_{idyn}(s)\tilde{i}_{dyn}(s) + G_{id}(s)\tilde{d}(s), \\ \tilde{v}_{out}(s) &= G_{vin}(s)\tilde{v}_{in}(s) + Z_{out}(s)\tilde{i}_{dyn}(s) + G_{vd}(s)\tilde{d}(s), \\ \tilde{d}(s) &= F_m\big(\tilde{i}_{com}(s) - \tilde{i}_m(s) - F_{in}\tilde{v}_{in}(s) - F_v\tilde{v}_{out}(s)\big). \end{aligned} \tag{2.49}$$

Eliminating $\tilde{d}(s)$ and $\tilde{i}_m(s)$ in Eq. (2.49) leads to

$$\tilde{v}_{out}(s) = G_{vc}(s)\tilde{i}_{com}(s) + G_{vin\_pcm}(s)\tilde{v}_{in} + Z_{out\_pcm}\tilde{i}_{dyn}(s) \tag{2.50}$$

where

$$\begin{aligned} G_{vc}(s) &= \frac{F_m G_{vd}(s)}{1 + F_m G_{id}(s) + F_m F_v G_{vd}(s)}, \\ G_{vin\_pcm}(s) &= \frac{G_{vin}(s)\big(1 + F_m G_{id}(s)\big) - F_m G_{vd}(s)\big(Y_{in}(s) + F_{in}\big)}{1 + F_m G_{id}(s) + F_m F_v G_{vd}(s)}, \\ Z_{out\_pcm}(s) &= \frac{Z_{out}(s)\big(1 + F_m G_{id}(s)\big) - F_m G_{vd}(s) G_{idyn}(s)}{1 + F_m G_{id}(s) + F_m F_v G_{vd}(s)}, \end{aligned} \tag{2.51}$$

while $G_{vd}(s)$, $G_{id}(s)$, $Y_{in}(s)$, $G_{idyn}(s)$, and $Z_{out}(s)$ are given by Eq. (2.34). Given the relationships between the output voltage, the input variables, and the control signal in Eq. (2.51), the small signal model of the closed-loop CCM flyback converter based on PCMC can be formed, which is graphically illustrated in Fig. 2.10.

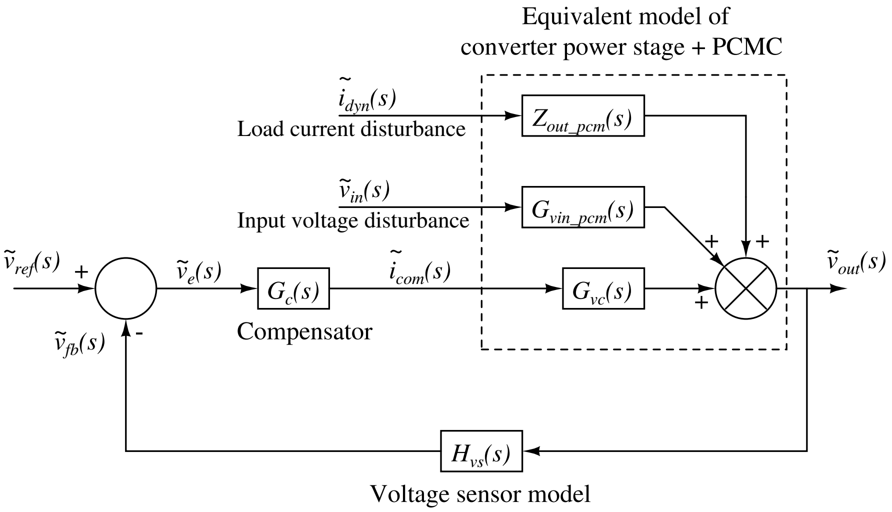

Figure 2.10: Small signal model of the peak current mode controlled flyback converter in CCM.

2.4.2.2 Small signal transfer functions in DCM

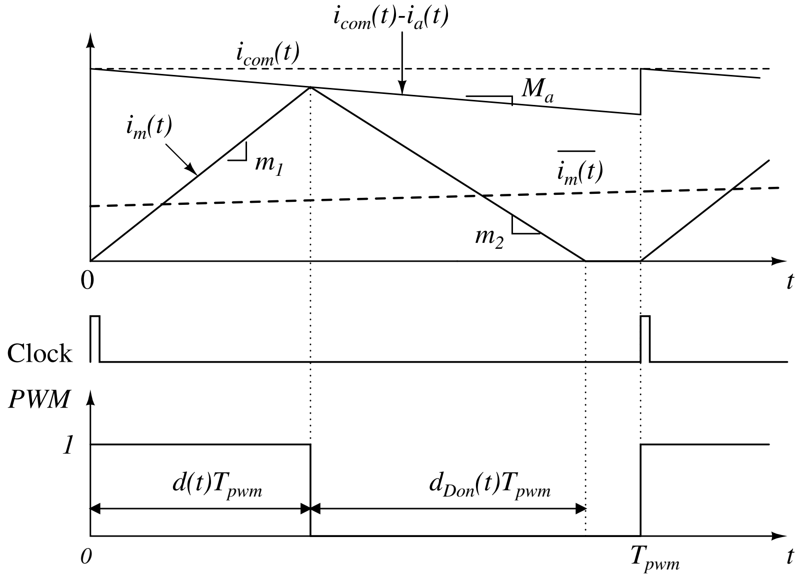

Figure 2.11: Operation of the current programmed controller with slope compensation in DCM

The transfer function of PCMC in DCM can be developed in a similar manner as discussed in Section. 2.4.2.1. In particular, based on the graphical illustration of the operation of the peak current modulator as shown in Fig. 2.11, the command current $i_{com}(t)$ can be expressed in terms of the duty ratio $d(t)$ as

$$i_{com}(t) = M_a d(t) T_{pwm} + m_1 d(t) T_{pwm}. \tag{2.52}$$

Substituting $m_1 = \frac{\overline{v_{in}(t)}}{L_m}$ into Eq. (2.52) produces

$$i_{com}(t) = M_a d(t) T_{pwm} + \frac{d(t) T_{pwm} \overline{v_{in}(t)}}{L_m}. \tag{2.53}$$

By perturbing and linearising Eq. (2.53) around an operating point, the relationship between variations of the command current and duty ratio can be found as

$$\tilde{d}(t) = F_m \left[\tilde{i}_{com}(t) - F_{in} \tilde{v}_{in}(t) \right] \tag{2.54}$$

where

$$F_m = \frac{1}{\left(M_a + \frac{V_{in}}{L_m} \right) T_{pwm}}, \quad F_{in} = \frac{D T_{pwm}}{L_m}. \tag{2.55}$$

Given the transfer functions of the DCM flyback converter in Eq. (2.36) and the model of the peak current modulator in Eq. (2.54), the small signal equivalent model for PCMC in the frequency domain can be derived as

$$\tilde{v}_{out}(s) = G_{vc}(s)\tilde{i}_{com}(s) + G_{vin\_pcm}(s)\tilde{v}_{in} + Z_{out\_pcm}\tilde{i}_{dyn}(s) \tag{2.56}$$

where

$$\begin{aligned} G_{vc}(s) &= F_m G_{vd}(s), \\ G_{vin\_pcm}(s) &= G_{vin}(s) - F_m F_{in} G_{vd}(s), \\ Z_{out\_pcm}(s) &= Z_{out}(s), \end{aligned} \tag{2.57}$$

where the formulas of $G_{vd}(s)$, $G_{id}(s)$, $Y_{in}(s)$, $G_{idyn}(s)$, and $Z_{out}(s)$ can be found in Eq. (2.37).

2.5 Power loss modelling and efficiency optimization in the flyback converter

Due to the rapid development of personal consumer electronics, such as mobile phones and tablets, in both number and processing power, the requirement for high efficiency AC-to-DC chargers has become vital. Such a requirement has spawned new energy programs and initiatives, for example U.S. Energy Start [42], European Code of Conduct (CoC). These energy programmes demand that external power supplies not only maintain a high efficiency over an entire load range, but also limit the power consumption during the sleep mode. Therefore, improving efficiency has recently emerged as a top priority in the design of flyback converters.

Modelling different types of losses inside the flyback converter is a prerequisite for efficiency characterization. Ideally, the model should encompass all the power dissipation from each circuit component. However, a highly accurate representation may require significant computation power and time, as a result, may not be useful in certain scenarios, for instance online efficiency optimization. For such a reason, this section adopts a sufficiently detailed model which focuses on describing the main loss mechanisms in the converter only. The formulae derived in this section are mainly based on the studies in [43–47].

Since the primary aim is to calculate the losses in each circuit component, the flyback converter model, as shown in Fig. 2.12, is constructed in such a way as to accurately describe the system losses, rather than to try to reproduce the real signal waveforms. For example, the purposes of the resistors r_{Qon} and r_{Don} are to model the conduction losses in the converter due to parasitic resistance, while the losses due to the switching action are considered by the capacitors and inductors, such as L_{leak} and C_{ds}. The switching devices D and Q in Fig. 2.12 are considered ideal and do not dissipate energy. Other sources of losses including the power supplied to the microcontroller, the leakage current loss, etc., are usually small and are not included in the analysis of this chapter.

Since the power loss is, in general, calculated based on the branch voltage and current waveforms, it is necessary to know these signals for each operating point of the converter. Given the presence of the parasitic capacitors and inductors, the signal waveforms in the circuit, as sketched in Fig. 2.12, will be rather complex and impossible to express in analytical formulae. Therefore,

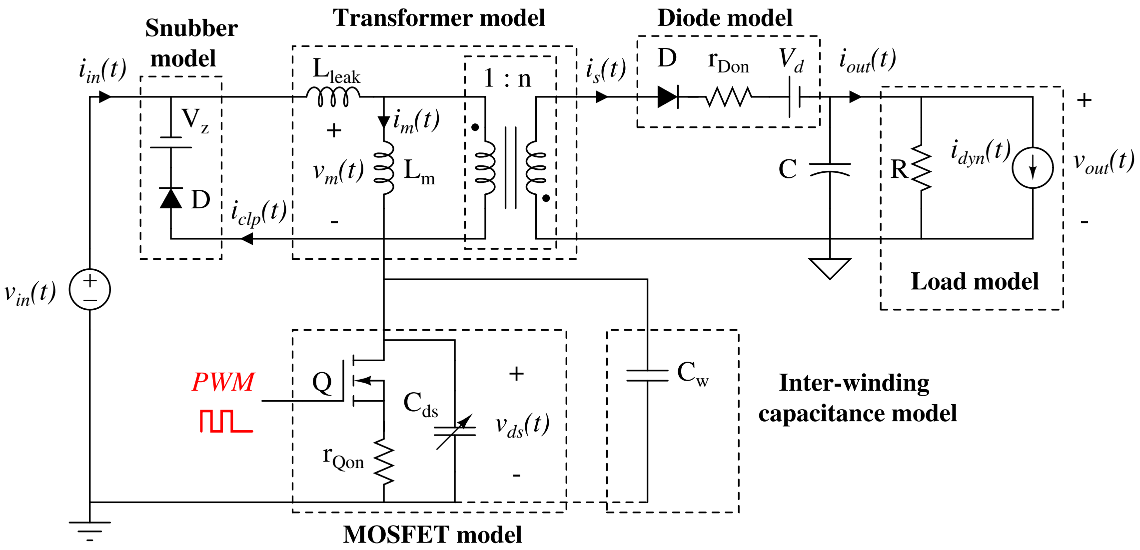

Figure 2.12: Flyback converter model which takes into account loss from each circuit component. For simplicity, the power dissipated by the transformer core and winding are not presented in this diagram.

the simple model in Fig. 2.2 will be used as a means to calculate the branch voltages and currents. For further simplification, the converter loss and efficiency is assumed to be considered only at steady state. This means that $v_{in}(t)$, $v_{out}(t)$, R and $i_{dyn}(t)$ are virtually constant.

The remainder of this section is organized as follows. The power dissipated in each component of the converter circuit is addressed in Sections 2.5.1, 2.5.2, 2.5.3, and 2.5.4, while a procedure for optimizing the efficiency of the flyback converter, based on varying the switching frequency according to the converter operating point, is presented in Section 2.5.5. Notice that a review of efficiency improvement techniques is reported in Section 2.6.

2.5.1 Conduction losses

Since the converter can operate in either CCM or DCM, depending on the external excitation and the switching frequency $f_{pwm} = \frac{1}{T_{pwm}}$, separate calculation of conduction losses is required for each operating mode.

2.5.1.1 In CCM

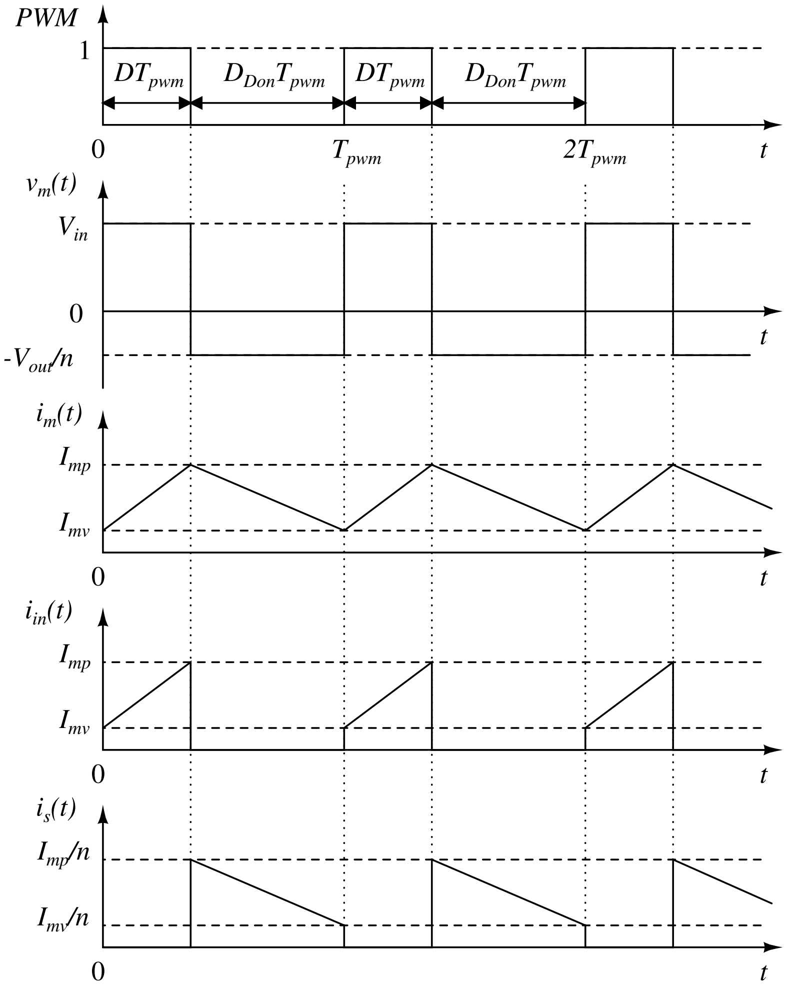

Figure 2.13: Branch voltages and currents in the flyback converter under CCM, where D and D_{Don} are the steady state values of the duty ratio and diode conduction ratio, respectively. T_{pwm} denotes the switching period.

In general, the conduction losses of the flyback converter as shown in Fig. 2.12 primarily come from the MOSFET via the resistance r_{Qon}, and the secondary diode via the forward voltage drop V_d and the series resistance r_{Don}. The total power dissipated in these components is expressed by

$$\begin{aligned} P_{cond}^{ccm} &= P_{r_{Qon}} + P_{r_{Don}} + P_{V_d} \\ &= \overline{i_{in}^2(t)} r_{Qon} + \overline{i_s^2(t)} r_{Don} + \overline{i_s(t)} V_d, \end{aligned} \tag{2.58}$$

where the overline operator $\overline{i_{in}^2(t)}$ denotes the average of $i_{in}^2(t)$ over a switching cycle T_{pwm}. Using the steady-state waveforms of the primary current, $i_{in}(t)$, and the secondary current , $i_s(t)$, in

Fig. 2.13, as a basis for calculation of $\overline{i_{in}^2(t)}$, $\overline{i_s^2(t)}$ and $\overline{i_s(t)}$, Eq. (2.58) can be developed to

$$\begin{aligned} P_{cond}^{ccm} &= D\frac{I_{mp}^2 + I_{mp}I_{mv} + I_{mv}^2}{3} r_{Qon} + D_{Don}\frac{I_{mp}^2 + I_{mp}I_{mv} + I_{mv}^2}{3n^2} r_{Don} \\ &+ D_{Don}\frac{I_{mp} + I_{mv}}{2n} V_d, \end{aligned} \tag{2.59}$$

where I_{mp}, I_{mv} represent the peak and valley values of the magnetizing inductor current, respectively. D and D_{Don} are the steady-state duty ratio and the steady-state diode conduction ratio, respectively, while $n = \frac{N_s}{N_p}$ is the voltage ratio of the flyback transformer.

Although the conduction losses P_{cond} in Eq. (2.59) is analytically represented as a function of D, D_{Don}, I_{mp} and I_{mv}, none of D, D_{Don}, I_{mp} and I_{mv} is directly available. A further step is required to calculate these quantities from the circuit component values and external signals. Following the DC analysis for the CCM flyback converter in Section 2.3.1, the following expressions can be derived:

$$\begin{aligned} D &= \frac{V_{out}}{V_{out} + nV_{in}}, \\ D_{Don} &= 1 - D, \\ I_{mp} &= \frac{n}{1-D}\left(\frac{V_{out}}{R} + I_{dyn}\right) + \frac{V_{in}DT_{pwm}}{2L_m}, \\ I_{mv} &= \frac{n}{1-D}\left(\frac{V_{out}}{R} + I_{dyn}\right) - \frac{V_{in}DT_{pwm}}{2L_m}. \end{aligned} \tag{2.60}$$

2.5.1.2 In DCM

Under certain loading conditions, the inductor current $i_m(t)$ starts dropping to zero before the MOSFET is turned on. As a result, both the secondary diode and MOSFET stop conducting for some amount of time during each switching period. The converter is then said to enter DCM. The signal waveforms in different branches of the converter circuit are illustrated in Fig. 2.14. Following the analysis method in Section 2.5.1.1, the conduction losses in DCM can be obtained by calculating total power dissipated in r_{Qon}, r_{Don} and V_d as

$$\begin{aligned} P_{cond}^{dcm} &= P_{r_{Qon}} + P_{r_{Don}} + P_{V_d} \\ &= \overline{i_{in}^2(t)} r_{Qon} + \overline{i_s^2(t)} r_{Don} + \overline{i_s(t)} V_d. \end{aligned} \tag{2.61}$$

The terms $\overline{i_{in}^2(t)}$, $\overline{i_s^2(t)}$ and $\overline{i_s(t)}$ in Eq. (2.61) can be computed, based on the waveforms of the signals $i_{in}(t)$ and $i_s(t)$ in Fig. 2.14, as

$$\begin{aligned} \overline{i_{in}^2(t)} &= D\frac{I_{mp}^2}{3}, \\ \overline{i_s^2(t)} &= D_{Don}\frac{I_{mp}^2}{3n^2}, \\ \overline{i_s(t)} &= D_{Don}\frac{I_{mp}}{2n}. \end{aligned} \tag{2.62}$$

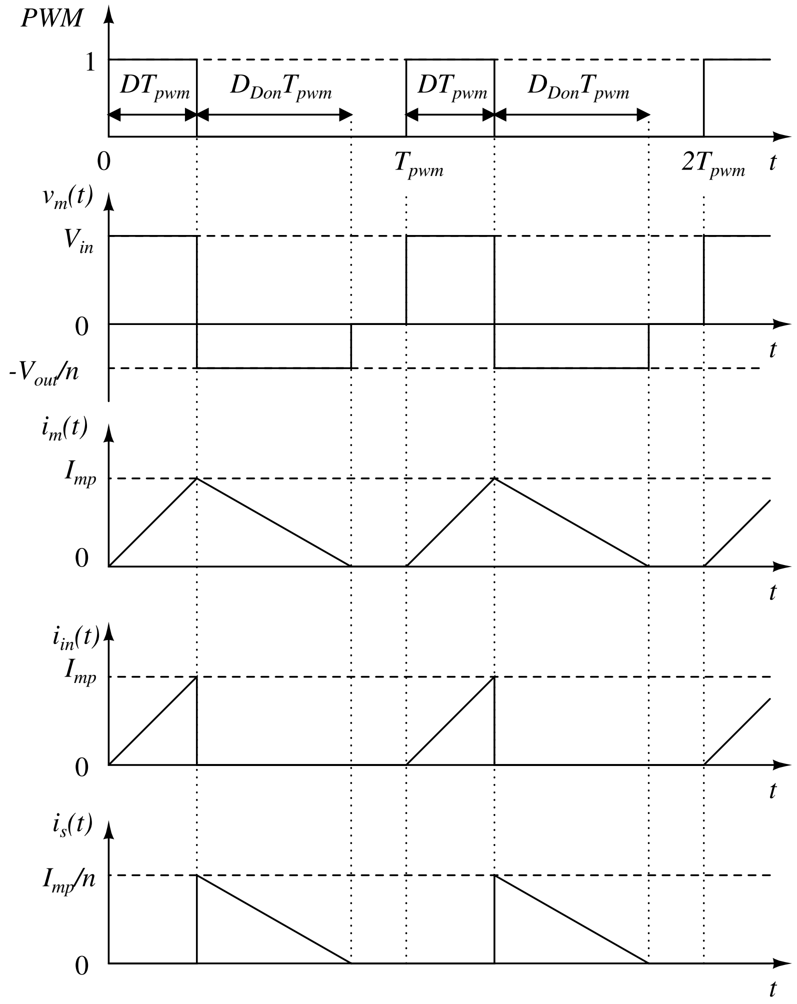

Figure 2.14: Branch voltages and currents in a flyback converter under DCM, where D and D_{Don} are the steady state values of the duty ratio and diode conduction ratio, respectively. T_{pwm} denotes the switching period.

Substituting Eq. (2.62) into Eq. (2.61) yields

$$P_{cond}^{dcm} = D\frac{I_{mp}^2}{3}r_{Qon} + D_{Don}\frac{I_{mp}^2}{3n^2}r_{Don} + D_{Don}\frac{I_{mp}}{2n}V_d. \tag{2.63}$$

It is interesting that Eq. (2.59) is general and valid for calculation of the conduction losses, not only in CCM, but also in DCM. Indeed, by setting I_{mv} in Eq. (2.59) to zero, we will arrive at Eq. (2.63). Based on the signal waveforms in Fig. 2.14, and the DC analysis results in Section 2.3.2, the expressions for D, D_{Don}, and I_{mp} can be obtained via

$$D = \sqrt{\frac{2L_m V_c}{T_{pwm} V_{in}^2}\left(\frac{V_c}{R} + I_{dyn}\right)}, \tag{2.64}$$

$$D_{Don} = \frac{nDV_{in}}{V_{out}}, \tag{2.65}$$

$$I_{mp} = \frac{DT_{pwm}V_{in}}{V}. \tag{2.66}$$

Unlike CCM, the valley magnetizing current I_{mv} is always zero in DCM and does not need to be computed.

2.5.2 Snubber circuit losses

Due to the presence of the leakage inductance L_{leak} and output capacitance C_{ds}, the switching device Q typically experiences a short voltage spike across it after the switch-off moment. Though the spike may last for only several microseconds, its magnitude can easily surpass the rating level of most MOSFETs and, as a result, can compromise the integrity of the MOSFET. In order to prevent such a potential fault, a snubber circuit, as shown in Fig. 2.12, is inserted to chop the excess voltage. Since the clamped energy is not recycled, this contributes to an extra loss in the flyback converter. The power dissipated in the snubber circuit, during the on-to-off transition of the switch Q, can be calculated via

$$P_{clamp} = \frac{1}{2} L_{leak} I_{mp}^2 \frac{nV_z}{nV_z - V} f_s \tag{2.67}$$

where V_z is the Zener breakdown voltage. Equation (2.67) can be applied equally to both CCM and DCM.

2.5.3 Switch-node capacitance losses

The switch-node capacitance, including C_w between the transformer windings and C_{ds} between the MOSFET drain and source, has a big impact on the converter efficiency, particularly at a light load condition. This type of loss comes from the fact that the energy accumulated in these capacitors during a switch-off period will be discharged in the consecutive switch-on period. The capacitance loss is generally given by

$$P_{cap} = \frac{1}{2} C_w v_{ds}^2(kT_{pwm}) f_{pwm} + E(v_d s(kT_{pwm})) f_{pwm}, \tag{2.68}$$

where C_w is the inter-winding capacitance, and $E(v_{ds}(kT_{pwm}))$ denotes the energy stored in the capacitor C_{ds} of the MOSFET. $V_{ds}(kT_{pwm})$ represents the drain-source voltage at the end of each switch-off time, or switching cycle if each cycle is assumed to start with an on-period. One can easily figure out that the value of $v_{ds}(kT_{pwm})$ in CCM depends only on the converter input and output voltages via

$$v_{ds}(kT_{pwm}) = V_{in} + \frac{(V_{out} + V_d)}{n}. \tag{2.69}$$

Unlike CCM, the ringing at the end of each switching period complicates the calculation of $V_{ds}(kT_{pwm})$ in DCM. Fortunately, these oscillations are a function of the magnetizing inductor, drain-source capacitor, and decay rate. Both the drain-source capacitor and decay rate can be obtained from the MOSFET specifications. The voltage $v_{ds}(kT_{pwm})$ in DCM, therefore, can be approximated by

$$v_{ds}(kT_{pwm}) = V_{in} + \frac{(V_{out} + V_d)}{n} e^{-\alpha(1-D-D_{Don})T_{pwm}} \cos\left(\omega_{osc}(1 - D - D_{Don})T_{pwm}\right), \tag{2.70}$$

where

$$\alpha = \frac{r_{damp}}{2L_m}, \tag{2.71}$$

and r_{damp} is a damping resistance, while ω_{osc} denotes the angular frequency of the ringing.

2.5.4 Transformer losses

2.5.4.1 Winding copper and proximity losses

The losses in the transformer winding can be estimated from the DC resistance of the conductor. For high frequency applications, this estimation is, however, too coarse and most of the time leads to inaccurate results [3]. The error is probably due to the contribution of the proximity and skin effects at high frequencies. Therefore, taking into account both DC and AC losses would be necessary to achieve an adequate estimation of the total winding losses.

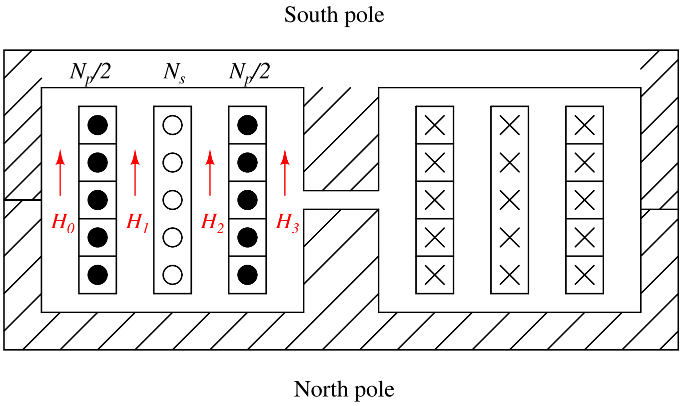

Figure 2.15: Interleaved transformer structure with 2-layers on the primary side and 1-layer on the secondary side. The dot symbols (• and ◦) indicate the current coming out of the paper, while the cross symbol (×) correspond with the current going into the paper.

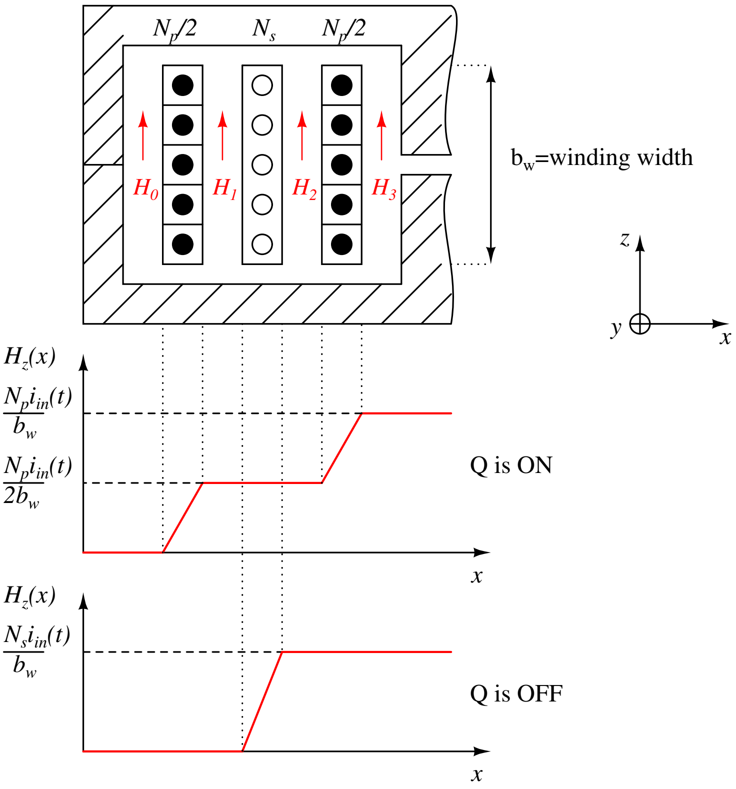

Figure 2.16: Magnetic field diagram in space for an interleaved winding.

The proximity loss model for a flyback transformer is derived based on the study in [48], which assumes that the winding is configured using the interleaved geometry as illustrated in Fig. 2.15. The primary winding is split into two layers between which the secondary layer is sandwiched. The total winding loss is now obtained via a separate calculation for each layer.

The magnetic field distribution H on both sides of each winding layer is required in order to compute the loss in that layer [48]. According to the winding geometry in Fig. 2.15, the H diagram in space can be found as in Fig. 2.16. Since each layer is considered as an infinitely long solenoid, and the cross section of the conductor is assumed to be much smaller than the length of a turn, the magnetic field generated by a layer is neglected outside the region enclosed by such a layer and has only a component in the z-direction inside the region enclosed by such a layer.

When the current waveform in the primary and secondary windings are known, the magnetic fields H_0, H_1, H_2 and H_3 can be easily plotted as a function of time. The calculation of the total copper losses in a winding layer are split into 3 steps including: (i) decomposing the obtained time-domain waveforms of H_0, H_1, H_2 and H_3 into sinusoidal harmonics by Fourier analysis, (ii) calculating the copper loss in the winding layer caused by each sinusoidal harmonic, and (iii) summing all losses incurred by all harmonics. The corresponding loss model in each winding layer is as follows [48]:

$$P_{layer} = b_w l_t \sum_{i=0}^{\infty} \frac{1}{g_i \eta \sigma \delta_i'} \left\{ \left[H_{zi}^2(h) + H_{zi}^2(0) \right] F_1(\phi_i) - 4Re \left[H_{zi}(h) H_{zi}(0) \right] F_2(\phi_2) \right\}, \tag{2.72}$$

where

$$\delta_i = \sqrt{\frac{2}{\omega_i \mu_0 \sigma}}, \tag{2.73}$$

$$\delta_i' = \frac{\delta_i}{\sqrt{\eta}}, \tag{2.74}$$

$$\eta = \frac{N_l b}{b_w}, \tag{2.75}$$

$$\phi_i = \frac{h}{\delta_i'}, \tag{2.76}$$

$$F_1(\phi_i) = \frac{sinh(2\phi_i) + sin(2\phi_i)}{cosh(2\phi_i) - cos(2\phi_i)}, \tag{2.77}$$

$$F_2(\phi_i) = \frac{sinh(\phi_i)cos(\phi_i) + cosh(\phi_i)sin(\phi_i)}{cosh(2\phi_i) - cos(2\phi_i)}, \tag{2.78}$$

$$g_i = \begin{cases} 1, & \text{if } i = 0 \\ 2, & \text{if } i \geq 1 \end{cases}, \tag{2.79}$$

where l_t is the length of a winding turn or mean length turn, b_w is the winding width, b is the breadth of the conductor used in a layer, N_l is the number of turns in a layer, σ is the conductivity, ω_i is the angular frequency of each harmonic, and μ_0 is the permeability of free space. Once the losses in each winding layer are given, the total winding losses can be computed by summing all losses over all winding layers.

2.5.4.2 Core losses

Traditionally, the time-averaged core losses due to the hysteresis and eddy currents is calculated by a power law equation [49] via

$$P_{core} = k f^{\alpha} B_{peak}^{\beta} V_{core}, \tag{2.80}$$

where f is the frequency of sinusoidal excitation, B_{peak} indicates the peak amplitude of the magnetic flux density, and k, α and β are termed Steinmetz-equation parameters and typically found by fitting the manufacturers data for the core material to Eq. (2.80) [49]. Since the model in Eq. (2.80) is proposed for a transformer working with sinusoidal AC excitation, a direct application of such a model to flyback converters, having arbitrary flux density waveforms, will result in a significant error. To overcome this problem, the improved Generalized Steinmetz Equation (iGSE) is introduced in [49], and states that

$$P_{core} = \left(\frac{1}{T_{pwm}} \int_0^{T_{pwm}} k_i \left| \frac{dB(t)}{dt} \right|^{\alpha} (\Delta B)^{\beta - \alpha} \mathrm{d}t \right) V_{core}, \tag{2.81}$$

$$k_i = \frac{K}{(2\pi)^{\alpha - 1} \int_0^{2\pi} |\cos\theta|^{\alpha} \mathrm{d}\theta}, \tag{2.82}$$

where ΔB indicates the peak-to-peak magnetic flux density, while V_{core} is the effective volume of the ferrite core. The improved model in Eq. (2.81) also uses the same Steinmetz parameters (k, α and β) for the calculation. Using the magnetizing current waveform analysed in Section 2.5.1.1, one can simplify Eq. (2.81) to

$$P_{core} = Dk_i\left(\Delta B\right)^{(\alpha-\beta)}\left|\frac{V_{in}}{N_pA}\right|^{\alpha}V_{core} + D_{Don}k_i\left(\Delta B\right)^{(\alpha-\beta)}\left|\frac{V_{out}}{N_sA}\right|^{\alpha}V_{core}, \tag{2.83}$$

$$\Delta B = \frac{DT_{pwm}V_{in}}{N_pA}, \tag{2.84}$$

where N_p and N_s represent the number of turns in the primary and secondary windings respectively, and A is the cross sectional area of the ferrite core. It should be noticed that Eq. (2.83) can be used equally for both CCM and DCM.

2.5.5 Off-line efficiency optimization

2.5.5.1 Energy conversion efficiency

Considering the flyback converter in Fig. 2.12 as a two-port network, whose input port is connected to a DC source and the output port connects to a load, the converter efficiency is a factor that evaluates the effectiveness of the system in delivering power from the source to the load. The efficiency factor η can be expressed as

$$\eta = \frac{P_{out}}{P_{in}} = \frac{P_{out}}{P_{out}+P_{loss}} = \frac{1}{1+\frac{P_{loss}}{P_{out}}}, \tag{2.85}$$

where P_{in} is the input power delivered to the converter, P_{out} denotes the output power demanded by the load and P_{loss} indicates the total converter losses. For a given working condition, the value of P_{loss} and P_{out} can be computed via

$$\begin{aligned} P_{loss} &= P_{cond} + P_{clamp} + P_{cap} + P_{winding} + P_{core}, \\ P_{out} &= V_{out}\left(\frac{V_{out}}{R} + I_{dyn}\right), \end{aligned} \tag{2.86}$$

where the expressions for P_{cond}, P_{clamp}, P_{cap}, $P_{winding}$ and P_{core} can be found in Sections 2.5.1, 2.5.2, 2.5.3, and 2.5.4.

2.5.5.2 Optimization procedure

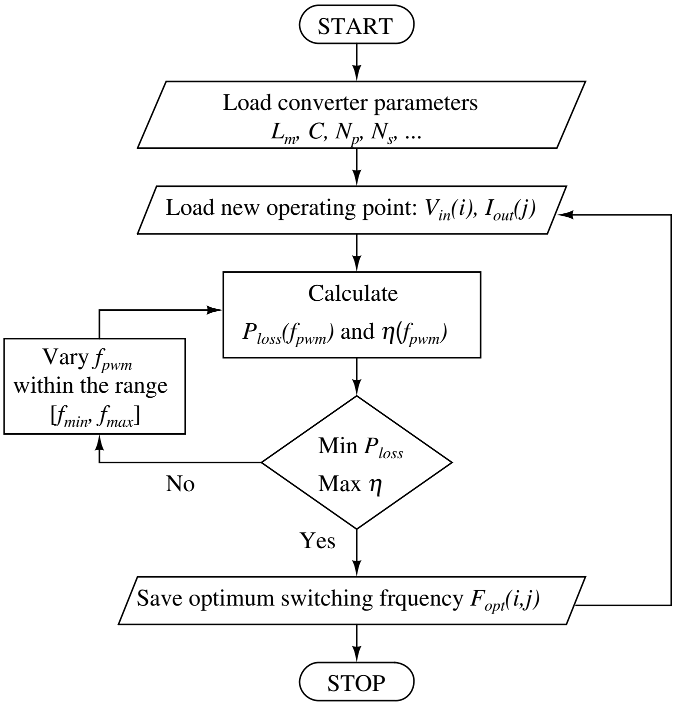

Figure 2.17: Block diagram of efficiency optimization procedure for a given set of operating conditions.

This section proposes a procedure for seeking the optimum switching frequencies which maximize the efficiency of a flyback converter over an operational range. However, unlike the study conducted in [44], we do not limit the control strategy to valley switching and assume that the parameters of the power stage of the flyback converter are given. The procedure uses the formulae in Section 2.5.5.1 to find the total power loss P_{loss} and efficiency η of the flyback converter at different combination of the input voltage $v_{in}(t)$, output load current $i_{out}(t)$, and switching frequency f_{pwm}. Since both P_{loss} and η are non-linear functions of f_{pwm}, an optimization routine is needed to find the global minimum of P_{loss} (or maximum of η) for each combination of $v_{in}(t)$ and $i_{out}(t)$. The flowchart of the optimisation procedure is shown in Fig. 2.17.

2.6 Efficiency improvement techniques

In this section, a brief review of existing efficiency enhancement methods for DC-to-DC converters is discussed. The knowledge obtained from this section can serve as a basis for control design of the flyback converter in Chapter 8.

2.6.1 Variable switching frequency

An approach to improve the light load efficiency using a variable switching frequency was first proposed by Arbetter *et al.* [43, 50]. By investigating different loss types of a fixed frequency converter as shown in Fig. 2.18(a), Arbetter *et al.* [43,50] believed that the switching losses were a main reason in causing a decline in the converter efficiency at light load, and that it was possible to reduce the switching losses by allowing a variable frequency operation as demonstrated in Fig. 2.18(b). Based on this observation, Arbetter *et al.* designed variable-frequency constant-peak-current control for a buck converter in DCM [43], and subsequently extended the control method to both CCM and DCM [50]. Since the switching frequency f_{pwm} is considered as a manipulated variable to regulate the output voltage, the technique proposed in [43, 50] is commonly known as pulse frequency modulation (PFM) control. The main feature of PFM is to reduce the operational frequency under light load conditions and consequently lower the switching losses. Although the variable-frequency method can greatly improve the converter efficiency, it also poses other major problems, such as poor output voltage regulation, EMI issue due to the dependence of f_{pwm} on the load, and many others.

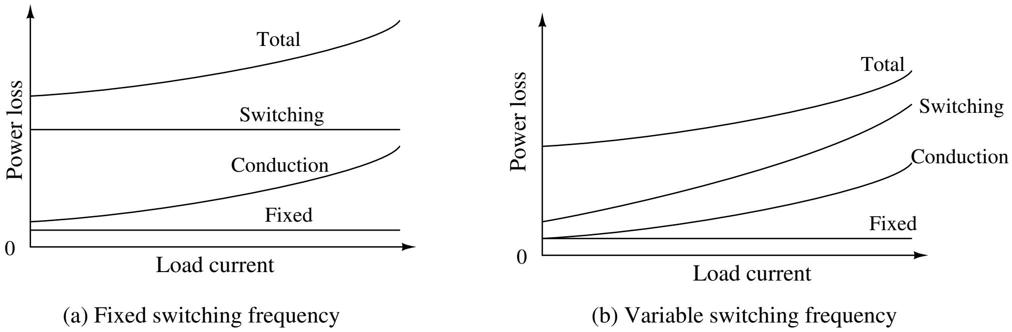

(a) Fixed switching frequency (b) Variable switching frequency

Figure 2.18: Converter loss vs. load current for different switching frequency schemes [43]

Another form of PFM control, known as constant on-time control, is commonly applied to buck converters [45, 46, 51, 52]. In such applications, the transistor on-time T_{on} is selected to maximize the overall converter efficiency, while the switching frequency is linearly modulated by the output current $i_{out}(t)$ in order to keep a constant output voltage. Though the authors in [51] claim that constant on-time control can avoid the instability and large current ripple issues of constant peak-current control, both the control approaches turn in quite similar performances. As an optimal value of T_{on} is only valid for a given input voltage [45, 53], the system efficiency could be further improved by updating T_{on} whenever a change in $v_{in}(t)$ is detected [53].

2.6.2 Pulse-skipping and burst-mode control

Pulse-skipping and burst mode control can be considered as a special case of PFM control during ultra light load and no-load conditions. Instead of applying a wide pulse with PFM, a burst of smaller pulses is typically employed to compensate for the energy wasted in the snubber circuit and possibly the output load [54–56]. The comparison between burst mode control and PFM control is best explained in Fig. 2.19. As a consequence of short pulses, burst mode control typically results in a smaller peak magnetizing current when compared with that of PFM control for the same values of $i_{out}(t)$ and f_{pwm}. The benefit of burst mode control is twofold. It not only simplifies EMI filter design but also brings a great benefit to acoustic noise cancellation.

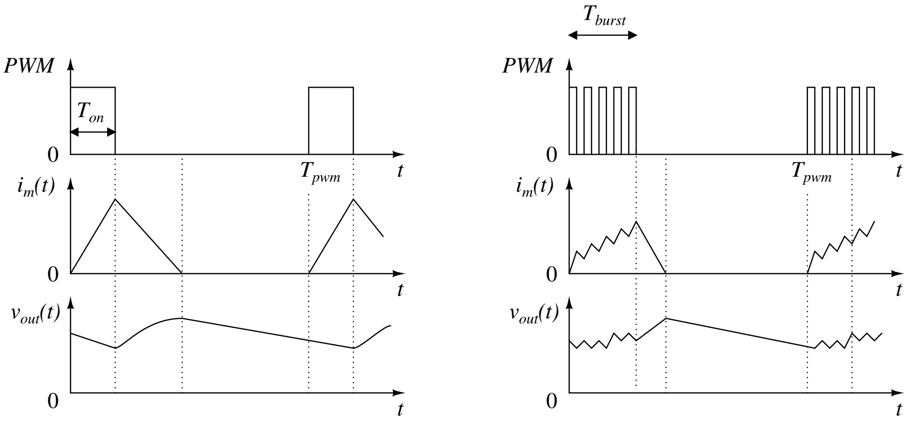

(a) PFM (b) Burst mode

Figure 2.19: Comparison waveforms of the control signal, inductor current and output voltage under (a) PFM and (b) burst mode control

Though burst mode control can easily be achieved using a hysteresis approach [54], it does not lend itself to the flyback converter with magnetic sensing (MS) regulation. The main obstacle is the indirect measurement of the output voltage.

2.6.3 Quasi-resonant operation

Since the voltage across the drain and source of the MOSFET $v_{ds}(t)$ is high at the end of the switching cycle, the switch-node capacitance losses, according to Eq. (2.68), become substantial under light load situations. One way to minimize such losses is to turn on the MOSFET at the point of the minimum value of $v_{ds}(t)$. Such a technique has been successfully applied to the flyback converter operating in DCM [57], where the MOSFET is turned on at the first valley of $v_{ds}(t)$, as exemplified in Fig. 2.20. In practice, the second or higher valley number could be selected, depending on the design specifications.

Since the choice of first or second or higher valley number switching directly decides the amount of power dissipation, a proper assignment is necessary in order to maximize the system efficiency over the entire operating range. The control strategy using valley switching is usually referred to as quasi-resonant control [57]. Like burst mode control, quasi-resonant control is also helpful in

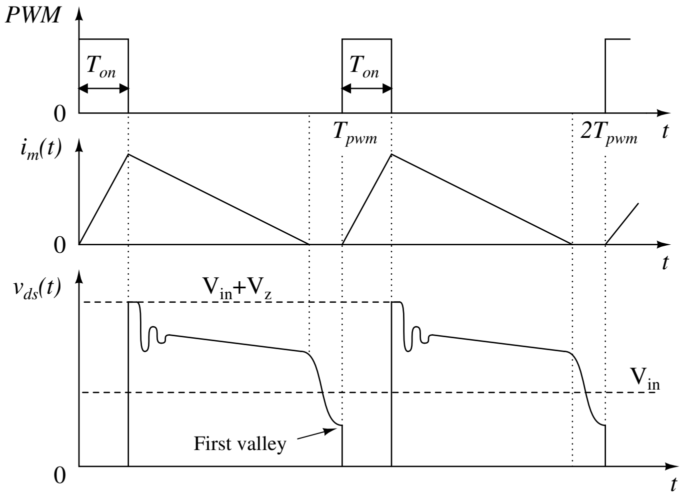

Figure 2.20: Example of quasi-resonant control with valley switching, where the transistor is turned on at the first valley of $v_{ds}(t)$.

reducing the size and cost of the EMI filter.

2.6.4 Multi-mode (hybrid) operation

All efficiency improvement methods in Sections 2.6.1, 2.6.2 and 2.6.3 have shown good performance under certain loading conditions, but none can maintain a high efficiency over the entire working range. For example, a fixed switching frequency converter can easily offer a high efficiency at heavy load, but not at light load. On the other hand, the variable frequency approach in [43] can achieve a constant efficiency over a relatively wide load range, except at heavy load and very light load. Under these two extremes, the variable-frequency controller needs too small and too large switching frequencies which make the design of the EMI filter and the magnetic components more difficult. Burst mode control is applicable in ultra light load and no-load scenario, while quasi-resonant control is only useful in DCM.

The idea of multi-mode (hybrid) control is to select certain existing power-saving techniques and combine them together. Ideally, multi-mode control should inherit all the advantages of each individual method and hence can guarantee a high efficiency operation under any loading condition. Various schemes of multi-mode control have been reported in [46, 47, 51, 58, 59]. Though most of these studies focus on a synchronous buck converter only, they can be a useful reference for flyback converter design.

2.6.5 Offline efficiency optimization

Table-based efficiency optimization control, which was proposed recently by Kang et al. [8, 44, 60], is the only study considering efficiency optimization for the flyback converter. In fact, the approach in [8,44,60] can be considered as multi-mode control, consisting of fixed-frequency control for CCM and variable frequency, with quasi-resonant control, for DCM. Unlike the formulae-based approaches in Section 2.6.1, the optimum switching frequency f_{pwm} in [44] is computed offline and looked up from a table, rather than calculated directly from $i_{out}(t)$ and $v_{in}(t)$. This offline optimization method has several advantages, such as requiring less computation power, offering higher efficiency due to more accurate calculation of f_{pwm}, and much simpler to implement. One main drawback of the offline-efficiency optimisation is that the approach usually requires a-priori knowledge of the converter parameters, which is not always available in practice.

Notice that the use of a look-up table has been exploited in various commercial products [58]. However, the switching frequency is specified to ease EMI filter implementation and controller design, rather than efficiency maximization.

Chapter 3

A review of power transformer modelling and simulation of DC-to-DC converters

3.1 Introduction

In this chapter, a review of the published literature related to modelling and simulation of DC-to-DC converters and power transformers, which is relevant to Chapters 5 and 6, is presented. Particularly, Section 3.2 begins with a brief review of approaches to the simulation of DC-to-DC converters in digital computers. Along with the simulation implementation, the selection of modelling techniques which maximizes the effectiveness of the simulation, i.e. minimize the computation time while preserving all the necessary information, is also discussed. We then proceed in Section 3.3 to summarize the existing studies into modelling of power transformers and identification of transformer models from experimental measurements. Finally, the discussion and rationale which leads to the research in Chapters 5 and 6, is presented in Section 3.4.

3.2 Simulation of DC-to-DC converters in digital computers

Supported by the rapid development in computing speed and memory storage, computer-based simulations and analysis are a vital step in the design process of power electronic systems in general, and of flyback DC-to-DC converters in particular. Simulation of electronic circuits in digital computers can be carried out by either specialized programs, such as PSpice, PSIM, etc., or general purpose computing software, such as MATLAB, MathCAD, etc. [61, 62]. Though both specialized and general purpose simulation programs differ considerably in the user interface and input data format used, they exploit the same fundamental principle, based on differential and algebraic equations, to obtain detailed operation of the system under investigation. Since power converter applications are generally described by circuit component models, rather than equation-based models, forming state space equations from circuit diagrams is required before implementing the simulation. The formation of such equations can be performed automatically by the simulator itself, or manually by the users. For this reason, computer simulation programs are typically classified into two broad categories: equation-oriented simulators and circuit-oriented simulators [61].

3.2.1 Equation-oriented simulators

For equation-oriented approaches, users play a major role in the simulation process. This role consists of: (1) deriving a set of differential and algebraic equations describing the relationship between branch voltages and currents of power converters under consideration and (2) choosing proper equation solvers, simulation time steps, and output data formats. Since the purpose of the computer software in this case is to solve a given set of equations and handle the raw data only, the simulation can be implemented with any high level programming language such as C++, Fortran, etc.. In practice, it is more convenient to use one of the many available simulation programs such as MATLAB, MathCAD, etc.. Although such computer programs are not deliberately designed to deal with specific problems in power electronics, they typically contain various libraries, for the solution of differential equations, matrix manipulation, and graphics, which help to greatly reduce the total time needed to implement the simulation.

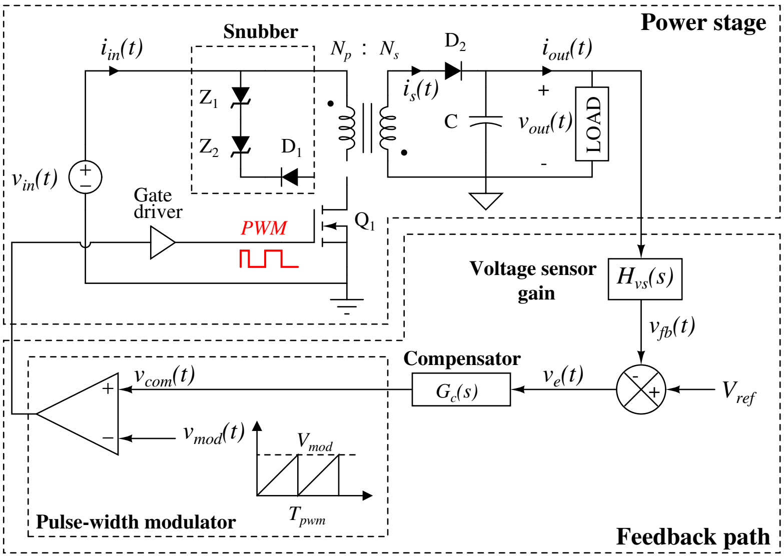

Figure 3.1: DC-to-DC flyback converter with a voltage mode controller

To demonstrate how an equation-oriented approach works, a PWM voltage-mode-controlled DC-to-DC flyback converter, whose functional diagram is sketched in Fig. 3.1, is taken as an example. For control design purposes, we are interested in the large-signal response of the output voltage of the closed loop converter, as shown in Fig. 3.1, for different input voltages $v_{in}(t)$ and output loads $i_{out}(t)$. In order to obtain such a response, it is necessary to mathematically formulate the behaviour of both the power stage and feedback path in Fig. 3.1. For simplicity, the model of the power stage, as sketched in Fig. 2.2, and the notation in Section 2.2, are re-used in this context. Since the operation mode of the flyback converter is generally not fixed and may not be known in advance, the switched state space models, developed in Section 2.2, for either CCM or DCM cannot be applied to the general case. Fortunately, by introducing the variables $s_q(t)$ and $s_d(t)$ describing the states of the switch Q and diode D, respectively, the models in Section 2.2 can be generalized to

$$\begin{aligned}\frac{d}{dt}\mathbf{x}(t) &= \Big(s_q(t)\mathbf{A}_1 + \big(1-s_q(t)\big)\mathbf{A}_2 + s_d(t)\mathbf{A}_3\Big)\mathbf{x}(t)\\ &\quad + \Big(s_q(t)\mathbf{B}_1 + \big(1-s_q(t)\big)\mathbf{B}_2 + s_d(t)\mathbf{B}_3\Big)\mathbf{u}(t),\\ \mathbf{y}(t) &= \Big(s_q(t)\mathbf{C}_1 + \big(1-s_q(t)\big)\mathbf{C}_2 + s_d(t)\mathbf{C}_3\Big)\mathbf{x}(t)\\ &\quad + \Big(s_q(t)\mathbf{E}_1 + \big(1-s_q(t)\big)\mathbf{E}_2 + s_d(t)\mathbf{E}_3\Big)\mathbf{u}(t),\end{aligned} \tag{3.1}$$

where

$$s_q(t) = \begin{cases} 1 & \text{if Q is on} \\ 0 & \text{if Q is off} \end{cases}, \qquad s_d(t) = \begin{cases} 1 & \text{if D is on} \\ 0 & \text{if D is off} \end{cases}. \tag{3.2}$$

The expressions for $\mathbf{A}_1$, $\mathbf{B}_1$, $\mathbf{C}_1$, $\mathbf{E}_1$, $\mathbf{A}_2$, $\mathbf{B}_2$, $\mathbf{C}_2$, $\mathbf{E}_2$, $\mathbf{A}_3$, $\mathbf{B}_3$, $\mathbf{C}_3$, and $\mathbf{E}_3$ can be found in Eqs. (2.3), (2.6) and (2.8), respectively.

Note that Eq. (3.1) is valid to describe the operation of open-loop flyback converters at any working point and time interval. Due to the non-linearity and discontinuity of $s_q(t)$ and $s_d(t)$, Eq. (3.1) is a time-varying and implicit differential equation. The implicitness arises from the fact that the state of the diode $s_d(t)$ has an algebraic dependence on the state variable $\mathbf{x}(t)$ and the excitation input $\mathbf{u}(t)$. Mathematically, this dependency can be expressed by

$$\begin{aligned}s_d(t) &= 0.5sign\big(i_s(t)\big) + 0.5\\ &= 0.5sign\Bigg(\Big(s_q(t)\mathbf{P}_1 + \big(1-s_q(t)\big)\mathbf{P}_2\Big)\mathbf{x}(t) + \Big(s_q(t)\mathbf{Q}_1 + \big(1-s_q(t)\big)\mathbf{Q}_2\Big)\mathbf{u}(t)\Bigg) + 0.5,\end{aligned} \tag{3.3}$$

where

$$\mathbf{P}_1 = \begin{bmatrix} 0 & 0 \end{bmatrix}, \qquad \mathbf{P}_2 = \begin{bmatrix} 1 & 0 \end{bmatrix}, \qquad \mathbf{Q}_1 = \begin{bmatrix} 0 & 0 \end{bmatrix}, \qquad \mathbf{Q}_2 = \begin{bmatrix} 0 & 0 \end{bmatrix}, \tag{3.4}$$

and $sign(x)$ is the sign function which returns 1 if x is greater than or equal to 0, otherwise returns -1. In contrast to the diode D, the switch Q is controlled directly by the PWM signal, so its state $s_q(t)$ is independent of the power stage, but indirectly depends on the converter output voltage $v_{out}(t)$ through the feedback regulation, as can be seen in Fig. 3.1.

The model of the feedback path, which is required to determine the PWM signal from the output voltage $v_{out}(t)$, is regulated by

$$s_q(t) = 0.5sign\Big(G_c(s)\big(V_{ref} - H_{vs}(s)v_{out}(t)\big) - v_{mod}(t)\Big) + 0.5. \tag{3.5}$$

For convenience, the time-domain variables and frequency-domain functions are mixed together in Eq. (3.5). For numerical calculations, all multiplications of transfer functions and time variables in Eq. (3.5) are always transformed into difference equations, where the simulation time step is used as a time basis for the discretisation [63]. Combining Eqs. (3.1), (3.3) and (3.5), the equation of the closed loop converter can be obtained as

$$
\begin{aligned}
\frac{d}{dt}\mathbf{x}(t) &= \Big(s_q(t)\mathbf{A}_1 + \big(1 - s_q(t)\big)\mathbf{A}_2 + s_d(t)\mathbf{A}_3\Big)\mathbf{x}(t) \\
&\quad + \Big(s_q(t)\mathbf{B}_1 + \big(1 - s_q(t)\big)\mathbf{B}_2 + s_d(t)\mathbf{B}_3\Big)\mathbf{u}(t), \\
\mathbf{y}(t) &= \Big(s_q(t)\mathbf{C}_1 + \big(1 - s_q(t)\big)\mathbf{C}_2 + s_d(t)\mathbf{C}_3\Big)\mathbf{x}(t) \\
&\quad + \Big(s_q(t)\mathbf{E}_1 + \big(1 - s_q(t)\big)\mathbf{E}_2 + s_d(t)\mathbf{E}_3\Big)\mathbf{u}(t), \\
s_d(t) &= 0.5 \times sign\Bigg(\Big(s_q(t)\mathbf{P}_1 + \big(1 - s_q(t)\big)\mathbf{P}_2\Big)\mathbf{x}(t) + \Big(s_q(t)\mathbf{Q}_1 + \big(1 - s_q(t)\big)\mathbf{Q}_2\Big)\mathbf{u}(t)\Bigg) + 0.5, \\
s_q(t) &= 0.5 \times sign\Big(G_c(s)\big(V_{ref} - H_{vs}(s)v_{out}(t)\big) - v_{mod}(t)\Big) + 0.5.
\end{aligned}
\tag{3.6}
$$

Equation (3.6) needs to be solved in order to find the transient response of the flyback converter. The solver can be selected from any existing numerical integration methods such as the forward Euler method, the trapezoidal method, the Runge-Kutta method, etc. [61]. This selection, however, needs to be made with care if the accuracy of the solution and the speed of execution are both required. Firstly, Eq. (3.6) is a time-varying non-linear and stiff equation. The stiffness is caused by the large disparity in the time constants of the closed loop circuit and can be examined via calculation of the eigenvalues of the state space matrices $\mathbf{A}_1$, $\mathbf{A}_2$ and $\mathbf{A}_3$ of Eq. (3.6). Various numerical methods have been proposed for stiff systems in general, but not all are applicable to the simulation problem in Eq. (3.6). Some commonly used methods for stiff systems include the backward differential and trapezoidal methods. Secondly, the implicit form of Eq. (3.6) makes the problem harder to handle and can result in an unstable solution if the simulation time step is not properly chosen. To avoid such a situation, it is necessary to transform Eq. (3.6) to an explicit form or choose an appropriate implicit numerical integration technique. A detailed investigation into the selection of the equation solver and the improvement of the execution speed is presented in Chapter 6.

One of the disadvantages of equation-oriented approaches is the initial time required to establish the differential equations and configure the solver. Since the initialisation is done manually, a slight change in the power stage circuit can be very costly in terms of the set-up time. Hence, equation-oriented approaches are not recommended for the design phase, where converter configurations are not yet decided, such as during the test of new circuit concepts.

Another drawback of equation-oriented simulators is the power relationship between the set-up time and model complexity. For example, if we consider the effect of the snubber circuit in the power stage model, as shown in Fig. 2.2, the set-up time is roughly twice as much as that without the snubber circuit. Moreover, when the system model contains many switching devices and energy storage elements, i.e. capacitors and inductors, it is very difficult to manually determine all combinations of the switches and corresponding differential equations for each configuration, without committing errors. Therefore, equation-oriented simulators are generally suited to examining the system behaviour rather than the detailed device level operation. This explains why we also need circuit-oriented simulators, which are mentioned in Section 3.2.2.

Equation-oriented approaches are very useful in the cases where users want to gain some insight into the operation of the designed system, or to customize the simulation for a specific application. Since it is much easier to describe continuous or discrete time control laws using mathematical expressions than using electronic circuits, equation-oriented simulators are also well suited for the purpose of testing a new control strategy.

3.2.2 Circuit-oriented simulators

Circuit-oriented simulators are developed to provide a highly interactive interface, which can automatically form differential equations from the circuit diagram, and can dynamically select a proper time step for numerical integration [61]. The use of equation solvers, the treatment of non-linearities, and the search for breakpoints in circuit-oriented programs, are almost transparent to the user who needs only to supply the interconnection between the circuit component models and their parameters. In general, basic component models are given in all simulators such as Pspice, PSIM, EMTP, PLECS, Simscape (Simulink/MATLAB), some of which also allow user-defined models in the form of differential equations or piecewise linear functions.

For demonstration purposes, the voltage-mode-controlled flyback converter in Section 3.2.1 is reconsidered in this section. Since circuit-oriented programs are unable to handle the controller transfer functions in the complex Laplace domain, i.e. $G_c(s)$ and $H_{vs}(s)$ in Fig. 3.1, implementation of these transfer functions using analogue or digital circuit component models is necessary. Figure 3.2 shows an example of a DC-to-DC flyback converter, in which the voltage mode controller is implemented by an operational amplifier, a comparator, and individual R and C components. The implementation in Fig. 3.2 assumes that the compensator is represented by a second order transfer function and the voltage sensor is simply a low-pass filter. Given the circuit diagram in Fig. 3.2, the transient response of the converter over time may be obtained using any circuit-oriented simulator, such as Pspice.

Since the system equations are developed and solved automatically in circuit-oriented approaches, only a very short time is taken to set up or modify the simulation, and little knowledge about the differential equations and numerical integration is required in order to implement the simulation. Another feature of circuit-oriented approaches is that very complex systems can be handled by segmenting them into smaller modules, which are separately tested and then combined in the final stage.

Along with these advantages, circuit-oriented approaches have several disadvantages, such as non-convergence problems due to the uncontrollable time step of simulators, difficulties in selecting numerical integration techniques, and the incompatibility with power electronics; for instance, Pspice is well suited to the simulation of integrated circuits, rather than power electronic systems.

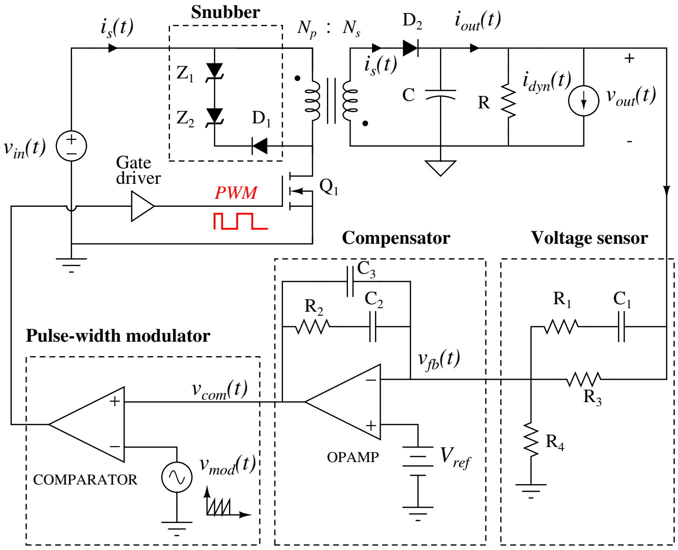

Figure 3.2: Implementation of a voltage mode controlled DC-to-DC flyback converter using analogue circuits.

3.2.3 Hierarchical approach to simulate DC-to-DC converters

Sections 3.2.1 and 3.2.2 have presented two approaches to implement the simulation of DC-to-DC power converters in digital computers, and have discussed the role of differential equation solvers on the performance of simulators. Although a proper choice of the numerical integration method can improve the execution speed, the effectiveness of a simulator mostly relies on modelling methods, used to describe the operation of a switching power converter, rather than on the simulator itself. For example, if only a transient inter-cycle analysis is needed, a large-signal averaged model is obviously more efficient, in terms of the computation time and power consumption, than a detailed circuit description. Hence, various authors have come up with different ideas to analyse DC-to-DC converters depending on the level of detail and accuracy required. Some suggestions include a device level simulation and analysis [64, 65], behavioural modelling, where switches are modelled as piecewise linear functions or conceptual blocks [66–70], and the use of small-signal and large-signal analysis, such as sampled-data models [71, 72] and averaging modelling techniques [73–75]. Due to the trade-off between the accuracy and data processing time, none of these models can efficiently and completely satisfy all aspects of the computer-aided simulation and analysis of power converters.

Several studies [61, 62, 65, 76] propose hierarchical approaches, which classify the modelling methods into 5 categories. However, such a classification only deals with a specific converter topology, i.e. a boost converter using current mode control, and may be not suitable for a general case. For the purpose of making a clear separation between categories, converter modelling approaches are divided into 3 main groups in Sections 3.2.3.1 to 3.2.3.3.

3.2.3.1 Device level modelling

In device level modelling, circuit elements in the system are typically described by highly accurate models. Although the rapid development in computing speed and storage can support a billion calculations per second, the simulation of a detailed converter model for a full transient event, such as from start-up to steady-state, still remains an untouchable target [61]. For example, even with the simple flyback converter, as depicted in Fig. 3.2, a full event simulation using Pspice will take significant computation time and produces an overwhelming amount of data, if large signal transient models of the MOSFET, diodes and transformer are utilized [61]. The same observation can be made when running the simulation with other simulators, e.g. Simscape (Simulink/MATLAB). The significant simulation time is due to the fact that the simulator has to use a very fine time step in order to keep track of the system behaviour around the switch transition moments. More precisely, when the switching cycle of the semiconductor devices, like MOSFETs, is of the order of microseconds, the simulation requires at least nanoseconds or even picoseconds resolution [77]. Hence, the device level simulations are useful in the cases where the focus is on the detailed intra-cycle response of power converters, over a few switching periods, rather than a full transient event, arising from input and load variations. Traditionally, the main application of the device level modelling is to obtain device stresses and to evaluate snubber topologies.

3.2.3.2 Behavioural modelling

By replacing semiconductor devices in DC-to-DC converters with ideal switches, where the transitions between on and off state are assumed to be instantaneous, converter circuits can now be modelled as piecewise linear systems. As a result, the operation of converters can be represented by a set of linear systems, each of which corresponds to one configuration of the switching devices. The transition from one configuration to another is made based on the state variables and control signal. An application of behavioural modelling can be found in Section 3.2.1, where the model of the voltage mode controlled flyback converter, as given in Eq. (3.6), is derived with assumptions of ideal switching devices.

In contrast to device level modelling, information around state transition points of semiconductor devices is ignored in behavioural modelling; therefore, a large amount of computation is saved in each switching cycle. This greatly helps to reduce the total computation time, as well as the amount of data processed at the end of the simulation. The advantages of the behavioural modelling are the ability to investigate the responses of the systems in both long- and short-transient events. Such an ability is useful for applications where accurate representation of ripples in current and voltage signals are critical for the operation of controllers.

Behavioural modelling approaches [66–70] are often different in the numerical integration techniques used to solve the linear differential equations, in the search methods applied to predict state transition instances of switches, and in the mechanisms employed to determine the correct switch configuration after transition.

3.2.3.3 Simplified modelling

Time-varying models in Section 3.2.3.2 can well serve simulation of both short and long transient events. However, if only inter-cycle responses of power converters are of interest, such as for control design purposes, behavioural modelling is too general and not an ideal choice. Therefore, a simplification needs to be considered, in order to obtain time-invariant models. The most popular approach is to replace switching elements with non-switching devices. The replacement should retain the most appropriate information, but skip intra-cycle ripples due to switching effects. There are two systematic ways to suppress the detailed switching artefacts in each cycle: (1) averaging techniques [73, 78–82] and (2) sampled-data modelling [71, 72, 83–85]. The treatment of these two techniques is carefully reviewed and discussed in [62].

As the simplification procedure can be applied to converter models in either DCM or CCM, the resulting simplified models are valid in predicting inter-cycle responses of DC-to-DC converters in only one mode of conduction, i.e. either CCM or DCM. This situation is acceptable, if power converters operate permanently in one of the two conduction modes. However, difficulties arise when systems encounter both continuous and discontinuous modes, in response to large input voltage disturbances or load current variations. Fortunately, a unified simplified model can be derived by incorporating the models from both the conduction modes [86, 87]. Moving from one operational mode to the other is automatically performed by adding an extra function to detect such transitions.

3.3 Transformer models and parameters identification

The transformer is the most important, and also most complicated, part of the DC-to-DC flyback converter. Therefore, it is necessary to understand operation and characteristics of the transformer in order to customize the power stage and to design the controller. The topics of characterizing and estimating transformer models, which have been investigated over decades [9, 88, 89], cover a wide variety of studies, spanning from theoretical to experimental analysis, and from two-winding to multi-winding transformers, see [90] and the references therein. However, there is no unique modelling approach and other issues exist, relating to the flyback transformer, which have not been considered before.

In this section, a full and detailed review of transformer models is not attempted, but rather the focus is on existing techniques which allow the development of models of multi-winding transformers and the identification of model parameters from experiments. Such a focus allows us to determine the research direction, and also serves as a basis for our study in Chapter 5. Essentially, modelling of power transformers can be classified into two problems: frequency dependent responses of the transformer windings and non-linearity of the ferrite core. Approaches to modelling the transformer windings are presented in Section 3.3.1 while models of the ferrite core are reviewed in Section 3.3.2.

3.3.1 Modelling of the transformer windings

3.3.1.1 General magnetic models

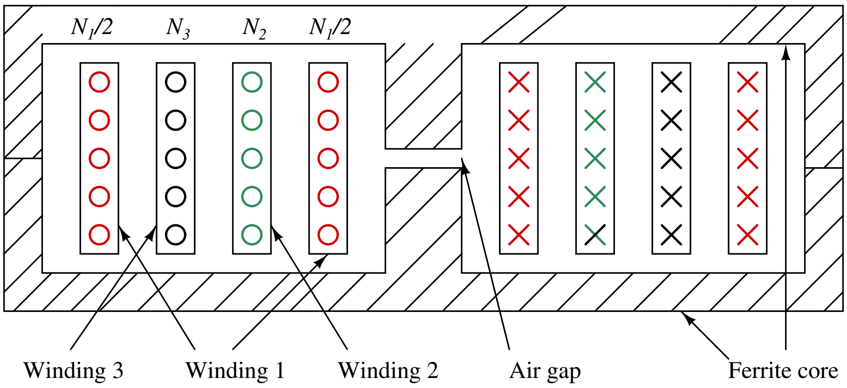

(a) Winding geometry

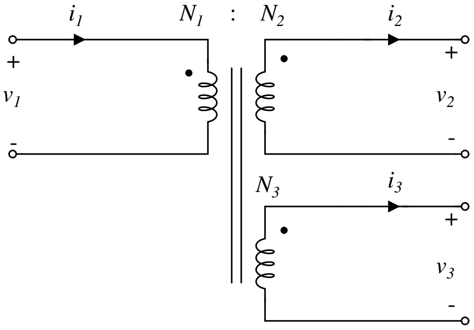

(b) Electrical symbol

Figure 3.3: Three-winding flyback transformer example

For simplicity, a 3-winding transformer, whose structure is illustrated in Fig. 3.3(a), is used as a case study in this section. The number of turns of the first, second and third windings are N_1, N_2 and N_3, respectively. It is assumed that the magnetic component behaves linearly, i.e. saturation effects are ignored, and does not incur any losses during its operation. In such a case, the most general magnetic model is the mathematical description which relates the currents and voltages at the transformer terminals [9] via

$$\begin{bmatrix} v_1(t) \\ v_2(t) \\ v_3(t) \end{bmatrix} = \mathbf{L}\frac{d}{dt}\begin{bmatrix} i_1(t) \\ i_2(t) \\ i_3(t) \end{bmatrix} \quad , \tag{3.7}$$

where

$$\mathbf{L} = \begin{bmatrix} L_{11} & M_{12} & M_{13} \\ M_{21} & L_{22} & M_{23} \\ M_{31} & M_{32} & L_{33} \end{bmatrix} \tag{3.8}$$

indicates the inductance matrix while $i_1(t)$, $i_2(t)$, $i_3(t)$, and $v_1(t)$, $v_2(t)$ and $v_3(t)$ denote the terminal currents and voltages of the transformer windings, as demonstrated in Fig. 3.3(b), respectively. L_{11}, L_{22} and L_{33} represent the self inductance of the first, second and third coils, respectively, while $\{M_{ij}\}_{i,j=1,2,3 \text{ and } i \neq j}$ are the mutual inductance between the transformer windings. Due to the mutual coupling relation between windings, it is always true that

$$M_{13} = M_{31}, \qquad M_{23} = M_{32}, \qquad M_{12} = M_{21}. \tag{3.9}$$

Based on Eqs. (3.7) and (3.9), one can state that the number of independent parameters constituting the three-winding transformer model is 6. Such a statement can be generalized to the case of an N-winding transformer, where the inductance matrix in the general magnetic model has $\frac{N(N+1)}{2}$ independent parameters. Since the relation in Eq. (3.7) is developed through analysis of flux linkages in transformer coils using Faraday's Law, the general magnetic model can be used to describe any transformer winding geometry.

The model in Eq. (3.7) includes physical winding-to-winding coupling relations and terminal voltage-current characteristics, but does not directly show differences in winding or core topologies. Moreover, the mathematical description in Eq. (3.7) is not convenient for circuit analysis, particularly in switched mode power converters. For example, if the general magnetic model is used in place of the equivalent circuit of the flyback transformer in Fig. 2.2, it will be hard to differentiate the working modes of the converter, and develop the voltage-current relations for each mode.

3.3.1.2 Equivalent circuit models

In order to overcome the limitations of the general model in Eq. (3.7), different approaches have been adopted in [9–14]. The main ideas of such approaches are to find electrical circuit representations which are best to describe magnetic devices. Some methods, such as [9, 11, 91], exploit physical geometries of windings and the magnetic-electrical duality principle [92] to find equivalent circuits. Although such methods typically result in simple models and allow the analytical calculation of the leakage inductance, they experience two major disadvantages including their lack of generality and accuracy [12]. For example, the methods in [9, 11, 91] cannot be applied to toroidal transformers.

Other approaches [10, 12, 13] are to construct circuit models such that the input-output relations in Eq. (3.7) are satisfied. There is no unique way to form an equivalent circuit from the mathematical relations. Some commonly used techniques can be listed as: (1) extending the well-known model topologies for two-winding transformers to general cases for N-winding transformers [12, 13, 93], and (2) proposing specific models aimed at a high level of accuracy or ease of parameter determination [10, 94].

In general, the equivalent circuits of multi-winding transformers can be classified into: the conventional T model [9, 11], the extended cantilever model [12], and the cross coupled secondary model [10]. The illustration of these models for a three-winding flyback transformer are given in Figs. 3.4, 3.5 and 3.6, respectively, where the magnetizing inductor L_m represents the model of the ferrite core while other inductors describe the leakage or coupling inductance of the transformer coils. The transformer voltage gains n_2 and n_3 account for the coupling between transformer windings. In addition to the three basic modelling approaches, other transformer models exist including the ladder model [95], the extended T model [93], the generalized extended cantilever model [13, 14] and many others [94, 96, 97] . However, such models are mainly based on the three basis models in Figs. 3.4, 3.5 and 3.6, and are customized to accurately predict the response of the magnetic devices at high frequencies or under certain working scenarios.

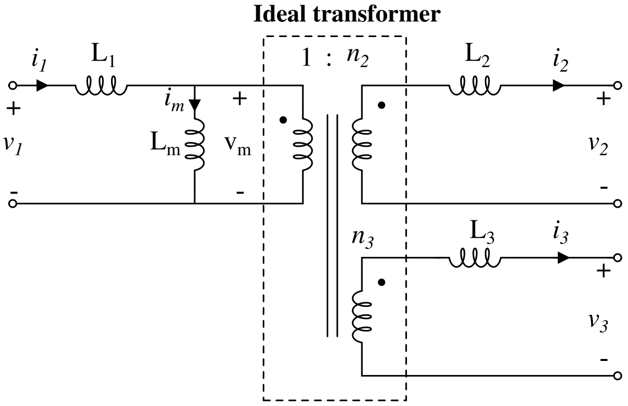

Figure 3.4: Conventional T model for the three-winding transformer

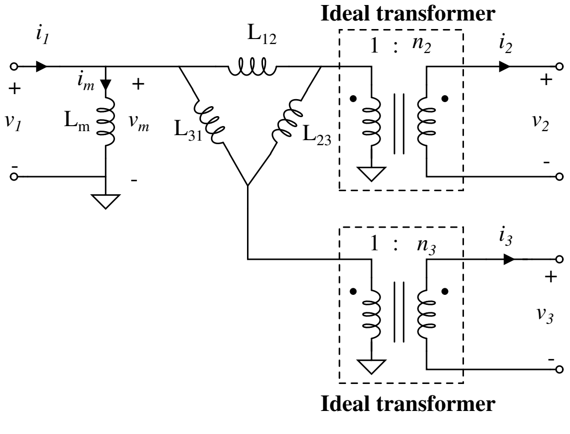

Figure 3.5: Extended cantilever model for the three-winding transformer

Mathematically, the conventional T model, the extended cantilever model, and the cross coupled secondary model, as illustrated in Figs. 3.4, 3.5 and 3.6, respectively, are equivalent, and there exist one-to-one relationships between the parameters of such models with the inductance matrix in Eq. (3.8). However, such basic models are different in terms of usage and parameter identification. For example, the conventional T model should not be used for the case where the number of

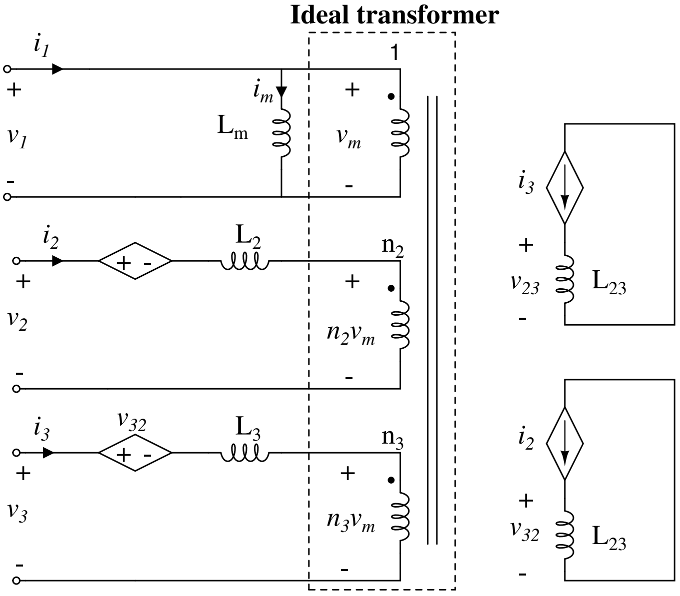

Figure 3.6: Cross coupled secondary model for the three-winding transformer

windings $N > 3$. Both the extended cantilever and cross coupled secondary models are valid for any number of windings. The T model lends itself to applications in which the leakage inductance of each winding is important and has a large effect on the response of the system, while the extended cantilever and cross coupled secondary models focus on the cross coupling between windings. More precisely, the extended cantilever model is useful in analysing the cross regulation in multi-output flyback converters [98].

3.3.1.3 Modelling of proximity and skin effects

It should be noted that the general transformer model in Eq. (3.7), and its equivalent circuit models, are only valid for low frequency applications where the losses due to proximity and skin effects are negligible. Unfortunately, the zero loss assumption cannot be applied to switched mode power converters which typically operate with mid to high frequencies, for example in the range of 100kHz to 1MHz, and have high frequency harmonics in the voltage and current waveforms. Therefore, the frequency-independent models, as presented in Sections 3.3.1.1 and 3.3.1.2, should be modified in order to take eddy current losses inside transformers into account. Essentially, high frequency excitations not only cause extra losses in the transformer copper, but also alter the value of the inductance matrix in Eq. (3.8). Such frequency-dependent effects can be modelled by [90]

$$\begin{bmatrix} v_1(t) \\ v_2(t) \\ v_3(t) \end{bmatrix} = \mathbf{Z}(s) \begin{bmatrix} i_1(t) \\ i_2(t) \\ i_3(t) \end{bmatrix} , \tag{3.10}$$

where

$$\mathbf{Z}(s) = \begin{bmatrix} R_{11}(s) + sL_{11}(s) & R_{12}(s) + sM_{12}(s) & R_{13}(s) + sM_{13}(s) \\ R_{21}(s) + sM_{21}(s) & R_{22}(s) + sL_{22}(s) & R_{23}(s) + sM_{23}(s) \\ R_{31}(s) + sM_{31}(s) & R_{32}(s) + sM_{32}(s) & R_{33}(s) + sL_{33}(s) \end{bmatrix} \tag{3.11}$$

is termed the impedance matrix. The resistance $\{R_{ij}(s)\}_{i,j=1,2,3}$ represent the power losses in the transformer windings while $\{L_{ii}(s)\}_{i=1,2,3}$ and $\{M_{ij}\}_{i,j=1,2,3 \text{ and } i \neq j}$ are the self and mutual inductance of the transformer. Both the resistance and inductance of $Z(s)$ are functions of frequency. It is important to note that the model in Eq. (3.10) is a generalized version of Eq. (3.7) and can accurately predict the response of the transformer over a wide frequency range.

Similarly, the effects of eddy currents can be included in the circuit models of Section 3.3.1.2 by replacing the frequency-independent inductor in each circuit branch with a frequency-dependent resistor and inductor in series [10, 13, 14, 94, 96, 97]. These modelling approaches encounter a particular difficulty in describing the dependence of series RC circuits on frequency. By observing that the effective resistance of transformer windings is an increasing function of frequency while the value of the leakage inductance reduces as the frequency increases, Leon *et al.* [99] found that such trends in the winding resistance and leakage inductance can be accurately represented by series/parallel Foster networks, as shown in Fig. 3.7. In order to exactly reproduce the impedance of the transformer windings at all frequencies, the circuits in Fig. 3.7 should have infinite order, i.e. $K = \infty$. However, for practical use, Foster networks are limited to an order of 5 or less, and their parameters are obtained by fitting only at certain measured frequencies using iterative methods or system identification [10,13,14,94,96,97].

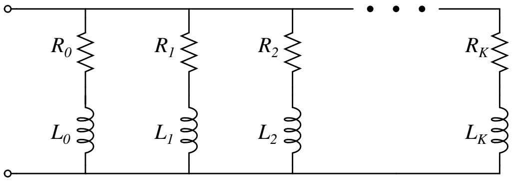

(a) Parallel Foster

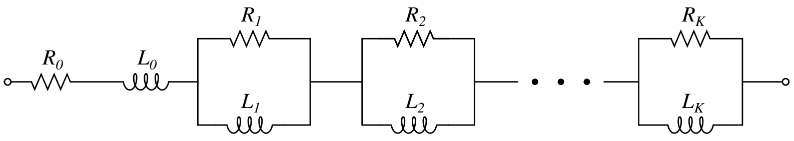

(b) Series Foster

Figure 3.7: Foster equivalent circuits for modelling eddy current effects in transformer windings

In addition to the proximity and skin effects, transformer dynamics are also affected by stray capacitance, and parasitic capacitance between and within transformer windings, at high frequencies. For applications, whose operating frequencies are far below the first winding resonant, the inter-winding and intra-winding capacitance is far less important than the leakage inductance and can be ignored. However, the effects of such capacitance should be considered in the prediction of the behaviour of practical transformers, up to the first resonant frequency or higher [97,100,101].

3.3.1.4 Identification of model parameters

In general, the parameters of the transformer models, as discussed in Sections 3.3.1.1 and 3.3.1.2, can be determined by: (1) deriving a mathematical expression for each parameter based on transformer geometries [102, 103], (2) using Maxwell's equations and finite element analysis (FEA) tools to simulate the frequency response of transformer windings, and then employing the resulting data as inputs for system identification [97,104], and (3) using experimental tests including excitation, short- and opened-circuit measurements, and manufacturer data-sheets [14, 105–107]. The first approach facilitates the determination of the model parameters; therefore, is convenient for the transformer design phase. However, such an approach is limited to calculation of certain parameters for some specific geometries only. Studies based on FEA tools have been intensively carried out in recent years, thanks to the rapid development of computing software and hardware. In theory, models of any transformer configuration can be obtained using FEA techniques [97,104]. The only remaining concern is the total computation time and accuracy. For example, in order to reach the same level of accuracy as the experimental results, a significant amount of time is taken to set up and run the FEA simulation. The benefit of FEA approaches is the ability to examine the performance of a transformer design before prototyping.

Although much theoretical works and many FEA-based investigations are presented in literature, estimation of model parameters is relied primarily on experimental measurements. The reason behind such a selection is the generality, accuracy and availability of experimental data. For example, in most cases, experimental results are far more accurate and much easier to produce than simulated results. Depending on the model selected to represent a particular effect, different measurement configurations and excitation signals are typically required [14, 104–107]. It should be noted that both time-response and frequency-response data can be used to identify the model parameters [105–107]. However, due to some difficulties in generating time-domain signals, studies for high frequency transformers are carried out in the frequency domain only [14, 104].

3.3.2 Modelling of the ferrite core

The equivalent circuits, presented in Section 3.3.1.2, use the linear inductor L_m to represent the behaviour of a ferrite core. This representation is only adequate for small signal operation, or when the core is not saturated, and the hysteresis losses are negligible. For large signal cases, where the saturation and hysteresis cause significant distortion in signal waveforms, a better core model is necessary. Essentially, a transformer core is characterized by a relationship between the magnetic flux density B and the magnetic field intensity H. Such relationship is composed of an infinity of possible magnetization curves which describe the evolution of B in response to any changes in H. These $B - H$ curves are usually non-linear and depend on the past values of B and H. Examples of some typical magnetization curves are plotted in Fig. 3.8, where a major loop is the largest possible outer loop while any loops inside the major loop is called minor loops. It is important to note that minor loops can be symmetric or asymmetric. In order to fully model the core behaviour, construction of all magnetization curves is required.

In the field of electromagnetism, two techniques are typically used to describe magnetization processes: physical modelling and phenomenological modelling [108, 109]. In physical modelling,

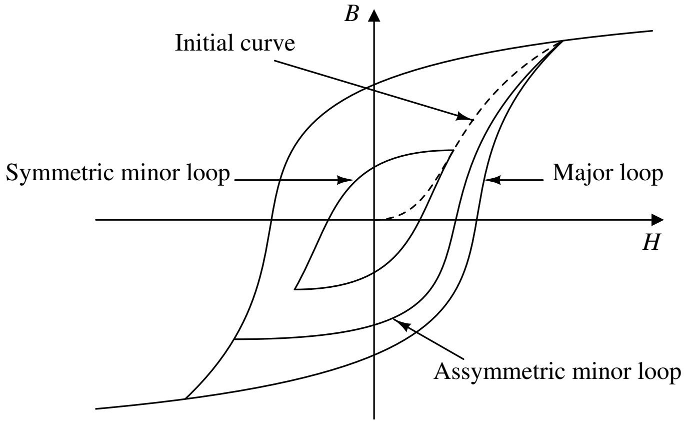

Figure 3.8: Magnetic hysteresis loops

basic elements, constituting magnetization processes, are separately modelled and simulated with the aim of understanding the phenomena involved. In phenomenological modelling, mathematical equations are derived based on properties of magnetic materials, and used as a means of generating magnetization curves. Phenomenological models are typically obtained through experimental data and curve fitting [18,19,109–115]. Since phenomenological models focus on reproducing the $B-H$ relationship, rather than providing insight into the physical process involved, they are usually simpler to implement and are computationally more efficient than physical models.

In addition to physical and phenomenological modelling techniques, another class of core models exists, which is heavily relied on mathematical studies, and is commonly found in power electronic applications [15–17,116]. As in the phenomenological approach, models for this mathematical approach are also obtained by finding the mathematical functions which fit the experimental data. However, functions are developed in such a way as to ease the implementation of the simulation rather than to accurately capture the behaviour of the magnetic material. Due to the complexity and determination of the parameters involved in physical and phenomenological modelling, mathematical models have been the most common choice for the simulation of power converters [15–17]. Recently, some phenomenological models, such as the Jiles-Atherton model [18], the Hodgdon model [19] and the Preisach model [112], have been also used in certain applications [116–118].

There are no standard procedures to determine the parameters of hysteresis core models. The appropriate procedure largely depends on the core model chosen for studies, transformer geometries, magnetic materials and types of the experimental measurements performed. For example, the determination of the Jiles-Atherton model parameters from experimental data can be found in [110, 119], while, for other models, one can refer to the examples in [15–17, 111–113, 115]. It should be highlighted that existing approaches try to model the behaviour of the transformer core through a study of the core material only [120]. In particular, a separate magnetic component, typically a toroidal core transformer, is developed for the purpose of analysing the properties of the core material under different excitation levels, i.e. from low to high voltages. Data from such experiments is then utilized to construct the hysteresis model for the core. Such a modelling procedure can be applied to transformers with a continuous core, i.e. a core with out an air gap; however, the procedure is not adequate for cores consisting of one or more air gaps, such as in a flyback transformer.

3.4 Discussion and perspective

This literature survey has revealed the majority of the significant literature covering the subject of simulation of DC-to-DC converters, modelling of power transformers, and parameter determination for transformer models. Section 3.2 shows that simulation of any practical DC-to-DC converter includes two tasks. The first task is to determine the mathematical model describing the operation of converter circuits and the second task is to select methods to simulate the obtained model in a digital computer. As pointed out in Section 3.2, circuit-oriented simulators are very convenient to examine the operation and performance of power converters in the cases, where models of all circuit components exist and are integrated into simulator libraries. However, if the simulation needs to be customized in order to perform some specific tasks, for example the verification of new control schemes, the design of equation solvers, equation-oriented simulators should be a primary choice.

For control design, transformers are traditionally described by a linear model; however, in practice, transformers behave non-linearly, particularly around the saturation region. Hence, a comparison between linear and non-linear models need to be made to confirm the validity of the linear model during control synthesis. In contrast to electronic components, such as resistors, capacitors and semiconductor devices, transformers have been intensively investigated over decades. However, there is no unique modelling approach and other issues exist, relating to the flyback transformer, which have not been considered before. Therefore, a particular study on the flyback transformer is necessary.

The modelling, and determination of model parameters, for a high frequency transformer has been investigated previously. In general, existing studies, as presented in Sections 3.3.1 and 3.3.2, focus on either identifying a frequency-dependent winding model with an ideal core assumption using small signal excitation, or estimating a dynamic core loss model of a specific magnetic material using both a high amplitude and high frequency voltage input signal. Although the authors in [121,122] claimed that the frequency-dependent and hysteresis effects inside the transformer can be handled at the same time, such models are obtained from an analytical [121,123] or numerical [122] approach, i.e. based on physical equations or finite element analysis, rather than a measurement-based analysis. To the best of the author's knowledge, no investigation, that tries to model both non-linear and winding effects together using experimental data and system identification, is available.

As mentioned in Section 3.3.1.4, for low frequency applications, estimation of transformer model parameters has been widely studied using both time and frequency domain data. However, studies for high frequency transformers have been carried out in the frequency domain only. The reason behind such a selection is due to the advantages of the frequency domain approach over the time domain approach. Particularly, with the help of an impedance analyzer, the response of a system over a wide frequency range is much easier to collect in the frequency domain rather than in the time domain. In addition, frequency domain data, which is returned by an impedance analyzer, is also less noisy than equivalent time domain data collected by a data acquisition card. Despite such difficulties in data collection, the time domain approach is still preferred since it requires only a simple measurement facility (such as a digital oscilloscope) and provides an easy way to deal with a complex transformer model.

Chapter 4

Control methods for wide operating range DC-to-DC converters: A literature review

4.1 Introduction

In general, all practical DC-DC power converters can be split into two parts, consisting of a power circuit and a control module, as illustrated in Fig. 4.1. The power circuit is responsible for transferring energy from the input source to the output load, while the control circuit manages the amount of energy delivered in order to maintain a constant DC level at the output port. The controller is unnecessary when the load is constant and the input supply voltage is regulated; however, such a condition rarely exists in practice. Even in such a condition, the control module is also needed to compensate for the variations of circuit elements due to ageing, as well as modelling errors. The main mechanism to achieve a constant output voltage is through feedback regulation, where the output voltage and other converter signals are measured and compared with reference signals to form the pulse-train control signal $q(t)$, as shown in Fig. 4.1. Although the format of $q(t)$ is directly connected with the control method used, understanding the characteristics of switching formats can help find a proper control solution, for a given set of design specifications.

The main aim of this chapter is to firstly study the effect of switching formats on the design and performance of converter power stages, and to then provide a comprehensive review of existing trends in designing controllers for broad operating range DC-to-DC converters. The knowledge from this chapter can then serve as a basis for the study of the optimal digital control in Chapter 8.

The structure of this chapter is organised as follows. Section 4.2 presents a detailed investigation of different modulation techniques, which are commonly deployed to generate the pulse-train control signal $q(t)$ in DC-to-DC converters. For clarification, control applications are classified according to the particular converter mathematical model used to determine control laws. In particular, Section 4.3 summarizes existing controllers which are designed based on the switched-state space models of power converters while the synthesis of controllers, based on large-signal averaged models and small-signal models, is reviewed in Sections 4.4 and 4.5, respectively.

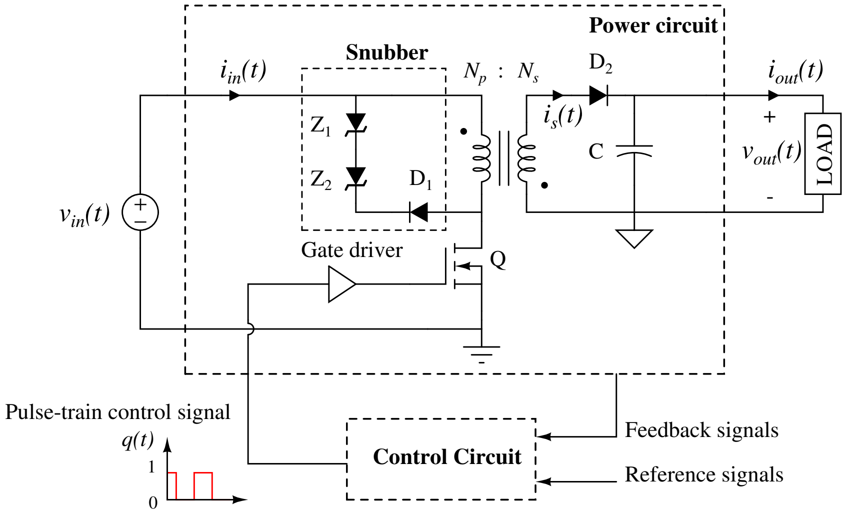

Figure 4.1: Block diagram of a flyback converter power stage and a control circuit. The feedback signals can be the output voltage, the inductor current, or both.

4.2 Classification of control signal formats

Various modulation techniques have been proposed to generate the switching waveform $q(t)$. Such techniques can be classified as pulse-width modulation (PWM), delta-sigma modulation, pulse-frequency modulation (PFM) and many others. Since only PWM and PFM have been widely applied in control of power converters, they will be the main consideration of this section.

4.2.1 Pulse width modulation

PWM makes use of a fixed-frequency rectangular pulse wave, whose pulse width is modulated. The cyclic nature of PWM signals leads to the T_{sw}-periodic response of output voltages of DC-to-DC converters. The spectrum of the output voltage, as illustrated in Fig. 4.2, consists of a dominant DC component, modulation frequencies, a high density spectrum around the switching frequency $f_{sw} = \frac{1}{T_{sw}}$, and negligible high-frequency harmonics which are not presented in Fig. 4.2. With a sufficiently high switching frequency, the contaminated frequencies from power converters can be simply filtered out using a straightforward low-pass filter. As a result, PWM converters usually offer low output voltage ripple and low switching noise, which help to ease the design of electromagnetic interference (EMI) filters.

In contrast to the simple EMI filter design, the periodic property poses a significant drawback to the system operating under light load, or in a standby condition. In such modes, PWM control circuits continue to force semiconductor devices into cyclically switching between the on-state and the off-state, even though such light loads draw only a very small current, or even no current, from the power circuit. The constant power consumption, due to switching actions, causes a dramatic decline in the power conversion efficiency of the whole system. The smaller the power a load

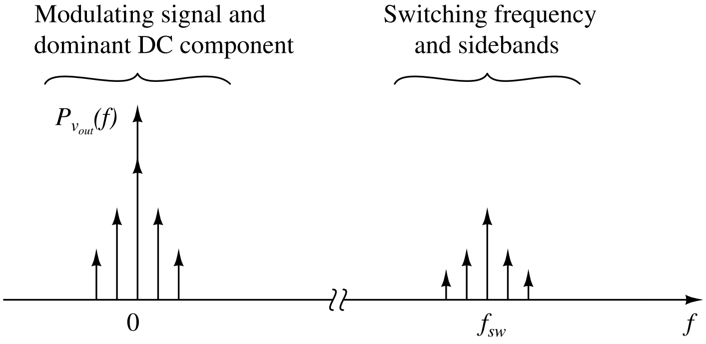

Figure 4.2: Spectrum of the converter output voltage $v_{out}(t)$ using PWM.

consumes, the less efficient a converter is in this low-load switching mode. In addition to constant losses, the fixed frequency approach runs into another difficulty, in that converters are unstable when regulating the output voltage at no load [124]. To overcome such a problem, a resistor is inserted in parallel at the output port to emulate the presence of a minimum payload. Though the power loss due to the emulated load is typically insignificant, such an implementation should be avoided in energy-limited systems like mobile phones and laptops.

The true merits of PWM controllers are only exploited at mid- to full-load operation, where the energy transferred to the load is much greater than the amount of energy lost due to conduction and switching losses. The efficiency obtained is typically above 80%, and is largely determined by the quality of circuit components and the switching frequency employed, rather than compensation algorithms. In other words, for similar converter circuits and switching frequencies, the differences between control methods are merely complexity, stability, and performance.

The control approaches, utilizing PWM signals, include feed-forward PWM control [125, 126], voltage mode control [3, 127–129], peak current programmed mode control [130], average current mode control [35, 131] and one-cycle control [132]. Besides their distinctive features, PWM control methods inherently suffer from the fixed-frequency modulation constraint and hence tend to exhibit slower dynamic response than pulse frequency modulation (PFM) controllers.

4.2.2 Pulse frequency modulation

Pulse frequency modulation implies any type of rectangular pulse waves that possess a variable switching period T_{sw}. Three typical forms of PFM are highlighted in Table 4.1, where T_{on}, T_{off} are the on-time and off-time of pulse waves, respectively. The three PFM patterns of Table 4.1 all give designers freedom to play with the switching cycle T_{sw}, which is a key factor in the improvement of the system response. Therefore, PFM-type controllers generally offer a faster transient performance than their PWM counterparts.

Unlike PWM signals, whose spectral pattern is predictable, switching frequencies in PFM converters are poorly defined and strongly depend on converter parameters, the input voltage and the load current. The values of circuit components may assist in tracing the operating frequency at steady state; nonetheless, the tolerance of components and parasitic issues unexpectedly modify

Table 4.1: Classification of switching waveforms used in PFM converters.

Switching format	$\mathbf{T_{on}}$	$\mathbf{T_{off}}$	$\mathbf{T_{sw}}$
constant on-time	constant	variable	variable
constant off-time	variable	constant	variable
undetermined	variable	variable	variable

the nominal switching behaviour. Such unavoidable variation becomes severe when converters encounter large transient responses caused by large variations in the current demand or input voltage. A large deviation from the nominal frequency induces significant challenges in keeping EMI noises under control and in selecting semiconductor devices. To alleviate the tight constraint on practical production, a limited frequency range is imposed on the design specifications at the expense of a degradation in the dynamic response.

Ignoring the EMI noise issue, PFM controlled converters are promising candidates for state-of-the-art applications, such as microprocessor load types [133]. For such systems, power supplies must cover all working scenarios, including very high slew-rate load changes from active modes to sleep modes and vice versa, tight output voltage regulation, and minimum power consumption in standby modes. Obviously, the inherent features of PFM approaches, consisting of high slew-rate transient behaviour [134–138] and adjustable power losses [43, 45, 124], lend themselves well to coping with such challenges.

4.3 Switched state-space model based approaches

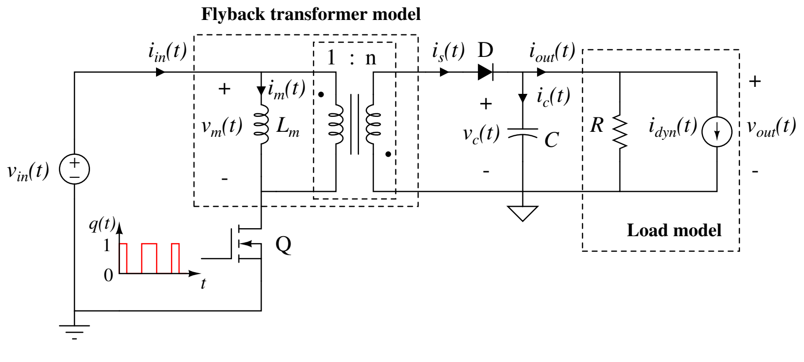

Figure 4.3: Ideal model of the power stage of flyback converters

Switched state-space models, also called hybrid models, provide the most accurate description of DC-to-DC converters used in control design. Such models typically consist of two or more sets of linear differential equations. Each equation set corresponds to a configuration of switching devices in a converter topology under consideration. For example, a flyback converter model, as illustrated in Fig. 4.3, is considered. For simplicity, the converter is assumed to operate in CCM.

By choosing the magnetizing inductor current $i_m(t)$ and the capacitor voltage $v_c(t)$ as the state variables, picking the output voltage $v_{out}(t)$ as the output signal, and following the analysis in Section 2.2, the general state-space description of such a converter can be derived as

$$\begin{aligned} \tfrac{d}{dt}\mathbf{x}(t) = &\quad \mathbf{A}\mathbf{x}(t)+\mathbf{B}\mathbf{u}(t) &&, \mathbf{A}\in\{\mathbf{A}_1,\mathbf{A}_2\} \text{ and } \mathbf{B}\in\{\mathbf{B}_1,\mathbf{B}_2\}, \\ y(t) = &\quad \mathbf{C}\mathbf{x}(t)+\mathbf{E}\mathbf{u}(t) &&, \mathbf{C}\in\{\mathbf{C}_1,\mathbf{C}_2\} \text{ and } \mathbf{E}\in\{\mathbf{E}_1,\mathbf{E}_2\}, \end{aligned} \tag{4.1}$$

where

$$\begin{cases} \mathbf{A}=\mathbf{A}_1, \quad \mathbf{B}=\mathbf{B}_1, \quad \mathbf{C}=\mathbf{C}_1, \quad \mathbf{E}=\mathbf{E}_1 \text{ when } q(t)=1 \text{ , i.e. Q is on,} \\ \mathbf{A}=\mathbf{A}_2, \quad \mathbf{B}=\mathbf{B}_2, \quad \mathbf{C}=\mathbf{C}_2, \quad \mathbf{E}=\mathbf{E}_2 \text{ when } q(t)=0 \text{ , i.e. Q is off} \end{cases} \tag{4.2}$$

The vectors $\mathbf{x}(t)$, $\mathbf{u}(t)$ and $\mathbf{y}(t)$ are defined in Eq. (2.4), while the expressions for $\mathbf{A}_1$, $\mathbf{B}_1$, $\mathbf{C}_1$, $\mathbf{E}_1$, $\mathbf{A}_2$, $\mathbf{B}_2$, $\mathbf{C}_2$ and $\mathbf{E}_2$ are given in Eqs. (2.3) and (2.6), respectively. $q(t)$ in Eq. (4.2) is the general pulse-train control signal. Although the model in Eq. (4.1) exhibits linear behaviour when the switch Q is frozen, i.e. $q(t)$ is fixed, the overall system response is highly non-linear due to the discontinuity of the state space matrices $\mathbf{A}$, $\mathbf{B}$, $\mathbf{C}$ and $\mathbf{E}$ at points where the switch Q changes its states. The output signal $y(t)$ not only depends on the circuit parameters and the input signal $u(t)$, but is also influenced by the control signal $q(t)$. For given values of the input signal and the converter parameters, the output voltage can be regulated by varying the on-time and off-time of the switch Q.

Essentially, hybrid models, e.g. in Eq. (4.1), lend themselves to non-linear control techniques, which exploit the switching between linear subsystems as a means to stabilize DC-to-DC converters, and to simultaneously achieve the output voltage regulation. Although several methods and frameworks have been developed to cope with switched systems, see [139] and the references therein, only hysteresis control, sliding mode control and boundary control [140–144] have been successfully applied in DC-to-DC power converters. Various studies on boundary control, sliding mode control and hysteresis control are reviewed in Sections 4.3.1, 4.3.2 and 4.3.3, respectively.

4.3.1 Boundary control

Boundary control is a geometric based approach to designing controllers for DC-to-DC converters. In general, boundary control uses switched state-space models and phase plane analysis to develop control laws for switching devices in power converters [145–147]. Such control laws typically use both the on-time and off-time of switching devices as a means to shape the system response. Due to the generality of switching waveforms, boundary control can offer an optimum transient response [142] and fast reference tracking [138, 148] at the expense of unpredictable switching frequencies and potential instability [149].

System trajectories, which are the visual description of the relationship between the capacitor voltage $v_c(t)$ and the inductor current $i_m(t)$, under different switch configurations, are frequently exploited for design and analysis of boundary control. System trajectories can be mathematically established by solving the state-space equations of DC-to-DC converters, with different initial conditions. For demonstration purposes, the flyback converter in Fig. 4.3 is assumed to have

$v_{in}(t) = 5V$, $L_m = 1H$, $n = 1$, $C = 1F$, $R = 1\Omega$, and $i_{dyn}(t) = 0A$. By solving Eq. (4.1) for $i_m(t)$ and $v_c(t)$, two families of trajectories for the flyback converter, corresponding to the switch-on and switch-off positions can be obtained, and are sketched in Fig. 4.4. Each trajectory family converges to a single equilibrium point, which corresponds to the steady state values of the state variables of the converter when the switch Q keeps its state unchanged. The equilibrium points, for the Q-on and Q-off families of trajectories for the flyback converter, are ($v_c = 0$, $i_m = \infty$) and ($v_c = 0$, $i_m = 0$), respectively.

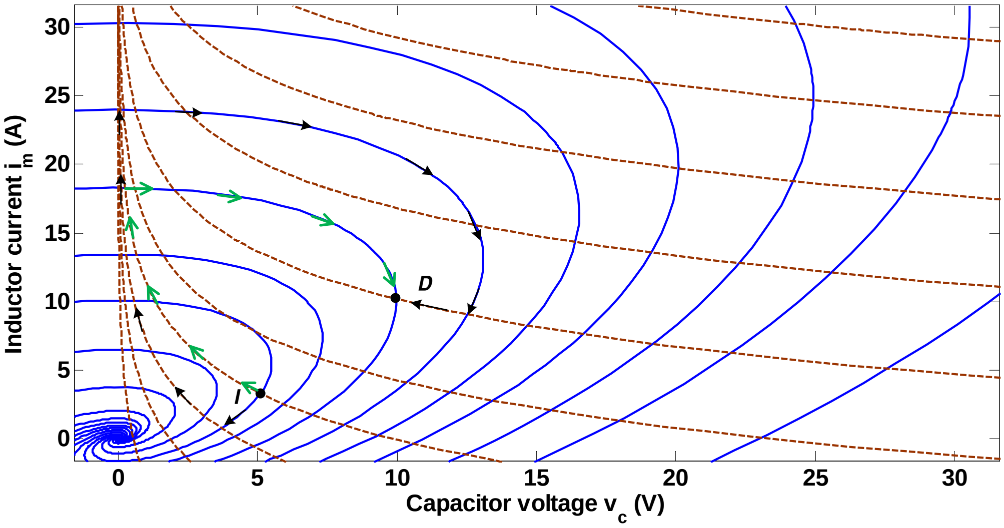

Figure 4.4: Two trajectory families of the flyback converter, where dashed lines are switch-on trajectories, and solid lines are switch-off trajectories. The equilibrium points for the families of Q-on and Q-off trajectories are $(0, \infty)$ and $(0, 0)$, respectively.

When the initial conditions of the state variables $v_c(t)$ and $i_m(t)$ are known, the trajectories of the flyback converter for arbitrary switching functions can be obtained by combining the Q-on and Q-off trajectories. Since the number of possible trajectories is infinite, various switching waveforms, $q(t)$, can be utilized to drive the converter to a desired response from any initial condition. Figure 4.4 shows an example of two possible control strategies, one corresponding to the green arrow and the other corresponding to the black arrow, which can be used to bring the flyback converter from the initial state **I** to the desired state **D**. After reaching **D**, the switching action has to be continued in order to keep the operating state of the converter close to the desired point. Since the state trajectories of the flyback converter are closed-loop curves at steady state, it is impossible to maintain the system operating state exactly at the point **D**, unless the converter switches on and off infinitely fast. In such cases, the system exhibits *chattering*.

The green arrow solution in Fig. 4.4 is obviously more optimal, in terms of time and energy consumed, than the black arrow approach. Such an observation implies that when the Q-on and Q-off trajectory families are fixed, and the initial condition as well as the desired operating point is provided, the optimal switching path, which brings the system to the desired state in the minimum time and for the least energy consumption, can always be located [142]. Unfortunately, the Q-on and Q-off trajectories for power converters are generally dependent on the output load and the input voltage; moreover, the initial states of power converters are not always given. Therefore, the optimal control design, based on the phase plane, is a significant challenge.

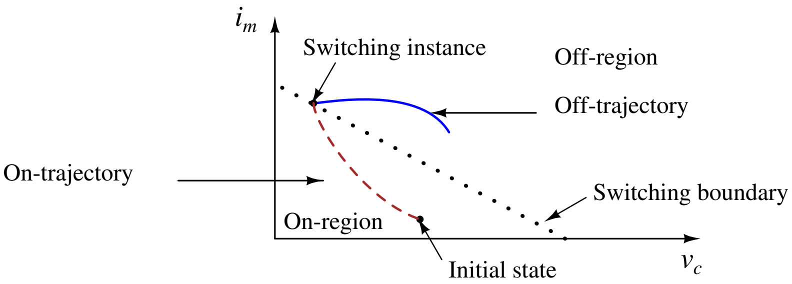

(a) The active switch Q is on at start-up

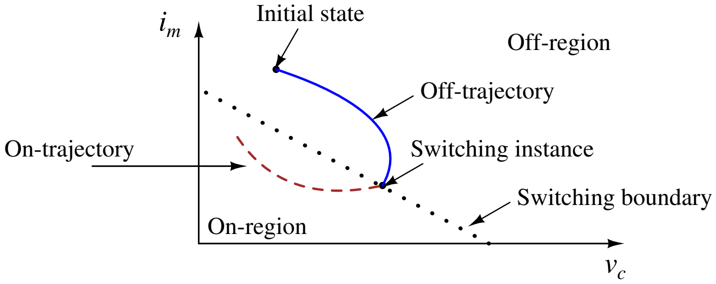

(b) The active switch Q is off at start-up

Figure 4.5: An example of switching surfaces and switching instances established through the interaction of a switching surface and state trajectories of flyback converters.

In principle, boundary control does not rely on particular Q-on and Q-off trajectories associated with the initial states and desired states of DC-to-DC converters, but rather on predefined switching boundaries (or switching surfaces) in the state plane. Each switching boundary splits the state plane into two halves. In each half, the control command for the switch is decided in advance, which means that switching only takes place when the state trajectory of a converter move towards, and intersect, the boundary. The illustration of control interaction, between the state trajectories of flyback converters and a switching boundary under different initial conditions, is presented in Fig. 4.5. The expression for a straight line or a flat boundary, as exemplified in Fig. 4.5, can be found [147] via

$$\sigma(\mathbf{x}) = \mathbf{k}_\sigma(\mathbf{x} - \mathbf{x}_{ref}), \tag{4.3}$$

where $\mathbf{x}_{ref}$ is the reference state vector, $\mathbf{k}_\sigma$ is a constant gain vector which defines the slope of the switching surface, and $\sigma(\mathbf{x})$ denotes the switching surface. According to Eq. (4.3), the slope $\mathbf{k}_\sigma$ is the primary parameter deciding the performance and stability of a closed-loop converter. Given the mathematical description of the switching surface in Eq. (4.3), the control signal can be computed via

$$q(t) = 0.5\Big(1 - sign\big(\sigma(\mathbf{x})\big)\Big), \tag{4.4}$$

where $sign(.)$ is the sign function.

Generally, switching surfaces can have different shapes and can be designed in different ways. Such design flexibility leads to various forms of boundary control, such as sliding mode control [140, 143, 150–152] and hysteresis control [153, 154].

4.3.2 Sliding mode control

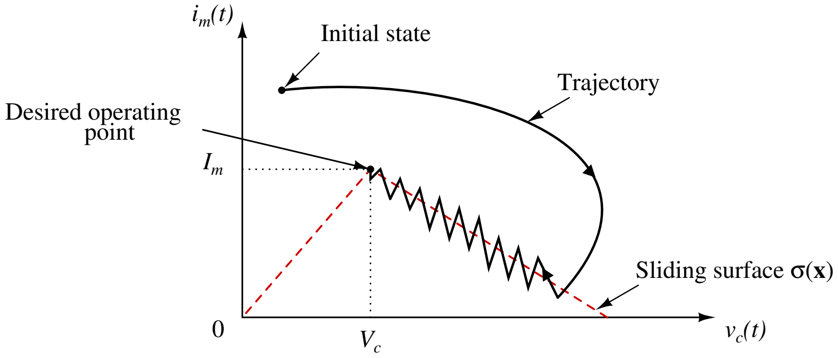

Figure 4.6: Phase portrait of a flyback converter under sliding mode control. Switching laws are designed such that system trajectories can reach the sliding surface $\sigma(\mathbf{x})$. $i_m(t)$ is the magnetizing inductor current, while $v_c(t)$ is the capacitor voltage. I_m and V_c denote the desired values of $i_m(t)$ and $v_c(t)$.

Sliding-mode control is a specific case of boundary control, where certain switching boundaries are exploited. The role of such switching surfaces in sliding mode control is to establish paths for the state variables directing toward the desired equilibrium [140, 150]. Figure 4.6 demonstrates the phase portrait of a sliding mode controller for a flyback converter. The switching function $q(t)$ of sliding mode control can be formed in a similar way to boundary control, i.e. based on Eq. (4.4).

The earliest work on developing sliding mode controllers for DC-to-DC converters are presented in [140, 150]. In these studies, the application of sliding mode control to various basic topologies of second order power converters is considered. In addition to basic converter topologies, various studies have also extended sliding mode control to high order converters [155], and parallel-connected converters [156]. Although early investigations on sliding model control are based on theoretical analysis and simulation [140, 150, 155], some experimental evaluation of sliding mode controlled DC-to-DC converters has been recently reported in the literature [143, 151, 157, 158]. Due to the inherently unpredictable switching frequency, traditional sliding mode control is not suitable for certain applications which are sensitive to high frequency noise. In order to overcome such drawbacks, various methods have been proposed to maintain a constant switching frequency for sliding mode controllers [159, 160]. A comprehensive review of sliding-mode control, used in DC-DC power converters, can be found in [161].

Although various works on developing sliding mode control for basic topologies as well as high order topologies were reported in the literature [161], the application of sliding mode control to flyback converters is very limited due to the difficulty in generating a correct phase portrait. The main reason causing the distortion in the phase portrait is the optical isolator which is always required for isolation purposes.

4.3.3 Hysteresis control

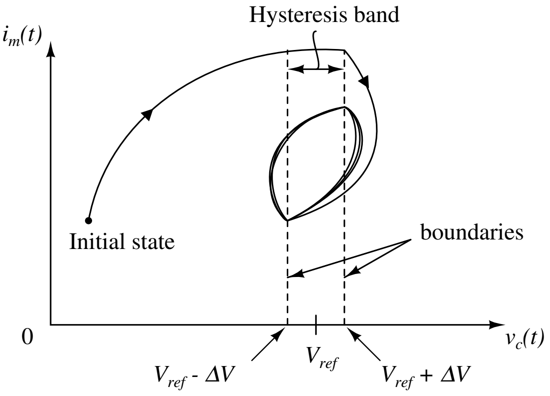

Figure 4.7: Phase portrait of buck converters under hysteresis control.

For voltage mode hysteresis control [153, 154], two switching boundaries, which are parallel to the i_m-axis and intersect the v_c-axis at $V_{ref} - \Delta V$ and $V_{ref} + \Delta V$, as illustrated in Fig. 4.7, are typically employed. The space between such vertical boundaries defines a hysteresis band, in which no control action occurs. If the hysteresis band is not present, or is too narrow, the system may chatter. Since the control signal is obtained directly through comparison between the capacitor voltage $v_c(t)$ and a pair of reference values $V_{ref} - \Delta V$ and $V_{ref} + \Delta V$, hysteresis controllers are very simple to implement, are robust to both large-signal and small-signal disturbances, and can offer very fast dynamic characteristics. One of the major drawbacks of hysteresis control is the dependence of the switching frequency on the dynamics of the converter state variables. If the parameters of the converter is assumed to be constant, the switching frequency will vary according to the input voltage and output load.

By adjusting the width of the hysteresis band according to operating conditions, switching frequencies can be locked to a fixed value [162]; however, such implementation tends to degrade the performance of hysteresis controllers. Another drawback of hysteresis control based on the output voltage is the limitation of the number of application possibilities in power electronics. For example, hysteresis controllers can be applied to buck converters but not to other converter topologies. Such a conclusion can be verified through interaction between system trajectories and two switching boundaries.

4.4 Large-signal model based approaches

Switched state space models, e.g. in Eq. (4.1), can accurately predict both the intra-cycle and inter-cycle behaviour of DC-to-DC power converters; however, not all conventional feedback controllers can deal with variable structure systems and directly generate the switching function $q(t)$ from feedback signals, without the need for auxiliary modulation circuits. Thus, forming simplified time-invariant models, which are well matched to conventional analysis and control design procedures, is necessary.

In general, the simplification of detailed switching models can be obtained through an averaging process, which smoothes out all switching ripples in the waveforms of state variables, or through sampled-data modelling, which ignores intra-cycle switching details, but focuses instead on cycle-to-cycle behaviour [62,163]. Based on such principles, various approaches [31,73,83,164–167] have been proposed in the literature to find time-invariant models for different converter topologies operating in either CCM or DCM, or both. Some commonly used techniques can be listed as: (a) state-space averaging modelling [31, 73, 168–170], (b) averaged circuit/switch modelling [78, 164, 165, 171–174], (c) sampled-data modelling [83, 85, 175–179], (d) equivalent non-linearity modelling [166, 180], (e) energy-based modelling [181, 182] and (f) enhanced modelling [167, 183, 184]. Although different mathematical derivation and approximation forms are used in averaging techniques and sampled-date modelling, the resulting simplified models from such approaches are mathematically equivalent. Therefore, without loss of generality, only state-space averaging techniques are employed to obtain the time-invariant equivalent of Eq. (4.1).

The state-space averaging technique was developed in 1976 by Middlebrook and Cuk [73], where the authors reviewed the limitations of existing methods [80] and suggested a unified approach to deriving the equivalent large-signal and small-signal models of DC-to-DC power converters. Such methods immediately became an industrial standard for designing controllers for power converters. Generally, averaged state-space models are the direct results of taking the local average of general switched models over a switching cycle, e.g. T_{pwm} of PWM control signals. To clarify the idea, such a procedure is applied to the flyback converter model described in Eq. (4.1) with an assumption that the switching function $q(t)$ is a PWM signal with a period of T_{pwm}. The result of averaging the state space model in Eq. (4.1) is given by

$$\begin{aligned} \frac{d}{dt}\overline{\mathbf{x}(t)} &= \Big(d(t)\mathbf{A}_1 + \big(1-d(t)\big)\mathbf{A}_2\Big)\overline{\mathbf{x}(t)} + \Big(d(t)\mathbf{B}_1 + \big(1-d(t)\big)\mathbf{B}_2\Big)\overline{\mathbf{u}(t)}, \\ \overline{\mathbf{y}(t)} &= \Big(d(t)\mathbf{C}_1 + \big(1-d(t)\big)\mathbf{C}_2\Big)\overline{\mathbf{x}(t)} + \Big(d(t)\mathbf{E}_1 + \big(1-d(t)\big)\mathbf{E}_2\Big)\overline{\mathbf{u}(t)}, \end{aligned} \tag{4.5}$$

where $d(t) = \frac{1}{T_{pwm}}\int_t^{t+T_{pwm}} \mathbf{q}(\tau)d\tau$ indicates the instantaneous duty ratio. The over-line operator, implying the local average over an interval of length T_{pwm}, is defined in Eq. (2.10). Since the term $\Big(d(t)\mathbf{B}_1 + \big(1-d(t)\big)\mathbf{B}_2\Big)\overline{\mathbf{u}(t)}$ is typically non-zero, regardless of the duty ratio chosen, the system in Eq. (4.5) is not at equilibrium at the origin. Such a condition is not convenient for control design and analysis; hence, a translation of the quiescent operating point of the converter to the origin is required. The flyback converter in Eq. (4.5) is assumed to have a desired operating point at

$$\overline{\mathbf{x}(t)} = \mathbf{X} = \begin{bmatrix} I_m \\ V_c \end{bmatrix}, \quad \overline{\mathbf{y}(t)} = \mathbf{Y} = [V_{out}], \quad \overline{\mathbf{u}(t)} = \mathbf{U} = \begin{bmatrix} V_{in} \\ I_{dyn} \end{bmatrix}, \quad d(t) = D. \tag{4.6}$$

In order to perform the axis translation, new variables, defined by

$$\begin{aligned}
\mathbf{x}^*(t) &= \overline{\mathbf{x}(t)} - \mathbf{X},\\
\mathbf{y}^*(t) &= \overline{\mathbf{y}(t)} - \mathbf{Y},\\
\mathbf{u}^*(t) &= \overline{\mathbf{u}(t)} - \mathbf{U},\\
d^*(t) &= d(t) - D,
\end{aligned} \tag{4.7}$$

are introduced. Substituting Eq. (4.7) into Eq. (4.5) and the resulting equation simplifies to

$$\begin{aligned}
\frac{d}{dt}\mathbf{x}^*(t) &= \big(D\mathbf{A}_1 + (1-D)\mathbf{A}_2\big)\mathbf{x}^*(t) + \big(\left(\mathbf{A}_1 - \mathbf{A}_2\right)\mathbf{X} + \left(\mathbf{B}_1 - \mathbf{B}_2\right)\overline{\mathbf{u}}\big)d^*(t)\\
&\quad + \big(\mathbf{A}_1 - \mathbf{A}_2\big)\mathbf{x}^*(t)d^*(t),\\
\mathbf{y}^*(t) &= \big(D\mathbf{C}_1 + (1-D)\mathbf{C}_2\big)\mathbf{x}^*(t) + \big(\left(\mathbf{C}_1 - \mathbf{C}_2\right)\mathbf{X} + \left(\mathbf{E}_1 - \mathbf{E}_2\right)\overline{\mathbf{u}}\big)d^*(t)\\
&\quad + \big(\mathbf{C}_1 - \mathbf{C}_2\big)\mathbf{x}^*(t)d^*(t),
\end{aligned} \tag{4.8}$$

or

$$\begin{aligned}
\frac{d}{dt}\mathbf{x}^*(t) &= \mathbf{A}_{bi}\mathbf{x}^*(t) + \big(\mathbf{B}_{bi}\mathbf{x}^*(t) + \mathbf{b}_{bi}\big)d^*(t),\\
\mathbf{y}^*(t) &= \mathbf{C}_{bi}\mathbf{x}^*(t) + \big(\mathbf{E}_{bi}\mathbf{x}^*(t) + \mathbf{e}_{bi}\big)d^*(t).
\end{aligned} \tag{4.9}$$

where

$$\begin{aligned}
&\mathbf{A}_{bi} = D\mathbf{A}_1 + (1-D)\mathbf{A}_2, \quad \mathbf{B}_{bi} = \mathbf{A}_1 - \mathbf{A}_2, \quad \mathbf{b}_{bi} = \left(\mathbf{A}_1 - \mathbf{A}_2\right)\mathbf{X} + \left(\mathbf{B}_1 - \mathbf{B}_2\right)\overline{\mathbf{u}},\\
&\mathbf{C}_{bi} = D\mathbf{C}_1 + (1-D)\mathbf{C}_2, \quad \mathbf{E}_{bi} = \mathbf{C}_1 - \mathbf{C}_2, \quad \mathbf{e}_{bi} = \left(\mathbf{C}_1 - \mathbf{C}_2\right)\mathbf{X} + \left(\mathbf{E}_1 - \mathbf{E}_2\right)\overline{\mathbf{u}},
\end{aligned} \tag{4.10}$$

Since no small signal assumption has been made, Eq. (4.9) is valid for large signals. Close examination of Eq. (4.9) reveals that the averaged converter model is linear both with respect to the state variable $\mathbf{x}^*(t)$ and the control signal $d^*(t)$ considered separately, but is non-linear when considering $\mathbf{x}^*(t)$ and $d^*(t)$ together. Systems having such a characteristic are typically referred to as bilinear systems. In the field of DC-to-DC power converters, non-linear control laws are mostly synthesized based on bilinear large-signal averaged models, e.g. in Eq. (4.9).

Figure 4.8 illustrates the block diagram of a general PWM non-linear control architecture for power converters. As highlighted in Fig. 4.8, the differences between non-linear control approaches reflect the way in which the feedback signals are processed, and the switching laws are formed. Two threshold levels, d_{min} and d_{max}, of the PWM modulator account for saturation occurring in the comparator circuit, when the command signal output v_c^* is too high or too low. Notice that the saturation effect is not taken into consideration in synthesizing linear controllers, since the small-ripple assumption does not allow the examination of the saturation of the continuous-time duty ratio.

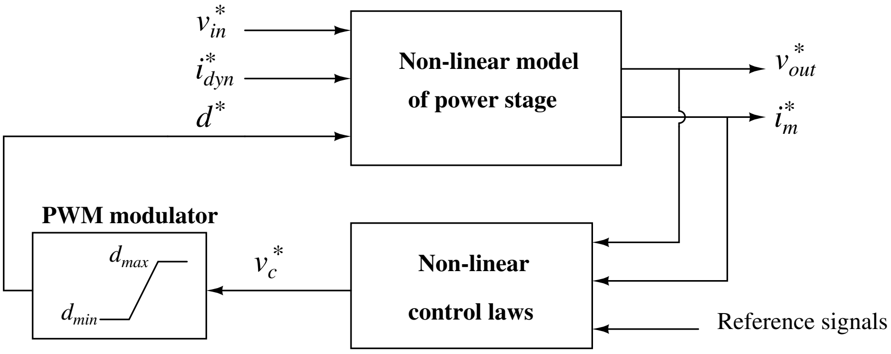

Figure 4.8: Typical structure of PWM non-linear feedback control for DC-to-DC converters.

4.4.1 Phase plane analysis

The first study, based on a bilinear large-signal model of DC-to-DC converter, was conducted by Erickson *et al.* in [185], where the large-signal stability of a boost regulator is analysed by means of state plane trajectories. Particularly, Erickson *et al.* [185] pointed out that other equilibrium points, different from the desired quiescent operating point, may exist, and that during large transient responses, the regulator may escape from the desired operating point and move on to other stable equilibrium points. The existence of more than one equilibrium point can cause instability in power converters. To avoid such instability, the authors in [185] proposed placing a constraint $[d_{min}, d_{max}]$ on the variation range of the duty ratio $d(t)$. The values of d_{min} and d_{max} are typically chosen such that the displacement of the state variables from the desired operating point, with respect to any input disturbances, should be limited to the attraction region of the desired operating point. Notice that the saturation constraints on $d(t)$ can lead to windup errors which in turn limit the system performance. However, such an issue can be alleviated by an anti-windup mechanism.

The principle in [185] is reused in [186], for the purpose of synthesizing controllers for boost converters; however, [186] relies on state-space geometry modelling [187], rather than bilinear averaged models. To provide sufficient insight into the global stability study, Leyva *et al.* [188] made use of a circuit-oriented representation and an incremental energy analysis to determine the control signal $d(t)$ and its saturation region. Although the phase plan method is a useful tool to verify the stability of both open-loop and closed-loop systems, such a method does not allow the direct synthesis of non-linear controllers.

4.4.2 Lyapunov function based control

Most non-linear controllers for power converters are obtained through directly applying Lyapunov functions, or indirectly exploiting the energy-based idea from such theory. Many remarkable studies have been published in the literature. The main difference between such studies is only the technique which each author employs to seek Lyapunov functions and derive feedback rules. The first controller for DC-to-DC converters, based on Lyapunov functions, can be found in [189, 190], where the authors use incremental energy as a basis to define the Lyapunov function, as

$$V(\mathbf{x}^*) = \frac{1}{2}\mathbf{x}^{*T}\mathbf{Q}\mathbf{x}^*, \tag{4.11}$$

where $\mathbf{Q}$ is symmetric and positive definite. For example, [190] suggested the form of $\mathbf{Q}$ as

$$\mathbf{Q} = \begin{bmatrix} L_m & 0 \\ 0 & C \end{bmatrix}. \tag{4.12}$$

Using the Lyapunov function $V(\mathbf{x}^*)$ in Eq. (4.11) for the bilinear system in Eq. (4.9), and differentiating $V(\mathbf{x}^*)$ along the system trajectories, yields

$$\frac{d}{dt}V(\mathbf{x}^*) = \frac{1}{2}\mathbf{x}^{*T}\left(\mathbf{Q}\mathbf{A}_{bi} + \mathbf{A}_{bi}^T\mathbf{Q}\right)\mathbf{x}^* + \frac{1}{2}\Big(\mathbf{x}^{*T}\left(\mathbf{Q}\mathbf{B}_{bi} + \mathbf{B}_{bi}^T\mathbf{Q}\right)\mathbf{x}^* + 2\mathbf{b}_{bi}^T\mathbf{Q}\mathbf{x}^*\Big)d^*. \tag{4.13}$$

Many control laws can be constructed to guarantee non-positivity of $\frac{d}{dt}V(\mathbf{x}^*)$. For simplicity, the feedback control law is assumed to be linear and given by

$$d^* = \mathbf{k}\mathbf{x}^*, \tag{4.14}$$

where $\mathbf{k}$ is the feedback vector gain and can be determined by substituting Eq. (4.14) into Eq. (4.13), and solving the inequality $\frac{d}{dt}V(\mathbf{x}^*) < 0$ for $\mathbf{k}$.

4.5 Small-signal model based approaches

Theoretically, linear control theory should be used for linear systems only. However, most practical systems are non-linear, and control approaches to handling non-linearity either have not been fully established in the literature or are too complicated to be used in practice. Therefore, linear control theory is still prevalent in many fields, including power converter applications. In order to synthesize controllers based on linear control theory, small signal models of DC-to-DC converters are required. Such models can be obtained by linearising large-signal models around nominal operating points. For example, linearisation of the averaged state space model in Eq. (4.5), at the operating point $\overline{\mathbf{x}(t)} = \mathbf{X}$, $\overline{\mathbf{y}(t)} = \mathbf{Y}$, $\overline{\mathbf{u}(t)} = \mathbf{U}$, and $d(t) = D$, yields

$$\begin{aligned} \frac{d}{dt}\tilde{\mathbf{x}}(t) &= \mathbf{A}_{ccm}\tilde{\mathbf{x}}(t) + \mathbf{B}_{ccm}\tilde{\mathbf{u}}(t) + \mathbf{F}_{ccm}\tilde{d}(t), \\ \tilde{\mathbf{y}}(t) &= \mathbf{C}_{ccm}\tilde{\mathbf{x}}(t) + \mathbf{E}_{ccm}\tilde{\mathbf{u}}(t) + \mathbf{K}_{ccm}\tilde{d}(t), \end{aligned} \tag{4.15}$$

where $\tilde{\mathbf{x}}(t)$, $\tilde{\mathbf{y}}(t)$, $\tilde{\mathbf{u}}(t)$ and $\tilde{d}(t)$ are the small-signal deviations of the state variable vector, output vector, input vector, and duty ratio from their nominal values, respectively. The expressions for $\mathbf{A}_{ccm}$, $\mathbf{B}_{ccm}$, $\mathbf{F}_{ccm}$, $\mathbf{C}_{ccm}$, $\mathbf{E}_{ccm}$ and $\mathbf{K}_{ccm}$ can be found in Eq. (2.18).

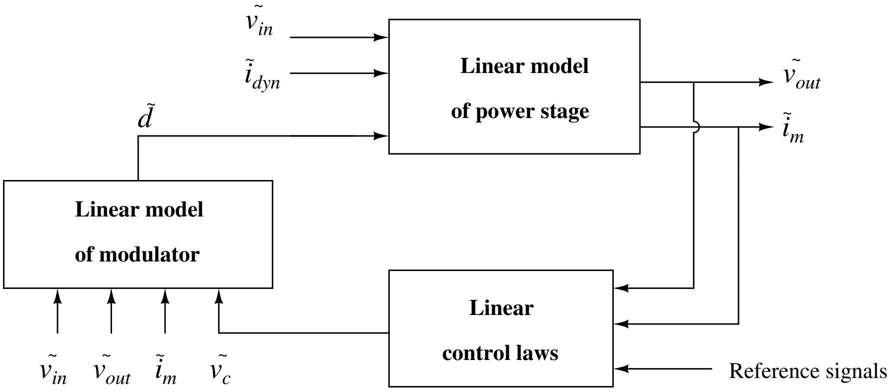

Figure 4.9: Typical structure of PWM/PFM linear feedback control for DC-to-DC converters.

In addition to the power stage of DC-to-DC converters, modulator circuits, whose main roles are to generate PWM/PFM signals from control variables, also need to be modelled. Modulator circuits are typically associated with particular control approaches. For example, voltage mode controllers make use of PWM modulators, while peak current programmed controllers use peak current modulators. Different modulator circuits and their mathematical models have been reported in [3,35,36,129,132].

Given the models of power stages and modulator circuits, the general architecture of linear feedback controllers for DC-to-DC converters can be established as in Fig. 4.9. The purpose of the control techniques is to synthesize linear control laws, such that the closed-loop system in Fig. 4.9 has a fast transient response and is stable, regardless of large disturbances in the input voltage and output load. Three main control schemes, consisting of PID control, robust control and adaptive control, have been widely employed to handle the wide operating range of power converters. The applications of PID control, robust control and adaptive control to power converters are, in turn, reviewed in Sections 4.5.1, 4.5.2 and 4.5.3.

4.5.1 Classical PID control

Classical PID compensators provide the simplest approach to the control of DC-to-DC converters [3,147,191]. Compensators are obtained by tuning proportional (P), integral (I), and derivative (D) terms, such that the closed-loop system satisfies both performance specifications and stability requirements. In addition to PID approaches, controllers can be also synthesized based on either lead-lag compensation techniques [3] or direct pole placement [192].

Recent advances in digital computing and processing speed have raised the feasibility of replacing conventional analogue controllers by their digital counterparts. The first study on digital control strategies for power converters was conducted by Bocchetti *et al.* [193]. The paper determines the linearised discrete model of a PWM buck converter, and works out the control law using digital pole placement techniques. Martin *et al* [129] used a small signal model of a boost converter to evaluate the accuracy of redesign approaches and direct digital designs, in term of output voltage transients.

Classical PID controllers suffer from the drawback of the small signal assumption, which limits the system operation on local stability, rather than global stability. For example, converters may experience unexpected performance or instability behaviour during a large transient event [185]. Moreover, linear control theory is currently unsuited to dealing with the non-minimum phase nature of boost converter families, such as boost, buck-boost and flyback converters. In order to handle plant uncertainty, classical control designs deliberately reduce the open-loop gain to preserve a necessary phase margin and gain margin, at a cost of a significant reduction in operating bandwidth.

4.5.2 Robust control

Designing a robust control that guarantees stable operation and good performance, regardless of the plant uncertainty, has drawn attention from researchers in both academia and industry [194–197]. In the field of power converters, such control strategies, e.g. H_∞ analysis, $\mu-$synthesis, etc., have been widely applied to various power electronic applications, ranging from buck converters to resonant converters.

The first H_∞ control for DC-to-DC converters can be traced back to the publication of Naim *et al.* in [198], where H_∞ theory is applied to stabilize the operation of a fixed switching frequency boost converter, and to simultaneously achieve good performance. Though the study in [198] showed interesting comparisons between robust control, current programmed control and feed-forward control, such results are only valid for small deviations of the input voltage and the output load from their nominal values. Such a limitation is due to the modelling approach used in [198], which simply considers the changes in the supply voltage and the load current as exogenous signal disturbances rather than model uncertainty. Encouraged by the work of Naim *et al.* [198], other authors have subsequently extended the work to different converter configurations [199, 200], and have improved many shortcomings in [198], such as the presence of non-zero steady state error and a lack of experimental verification. However, the studies in [199, 200] still suffer from the small signal assumption of the model used, and need to be applied with care for large signal scenarios.

In addition to H_∞ robust approaches, the applications of μ-analysis in the control design for power converters can be found in [201–205]. Particularly, Wang *et al.* [201] modelled parameter variations in a series resonant converter as input multiplicative perturbations, and employed a μ-synthesis procedure to obtain a robust controller. In a very similar manner, [202] presented a study for a parallel resonant converter while [203] demonstrated a robust design for a current-programmed controlled buck-boost converter. Since the effects of operating point movement were included in the modelling processes, the designs in [201–203] can satisfy both robust stability and performance over a wide range of operating conditions. The only concern is that the use of unstructured uncertainty, to describe the plant variations, can lead to a very conservative model and, thus, results in poor closed-loop performance. Addressing such a limitation, Tymerski [204, 205] suggested using structured uncertainty to evaluate component tolerances in DC-to-DC converters, and represented the system equations in an $\Delta - M$ form, which is most convenient for structured singular value (μ) analysis. The comparisons in [205] show that, for a given set of parameter variations, structured uncertainty modelling techniques yield controllers which outperform those returned by unstructured uncertainty representation. Although it is more advantageous, in terms of achievable performance, to use structured uncertainty and μ-analysis as control synthesis for DC-to-DC converters [204, 205], certain types of perturbations, such as variations in operating modes or in switching frequencies, cannot be rearranged in the $\Delta - M$ form proposed in [204,205].

Other robust control techniques are also considered and applied to the area of PWM converters in [206–210]. For example, [207] makes use of the loop transfer recovery (LTR) methodology to obtain a compensator for a series parallel resonant converter while, in [208], the combination of H_∞ and classical loop-shaping control is employed to enhance the transient response of a buck converter, as well as to ensure robustly stable operation. Realizing the practical limitations of H_∞ and μ-analysis strategies, Olalla *et al.* [206] proposed an alternative control approach, based on Quantitative Feedback Theory (QFT), to tackle a wide change in the parameters and operating mode of a buck converter. Experimental results of the QFT-based controller in [206] show good rejection to input voltage disturbances and output load variations, fast tracking of the reference signal, and stability under any excitation condition. The applications of QFT to other converter topologies have been carried out in [209, 210], though no experimental results are available.

In another series of studies [211,212], Olalla *et al.* sought a linear matrix inequality (LMI)-based framework to synthesize robust controllers for switched mode DC-to-DC converters. The main idea behind such an LMI-based method is to model power converters with a wide operating range as linear parameter varying (LPV) systems, rather than as nominal models with parametric/non-parametric uncertainty. As presented in [211–213], the synthesized controllers show good results in both simulation and experiments; however, the LMI-based framework relies on detailed mathematical derivation and, as a result, is not easy to use in practice.

4.5.3 Adaptive control

In contrast to PID control in Section 4.5.1 and robust control in Section 4.5.2, adaptive controllers vary their parameters in order to handle uncertainty in converter models and input disturbances. Three types of adaptive control schemes, including gain scheduling, model reference adaptive control (MRAC) and self-tuning regulators (STR), have been widely used in various applications of power electronics.

The basic idea of gain scheduling is to change the control parameters with the system operating point. Such a technique have been considered and applied to a boost converter [214], where the coefficients of a PI regulator depend on the output voltage and output current. Similarly, Su *et al.* [215] used an averaged inductor current to tune the parameters of a PID controller for a buck converter. Recent applications of gain scheduling can also be found in [60], where the parameters of a PI compensator depend on the switching frequency used in a flyback converter. Controllers designed based on gain scheduling typically provide very fast transient responses with minimum undershoot and overshoot. However, the stability of such controllers cannot be verified. Realizing such a limitation of classical gain scheduling approaches, Olalla *et al.* [213] proposed a framework, based on LMI formulation, to synthesize gain scheduling controllers which are robustly stable over the whole operating range.

MRAC has been successfully applied to tune digital PID controllers for CCM buck converters in [216] as well as for DCM buck converters in [217]. In these studies, small oscillations are injected to the duty ratio command with the converter operating in closed loop. The parameters of digital PID controllers are adjusted in an adaptive feedback loop to achieve crossover frequency and phase margin specifications. Adaptive control using the STR concept has also been used to tune predictive controllers for a CCM buck converter in [218] and a phase controlled rectifier in [219].

4.6 Discussion and perspective

This chapter has described the characteristics and applications of two switching formats, i.e. PFM and PWM, which are commonly deployed in the control of power converters. In addition to the study of modulation techniques, various control methods for DC-to-DC converters with a wide operating range are also reviewed.

Non-linear controllers, which are synthesized based on switched state-space models, are globally stable and robust to plant uncertainty and input disturbances. However, such controllers typically determine the switching function $q(t)$ by themselves, which introduces unpredictable switching waveforms, generally consisting of both high- and low-frequency harmonics. As a result, a high quality low-pass filter with a low cut-off frequency is usually required at the converter input port and output port to cancel unwanted sinusoidal components. Since the sizes of low-pass filters are proportional to the cut-off frequency, the utilization of such filters is typically limited to particular applications. To reduce the switching noise, some modifications have been introduced in [161, 220, 221] to shape the switching waveform using a PWM circuit. However, the downside of PWM is a considerable reduction in the dynamic characteristics of the feedback system in response to large input voltage and load variations.

Although some simplifications have been made during the derivation of the large-signal averaged models of DC-to-DC converters, non-linear controllers based on such models can be proven to be globally stable. In addition to the distinctive features of each large-signal modelling approach, all non-linear controllers generally call for high computation and complex processing steps which consequently slows the system dynamic response down, and precludes their implementation on analogue devices.

Modelling and design of a robust controller for fixed PWM frequency DC-to-DC power converters are well-known problems and have been intensively investigated in the literature. However, none of the existing studies considers the converter applications with a variable switching frequency.

Chapter 5

Non-linear dynamic transformer model identification

5.1 Introduction

Given the success of the magnetic-sensing (MS) regulation for flyback converters in discontinuous conduction mode (DCM), the extension to continuous conduction mode (CCM), with the aim of achieving a higher performance and a lower production cost, is of significant interest. However, the study of the MS regulation in CCM requires an accurate dynamic model of the flyback transformer at high frequencies. In addition to the MS applications, an accurate model of the flyback transformer is also necessary for the study of power converters, as well as for model-based controller design.

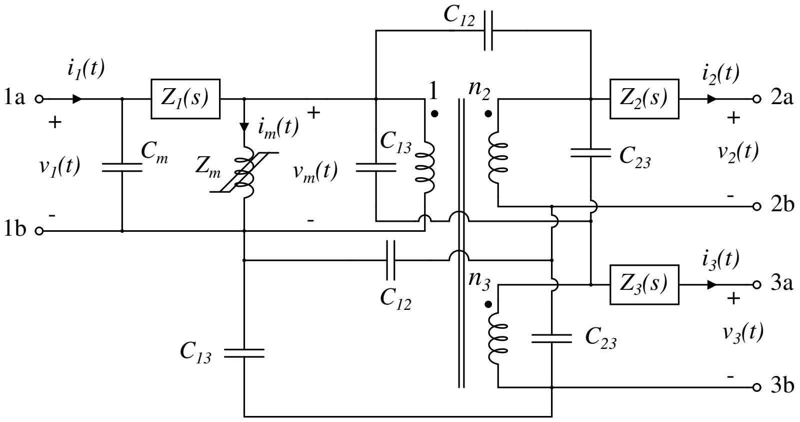

Figure 5.1: A nonlinear dynamic model of a 3-winding transformer.

As discussed in Chapter 3, previous studies on transformer modelling have either focussed on the winding model, using frequency-domain methods, or on the non-linear core model, using time domain methods. Non-linear modelling is confined to the time-domain while certain difficulties, as discussed in Section 5.3.2 of this chapter, have precluded the use of time-domain methods for winding model estimation. These challenges are the main reason resulting in the lack of integrated modelling approaches. Therefore, this chapter focuses on identifying a complete non-linear dynamic model of a 3-winding transformer using time-domain system identification approaches. The transformer under investigation is typically employed in a flyback converter. The equivalent model, as shown in Fig. 5.1, is generalized from the T-model for a 3-winding transformer, as illustrated in Fig. 3.4. The core behaviour, consisting of a hysteresis effect and a non-linear magnetic inductance, is characterized by Z_m. The impedance $\{Z_i(s)\}_{i=1}^3$, which represents the effect of the parasitic components in the i^{th} winding, is generally defined by,

$$Z_i(s) = R_i(s) + sL_i(s), \quad i = 1, 2, 3, \tag{5.1}$$

where $\{R_i(s)\}_{i=1}^3$ and $\{L_i(s)\}_{i=1}^3$ represent the power losses and the leakage inductance in the i^{th} winding, respectively. As both $\{R_i(s)\}_{i=1}^3$ and $\{L_i(s)\}_{i=1}^3$ are functions of frequency, the winding impedance $\{Z_i(s)\}_{i=1}^3$ does not have a fixed form and depends on the configuration of each transformer. The capacitor C_m describes the electric energy storage in all windings referred to the primary winding, while the electric energy storage between windings is symbolized by C_{12}, C_{13} and C_{23}. The transformer voltage gains n_2 and n_3 account for the coupling between transformer windings. The capacitances C_m, C_{12}, C_{13}, C_{23} and the voltage gains n_2, n_3 are presumed constant with respect to frequency, in this study. The model in Fig. 5.1 is identified using two steps. Firstly, the winding parameters are obtained using a small excitation signal, while the core model is estimated separately using a high voltage source.

For low frequency applications, transformer winding model estimation has been widely studied using both time and frequency domain data. However, the studies for high frequency transformers have been carried out in the frequency domain only. The reason behind this selection is due to the advantages of data collection in the frequency domain (by an impedance analyser) over the time domain (by an oscilloscope). In particular, for systems having wide variations in their frequency response, the collected time response data typically suffers from a round-off error due to finite bit resolution of the acquisition device. Despite these limitations, the time domain approach is still preferred, as it requires only a simple measurement facility and offers an easy way to deal with a complex transformer model. In Section 5.3.2, a methodology is suggested to handle the numerical difficulties occurring during the measurement, and to obtain a frequency-dependent winding model of a transformer using system identification techniques.

A variety of modelling techniques has been suggested to emulate the hysteresis properties in the magnetic material, see Chapter 3 and the references therein. Among them, the Jile-Atherton (J-A) model [18, 222], which offers the best trade-off between simplicity and accuracy, can be considered as the most suitable approach for our application. Due to the effect of the air-gap, the gap-length is also considered as a variable during estimation of the Jiles-Atherton model.

The remainder of this chapter is organized as follows; Section 5.2 introduces two nominal approaches to continuous-time system identification, while the data collection and application of these identification algorithms to the transformer winding model are examined in Section 5.3. The core model is described in Section 5.4. The flyback transformer is identified and verified in Section 5.5, while conclusions are drawn in Section 5.6

5.2 Time-domain identification of continuous-time LTI systems

System identification has been widely applied in many fields to seek mathematical models of actual systems from their input-output behaviour. A typical identification procedure, for a single input single output (SISO) system, as illustrated in Fig. 5.2, requires a set of N input-output data points $\{u(t_k), y(t_k)\}_{k=1}^{N}$, a model structure (i.e. black box, grey box, etc.) and an estimation technique (i.e. least squares, maximum likelihood, etc.). For a given model structure, model parameters are obtained by minimizing a chosen norm of the modelling error $\{\xi(t_k)\}_{k=1}^{N}$ between the model output $\{x(t_k)\}_{k=1}^{N}$ and the measured output signal $\{y(t_k)\}_{k=1}^{N}$. Dynamic system models can be linear or non-linear, and can be described by either discrete-time or continuous-time frameworks. A high-fidelity continuous-time linear time invariant (LTI) model is of primary interest in this section. Identification of non-linear continuous-time models is considered in Section 5.4.

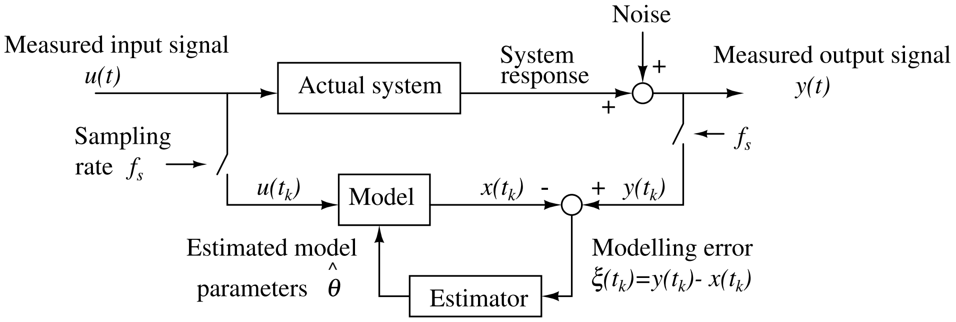

Figure 5.2: A generic procedure to estimate a model of an actual SISO system from sampled data.

Referring to the scheme of Fig. 5.2, the continuous-time relation between the measured input signal $u(t)$ and measured output signal $y(t)$ of an actual SISO system can be modelled [223] by

$$\begin{aligned} y(t) &= x(t) + \xi(t) \\ &= g(t) * u(t) + h(t) * e(t) \end{aligned} \tag{5.2}$$

where

$$g(t) = \mathcal{L}^{-1}\{G(s)\}, \quad h(t) = \mathcal{L}^{-1}\{H(s)\} \tag{5.3}$$

where $x(t)$ is the noise-free output of the model, $\xi(t)$ denotes the modelling error, and $e(t)$ is a zero mean, normally distributed, white noise process. The * symbol denotes the convolution operator while $\mathcal{L}^{-1}$ indicates the inverse Laplace transform. $g(t)$ and $h(t)$ are the impulse responses of the system model $G(s)$ and the noise model $H(s)$, respectively. The right hand side of Eq. (5.2) contains two terms, $g(t) * u(t)$ and $h(t) * e(t)$. The first term $g(t) * u(t)$ accounts for the response of the actual system when the stochastic disturbances are not present and the system is ideally modelled by the transfer function $G(s)$. The second term $h(t) * e(t)$ represents the combined effects of stochastic noise, unmodelled dynamics due to model simplification, and possibly of unknown initial conditions. The visual representation of Eq. (5.2) is shown in Fig. 5.3.

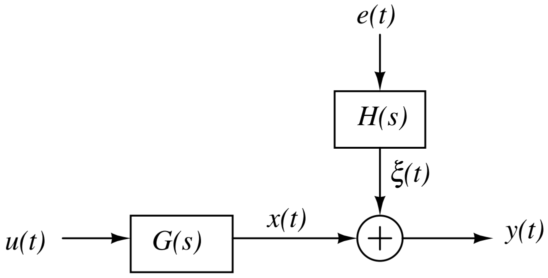

Figure 5.3: Model structure of a SISO system. $x(t)$ is the hypothetical noise-free deterministic output of the system while $\xi(t)$ is the additive stochastic disturbance.

The system model $G(s)$ and the noise model $H(s)$ can be parametrised in different ways. The most effective approach is to represent $G(s)$ and $H(s)$ as rational functions, whose denominator and numerator coefficients are parameters to be estimated [223]. Such a parametrisation approach is also known as back-box modelling. Depending on the choice of the denominators and numerators of $G(s)$ and $H(s)$, different model structures, as summarized in Table 5.1, can be obtained. The functions $A(s)$, $B(s)$, $C(s)$, $D(s)$, and $F(s)$, in Table 5.1 are polynomials in s while $A(s)$, $D(s)$, $F(s) \neq 0$. Notice that the model structure in Fig. 5.3 and the classification in Table 5.1 are valid for both continuous-time and discrete-time modelling frameworks.

Table 5.1: Family of commonly used model structures for system identification

SISO model structure	$G(s)$	$H(s)$
Autoregressive model with exogenous input (ARX)	$\frac{B(s)}{A(s)}$	$\frac{1}{A(s)}$
Autoregressive-moving-average model with exogenous input (ARMAX)	$\frac{B(s)}{A(s)}$	$\frac{C(s)}{A(s)}$
Output error (OE) model	$\frac{B(s)}{F(s)}$	1
Finite impulse response (FIR) model	$B(s)$	1
Box-Jenkins (BJ) model	$\frac{B(s)}{F(s)}$	$\frac{C(s)}{D(s)}$
General model	$\frac{B(s)}{A(s)F(s)}$	$\frac{C(s)}{A(s)D(s)}$

The procedure for determining the coefficients of $G(s)$ and $H(s)$ from time-domain data is not fixed, but rather depends on the model structure and the identification method chosen, e.g. the prediction error method (PEM), the maximum likelihood (ML) method, the instrumental variable (IV) method. Since output error (OE) models are often the most realistic model structure and generally outperform other structures in terms of modelling accuracy, they will be primarily considered in this study. Identification of OE models, based on prediction error minimization, is presented in Sections 5.2.1 and 5.2.2.

Identification methods for a continuous-time system are typically classified as: (i) direct approaches which handle a continuous-time model of the system directly, and (ii) indirect approaches, in which a discrete-time model of the system is firstly identified and is then transformed into continuous-time form [224]. The direct and indirect approaches are comprehensively discussed in Sections 5.2.1 and 5.2.2, respectively.

5.2.1 Direct continuous-time method

Due to the continuous-time nature of the transformer model in Fig. 5.1, a direct identification procedure is perfectly suited for the estimate of the transformer parameters. Various methods can be applied to the problem of transformer model estimation [224]. However, only the most reliable method, denoted the simplified refined instrumental variable method for continuous time system identification (SRIVC) [225], is chosen for our study. The actual process is assumed to be described by an OE model structure, whose $G(s)$ has the form

$$G(s) = \frac{B(s)}{F(s)} = \frac{b_{n_b}s^{n_b} + b_{n_b-1}s^{n_b-1} + \cdots + b_0}{s^{n_f} + f_{n_f-1}s^{n_f-1} + \cdots + f_0}. \tag{5.4}$$

Since only causal systems are considered, the transfer function $G(s)$ is assumed to be proper, i.e. $0 \leq n_b \leq n_f$. The optimal OE predictor is defined in [225] as

$$\hat{y}(t) = \mathcal{L}^{-1}\left\{\frac{B(s)}{F(s)}\right\} * u(t). \tag{5.5}$$

The prediction error of an OE model is

$$\varepsilon(t) = y(t) - \hat{y}(t) = y(t) - \mathcal{L}^{-1}\left\{\frac{B(s)}{F(s)}\right\} * u(t), \tag{5.6}$$

which can be rearranged to

$$\varepsilon(t) = \mathcal{L}^{-1}\big\{F(s)\big\} * \mathcal{L}^{-1}\left\{\frac{1}{F(s)}\right\} * y(t) - \mathcal{L}^{-1}\big\{B(s)\big\} * \mathcal{L}^{-1}\left\{\frac{1}{F(s)}\right\} * u(t). \tag{5.7}$$

Let's assume that $F(s)$ in Eq. (5.7) can be estimated by some means and is known, hence $L(s) = \frac{1}{F(s)}$ can be considered as a continuous-time filter. Using $L(s)$ to filter the input signal $u(t)$ and output signal $y(t)$, the new stable variables $y_l(t)$ and $u_l(t)$ can be obtained as

$$\begin{aligned} y_l(t) &= \mathcal{L}^{-1}\left\{L(s)\right\} * y(t) = l(t) * y(t), \\ u_l(t) &= \mathcal{L}^{-1}\left\{L(s)\right\} * u(t) = l(t) * u(t), \end{aligned} \tag{5.8}$$

where $l(t)$ is the impulse response of the filter $L(s)$ and can be derived via

$$l(t) = \mathcal{L}^{-1}\left\{\frac{1}{F(s)}\right\}. \tag{5.9}$$

Substituting Eq. (5.8) into Eq. (5.7) yields

$$\varepsilon(t) = \mathcal{L}^{-1}\big\{F(s)\big\} * y_l(t) - \mathcal{L}^{-1}\big\{B(s)\big\} * u_l(t), \tag{5.10}$$

or

$$\varepsilon(t) = y_l^{(n_f)}(t)+f_{n_f-1}y_l^{(n_f-1)}(t)+\cdots+f_0y_l^{(0)}(t)-b_{n_b}u_l^{(n_b)}(t)-b_{n_b-1}u_l^{(n_b-1)}\cdots-b_0u_l^{(0)}(t), \quad (5.11)$$

where $y_l^{(n)}(t)$ is the n^{th} time-derivative of the continuous-time signal $y_l(t)$. Evaluating Eq. (5.11) at the sampling instants $t = \{t_k\}_{k=1}^{N}$, yields

$$\begin{aligned}\varepsilon(t_k) = y_l^{(n_f)}(t_k) - \big[- f_{n_f-1}y_l^{(n_f-1)}(t_k) - \cdots - f_0y_l^{(0)}(t_k) \\ + b_{n_b}u_l^{(n_b)}(t_k) + b_{n_b-1}u_l^{(n_b-1)}\cdots + b_0u_l^{(0)}(t_k)\big], \text{ for } k = 1, 2, \ldots, N.\end{aligned} \quad (5.12)$$

By introducing the state variable vector

$$\varphi_l(t_k) = [-y_l^{(n_f-1)}(t_k) \ -y_l^{(n_f-2)}(t_k) \ \ldots \ -y_l^{(0)}(t_k) \ u_l^{(n_b)}(t_k) \ u_l^{(n_b-1)}(t_k) \ \ldots \ u_l^{(0)}(t_k)]^T \quad (5.13)$$

and the parameter vector

$$\theta = [f_{n_f-1} \ f_{n_f-2} \ \ldots \ f_0 \ b_{n_b} \ b_{n_b-1} \ \ldots \ b_0]^T, \quad (5.14)$$

Eq. (5.12) can be written in matrix form as

$$\varepsilon(t_k) = y_l^{(n_f)}(t_k) - \varphi_l^T(t_k)\theta, \text{ for } k = 1, 2, \ldots, N. \quad (5.15)$$

For determination of the model parameter vector θ, the least-squares criterion for the prediction error $\varepsilon(t_k)$, whose cost function is defined as

$$J(\theta) = \frac{1}{N}\sum_{k=1}^{N}\frac{1}{2}\varepsilon^2(t_k) = \frac{1}{N}\sum_{k=1}^{N}\frac{1}{2}\big[y_l^{(n_f)}(t_k) - \varphi_l^T(t_k)\theta\big]^2, \quad (5.16)$$

is chosen [223]. Since the criterion function $J(\theta)$ in Eq. (5.16) is a quadratic function in θ, $J(\theta)$ can be minimized analytically, which gives

$$\hat{\theta}_N^{LS} = \left[\sum_{k=1}^{N}\varphi_l(t_k)\varphi_l^T(t_k)\right]^{-1}\sum_{k=1}^{N}\varphi_l(t_k)y_l^{(n_f)}(t_k), \quad (5.17)$$

provided that the matrix inverse in Eq. (5.17) exists. The solution given by Eq. (5.17) is typically referred to as the least-squares (LS) estimate [223]. Although the LS method is simple and computationally efficient, it generally yields asymptotically biased and inconsistent results if the disturbance, presented in Eq. (5.2), is not a white noise process. A solution to such an asymptotically biased problem is to use either a different noise model or an alternative estimation method, which should not require a priori knowledge of the noise statistics. The later solution is commonly used in practice due to its robustness and flexibility.

Among bias-free estimators, the instrumental variable (IV) method is the most popular and robust method to handle both white noise and coloured noise [223]. Unlike the LS method, the instrumental variable (IV) algorithm operates in an iterative manner. In particular, at each iteration of the algorithm, the IV vector, which is given by

$$\hat{\varphi}_l(t_k) = [-\hat{x}_l^{(n_f-1)}(t_k)\ -\hat{x}_l^{(n_f-2)}(t_k)\ \ldots\ -\hat{x}_l^{(0)}(t_k)\ u_l^{(n_b)}(t_k)\ u_l^{(n_b-1)}(t_k)\ \ldots\ u_l^{(0)}(t_k)]^T, \tag{5.18}$$

is formed to support the determination of the model parameters. The signal $\hat{x}_l(t)$ in Eq. (5.18) is calculated via

$$\hat{x}_l(t) = \frac{\hat{x}(t)}{F\left(s, \hat{\theta}_N^{IV}\right)}, \tag{5.19}$$

where $\hat{x}(t)$ is the estimated noise-free output calculated from

$$\hat{x}(t) = \frac{B\left(s, \hat{\theta}_N^{IV}\right)}{F\left(s, \hat{\theta}_N^{IV}\right)} u(t). \tag{5.20}$$

The variable $\hat{\theta}_N^{IV}$ in Eqs. (5.19) and (5.20) is the estimated parameter vector obtained at the previous iteration of the algorithm. The IV estimate of the model parameter vector θ, for each iteration, is given by

$$\hat{\theta}_N^{IV} = \left[\sum_{k=1}^{N} \hat{\varphi}_l(t_k)\varphi_l^T(t_k)\right]^{-1} \sum_{k=1}^{N} \hat{\varphi}_l(t_k) y_l^{(n_f)}(t_k), \tag{5.21}$$

provided that the matrix inverse in Eq. (5.21) exists.

Notice that the derivation of the formulae in Eqs. (5.17) and (5.21) requires that the $F(s)$ polynomial is known a priori. Such a requirement can be not be fulfilled directly because $F(s)$ is a part of the model structure and needs to be determined, and is obviously unknown at the start of the identification process. However, such a problem can be solved through an iterative procedure, which starts with an initial estimate of $F(s)$ and then iteratively adjusts the coefficients of the $F(s)$ polynomial until they converge.

The SRIVC algorithm generally consists of two stages [226], which are summarized as follows:

Stage 1 - Initialisation:

1. Estimate the model of the actual system in discrete-time using any identification method, e.g. the LS method presented in Section 5.2.2.
2. Transform the obtained discrete-time model to an equivalent continuous-time model, called $G_0(s)$, using the Tustin's transformation. The parameters of $G_0(s)$ is named θ_0.
3. Use $G_0(s)$ to initialize the $B(s)$ and $F(s)$ polynomials for the stage 2, i.e. $\hat{\theta}_N^{IV} = \theta_0$.

Stage 2 - Iterative IV estimation:

For j = 1 : maximum iteration

1. Compute the estimate $\hat{x}(t)$ of the noise-free output $x(t)$, based on Eq. (5.20).
2. Filter $y(t)$, $u(t)$ and $\hat{x}(t)$ with the continuous time filter $L(s) = \frac{1}{F\left(s, \hat{\theta}_N^{IV}\right)}$ producing $y_l(t)$, $u_l(t)$ and $\hat{x}_l(t)$, respectively.

3. Update the estimate $\hat{\theta}_N^{IV}$ of the model parameter vector θ using Eq. (5.21).

End for

A detailed investigation of the SRIVC and a generalized version of the SRIVC for other model structures are documented in [225]. The implementation of the SRIVC method can also be found in the CONTSID toolbox for Matlab [227].

5.2.2 Indirect continuous-time method

Though the indirect identification of a continuous-time model contains some potential issues induced by the discretisation of a continuous-time system [224], this approach has been successfully applied in various applications, including the transformer model determination [106, 228]. For comparison purposes, an indirect continuous-time approach based on the IV estimation method is presented in this section. The actual system is assumed to be described by an OE model structure, however, the system model, in contrast to the model in Section 5.2.1, is formulated in the discrete-time framework, which gives

$$G_d(z) = \frac{B_d(z)}{F_d(z)} = \frac{b_0^d + b_1^d z^{-1} + \cdots + b_{n_{bd}}^d z^{-n_{bd}}}{1 + f_1^d z^{-1} + \cdots + f_{n_{fd}}^d z^{-n_{fd}}}. \tag{5.22}$$

Due to the negative power representation of the variable z in Eq. (5.22), the system $G_d(z)$ is causal if n_{bd} and n_{fd} are chosen to be non-negative. The prediction $\hat{y}(t_k)$ of the output signal $y(t_k)$ at the sampling time t_k can be computed from past observation of the input signal $\{u(t_h)\}_{t_h \leq t_k}$ and output signal $\{y(t_l)\}_{t_l \leq t_k - 1}$ via

$$\hat{y}(t_k) = \frac{B_d(z)}{F_d(z)} u(t_k). \tag{5.23}$$

The prediction error, at the sampling time $t = t_k$, is

$$\varepsilon(t_k) = y(t_k) - \hat{y}(t_k) = y(t_k) - \frac{B_d(z)}{F_d(z)} u(t_k), \tag{5.24}$$

which can be rearranged to

$$\varepsilon(t_k) = F_d(z) \frac{y(t_k)}{F_d(z)} - B_d(z) \frac{u(t_k)}{F_d(z)}. \tag{5.25}$$

Following the principle discussed in Section 5.2.1, which considers the transfer function $L_d(z) = \frac{1}{F_d(z)}$ in Eq. (5.25) as a state variable filter, and rewriting Eq. (5.25) as

$$\varepsilon(t_k) = F_d(z) y_{ld}(t_k) - B_d(z) u_{ld}(t_k), \tag{5.26}$$

where

$$\begin{aligned} y_{ld}(t_k) &= L_d(z)y(t_k) = \frac{1}{F_d(z)}y(t_k), \\ u_{ld}(t_k) &= L_d(z)u(t_k) = \frac{1}{F_d(z)}u(t_k), \end{aligned} \tag{5.27}$$

equation (5.26) can be written, in terms of time-domain variables, as

$$\varepsilon(t_k) = y_{ld}(t_k) - \varphi_{ld}^T(t_k)\theta_d, \tag{5.28}$$

where

$$\theta_d = [b_1^d \; b_2^d \; \dots \; b_{n_{bd}}^d \; f_1^d \; f_2^d \; \dots \; f_{n_{fd}}^d]^T \tag{5.29}$$

is the vector containing the model parameters and

$$\begin{aligned} \varphi_{ld}(t_k) = [&-y_{ld}(t_k - 1) \; - y_{ld}(t_k - 2) \; \dots \; - y_{ld}(t_k - n_{bd}) \\ &u_{ld}(t_k) \; u_{ld}(t_k - 1) \; \dots \; u_{ld}(t_k - n_{fd})]^T, \end{aligned} \tag{5.30}$$

denotes the state variable vector, also called the regression vector in [223]. If the criterion function for the prediction error is chosen to be similar to Eq. (5.16), i.e. LS criterion, the model parameter vector θ_d can be easily estimated by the IV method, which gives

$$\hat{\theta}_{dN}^{IV} = \left[\sum_{k=1}^{N} \hat{\varphi}_{ld}(t_k)\varphi_{ld}^T(t_k)\right]^{-1} \sum_{k=1}^{N} \hat{\varphi}_{ld}(t_k)y_{ld}(t_k), \tag{5.31}$$

provided that the matrix inverse in Eq. (5.31) exists. The IV vector $\hat{\varphi}_{ld}(t_k)$ in Eq. (5.31) is given by

$$\begin{aligned} \hat{\varphi}_{ld}(t_k) = [&-\hat{x}_{ld}(t_k - 1) \; - \hat{x}_{ld}(t_k - 2) \; \dots \; - \hat{x}_{ld}(t_k - n_{bd}) \\ &u_{ld}(t_k) \; u_{ld}(t_k - 1) \; \dots \; u_{ld}(t_k - n_{fd})]^T, \end{aligned} \tag{5.32}$$

where

$$\hat{x}_{ld}(t_k) = \frac{1}{F_d\left(z, \hat{\theta}_{dN}^{IV}\right)}\hat{x}_d(t_k), \tag{5.33}$$

and $\hat{x}_d(t_k)$ denotes the estimate of the noise-free output signal, and can be generated via

$$\hat{x}_d(t_k) = \frac{B_d\left(z, \hat{\theta}_{dN}^{IV}\right)}{F_d\left(z, \hat{\theta}_{dN}^{IV}\right)}u(t_k). \tag{5.34}$$

A detailed examination of Eqs. (5.31), (5.32), (5.33), and (5.34) reveals that the estimated parameter vector $\hat{\theta}_{dN}^{IV}$ has an implicit relation with the measured input and output data. In order to solve such an implicit equation, the formula in Eq. (5.31) is applied iteratively until convergence is reached.

The IV algorithm for OE model estimation can be summarized as follows:

Stage 1 - Initialisation:

1. Estimate an ARX model $y(t_k) = \frac{B(z)}{A(z)}u(t_k) + \frac{1}{A(z)}e(t_k)$ from the measured input-output data set $\{u(t_k), y(t_k)\}_{k=1}^{N}$ using the LS method, as developed in [223].
2. Use the obtained parameters of the ARX model to initialize the estimated parameter vector $\hat{\theta}_{dN}^{IV}$ in Stage 2.

Stage 2 - Iterative IV estimation:

For j = 1 : maximum iteration

1. Compute the estimate $\hat{x}_d(t_k)$ of the noise-free output $x(t_k)$, based on Eq. (5.34).
2. Filter $y(t_k)$, $u(t_k)$ and $\hat{x}_d(t_k)$ with the discrete-time filter $L_d(z) = \frac{1}{F_d\left(z, \hat{\theta}_N^{IV}\right)}$ producing $y_{ld}(t_k)$, $u_{ld}(t_k)$ and $\hat{x}_{ld}(t_k)$.
3. Update the estimate $\hat{\theta}_{dN}^{IV}$ of the model parameter vector θ_d using Eq. (5.31).

End for

Notice that the IV algorithm presented above and the SRIVC algorithm in Section 5.2.1 exploits the same technique to estimate the parameters of OE models, which uses the denominator of the system model as a state filter and relies on the IV estimator to avoid an bias estimation.

Given the parameters of the discrete-time system model $G_d(z)$, a continuous-time model $G(s)$ of the actual system can be determined through a discrete-to-continuous (D2C) time transformation. Though various mappings between the discrete- and continuous-time domain are available, only the Tustin's transformation with pre-warping is considered to preserve the frequency response of the system with similar fidelity.

One limitation of indirect system identification is the non-preservation of model order information during a D2C transformation. This is partly due to the fact that n_b, n_f in Eq. (5.4) and n_{bd}, n_{fd} in Eq. (5.22) have different roles in the representation of system properties. The non-preserved model order implies that the orders of the numerator and denominator of $G(s)$ cannot be controlled by specification of the orders of their discrete-time counterparts. Fortunately, by imposing a constraint on the model parameters of $G_d(z)$, the orders of the numerator and denominator of $G(s)$ can be fully preserved under the $G(s) \to G_d(z)$ warping. Starting with $G(s)$ described by Eq. (5.4), discretizing $G(s)$ using the Tustin's transformation with pre-warping $s = \frac{\omega_0}{\tan\left(\frac{\omega_0 T}{2}\right)} \frac{1-z^{-1}}{1+z^{-1}}$ yields

$$G_d(z) = \frac{b_{n_b}\left(\frac{\omega_0}{\tan\left(\frac{\omega_0 T}{2}\right)}\frac{1-z^{-1}}{1+z^{-1}}\right)^{n_b} + b_{n_b-1}\left(\frac{\omega_0}{\tan\left(\frac{\omega_0 T}{2}\right)}\frac{1-z^{-1}}{1+z^{-1}}\right)^{n_b-1} + \cdots + b_0}{\left(\frac{\omega_0}{\tan\left(\frac{\omega_0 T}{2}\right)}\frac{1-z^{-1}}{1+z^{-1}}\right)^{n_f} + f_{n_f-1}\left(\frac{\omega_0}{\tan\left(\frac{\omega_0 T}{2}\right)}\frac{1-z^{-1}}{1+z^{-1}}\right)^{n_f-1} + \cdots + f_0}.$$

where w_0 is the frequency at which the frequency response of $G(s)$ and $G_d(z)$ are matched.

Multiply both the numerator and denominator of $G_d(z)$ by $\left(1+z^{-1}\right)^{n_f}$ and rearrange the result to the form

$$\begin{aligned} G_d(z) &= \left(1+z^{-1}\right)^{n_f-n_b}\left[\frac{a_0+a_1z^{-1}+\cdots+a_{n_b}z^{-n_b}}{c_0+c_1z^{-1}+\cdots+c_{n_f}z^{-n_f}}\right] \\ &= \left(1+z^{-1}\right)^{n_f-n_b} G_i(z), \end{aligned} \tag{5.35}$$

where

$$G_i(z) = \frac{a_0+a_1z^{-1}+\cdots+a_{n_b}z^{-n_b}}{1+c_1z^{-1}+\cdots+c_{n_f}z^{-n_f}}.$$

The numerator coefficients $a_0,\ a_1,\ \ldots,\ a_{n_b}$ are linear functions of $b_0,\ b_1,\ \ldots,\ b_{n_b}$ while the denominator coefficients $c_0,\ c_1,\ \ldots,\ c_{n_f}$ are linear functions of $f_0,\ f_1,\ \ldots,\ f_{n_f-1}$. It can be demonstrated that there exist one-to-one mappings between $a_0,\ a_1,\ \ldots,\ a_{n_b}$ and $b_0,\ b_1,\ \ldots,\ b_{n_b}$, and also between $c_1,\ \ldots,\ c_{n_f}$ and $f_0,\ f_1,\ \ldots,\ f_{n_f-1}$. Such one-to-one mappings mean that the numerator order n_b and denominator order n_a of $G(s)$ can always be preserved if $G_d(z)$ satisfies Eq. (5.35) and Tustin's transformation with pre-warping is used. Identifying $G_d(z)$ from the input-output data $\{u(t_k), y(t_k)\}_{k=1}^{N}$ now reduces to the estimation $G_i(z)$ from the filtered data $\{u(t_k)\left(1+z^{-1}\right)^{n_f-n_b}, y(t_k)\}_{k=1}^{N}$ and then applying Eq. (5.35). It should be noted that the idea, which uses a pre-filter to establish a unique mapping between the parameters of a continuous-time model and of its equivalent discrete-time counterpart, has been exploited elsewhere in [229]. However, the study in [229] is not general and can only be applied when the model structure is known and simple.

5.3 Identification of dynamic transformer windings

This section presents a step-by-step procedure for the selection of a stimulus input signal having the necessary properties for system identification, how to produce the chosen stimulus waveform from an electric circuit, and how to collect time-domain data and estimate the parameters of the dynamic winding model from experimental data. In particular, the design and generation of the stimulus input is discussed in Section 5.3.1, while a generic procedure for collecting time-domain data is presented in Section 5.3.2. Given the designed input stimulated signal and the data collection procedure, Section 5.3.3 proposes a set of experiments and a systematic framework for determination of all the parameters of the winding model based on collected experimental data.

5.3.1 Input signal design

The accuracy of the identification result depends significantly on the input signal $u(t)$, which is used to stimulate the actual process during the data collection step. The choice of $u(t)$ should take into account the following requirements:

1. The stimulus signal should contain as many unique frequencies, within the frequency band of interest, as possible. The requirement on the input spectrum is to ensure that the matrix $\left[\sum_{k=1}^{N} \hat{\varphi}_l(t_k)\varphi_l^T(t_k)\right]$ in Eq. (5.21) and $\left[\sum_{k=1}^{N} \hat{\varphi}_{ld}(t_k)\varphi_{ld}^T(t_k)\right]$ in Eq. (5.31) are non-singular and well conditioned, i.e. invertible. As a rule of thumb, the number of frequencies in the input spectrum should be larger or, at least, equal to the order of the system model to be built [223]. In addition to the existence of the matrix inverse, the input spectrum also affects the asymptotic properties of the estimated model parameters, see [223] for a mathematical treatment.

2. The stimulus signal $u(t)$ should have a small Crest factor, generally defined by

   $$C_r = \frac{max|u(t)|}{\lim_{T\to\infty}\sqrt{\frac{1}{T}\int_0^T u^2(t)dt}}, \tag{5.36}$$

   i.e. the ratio of the peak value of the input signal to its average power. Input signals with a small Crest factor tend to deliver more power to the system and provide a higher signal-to-noise ratio (SNR) than signals having the same peak value and a large Crest factor.

3. In theory, the input level should be chosen as large as possible. Larger input signals will result in larger output responses which obviously give a better SNR and a significant benefit to estimation algorithms. However, when the actual process is non-linear and is approximated by a linear model, a large input may be problematic because the linearisation may be invalid. Therefore, the amplitude of the excitation input should be determined such that both requirements on the SNR and the linearity can be simultaneously satisfied.

Since the variance of the estimate of the model parameters depends on the input spectrum [223], an optimal design of the input resulting in a minimum variance of the estimated parameters is feasible. However, such an input design requires certain prior knowledge about the frequency response of the actual system, which is not available, in most cases. Therefore, for general scenarios, it is advisable to firstly decide the frequency band on which the system model is of interest and then select an input signal having a relatively flat spectrum over the chosen band [223].

Many common waveforms with a more or less flat spectrum have been successfully used as excitation inputs for system identification. Some of them can be listed as filtered Gaussian white noises, random binary signals (RBS), pseudo-random binary signals (PRBSs), multi-sine signals, and chirp signals. Each signal type has its own advantages and disadvantages and is suitable for certain applications only. For transformer identification problems, two waveforms, including a PRBS and an RBS, can be considered as the best input candidates because they have the smallest Crest factor, i.e. $C_r = 1$, and can be easily generated by simple circuits in practice. Apart from the finite period and deterministic nature of PRBSs, both RBSs and PRBSs have quite similar

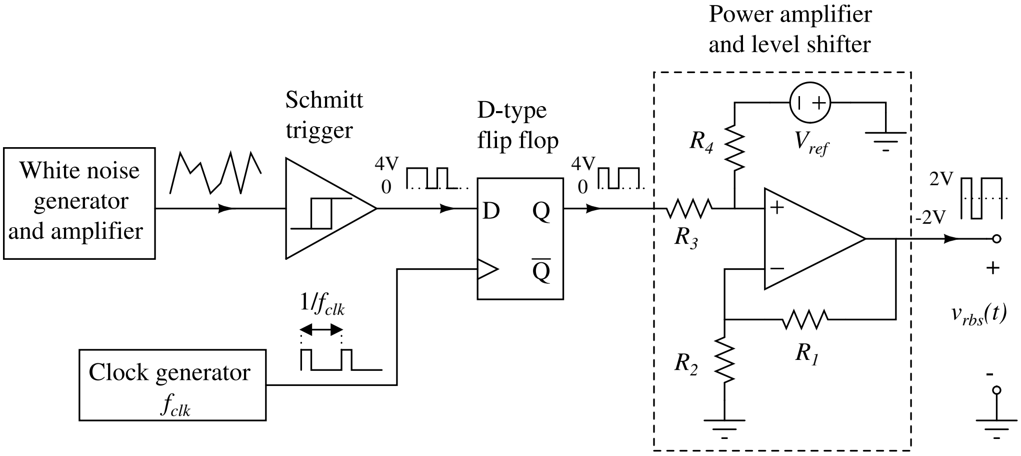

Figure 5.4: Block diagram of the random binary signal generator

properties and as a result can be equally used as stimulus inputs. For simplicity, only an RBS is considered in the identification of the transformer winding model in Sections 5.3.2 and 5.3.3.

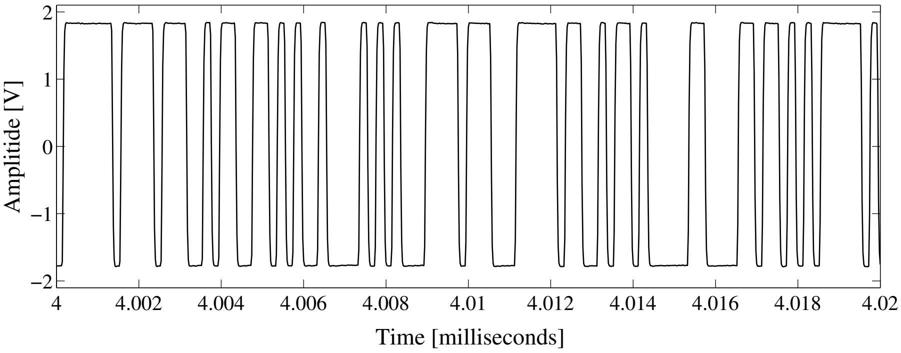

Figure 5.5: Random binary voltage $v_{rbs}(t)$ measured at the output of the RBS generator. The frequency of the clock generator is $f_{clk} = 5MHz$.

Since both fast and slow dynamics of the transformer need to be considered in the modelling process, the spectrum of the RBS input is expected to cover the range from 0Hz up to 10MHz. To provide extra flexibility for identification procedures, the upper bound of the input spectrum should not be fixed but should be adjustable through a simple mechanism. Based on these frequency band specifications, the RBS generator with an adjustable bandwidth is proposed. The general structure of the RBS generator is shown in Fig. 5.4, where the white noise generator outputs zero mean, white Gaussian, electrical noise with a uniform spectrum to 100MHz, or higher. Such electrical noise is obtained by amplifying shot noise in the emitter junction of an bipolar transistor [230]. The Schmitt trigger in Fig. 5.4 is employed to convert Gaussian noise to a binary signal, while the combination of the D flip-flop and the clock generator has the same role as a low-pass filter whose cut-off frequency can be varied through the clock frequency f_{clk}. Although the output of the D flip-flop is a random binary signal, such a signal cannot be used directly for experiments because it contains a non-zero DC component and the D flip-flop does not have enough power to drive the transformer circuit. Hence, a level shifter and power amplifier stage is required at the output of the RBS generator.

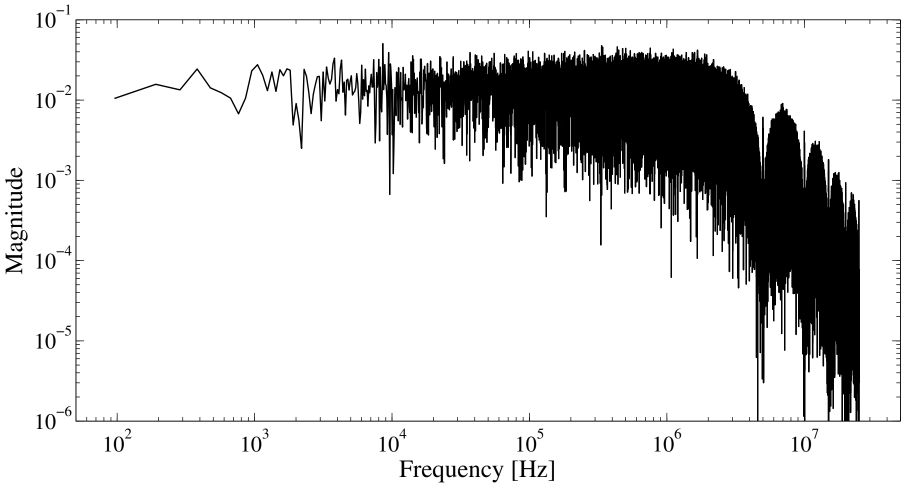

Figure 5.6: Magnitude spectrum of the random binary voltage $v_{rbs}(t)$ in Fig. 5.5. The spectrum is computed by FFT with a sampling frequency of $50MHz$.

Figure 5.5 plots a part of the output $v_{rbs}(t)$ of the RBS generator obtained by setting the frequency of the clock generator to $f_{clk} = 5MHz$. Performing a FFT of the RBS $v_{rbs}(t)$ gives the magnitude spectrum of Fig. 5.6. The highest frequency content of this spectrum is limited by the sampling frequency f_s, while the lowest frequency content is decided by the length of $v_{rbs}(t)$. The width of the spectrum can be customized by varying the sampling frequency and the length the data record. As can be seen in Fig. 5.6, the spectrum is not flat but varies from one frequency to another even within the frequency band of interest, say from 100Hz to around 2.5MHz $(= 0.5f_{clk})$. Such variations are due to the non-ideal waveform in Fig. (5.5), the distortion of the signal spectrum after the Schmitt trigger in Fig. 5.4, and possibly the imperfect spectrum of the generated white noise in Fig. 5.4. Although the random binary voltage $v_{rbs}(t)$ does not have a perfectly flat spectrum as in the case of ideal RBSs, it is very rich in frequencies and is entirely sufficient for most identification tasks.

5.3.2 Experiment configuration and data collection

Time-domain data can be collected in many ways, depending on the algorithm used to estimate the transformer model and the specifications of the measurement equipment [106, 228]. Since the transformer parameters in Fig. 5.1 generally exhibit different orders of magnitude, it is advisable to determine them separately using different sets of input/output data [106, 223]. Such an approach can be achieved by running different experiments, each of which is configured such that the response of some model parameters is dominant in the collected data while the effect of other parameters can be neglected. Though various experimental configurations, for example short-circuiting the transformer winding, removing the ferrite core, using different band-limited excitation signals, etc., have been proposed in [14, 104, 106], most of them either are too complicated to perform or only work well with certain transformer topologies. For simplicity, each experiment, designed for the study of the flyback transformer in this chapter, is carried out by the RBS signal, proposed in Section 5.3.1, in combination with a particular circuit configuration.

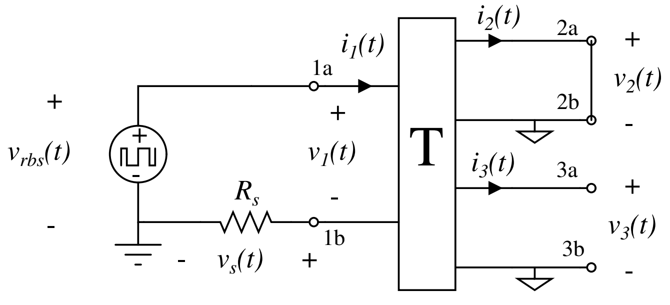

Figure 5.7: An experimental configuration to collect input-output data for identification of a 3-winding transformer model.

A circuit arrangement used to obtain time-series data for an experiment is exemplified in Fig. 5.7. The transformer is simply depicted by the 3-port network **T**. The random binary voltage $v_{rbs}(t)$, taken from the RBS generator in Fig. 5.4, is injected into the primary winding. The sensing resistor R_s is deliberately inserted to provide a current measurement. The resistor R_s is chosen such that its value is constant over the frequency range used in the experiment and can be precisely measured within a 0.5% error. Only a short-circuited connection of the secondary winding is involved in this experiment. The data for system identification (e.g. $v_{rbs}(t)$, $v_s(t)$ and $v_3(t)$) are collected by a digital oscilloscope. These measured voltages can serve as either input or output data for system identification depending on the objective of a particular test. For other experiments, the stimulus signal $v_{rbs}(t)$ might be applied to other transformer terminals with different short-circuiting configurations of the transformer windings; however, the resistor R_s is always kept in series with $v_{rbs}(t)$.

The difficulties of time domain identification methods arise when the responses of the system, e.g. $v_s(t)$ and $v_3(t)$ in Fig. 5.7, vary significantly over a wide frequency range and can not be sufficiently resolved by the digital oscilloscope. The round-off error occurring will distort the estimated result regardless of the identification techniques used. Two options can be used to reduce the round-off error. The first option is to increase the resolution of each sample, which obviously requires more expensive measurement equipment. The second option is to focus on the dominant dynamic response of the system only. The latter approach is exploited in Section 5.3.3 to enrich the dynamic content in $v_s(t)$ by adjusting R_s, which plays the same role as a ranging resistor in impedance measurement circuits [231].

5.3.3 Procedure for determination of model parameters

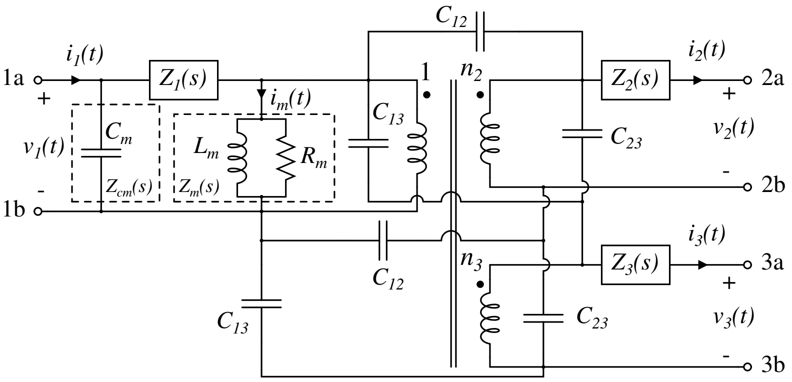

Figure 5.8: Transformer winding model with a linear core.

Under small signal excitation, the nonlinear core model in Fig. 5.1 is assumed to be linear and can be modelled by a parallel R_mL_m circuit, as shown in Fig. 5.8. A set of 6 different experiments is performed to derive all the parameters for the winding model in Fig. 5.8. The number of the experiments is decided based on the fact that 6 experiments provides adequate data for identification purposes. A more or less number of experiments can lead to either higher modelling errors or data redundancy. To clarify the measurement and identification procedure, a fixed template for each experiment, as described below, is introduced.

1. **Experimental configuration specification:** Describe how to set up the measurement circuit for each experiment. The information in this item includes: (i) the transformer terminals to which the voltage $v_{rbs}(t)$ is applied, (ii) the value of the sensing resistor R_s and (iii) the short circuit connection between transformer terminals. For example, AT_{1a1b}, $R_s = 2\Omega$, S_{2a2b} means that $v_{rbs}(t)$ is injected to the terminals $1a$ and $1b$ of the transformer, the value of the sensing resistor is 2Ω and a short circuit is made between terminals $2a$ and $2b$.
2. **Data collection:** Specifies which signal in the experimental circuit will be captured by the oscilloscope.
3. **Identification objective:** Denotes the transfer function and model parameters obtained from measured data in each experiment.

Experiment 1:

1. AT_{1a1b}, $R_s = 465.5\Omega$, no short connection
2. $v_{rbs}(t)$, $v_s(t)$
3. $\frac{Z_{cm}(s)Z_m(s)}{Z_{cm}(s)+Z_m(s)}$, R_m, L_m, C_m

Experiment 2:

1. AT_{1a1b}, $R_s = 6.84\Omega$, S_{2a2b}
2. $v_{rbs}(t)$, $v_s(t)$, $v_3(t)$

3. $Z_1(s)$, $Z_2(s)$

Experiment 3:

1. AT_{1a1b}, $R_s = 6.84\Omega$, S_{3a3b}
2. $v_{rbs}(t)$, v_s, $v_2(t)$
3. $Z_1(s)$, $Z_3(s)$

Experiment 4:

1. AT_{1a2a}, $R_s = 465.5\Omega$, S_{1a1b}, $S_{2a2b3a3b}$
2. $v_{rbs}(t)$, $v_s(t)$
3. $\frac{2R_s(C_{12}+C_{13})s}{2R_s(C_{12}+C_{13})s+1}$, $C_{12}+C_{13}$

Experiment 5:

1. AT_{1a2a}, $R_s = 465.5\Omega$, $S_{1a1b3a3b}$, S_{2a2b}
2. $v_{rbs}(t)$, $v_s(t)$
3. $\frac{2R_s(C_{12}+C_{23})s}{2R_s(C_{12}+C_{23})s+1}$, $C_{12}+C_{23}$

Experiment 6:

1. AT_{2a3a}, $R_s = 465.5\Omega$, $S_{1a1b2a2b}$, S_{3a3b}
2. $v_{rbs}(t)$, $v_s(t)$
3. $\frac{2R_s(C_{23}+C_{13})s}{2R_s(C_{23}+C_{13})s+1}$, $C_{23}+C_{13}$

The voltage transform ratios are computed as $n_2 = \frac{N_2}{N_1}$ and $n_3 = \frac{N_3}{N_1}$, where N_1, N_2 and N_3 are the number of turns in first, second and third windings respectively. In order to explain how to obtain the model parameters in Fig. 5.8 from each experiment, the following assumptions are made:

- The inter-winding capacitances C_{12}, C_{23} and C_{13} can be identified separately from the rest of the winding model.
- The impedance $Z_m(s)$ is typically much larger than $Z_1(s)$; hence, $Z_1(s)$ can be neglected in Exp. 1.
- The impedance of C_m, say $Z_{cm}(s)$, is much higher than $Z_1(s)$, $Z_2(s)$ and $Z_3(s)$ in the frequency range under investigation; therefore, $Z_{cm}(s)$ is ignored in Exps. 2, 3.

Given the measurement setup and assumption for Exp. 1, the relation between the measured voltages $v_{rbs}(t)$ and $v_s(t)$ can be established as follows

$$v_{rbs}(t) - v_s(t) = \mathcal{L}^{-1}\left\{\frac{Z_{cm}(s)Z_m(s)}{Z_{cm}(s)+Z_m(s)}\right\} * \frac{v_s(t)}{R_s}. \tag{5.37}$$

Equation (5.37) shows that by applying the techniques of Section 5.2 with input data $v_s(t)/R_s$ and output data $v_{rbs}(t) - v_s(t)$, the transfer function

$$\frac{Z_{cm}(s)Z_m(s)}{Z_{cm}(s)+Z_m(s)} = \frac{R_m L_m s}{R_m L_m C_m s^2 + L_m s + R_m}, \tag{5.38}$$

can be identified, and consequently can be used as a basis for the determination of R_m, L_m and C_m.

For Exp. 2, the identification of the impedance $Z_1(s)$, $Z_2(s)$ requires an extra processing step. Starting from Eq. (5.39) which relates the collected signals $v_3(t)$, $v_s(t)$ with transformer parameters via

$$v_3(t) = n_3\mathcal{L}^{-1}\left\{\frac{Z_2(s)Z_m(s)}{Z_2(s)+n_2^2Z_m(s)}\right\} * \frac{v_s(t)}{R_s}, \tag{5.39}$$

the convolution of both sides of Eq. (5.39) and $\mathcal{L}^{-1}\left\{\frac{Z_2(s)+n_2^2Z_m(s)}{Z_2(s)Z_m(s)}\right\}$ is computed and rearranged to

$$n_3\left(\frac{v_s(t)}{R_s} - \hat{i}_m(t)\right) = \mathcal{L}^{-1}\left\{\frac{1}{Z_2(s)}\right\} * n_2^2 v_3(t), \tag{5.40}$$

where

$$\hat{i}_m(t) = \mathcal{L}^{-1}\left\{\frac{1}{n_3 Z_m(s)}\right\} * v_3(t). \tag{5.41}$$

Since $Z_m(s)$ is available from Exp. 1, $\hat{i}_m(t)$ can be easily calculated from $v_3(t)$ via Eq. (5.41). Let's assume that $Z_2(s)$ is not proper. Using $n_2^2 v_3(t)$ and $n_3(v_s(t)/R_s - \hat{i}_m(t))$ as input and output data for system identification respectively, one can obtain $1/Z_2(s)$ according to Eq. (5.40) and $Z_2(s)$ through the inversion of $1/Z_2(s)$. In the case of a proper impedance $Z_2(s)$, by interchanging the input-output role of $n_2^2 v_3(t)$ and $n_3(v_s(t)/R_s - \hat{i}_m(t))$ when applying the identification algorithm, an estimation of $Z_2(s)$ can be achieved. For estimation of $Z_1(s)$, one can rely upon Eq. (5.42) and the data $v_{rbs}(t)$, $v_s(t)$ and $v_3(t)$ acquired in Exp. 2, via

$$\frac{v_s(t)}{R_s} = \mathcal{L}^{-1}\left\{\frac{1}{Z_1(s)}\right\} * \left(v_{rbs}(t) - v_s(t) - \frac{v_3(t)}{n_3}\right). \tag{5.42}$$

The determination of the impedances $Z_1(s)$ and $Z_3(s)$ in Exp. 3 can be carried out in a similar manner as proposed for Exp. 2. Since the impedance $Z_1(s)$ can be obtained from either Exps. 2 or 3, the similarity of the two results will act as a validation for the estimation technique.

Since the same procedure can be used to determine model parameters from captured data in Exps. 4, 5 and 6, only Exp. 4 is examined in detail. Thanks to the effect of the circuit layout in Exp. 4, only capacitors C_{12} and C_{13} are involved in regulating the voltage $v_s(t)$ via

$$v_s(t) = \mathcal{L}^{-1}\left\{\frac{2R_s(C_{12}+C_{13})s}{2R_s(C_{12}+C_{13})s+1}\right\} * v_{rbs}(t). \tag{5.43}$$

Equation (5.43) shows that when the signals $v_{rbs}(t)$ and $v_s(t)$ are known, the value of $C_{12}+C_{13}$ can be easily determined based on the procedure in Section 5.2. Combining the results from Exps. 4, 5 and 6, there exists a unique solution for C_{12}, C_{13} and C_{23}.

In addition to the input-output data, a properly chosen order for each transfer function is a prerequisite for the system identification procedure. Fortunately, the transfer function order can be computed based on the impedance of the model parameters that we want to determine in each experiment. For the constant parameters, say L_m, R_m, C_m, C_{12}, C_{23} and C_{13}, their corresponding impedances have a fixed order. By contrast, the impedance $Z_1(s)$, $Z_2(s)$ and $Z_3(s)$ of the frequency dependent parameters, as expressed by

$$\begin{aligned} Z_i(s) &= R_i(s) + sL_i(s) \\ &= \frac{b_{i1}s^{n_{bi}-1} + b_{i2}s^{n_{bi}-2} + \cdots + b_{in_{bi}}}{s^{n_{fi}} + f_{i1}s^{n_{fi}-1} + \cdots + f_{in_{fi}}},\ i = 1, 2, 3, \end{aligned} \tag{5.44}$$

have an undefined order.

The general description of $\{Z_i(s)\}_{i=1}^3$ in Eq. (5.44) is suitable for identification purposes but is difficult to implement in electrical simulators. This problem can be solved by imposing a constraint on the parameters of Eq. (5.44) such that $\{Z_i(s)\}_{i=1}^3$ can be represented by a series Foster's network, as described in Section 3.3.1.3. In most cases, it was found that a simple condition between $\{n_{bi}\}_{i=1}^3$ and $\{n_{fi}\}_{i=1}^3$, as given by

$$n_{bi} = n_{fi} + 2,\ i = 1, 2, 3, \tag{5.45}$$

is enough to obtain $\{Z_i(s)\}_{i=1}^3$ with a Foster's network form. The values of $\{n_{bi}\}_{i=1}^3$ in both Exps. 2 and 3 are obtained using a singular value decomposition (SVD) [223]. The result from the SVD is consistent with that from both the Akaike's information theoretic criterion (AIC) and Rissanen's minimum description length (MDL) [223], though these complexity weightings give a less definitive selection.

5.4 Identification of non-linear ferrite cores

The nonlinear effect of the ferrite core is represented by modeling the magnetizing inductance Z_m in Fig. 5.1 as a nonlinear inductor. Applying the Jile-Atherton model [18], the current $i_m(t)$ passing through Z_m can be computed from the voltage $v_m(t)$ across it, via

$$\frac{dB}{dt} = \frac{v_m(t)}{N_1 A_c}, \tag{5.46}$$

$$H = \frac{B}{\mu_0} - M, \tag{5.47}$$

$$H_e = H + \alpha M, \tag{5.48}$$

$$M_{an} = M_s \left[1 - coth\left(\frac{H_e}{a}\right) + \left(\frac{a}{H_e}\right)\right], \tag{5.49}$$

$$\frac{dM_{an}}{dH_e} = \frac{M_s}{a}\left[1 - coth^2\left(\frac{H_e}{a}\right) + \left(\frac{a}{H_e}\right)^2\right], \tag{5.50}$$

$$\frac{dM_{irr}}{dH_e} = \frac{\gamma(M_{an} - M_{irr})}{k\delta}, \tag{5.51}$$

where

$$\delta = \begin{cases} 1 & \text{if } \frac{dH}{dt} \geq 0, \\ -1 & \text{if } \frac{dH}{dt} < 0. \end{cases} \qquad \gamma = \begin{cases} 1 & \text{if } M_{an} - M_{irr} \geq 0, \\ 0 & \text{if } M_{an} - M_{irr} < 0. \end{cases}$$

$$\frac{dM}{dB} = \mu_0 \frac{(1-c)\frac{dM_{irr}}{dH_e} + c\frac{dM_{an}}{dH_e}}{1 + (1-\alpha)c\frac{dM_{an}}{dH_e} + (1-\alpha)(1-c)\frac{dM_{irr}}{dH_e}}, \tag{5.52}$$

$$\frac{dM}{dt} = \frac{dM}{dB}\frac{dB}{dt}, \tag{5.53}$$

$$i_m(t) = \frac{1}{N_1}\left[H(l_e - l_a) + \frac{Bl_a}{\mu_0}\right], \tag{5.54}$$

where B and H are the flux density and applied magnetic field inside the ferrite core, respectively. M, M_{irr} and M_{an} represent the total, irreversible and anhysteresis magnetization quantities. The rate-dependent effect of the magnetic material has not been considered, but could be incorporated in the static model by adding an extra dynamic to the magnetization M [222].

The nonlinear inductor model parameters include the primary winding turns N_1, effective magnetic path length l_e, air gap length l_a, effective core area A_c and Jile-Atherton model parameter vector (M_s, a, α, c, k). Apart from N_1, l_e and A_c, which can be determined from a transformer core datasheet, the other parameters, including the Jile-Atherton model parameters and the gap length l_a, will be estimated using an optimization method. In particular, M_s, a, α, c, k and l_a are selected to minimize the objective function in Eq. (5.55),

$$\varepsilon = \frac{1}{N}\sum_{k=1}^{N}\Big[i_{mexp}(k) - i_{msim}(k)\Big]^2, \tag{5.55}$$

where N denotes the total number of data points, and i_{mexp} and i_{msim} are the experimental and simulated inductor current, respectively. Since both α and l_a contribute to the slope of the hysteresis curve, the identification of the model parameters should be carried out in two stages. In the fist step, the gap length l_a is kept fixed, while the Jiles-Atherton parameters are found using the Differential Evolution (DE) method [232]. All parameters obtained in the first step including l_a are then used as an initial condition for the Nelder-Mead optimisation algorithm [233] in the second step. The value of l_a in the first step can be obtained based on the transformer design specifications.

5.5 Experimental results

5.5.1 Dynamic winding model

The identification procedure, described in section 5.3, is applied to a 3-winding flyback transformer designed for a power supply application. The transformer operates with a nominal switching frequency of 100kHz. The numbers of turns of the first, second and third transformer windings are 46, 10 and 6, respectively. The transformer is constructed with an E core, more precisely E25/13/7 type, material N87, manufactured by EPCOS. An air gap length of approximately 0.15mm is made at the centre leg of the core in order to achieve a magnetizing inductance of around 800μH. The RBS generator in Fig. 5.4 is implemented with a clock frequency of 5MHz. The generator output $v_{rbs}(t)$ is a symmetrical random binary voltage having an adjustable amplitude of 0V-2V and a relatively flat spectrum, as illustrated in Fig. 5.6.

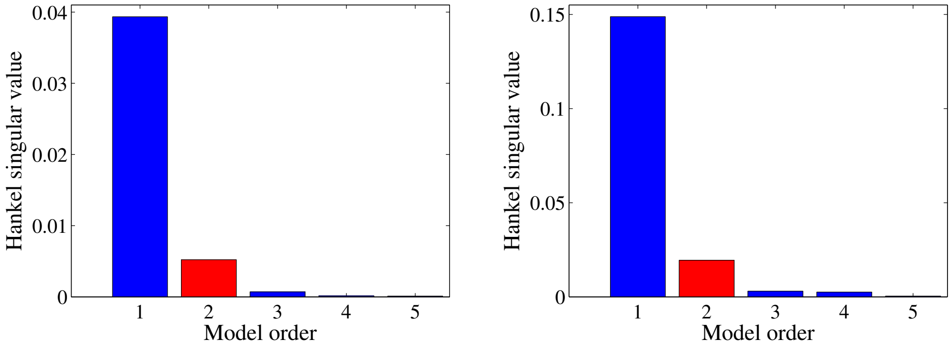

(a) $Z_1(s)$ in Exp. 2 (b) $Z_2(s)$ in Exp. 2

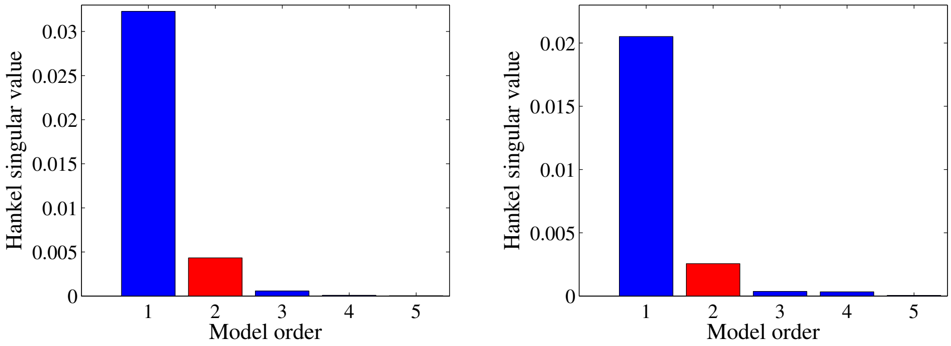

(c) $Z_1(s)$ in Exp. 3 (d) $Z_3(s)$ in Exp. 3

Figure 5.9: Singular values of Hankel matrices which are used to estimate the model orders of the impedance $Z_1(s)$, $Z_2(s)$ and $Z_3(s)$ in Exps. 2 and 3.

The input-output data is acquired by an Agilent digital oscilloscope (DSO6054A) with a pre-set sampling rate of 50MHz and 12 bits for each sample. Since the experiments in Section 5.3.3 involve high frequency signals and high speed data acquisition devices, the presence of parasitic elements in the measurement circuit, in addition to high frequency noise, can easily distort the collected data. In order to minimize such distortion during the data collection, surface-mounted sensing resistors are used and carefully soldered into a printed circuit board along with the flyback converter. In addition to the issues arising from non-ideal circuits, the loading effect of the oscilloscope probe at high frequencies is also problematic. Fortunately, such a problem can be handled by using active probes which have very low input capacitance and fairly constant impedance over a broad frequency range.

Following the procedure described in Section 5.3.3, different input-output data sets are collected and processed. The parameters of the winding model can be obtained by applying the SRIVC approach and the IV-based indirect approach discussed in Section 5.2. For Exps. 2 and 3, the model orders of the impedances $Z_1(s)$, $Z_2(s)$ and $Z_3(s)$ are unknown; therefore, estimation of these model orders is necessary. In general, the order of any continuous-time OE model includes two separate pieces of information: (i) the order of the numerator polynomial and (ii) the order of the denominator polynomial. These two parameters are generally independent and should be determined separately. In the cases of $Z_1(s)$, $Z_2(s)$ and $Z_3(s)$, the orders of their numerators and denominators have an algebraic relation according to Eq. (5.45), therefore, only the numerator orders need to be identified. The model order can be estimated through trialling different model structures and looking for the structure with a minimum cost function value, as in AIC and MDL, or selecting the minimum model order which is best to describe the system, as in SVD. Although these selection criteria can be equally used to find the orders of the numerators of $Z_1(s)$, $Z_2(s)$ and $Z_3(s)$, the SVD method is preferred due to its simplicity, computational efficiency and effectiveness.

Figure 5.9 plots the singular values of the Hankel matrices constructed from the experimental data of Exps. 2 and 3. The construction of the Hankel matrices includes two steps: (i) estimating the impulse responses of $Z_1(s)$, $Z_2(s)$ and $Z_3(s)$ from the time-domain data and (ii) transforming the resulting impulse responses into matrix forms and performing a SVD. The results from Fig. 5.9 suggest that the model order for $Z_1(s)$, $Z_2(s)$ and $Z_3(s)$ should be either 1 or 2. Since the computational complexity of the 2^{nd}-order model is not much higher than that of the 1^{st}-order model, the model order of 2 is selected for $Z_1(s)$, $Z_2(s)$ and $Z_3(s)$ in order to achieve higher accuracy.

Table 5.2 summarizes the parameters of the winding model estimated based on the SRIVC method and the IV-based indirect method. For comparison purposes, the impedance $Z_1(s)$ obtained from both Exps. 2 and 3 is included in Table 5.2. The data from Table 5.2 shows that the two independent estimates of $Z_1(s)$ are closely matched. The similarity between the two estimates effectively validate the framework proposed in Section 5.3.3. In addition, the results from SRIVC and IV demonstrate that, by imposing a proper constraint (see Eq. (5.35)) on the discrete time model, the IV approach can perform as well as the SRIVC method in estimating a continuous time model.

Table 5.2: Winding model parameters.

Component	SRIVC algorithm	IV-based indirect algorithm
L_m	791.67 μH	791.62 μH
R_m	85.522 kΩ	85.078 kΩ
C_m	8.9903 pF	8.9065 pF
C_{12}	3.298 pF	3.233 pF
C_{13}	59.64 pF	59.58 pF
C_{23}	29.304 pF	29.235 pF
n_2	0.21739	0.21739
n_3	0.13043	0.13043
$Z_1(s)$	$0.3522 + 9.745 \cdot 10^{-7}s + \frac{1.307s}{s+5.692 \cdot 10^6}$ from Exp. 2 $0.3485 + 9.636 \cdot 10^{-7}s + \frac{1.439s}{s+6.127 \cdot 10^6}$ from Exp. 3	$0.3546 + 9.7037 \cdot 10^{-7}s + \frac{1.372s}{s+5.927 \cdot 10^6}$ from Exp. 2 $0.3501 + 9.596 \cdot 10^{-6}s + \frac{1.504s}{s+6.334 \cdot 10^6}$ from Exp. 3
$Z_2(s)$	$0.0422 + 1.246 \cdot 10^{-7}s + \frac{0.0877s}{s+3.996 \cdot 10^6}$	$0.0422 + 1.245 \cdot 10^{-7}s + \frac{0.0895s}{s+4.0635 \cdot 10^6}$
$Z_3(s)$	$0.0425 + 7.525 \cdot 10^{-8}s + \frac{0.0364s}{s+2.448 \cdot 10^6}$	$0.0426 + 7.52 \cdot 10^{-8}s + \frac{0.0369s}{s+2.475 \cdot 10^6}$

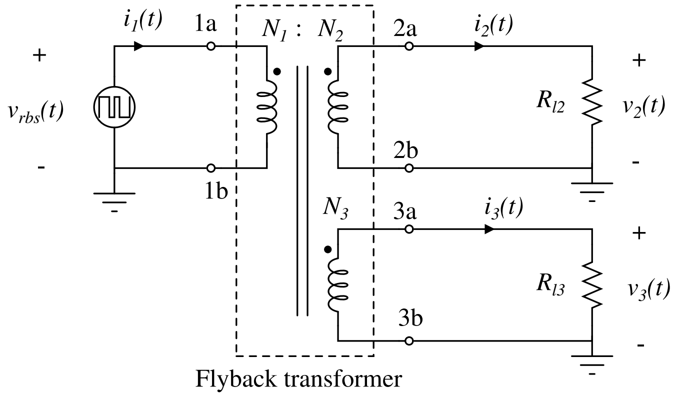

Figure 5.10: Circuit structure for validating the dynamic winding model in the time domain.

Table 5.3: Time domain test configurations.

Test case	Load configuration
1	$R_{l2} = 3.034\Omega$ and $R_{l3} = 1.056\Omega$
2	$R_{l2} = 19.995\Omega$ and $R_{l3} = 10.014\Omega$

Table 5.4: Frequency domain test configurations.

Test case	Winding configuration
1	Open circuit both secondary and third winding
2	Open circuit secondary winding and short-circuit third winding
3	Short-circuit secondary winding and open circuit third winding

Both time and frequency domain validation are essential to examine the accuracy of the obtained dynamic winding models. The circuit prototype, as shown in Fig. 5.10, is implemented to capture data for time-domain validation. A random binary voltage $v_{rbs}(t)$, a part of which is plotted in Fig. 5.11, is injected into the primary transformer winding. Two time-domain test cases, as described in Table 5.3, are employed to validate the winding model. The secondary and third winding voltage corresponding to the first test configuration in Table 5.3, returned from the experiment and simulation, are compared in Fig. 5.11. The excellent fit between the measured and simulated signals strongly confirm the accuracy of the obtained model. The comparison result for the second test case, as illustrated in Fig. 5.12, also shows a good agreement.

A frequency domain test is performed with the help of a HP4194A Impedance/Gain-Phase Analyzer which is employed to measure the primary impedance of the transformer between 500Hz and 15MHz in three different circuit configurations, as presented in Table 5.4. In addition to the frequency-domain data collected by the Impedance/Gain-Phase Analyzer, the primary impedance

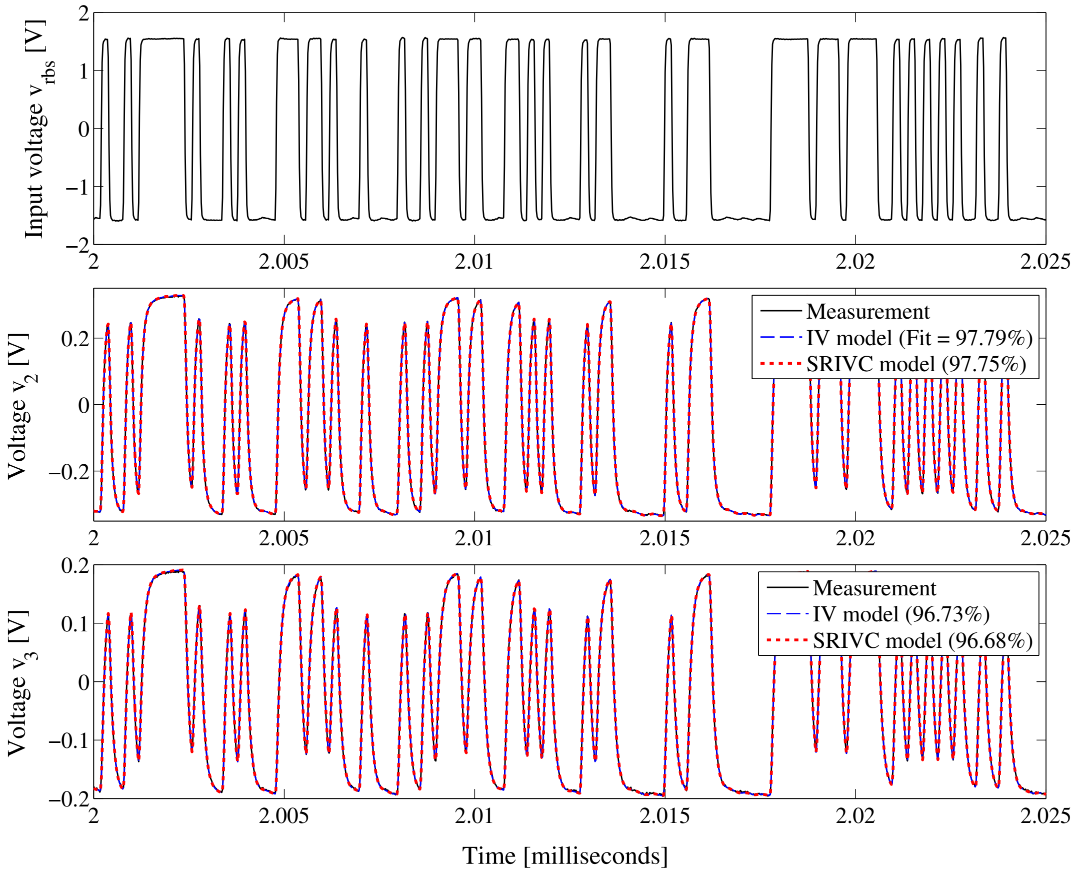

Figure 5.11: Measured and simulated results obtained from the model-validating circuit in Fig. 5.10. The loads are configured according to the test case 1 in Table 5.3

of the transformer can be also theoretically calculated using the model parameters shown in Table. 5.2, or estimated from time-domain data through spectral analysis. The theoretical calculations of the primary impedance are not straightforward and need some extra steps, including: (i) connecting the terminals of the secondary and third windings of the transformer model in Fig. 5.8 according to Table 5.4, (ii) referring all circuit components on the secondary and third winding sides to the primary side, and (iii) simplifying the resulting circuit to find the impedance between the two terminals of the primary winding. Both experimental and theoretically calculated results for each configuration in Table 5.4 are, in turn, depicted in Figs. 5.13, 5.14 and 5.15, respectively. In these figures, the estimated frequency response is obtained from the sampled time-domain voltage and current signals using spectral analysis [223], while the measured data is provided by the impedance analyzer.

The estimated frequency responses in Figs. 5.13, 5.14 and 5.15 have a big transition at multiples clock frequency of 5MHz. This is due to the excitation voltage (random binary signal), the spectrum of which typically has a notch at the clock frequency and its harmonics, which can be found in Fig. 5.6. When comparing the calculated, estimated, and measured frequency responses in Figs. 5.13, 5.14 and 5.15 corresponding to the three test cases of Table 5.4, one can conclude that both the SRIVC and IV models can accurately predict all the dynamics of the real transformer over

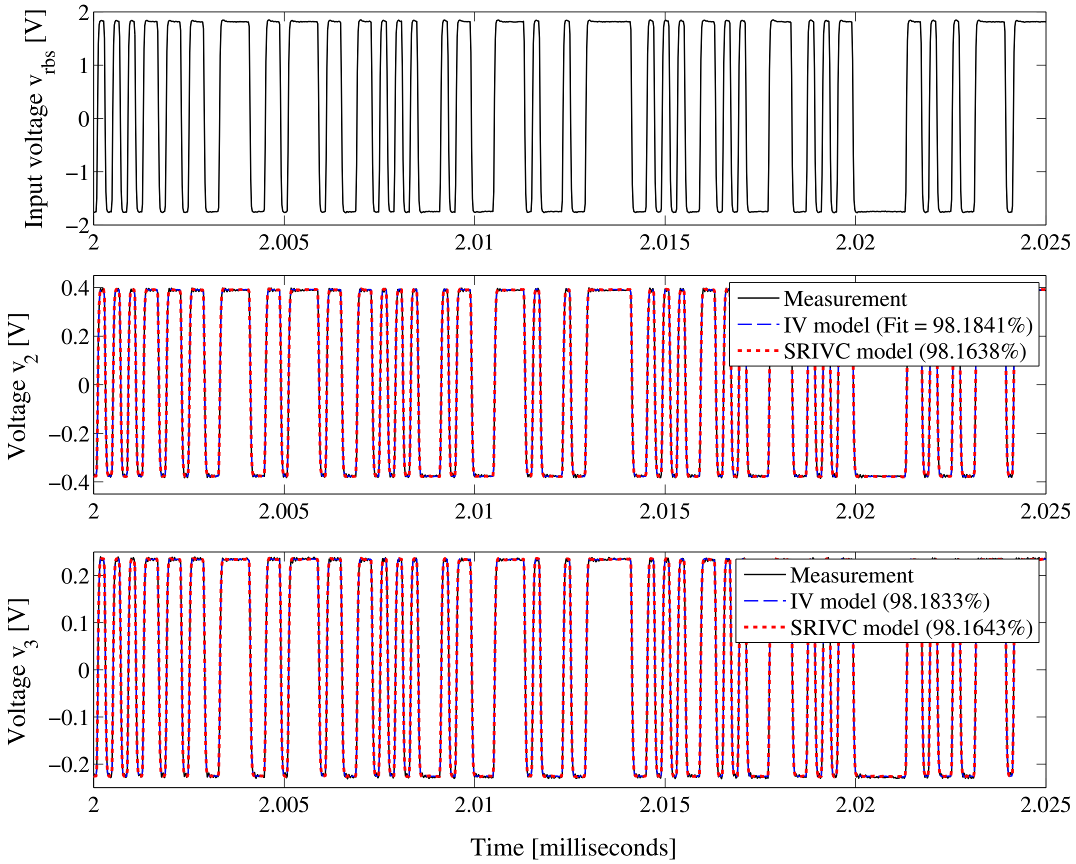

Figure 5.12: Measured and simulated results obtained from the model-validating circuit in Fig. 5.10. The loads are configured according to the test case 2 in Table 5.3

a wide frequency range. The only noticeable discrepancy between the measured and calculated results is in Fig. 5.15, when the frequency is smaller than 10kHz. This offset is probably due to the error when measuring the primary impedance at low frequencies using the impedance analyzer.

5.5.2 Non-linear core model

Table 5.5: Optimized nonlinear inductor model parameters.

Parameter	Initial value	DE	Nelder-Mead
$M_s(A/m)$	$10^5 - 10^6$	$4.0204 \cdot 10^5$	$4.025 \cdot 10^5$
$a(A/m)$	$5 - 500$	41.1123	41.7453
α	$10^{-5} - 10^{-3}$	$2.1467 \cdot 10^{-4}$	$2.1019 \cdot 10^{-5}$
c	$0.1 - 0.99$	0.5649	0.5751
$k_0(A/m)$	$5 - 500$	42.4702	43.4395
$l_a(mm)$	0.15	0.15	0.1514

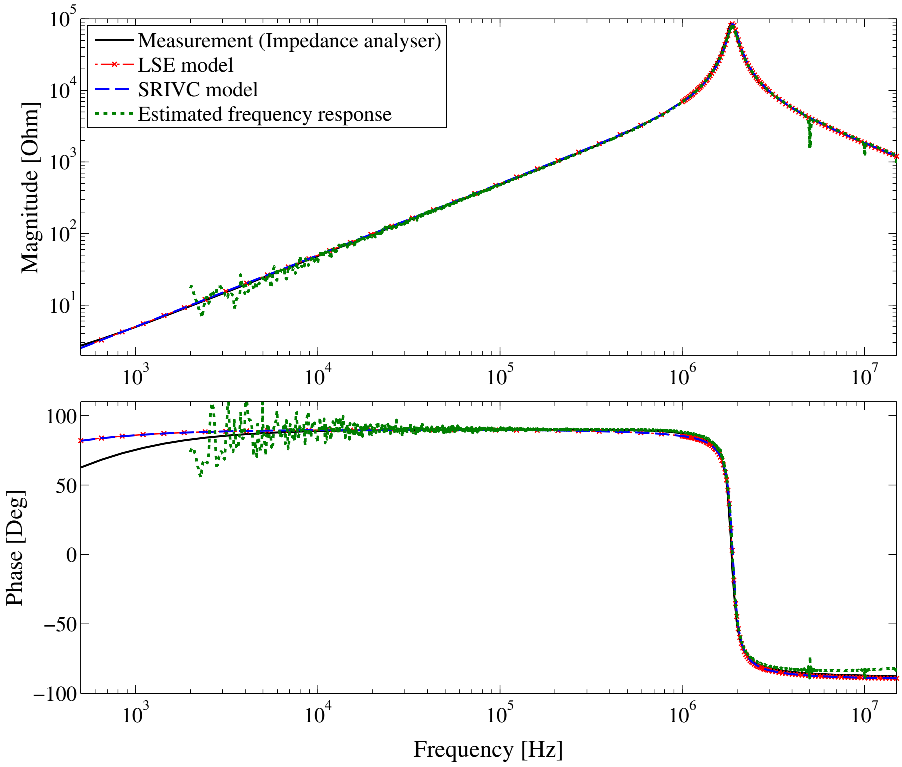

Figure 5.13: Primary transformer impedance for test case 1 (open circuit secondary and third windings).

The voltage V_m and current I_m data for the core model estimation in Section 5.4 are obtained using the conventional test method for ring cores [234, 235], except that the sample under investigation is now the flyback transformer. Specifically, the excitation source for the primary winding is a sinusoidal voltage having a frequency of 1kHz and a variable amplitude of 2V-12.5V, while the data is measured using a digital oscilloscope at the secondary winding and the current sensing resistor of 3.9Ω. To ensure the obtained model can work accurately over a wide variety of operating conditions, different levels of v_m and i_m (corresponding to different hysteresis curves) are included in the optimization procedure. The optimized parameters, which are returned by the DE and Nelder-Mead algorithms, are presented in Table 5.5. The initial values of the parameters in Table 5.5 are required by the DE method.

The obtained nonlinear model is verified by comparing the experimental and simulated inductor current $i_m(t)$ under two different levels of the excitation voltage $v_m(t)$. As can be seen in Fig. 5.16, the model can fully describe the nonlinear effect occurring in the ferrite core, although a small amount of accuracy is lost when increasing the excitation level.

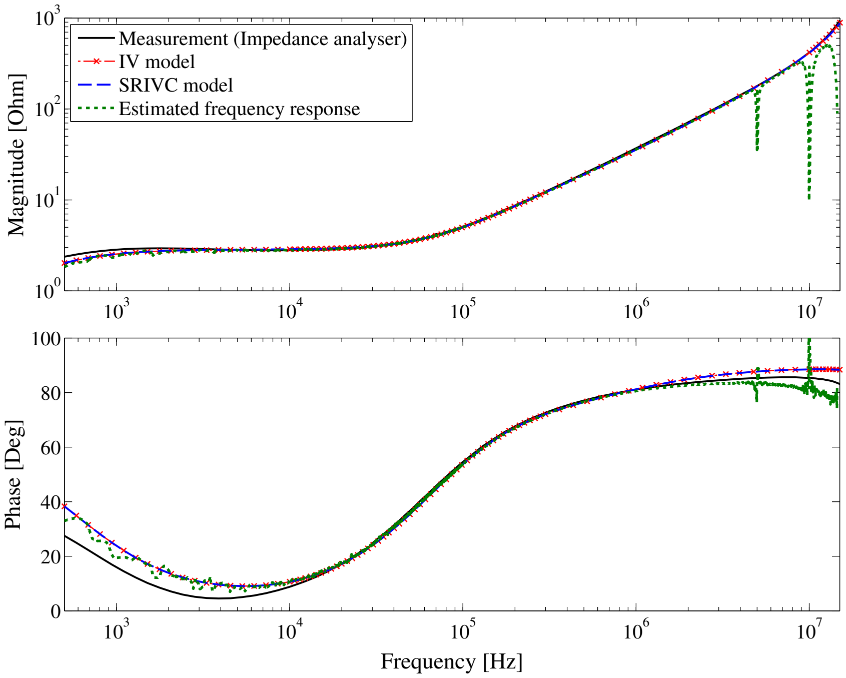

Figure 5.14: Primary transformer impedance for test case 2 (open circuit secondary and short-circuit third winding).

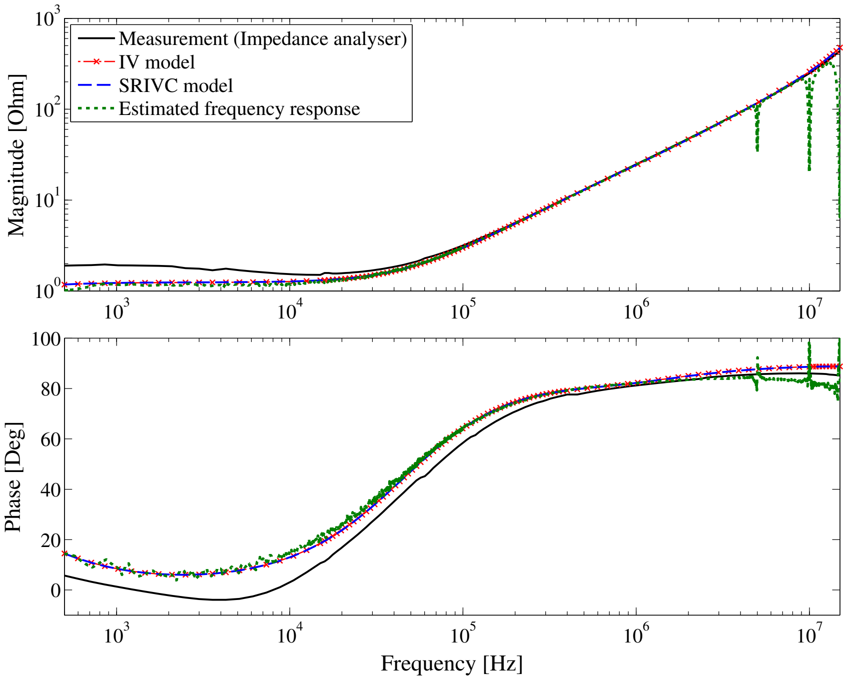

Figure 5.15: Primary transformer impedance for test case 3 (short-circuit secondary and open circuit third winding).

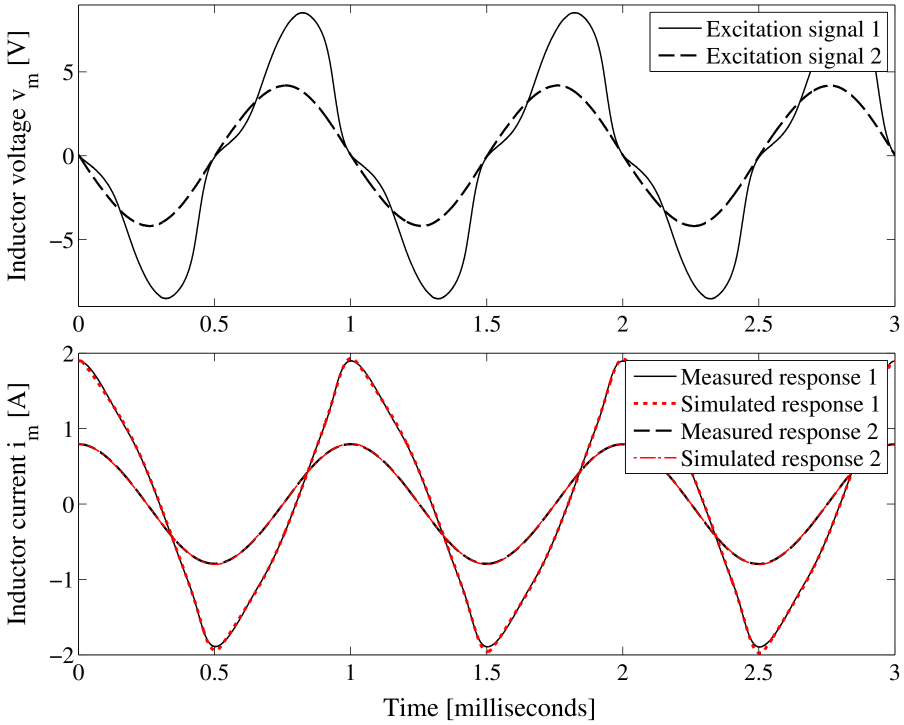

Figure 5.16: Nonlinear core model validation under different levels of excitation voltage.

5.5.3 Application of the non-linear dynamic transformer model to a flyback converter

Since the two winding models from the SRIVC and IV-based indirect methods in Section 5.5.1 achieve the same performance, one of these two results can be combined with the core model in Section 5.5.2 to form a dynamic transformer model. A direct validation of the dynamic model is to simulate a flyback converter application, as sketched in Fig. 5.17. Basically, the simulation can be carried out by any circuit-based simulator which allows analogue behavioural modelling (ABM); for convenience the SimElectronics/Simulink toolbox is employed. The ABM capability is required for the purpose of simulation of the dynamic transformer model. In particular, the non-linear algebraic relation describing the magnetic core Z_m in Fig. 5.1 is implemented by a behavioural block in SimElectronics. Once the block representing Z_m is available, the integrated transformer model in Fig. 5.1 can be easily established.

To fully characterize the transformer behaviour, the flyback converter in Fig. 5.17 should be run in open loop, i.e. with an independent PWM duty cycle and switching frequency. When the input voltage $v_{in}(t)$ and converter parameters are fixed as given in Fig. 5.17, the working condition of the flyback converter will be determined by the output load R, the duty ratio d and the switching frequency f_{pwm} of the PWM signal. Since the transformer model is mainly applied to primary side sensing control, only the primary current $i_{in}(t)$ and bias winding voltage $v_{bias}(t)$ are of interest. The transformer is examined under the two working conditions of the flyback converter. In the first condition, the converter is set up with $R = 16.97\Omega$, $d = 0.45$, and $f_{pwm} = 100$kHz, to

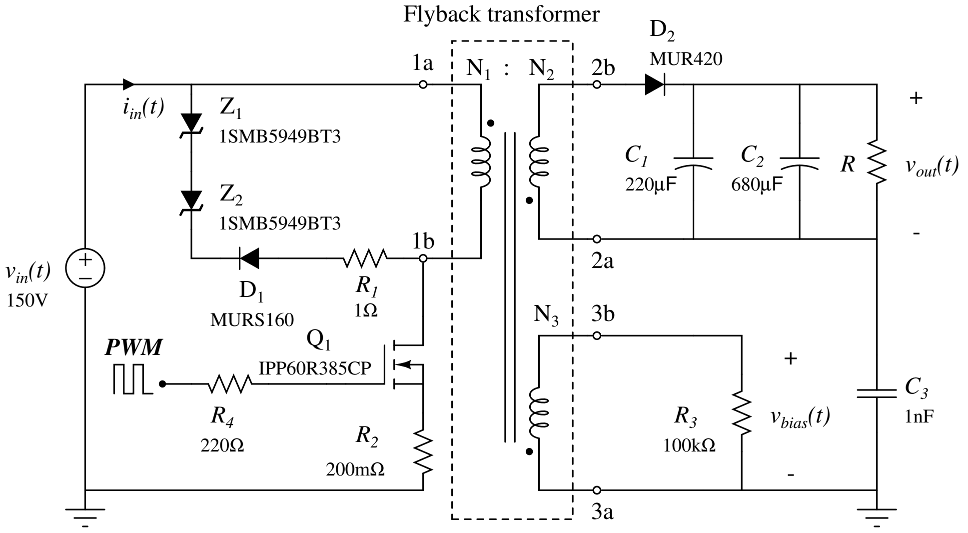

Figure 5.17: Circuit prototype of a flyback converter for verification of the dynamic transformer model in Fig. 5.1.

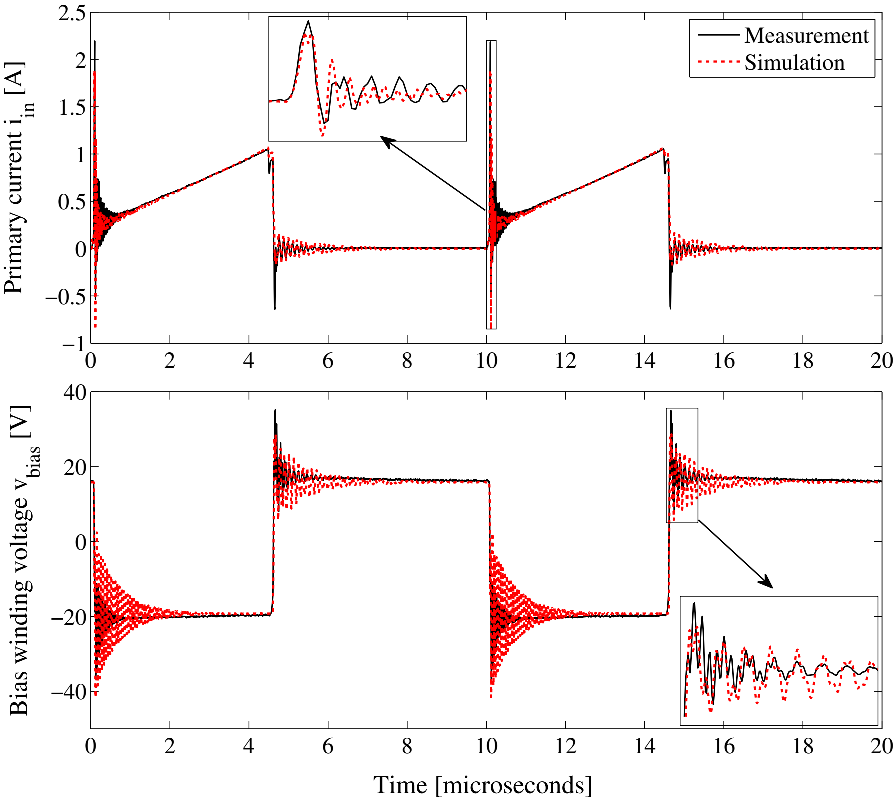

Figure 5.18: Comparison between measured and simulated primary current $i_{in}(t)$ and bias winding voltage $v_{bias}(t)$ under CCM. The open-loop flyback converter is operated with the output load $R = 16.97\Omega$, duty ratio $d = 0.45$, and switching frequency $f_{pwm} = 100$kHz.

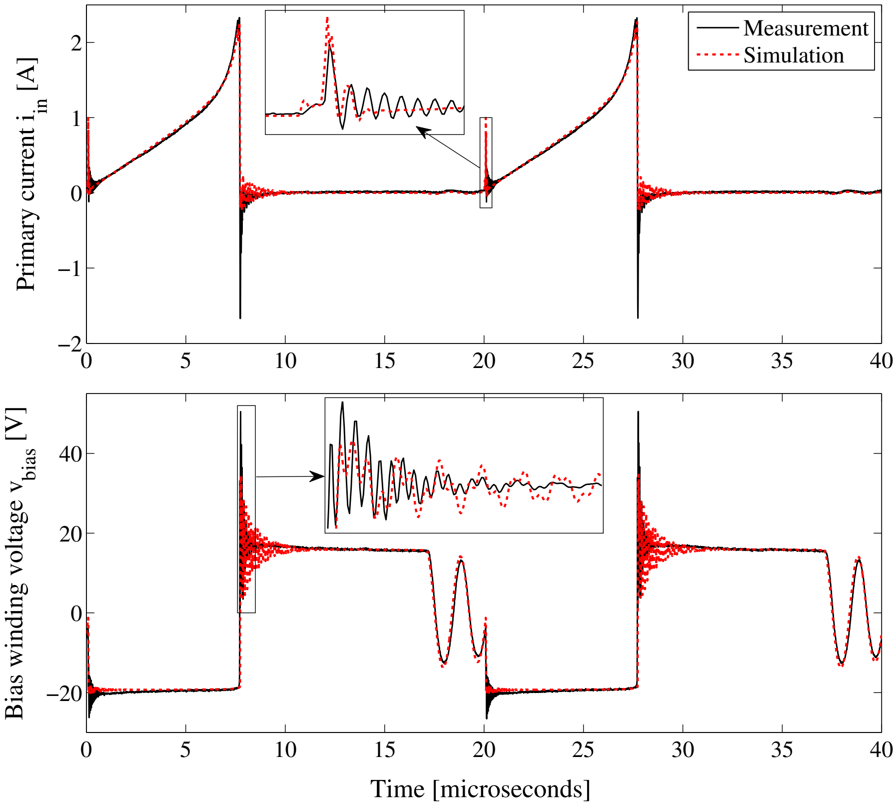

Figure 5.19: Comparison between measured and simulated primary current $i_{in}(t)$ and bias winding voltage $v_{bias}(t)$ under DCM. The open-loop flyback converter is operated with the output load $R = 16.829\Omega$, duty ratio $d = 0.38$, and switching frequency $f_{pwm} = 50\text{kHz}$.

operate in continuous conduction mode (CCM), while the second working condition is selected as $R = 16.829\Omega$, $d = 0.38$, and $f_{pwm} = 50\text{kHz}$, which helps to see the saturation in the core and the ringing effect in discontinuous conduction mode (DCM).

The results for the first and second test, which are presented in Fig. 5.18 and 5.19 respectively, show very good agreement between the measurement and simulation waveforms. By examining the primary current waveforms in Fig. 5.18 and 5.19, specifically during the MOSFET on-time, one can claim that the integrated transformer model can fully represent the behaviour of a practical transformer in both linear and non-linear regions. Such a conclusion could be further confirmed by observing the ringing in the voltage $v_{bias}(t)$ at the end of each switching cycle (Fig. 5.19). As can be seen from the magnified windows in Fig. 5.18 and 5.19, the simulation is unable to reproduce all the details of the experimental results during the ringing interval after each switching instance. Such a limitation is due to the imperfection of the simulation program in which the parasitics inside semiconductor devices and between circuit components have been not modelled properly or even ignored. In addition to any modelling impairment, thermal noise and shot noise, which always exist in practical systems, further aggravate the issue.

5.6 Conclusion

This chapter presents a systematic procedure to identify a non-linear dynamic model for a 3-winding transformer in time domain. The identification procedure includes an estimation of the transformer winding model using a time-domain system identification approach and a determination of a static core model using an optimization method.

The study points out the numerical difficulty, particularly round-off error, associated with the time-domain data collection and proposes the use of different sensing resistor R_s values to improve the estimation results. As demonstrated in Section 5.5.1, the time domain approach can provide a winding model at least as accurate as that obtained with the frequency response data. With a longer data time series record, a more accurate transformer model is obtained, particularly at low frequencies. Though the selection of different sensing resistor values for different experiments is quite tedious, the time-domain approach requires only simple measurement equipment (say a digital oscilloscope) and, most importantly, offers an easy way to calculate winding model parameters separately.

In addition to the parameters of the Jiles-Atherton model, which is used to describe the non-linear core behaviour, the air gap length is also computed from the experimental data to enhance the core model accuracy. The use of the air gap length, as a variable for estimation, significantly improves the model accuracy. As demonstrated in Section 5.5.2, the obtained core model can accurately predict all the non-linearity occurring throughout the operating regime.

The results in this chapter are valid for both small and large signals and are useful for controller design and system validation purposes. The application of the non-linear dynamic model to control design is presented in Chapter 6.

Chapter 6

Control-oriented modelling and simulation of flyback converters

6.1 Introduction

Driven by the new energy standards, e.g. U.S. Energy Star [42], and cost reduction demand for external AC-to-DC power supplies, the control solution for flyback converters is gradually transitioning from traditional analogue design to modern digital design with multi-function integration [7, 58]. Figure 6.1 exemplifies a digital control solution for a flyback converter, where several functions, consisting of magnetic sensing (MS), n^{th} valley switching operation (VSO), and efficiency optimisation (EO), are integrated into and wrapped around the digital compensator. In order to reduce the design time and costs, simulation is usually employed in the control design process for power converters in general, and for flyback converters in particular. Unfortunately, in contrast to analogue control, the performance and stability of the digital control solution in Fig. 6.1 can not be simply verified by an averaged small-signal model or an ideal switched model of the flyback converter. Such a challenge is due to the fact that the control method in Fig. 6.1 makes use of not only inter-cycle but also intra-cycle responses of the feedback signals to regulate the converter output voltage. Therefore, a detailed simulation model, which is able to reproduce both intra-cycle and inter-cycle behaviour of the flyback converter, is required for the design of such a control solution.

Flyback converters typically exhibit large disparities in their dynamic responses, consisting of very fast events due to switching devices, and much slower events arising from the variations of the input voltage, output load, and operating mode. In order to resolve both fast (intra-cycle) responses and slow (inter-cycle) responses in the simulation of flyback converters, a very fine time-step is typically required. Such a simulation time step can result in an overwhelming amount of data and a significant execution time, if a complete response of a slow event is considered. Since the detailed simulation of flyback converters over slow transient events, e.g. step load responses, is necessary for control performance assessment, the execution time (or speed) of the simulation becomes a critical factor. Therefore, a reasonably accurate and fast simulation of the digitally controlled flyback converter of Fig. 6.1 is a problem of considerable interest.

Emulating the behaviour of the open-loop flyback converter in Fig. 6.1 has been considered in Section 5.5.3 using a full modelling approach, i.e. with detailed complex models for circuit

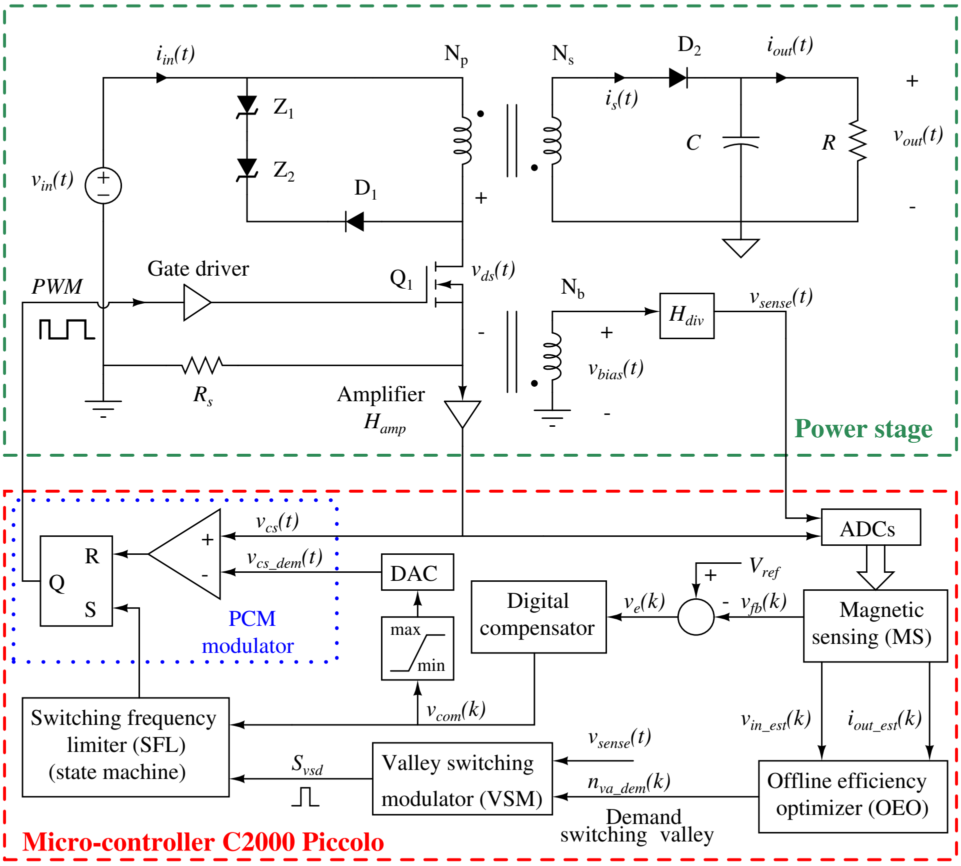

Figure 6.1: Circuit diagram of digital peak current mode control with magnetic sensing and offline efficiency optimization for a flyback converter application

devices, and in Section 2.2, using a simplified modelling approach, i.e. with simple idealized device models of electronic components. The differences between these two approaches are essentially the accuracy and computational complexity of the models employed. The full model in Section 5.5.3 can provide a very high level of accuracy and insight; however, its computational complexity is too great to permit its use as a basis for digital control design. On the other hand, the simplified model in Section 2.2 ignores most dynamics occurring within switching cycles, and consequently is not appropriate for control design either. Therefore, we require to develop a control-oriented model which, ideally, retains the essential dynamic characteristics of the flyback converter, but offers significantly reduced complexity. Such an objective is the focus of this chapter.

The simulation of a converter model can be performed by either deriving and solving a set of differential equations using general equation-solver programs, such as MATLAB/SIMULINK, or by directly employing a circuit-oriented simulator, like PSIM. Although the first method requires extra effort to prepare the equations and set up the solver, it offers full control of the solver configuration, physical insight into the operation of the system, and so is employed in this chapter.

6.2 Control-oriented model development

As discussed in Section 3.2, the execution speed of a simulation can be improved by either (i) selecting a proper model for the converter or (ii) customizing differential equation solvers. The former approach is mainly considered in this section. In particular, given specific knowledge about the dynamics of the open-loop flyback converter through the modelling study in Section 5.5.3, Section 6.2.1 proposes a procedure for forming a control-oriented model that offers a good trade-off between modelling accuracy and computational complexity. Section 6.2.2 presents general formulae for describing the circuit operation of the control-oriented model regulated by an external control signal. Based on such formulae, Section 6.2.3 derives the detailed LTI continuous-time state-space equations describing the converter operation for each switch configuration encountered in each cycle of operation, and the condition determining the transition from one switching configuration to another.

6.2.1 Model simplification

The execution time of the simulation and the modelling accuracy are strongly affected by the complexity of the model of the converter circuit, particularly for the transformer and semiconductor devices. For example, an idealized model needs only a short time to complete the simulation of the flyback converter over many switching cycles; however, the data generated by such an idealized model is mostly too poor, in terms of information content, and is not adequate for the design of the digital control in Fig. 6.1. Conversely, increasing model complexity allows the reproduction of all transient details in each switching cycle, but the simulation task may consume a significant amount of time if a full transient event, e.g. step load response, is of interest. It is obvious that the application of the full converter model to control design is technically impractical; however, the full model can be used as a basis to obtain a control-oriented model. More precisely, by considering the full converter model in Section 5.5.3 as the starting point of the simplification process, and taking the simulated voltage and current waveforms based on the full converter, as illustrated in Fig. 6.2, as a visual tool, we can decide which parts of the full model need to be simplified, and which parts need to be preserved in order to satisfy the requirements on both the simulation time and modelling accuracy.

In general, reducing model complexity results in losing information fidelity in the simplified model. Depending on the modelling purposes, some information is critical for the control design process and needs to be preserved, while other information can be eliminated. For example, n^{th} valley switching control in [7, 58] needs certain information from the feedback signals, including the oscillation in $v_{bias}(t)$ during discontinuous conduction mode (DCM), as covered by window C in Fig. 6.2, and the high frequency ringing in $v_{bias}(t)$ after the MOSFET turn-off instance, as shown in window B of Fig. 6.2, in order to make a correct decision. Without such information, the model should not be used for the control design process. Since the information contained inside the model itself is far more important than the complexity of the model, model simplification should focus on the impact of information lost rather than a pure focus on complexity. Ideally, we want to maximize complexity reduction for minimum impact on accuracy.

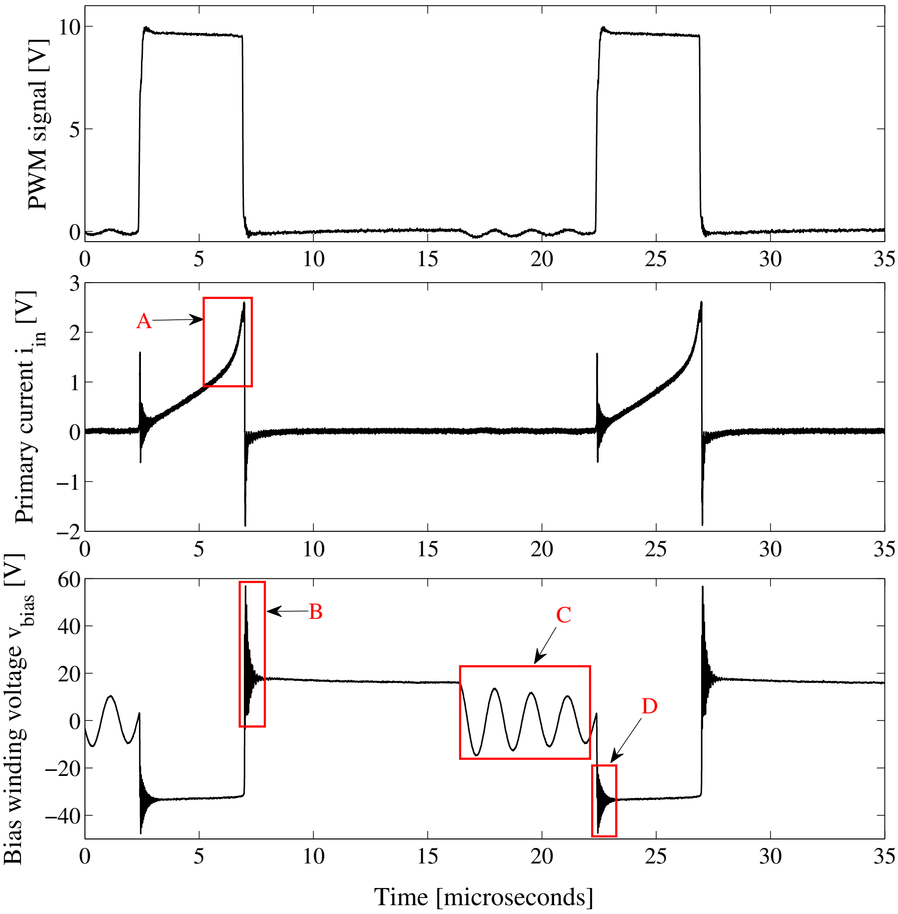

Figure 6.2: Simulated voltage and current waveforms obtained based on the full model of the open-loop flyback converter.

The amount of information contained inside the converter model is directly linked to the models of the electronic components used. For instance, the non-linear slope of the primary current $i_{in}(t)$ during the MOSFET on-time, as highlighted by window A in Fig. 6.2, is modelled by a non-linear core with saturation. However, if only a linear core model is considered in the modelling process, such non-linear behaviour will not be seen in the simulated data. The demonstration of this observation can be found in Section 6.4.1. Another example is the high frequency ringing in the bias winding voltage $v_{bias}(t)$ occurring right after the MOSFET turn-on instance, as covered by window D of Fig. 6.2. Such an oscillation is modelled by the leakage inductance of the transformer, the parasitic capacitance of the secondary diode D_2 in Fig. 6.1 and possibly the inter-winding capacitance of the transformer. Ignoring the models of these parasitic elements will lead to a simulated waveform of $v_{bias}(t)$ without such an oscillation.

All the non-linear responses and high-frequency oscillations in the voltage and current waveforms, as highlighted by windows A, B ,C and D in Fig. 6.2, are related to the practical properties of the electronic components used. For example, the non-linear slope of the primary current $i_{in}(t)$, see window A of Fig. 6.2, is due to the saturation of the transformer core, while the ringing surrounded by window B comes from the leakage inductance and parasitic capacitance of MOSFET. Window C in Fig. 6.2 highlights the oscillation caused by the magnetising inductance and MOSFET drain source capacitance.

A control-oriented model is typically developed from the full model through three steps (i) determining the dynamics in the signal waveforms of Fig. 6.2 which need to be preserved, (ii) relating the signal dynamics of interest to the component models in the full converter model, and (iii) removing unwanted component models from the full model.

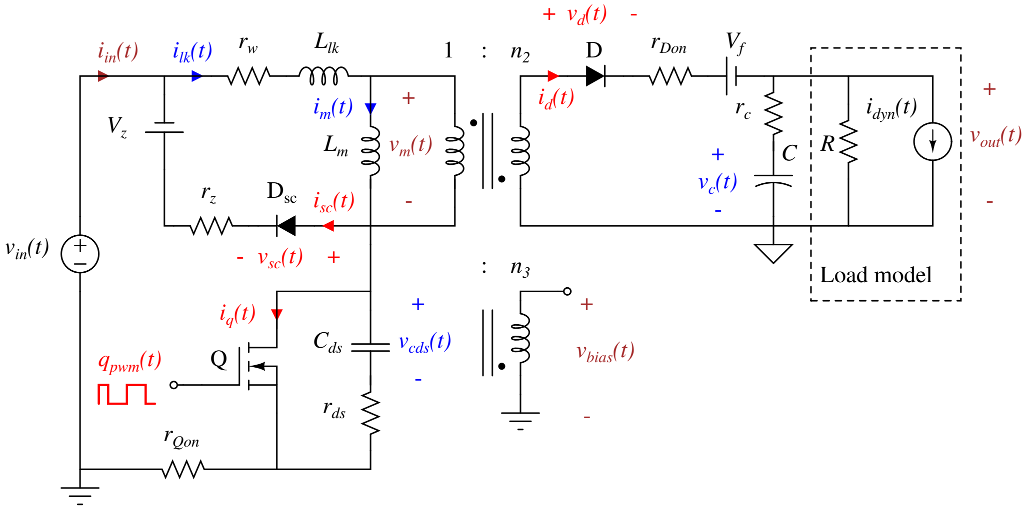

Figure 6.3: Control-oriented model of the flyback converter.

The flyback converter model obtained after a simplification step is sketched in Fig. 6.3, where the transformer is described by a traditional T-model with a leakage inductance L_{lk} and magnetizing inductance L_m, while the MOSFET is modelled by an ideal MOSFET Q in parallel with a parasitic RC circuit. The leakage inductance L_{lk} and capacitance C_{ds} are utilized in Fig. 6.3 to reproduce all the ringing in the bias winding voltage $v_{bias}(t)$, which is critical for control performance assessment. The Zener diodes, Z_1 and Z_2 in Fig. 6.1, are simply represented by a voltage source V_z in series with r_z in Fig. 6.3, while the Schottky diodes, D_1 and D_2 in Fig. 6.1, are modelled by ideal diodes D_{sc} and D in Fig. 6.3, respectively. To represent the conduction losses occurring in the MOSFET, transformer and diode, three resistors r_{Qon}, r_w, and r_{Don} are added to the control-oriented model in Fig. 6.3.

Generally, the snubber circuit, consisting of D_1, Z_1 and Z_2 in Fig. 6.1, does not have much effect on control operation; however, without such a circuit, the simulated bias winding voltage $v_{bias}(t)$ typically has large spikes in its waveform. Although such spikes are relatively short, and their presence does not alter the rest of the signal waveform, these spikes make the simulated data unrealistic. Hence, the model of the snubber circuit, represented by D_{sc}, r_z and V_z in Fig. 6.3, is purposely employed to suppress these unwanted spikes in $v_{bias}(t)$.

Notice that the MOSFET Q in Fig. 6.3 operates in a similar manner as an ideal switch controlled by the normalized PWM signal $q_{pwm}(t)$, while the diodes D and D_{sc} have ideal characteristics which are zero resistance when on and open circuit when off. The parameters of the control-oriented model can be obtained by directly taking values from the full model.

6.2.2 Continuous-time description of converter operation

Since most electronic components of the converter circuit model in Fig. 6.3 are linear and their operation can be easily found in many textbooks on power electronics [3], the focus of this section is on the IV characteristics of the semiconductor devices Q, D and $\mathrm{D_{sc}}$ in Fig. 6.3 and on the mathematical description of circuit operation over time.

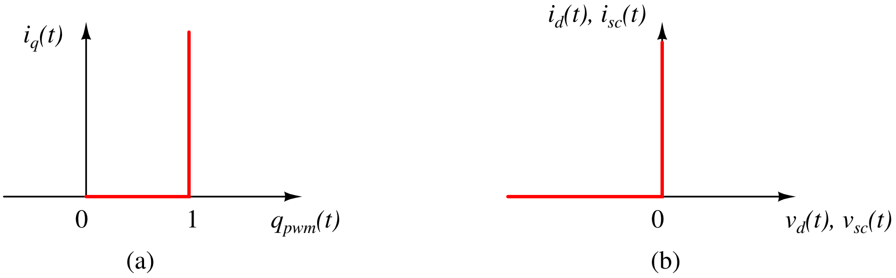

Figure 6.4: The static IV characteristics of the switching components in Fig. 6.3: (a) MOSFET Q, (b) diodes D and $\mathrm{D_{sc}}$.

The MOSFET Q is a 3-terminal semiconductor device, whose operation is externally controlled by the normalized PWM signal $q_{pwm}(t)$. Depending on the amplitude of $q_{pwm}(t)$, Q will be either on or off and behaves like either an open circuit or a short-circuit, respectively. Existing different options can be used to choose the threshold level for Q. For simplicity, the threshold level is chosen to be 1, i.e. Q is on if $q_{pwm}(t) = 1$ and off if $q_{pwm}(t) < 1$. The profile of the current $i_q(t)$ passing through Q is plotted as a function of $q_{pwm}(t)$ in Fig. 6.4(a), where $i_q(t)$ denotes the current passing through Q.

Unlike the MOSFET Q, the transition between the on- and off-states of the diodes D and $\mathrm{D_{sc}}$ is not directly controlled by external control action but rather occurs when the internal states, including diode terminal voltages and currents, reach particular boundaries or threshold conditions. Such boundaries can be easily established based on the IV characteristics of D and $\mathrm{D_{sc}}$, as sketched in Fig. 6.4(b), where $i_d(t)$ and $i_{sc}(t)$ denote the current passing through D and $\mathrm{D_{sc}}$, respectively, while $v_d(t)$ and $v_{sc}(t)$ are the voltage across the terminals of D and $\mathrm{D_{sc}}$, respectively. In general, two boundaries, one for on-to-off transition and another for off-to-on transition, are required for each diode. For example, the condition for the diode D turning on is $i_d(t) = 0$ and $v_d(t) > 0$, while the turning-off condition for D is $v_d(t) = 0$ and $i_d(t) < 0$. For convenience, the boundary conditions for the state transitions of the semiconductor devices are summarized in Table 6.1. Notice that all Q, D, and $\mathrm{D_{sc}}$ are equivalent to zero resistance when on, and open circuit when off.

Due to the cyclical changes in the control signal $q_{pwm}(t)$, the converter circuit model in Fig. 6.3 operates cyclically. Its operation, over the k^{th} switching cycle, can be governed by a set of J linear

Table 6.1: State transition conditions for switching devices.

Devices	State transition	Boundary condition
Q	off → on	$q_{pwm}(t) = 1$
	on → off	$q_{pwm}(t) < 1$
D	off → on	$i_d(t) = 0$ and $v_d(t) > 0$
	on → off	$v_d(t) = 0$ and $i_d(t) < 0$
$\mathrm{D_{sc}}$	off → on	$i_{sc}(t) = 0$ and $v_{sc}(t) > 0$
	on → off	$v_{sc}(t) = 0$ and $i_{sc}(t) < 0$

time invariant (LTI) state-space equations of the form

$$\begin{aligned}\frac{d\mathbf{x}(t)}{dt} &= \mathbf{A}_i\mathbf{x}(t) + \mathbf{B}_i\mathbf{u}(t) \\ \mathbf{y}(t) &= \mathbf{C}_i\mathbf{x}(t) + \mathbf{E}_i\mathbf{u}(t)\end{aligned} \qquad 1 \leq i \leq J, \tag{6.1}$$

where J is the number of different switch configurations (or topologies) which the converter may go through in the k^{th} cycle. $\mathbf{x}(t)$, $\mathbf{y}(t)$ and $\mathbf{u}(t)$ are the state variable vector, the input variable vector, and the output variable vector of the converter, respectively. The state space matrices $\mathbf{A}_i$ and $\mathbf{B}_i$, $\mathbf{C}_i$ and $\mathbf{E}_i$ are composed of numerical constants derived from the i^{th} switch configuration and the circuit parameters. The choice of the vectors $\mathbf{x}(t)$, $\mathbf{y}(t)$ and $\mathbf{u}(t)$, and the derivation of the state matrices $\mathbf{A}_i$ and $\mathbf{B}_i$, $\mathbf{C}_i$ and $\mathbf{E}_i$, are addressed in detail in Section 6.2.3.

When the external excitations $v_{in}(t)$, $i_{dyn}(t)$ and the PWM control signal $q_{pwm}(t)$ are known, the voltage and current signals in Fig. 6.3 can be obtained by solving the set of J LTI ordinary differential equations (ODEs), in Eq. (6.1), over time. Two difficulties arise when solving Eq. (6.1). The first difficulty is the sequence in which the differential equations are solved, which is unknown in advance and depends on the states of the MOSTFET Q, and diodes D and $\mathrm{D_{sc}}$. Fortunately, switching from one topology to another in the converter circuit can be simply determined through the transition in the states of the semiconductor devices, particularly through the transition in the values of $q_{pwm}(t)$, $i_d(t)$, $v_d(t)$, $i_{sc}(t)$ and $v_{sc}(t)$; refer to Table 6.1 for more detail. Once the active topology is known and the signals needed for state transition can be calculated, the next topology can be easily determined. Notice that when the simulation starts, the initial topology has to be defined in advance. The simplest choice is to set all of Q, D and $\mathrm{D_{sc}}$ to off. The second difficulty when solving Eq. (6.1) is how to guarantee the continuity of the state variable $\mathbf{x}(t)$ across each change in switch configuration. Such a difficulty can be overcome by using the final value of $\mathbf{x}(t)$ in the active configuration to initialize the state variable in the next configuration.

6.2.3 Mathematical equation derivation

Following the procedure described in Section 6.2.2, this section derives the detailed state space equations for each switch configuration of the converter circuit. Firstly, the state variable vector $\mathbf{x}(t)$, the input variable vector $\mathbf{u}(t)$, and the output vector $\mathbf{y}(t)$ are chosen as

$$\mathbf{x}(t) = \begin{bmatrix} i_{lk}(t) \\ i_m(t) \\ v_{cds}(t) \\ v_c(t) \end{bmatrix}, \qquad \mathbf{u}(t) = \begin{bmatrix} v_{in}(t) \\ i_{dyn}(t) \\ V_f \\ V_z \end{bmatrix}, \qquad \mathbf{y}(t) = \begin{bmatrix} i_{in}(t) \\ v_m(t) \\ v_{out}(t) \\ i_d(t) \\ v_d(t) \\ i_{sc}(t) \\ v_{sc}(t) \end{bmatrix}. \tag{6.2}$$

The output vector $\mathbf{y}(t)$ typically consists of several variables of interest in the converter, such as the input current $i_{in}(t)$, output voltage $v_{out}(t)$, which do not belong to the class of the state variables and the class of input variables. Although the responses of $i_d(t)$, $v_d(t)$, $i_{sc}(t)$ and $v_{sc}(t)$ are not of particular interest, such signals are important for the determination of the switch configuration, and as a result are also included in $\mathbf{y}(t)$.

In theory, 8 possible circuit configurations can be formed from 3 independent switches; however, only 5 combinations are feasible in the control-oriented model in Fig. 6.3, the other 3 configurations do not exist because D and $\mathrm{D_{sc}}$ are only 2-terminal semiconductors, whose states are controlled internally by the system states. The expressions for the state space matrices for the 5 switch configurations are presented in Appendix A.

6.3 Model implementation and convergence handling

Given the mathematical description of the simplified model in Section 6.2, a differential-equation solver is required to calculate the converter state and output variables for a given excitation condition. The calculation time is typically not fixed and depends on how the solver is designed and the level of accuracy required [62]. By combining the conditions in Table 6.1 and Eq. (6.1) together, one can realize that the operation of the control-oriented model is generally governed by differential algebraic equations (DAEs) rather than pure ordinary differential equations (ODEs). Since DAEs contain algebraic relations among state variables, input variables and output variables, a very fine time-step is typically utilized to ensure the convergence of the solution. Such a time-step will lead to a slow execution speed and a long simulation time, e.g. 5 hours, even for a short transient event. In order to perform faster simulations, it is essential to remove the algebraic loops and convert the DAEs to pure ODEs.

Breaking the algebraic relations in Eq. (6.1) and Table 6.1 can be achieved by sequencing these model equations and forcing an ending condition to avoid re-iteration. An equation-solving sequence, designed for the control-oriented model, is illustrated in Fig. 6.5. The principle of the procedure in Fig. 6.5 can be explained as follow. For each time step, the ODE in Eq. (6.1) is

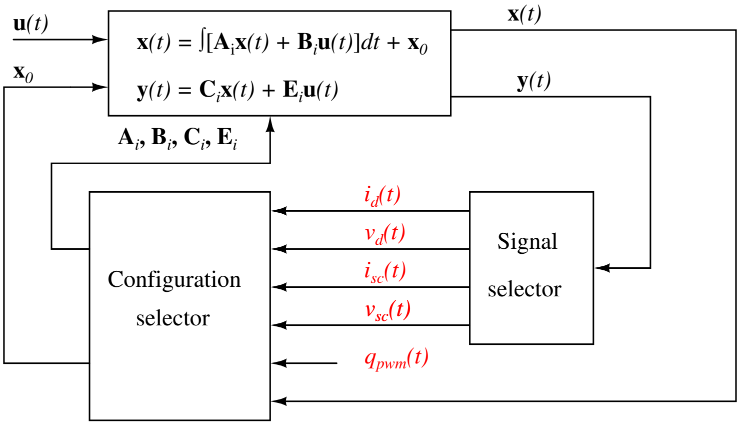

Figure 6.5: General approach to simulate the LTI piecewise model in Fig. 6.3.

solved using a numerical integration algorithm. The results from the equation solver are utilized to calculate the diode currents and voltages $i_d(t)$, v_d, $i_{sc}(t)$, and $v_{sc}(t)$. Based on these signals and the PWM signal $q_{pwm}(t)$, the configuration selector chooses the next circuit topology according to the conditions in Table 6.1 and then updates the equation parameters in the next time step.

The simulation of the simplified model in Fig. 6.3 consists of dividing the time duration into smaller time steps and calling the procedure in Fig. 6.5 at each time step. The selection of the time step can be fixed or variable in size. In this study, a fixed time step is preferred because it allows the implementation and verification of digital control functions. In addition to the algebraic loop removal, the choice and implementation of the ODE solver also affects the simulation speed and accuracy [62]. For simplicity, this study chooses the Explicit 4^{th}-order Runge-Kutta method [236] to obtain the solution of Eq. (6.1), but other numerical integration methods are also applicable.

For a fixed-time step simulation, the execution speed depends directly on the time-step chosen and indirectly on the parameters of the differential equations; as a result, the execution speed can be improved by locating and modifying the parameters which cause a bottleneck. In particular, varying the value of the resistor r_{ds} in Fig. 6.3 can help to increase the time constant of the circuit and hence alleviate the numerical stiffness issue.

6.4 Simulation and experimental results

6.4.1 Intra-cycle response evaluation

Though the procedure in Section 6.3 can be implemented in any numerical computing program, the MATLAB/SIMULINK environment is chosen in order to reduce the development time and to take advantage of our existing control design. The parameter values of the proposed simplified model, which are shown in Table 6.2, are derived based on the data-sheets of the circuit components in Fig. 6.1 and the previously determined converter model in Section 5.5.3.

Table 6.2: Parameter values of the control-oriented model

Input voltage $v_{in}(t)$	120V - 373V
Dynamic load $i_{dyn}(t)$	0
Magnetizing inductance L_m	791.76μH
Leakage inductance L_{lk}	8.03μH
Winding resistance r_w	0.3522Ω
Voltage transformation ratio n_2, n_3	0.2174, 0.1304
Output capacitor C	900μF
Output capacitor resistance r_c	10mΩ
Diode forward voltage drop V_f	0.45V
Resistance r_{Don}, r_{Qon}, r_{ds}	0.05Ω, 0.4Ω, 50Ω
Zener voltage V_z and resistance r_z	180V, 0.5Ω
MOSFET drain source capacitance C_{ds}	96.697pF

Table 6.3: Computational complexity of the full and control-oriented modelling approaches

Duration of hardware test (real-time)	Execution time for simulations	
	Full model	Simplified model
50 milliseconds	17.238 hours	99.252 seconds

Evaluating the accuracy of the intra-cycle responses of the control-oriented model can be achieved by comparing the simulated results, based on the previously determined model in Section 5.5.3 and the proposed model in Section 6.2. For comparison purposes, two working conditions of the flyback converter, which have been examined in Section 5.5.3, are reconsidered here. In the first condition, the converter is forced to operate in CCM by setting the resistive load $R = 16.97\Omega$, the dynamic load $i_{dyn}(t) = 0$, the input voltage $v_{in} = 150$V, the duty ratio $d = 0.453$, and the switching frequency $f_{pwm} = 100$kHz. The second operating condition is chosen as $R = 16.829\Omega$, $i_{dyn}(t) = 0$, $v_{in} = 150$V, $d = 0.38$, and $f_{pwm} = 50$kHz. Such a condition forces the flyback converter to stay in DCM and also forces the transformer to operate around the saturation region of the ferrite core. Both the CCM and DCM operating points are arbitrarily chosen.

The simulated results obtained from the simplified model and the full model for the two operating points of the flyback converter are plotted in Figs. 6.6 and 6.7, respectively. In addition to the simulated results, the experimental results are also added to Figs. 6.6 and 6.7, for comparison purposes.

In order to evaluate the computational complexity of the control-oriented model, the total execution time for a simulation based on the full model and the proposed model are computed and listed in Table 6.3. The data from Table 6.3 shows that using the control-oriented model allows us

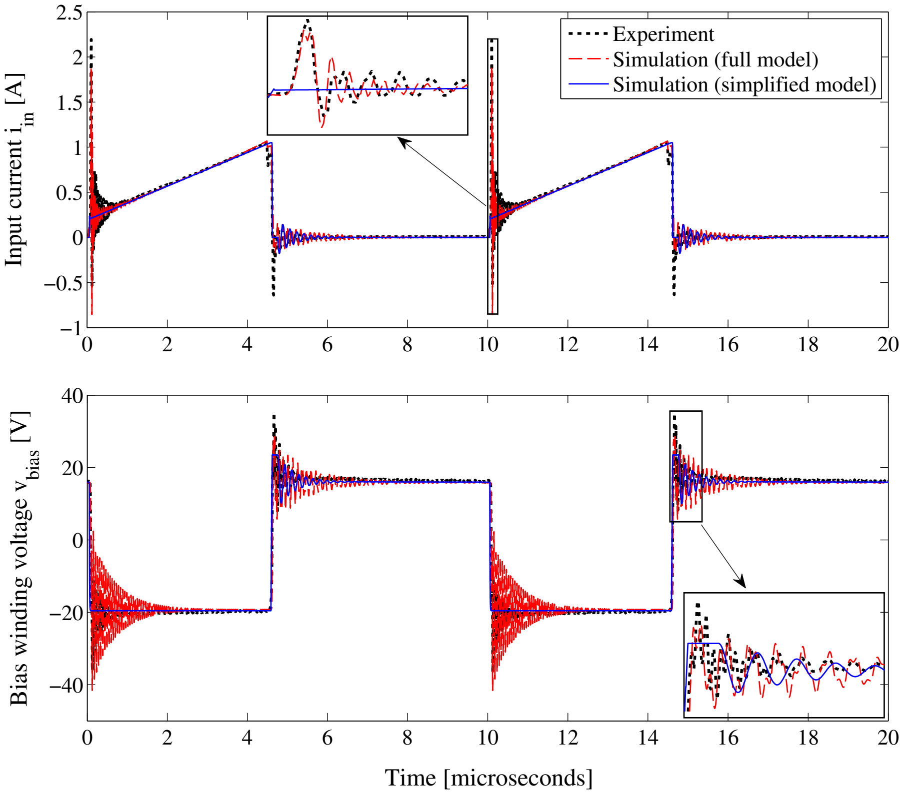

Figure 6.6: Converter waveforms obtained from hardware prototype, full and simplified models. The operating point is chosen as the resistive load $R = 16.97\Omega$, dynamic load $i_{dyn}(t) = 0$, input voltage $v_{in} = 150\text{V}$, duty ratio d $= 0.453$, switching frequency $f_{pwm} = 100\text{kHz}$

to reduce the execution time of the simulation by around 3 orders of magnitude, compared with the full model.

Examining the experimental and simulated waveforms in Figs. 6.6 and 6.7, and the data in Table 6.3, reveals that the full model is capable of accurately reproducing all the non-linear and high-frequency transient responses at the expense of a huge computation time. In contrast to the full model, the control-oriented model is unable to predict all non-linearity or high-frequency dynamics, but requires a significantly shorter time to finish the same job and, most importantly, can retain the fidelity of important information, e.g. ringing in $v_{bias}(t)$, required by control design needs.

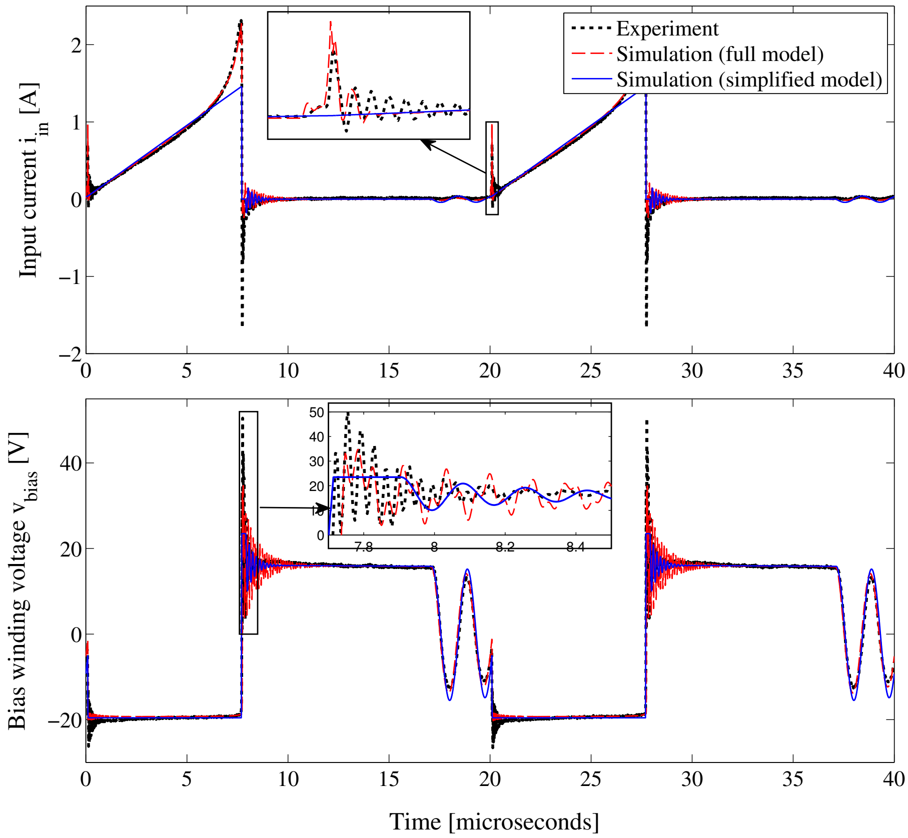

Figure 6.7: Converter waveforms obtained from hardware prototype, full and simplified models. The operating point is chosen as the resistive load $R = 16.829\Omega$, dynamic load $i_{dyn}(t) = 0$, input voltage $v_{in} = 150\text{V}$, duty ratio d = 0.38, switching frequency $f_{pwm} = 50\text{kHz}$

6.4.2 Inter-cycle response evaluation

Since the purpose of the proposed model is control design, the accuracy of the inter-cycle responses is as important as that of the intra-cycle responses. Two more tests are performed to verify the open-loop large-signal behaviour of the control-oriented model. In the first assessment, a voltage step $v_{in}(t)$, from 0 to 150V, is applied to the input of the converter while the output load and PWM signal are unchanged and configured as $R = 6.9\Omega$, with a duty ratio $d = 0.2$ and a switching frequency $f_{pwm} = 80\text{kHz}$. The simulation and experimental open-loop transient responses are plotted in Fig. 6.8. For the second test, a 6.9Ω to 53.8Ω step load is effected at the output of the flyback converter, while setting the input voltage $V_{in} = 150\text{V}$ and the PWM control signal with $d = 0.1$ and $f_{pwm} = 80\text{kHz}$. Fig. 6.9 illustrates the large-signal transient responses of the simulation and experimental output voltages from the second test. The results from both Figs. 6.8 and 6.9 confirm that the control-oriented model can generate an accurate inter-cycle transient response and is valid for large-signal verification.

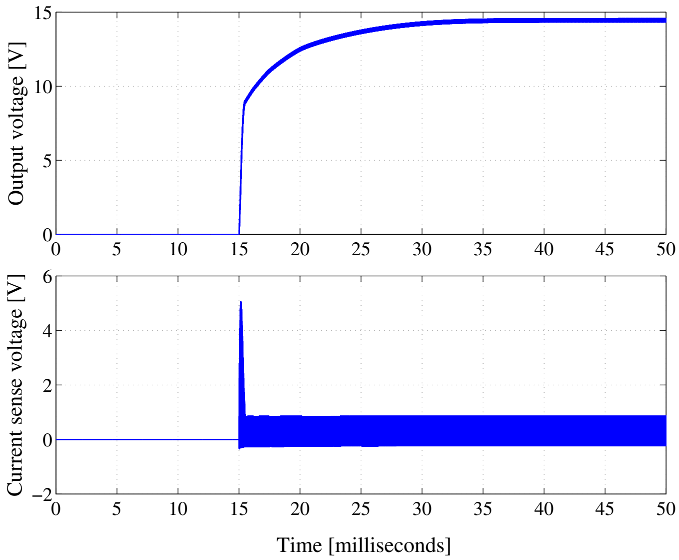

(a) Simplified model simulation results: v_{out} = upper curve, v_{cs} = lower curve

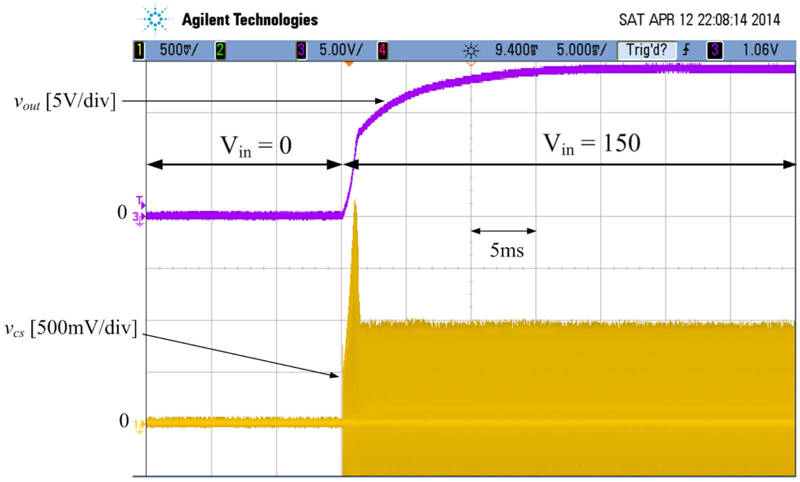

(b) Experimental results: v_{out} = Ch3 [5V/div], v_{cs} = Ch1 [500mV/div]

Figure 6.8: Simulation and experimental output voltages and inductor currents (through current sense voltages) of the open-loop converter in response to a 0 to 150V input voltage step, $R = 6.9\Omega$, $d = 0.2$ and $f_{pwm} = 80\text{kHz}$

6.5 Conclusion

In this chapter, a systematic approach was proposed which uses the knowledge of the previously determined full model in Section 5.5.3 as a starting point and simplifies this model to produce a control-oriented model. As pointed out in Section 6.2, the model reduction process allows us not only to preserve the bulk of the model fidelity, which is critical for an effective control design phase, but also to significantly reduce the computational complexity. In addition to the model simplification, the equation-solving sequencing technique, which is used to break the algebraic loops and improve the simulation speed, is also discussed.

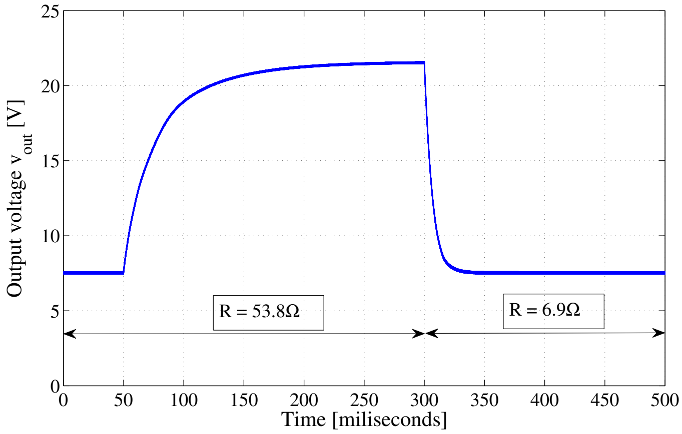

(a) Simplified model simulation results: v_{out}

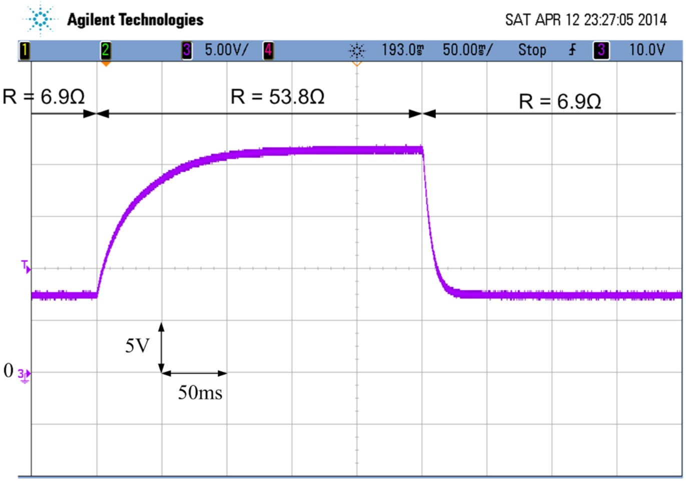

(b) Experimental results: v_{out} = Ch3 [5V/div].

Figure 6.9: Simulation and experimental output voltages of the open-loop converter in response to a 6.9Ω to 53.8Ω step load, $V_{in} = 150\text{V}$, $d = 0.1$ and $f_{pwm} = 80\text{kHz}$

The proposed control-oriented model, in addition to providing a basis for control design itself, can serve as an effective platform for the evaluation of various closed-loop flyback control strategies. The results, from both simulation and experiment, confirm that the control-oriented model can achieve adequate intra-cycle dynamic fidelity, accurate inter-cycle responses and, most importantly, offers significant computational complexity reduction compared to the full modelling approach.

Chapter 7

Unified CCM and DCM magnetic sensing technique

7.1 Introduction

For commercial AC-to-DC power supplies which operate off the line voltage, galvanic isolation between input and output is generally required. The main aim of such isolation is to prevent any shock hazard which operators may encounter when using the equipment. In general, a power transformer is inserted between the input and output sections of power supplies in order to achieve galvanic isolation. Since the switches, which need to be controlled, are on the input side of the transformer, while the signals, which need to be regulated, are on the output side of the transformer, a crossing of the isolation boundary must be required in order to send information back for control purposes. Although isolating the feedback path involves only control information, rather than power, such a task must still meet the same isolation requirements for the power path, as specified in many regulations, e.g. IEC950 in Europe and UL1950 in the U.S.

In principle, approaches to isolating control of power converters are different in two main aspects including: (i) the positions where isolation is inserted in the feedback path and (ii) the methods which are employed to implement galvanic isolation, e.g. transformers. For the locations of isolation, 4 options are commonly considered, which are: (a) isolating the measurement of the output voltage, (b) isolating the error signal or the amplified error signal, (c) isolating the digital signal if digital control circuits are used, and (d) isolating the switch-drive signal before going to semiconductor devices. For galvanic isolation methods, transformers and optical isolators (also termed opto-couplers) are mainly employed for power converters. Combining the possibilities for isolation locations and isolation methods allows the synthesis of different solutions for isolating the control feedback path. A detailed description of such solutions goes beyond the scope of this chapter and, consequently, is not included. However, any reader who is interested in the topic is suggested to refer back to the comprehensive review of isolating control in [237, 238] and the references therein.

In the field of single-stage flyback converters, isolating the analogue error signal with an optical isolator is conventionally applied to achieve galvanic isolation in the feedback path. Although the opto-coupler based control, as illustrated in Fig. 7.1, can provide good voltage tracking ability and load regulation, its performance depends heavily on the current transfer ratio (CTR) of the

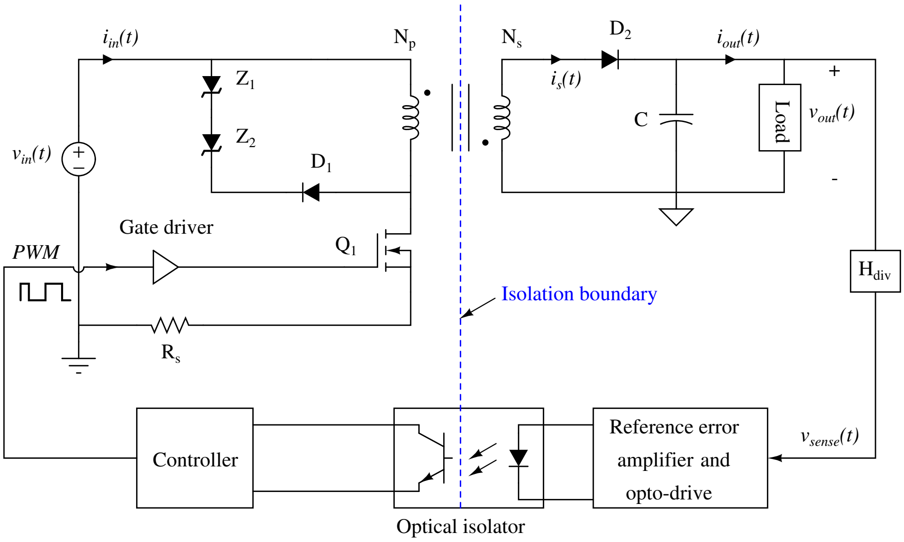

Figure 7.1: Conventionally optical isolator based control for a flyback converter.

opto-coupler, which is a non-linear function of the ambient temperature and time [237]. Such non-linearities present considerable difficulties in compensating for thermal and age degradation. In addition to the non-linear properties, the presence of the opto-coupler introduces a low frequency pole to the control loop. The value of such a pole varies between 1kHz to 40kHz depending on the operating condition [237]. Such a pole imposes an upper limit on the bandwidth of the closed-loop system and also complicates the design of the controller. Furthermore, the use of the optical isolator increases the manufacturing costs of the system and requires extra PCB board space for the opto-coupler itself, as well as its driving circuitry. The drawbacks on the performance, costs and power density make the opto-coupler based approach less attractive to modern flyback converter applications. Therefore, a different isolating solution, which is capable of providing better system performance with lower production costs, is of great interest.

Recently, an isolating control methodology, which uses the flyback transformer as an isolation means for transferring both power and control information, is introduced in [5]. Such a method exploits an interesting feature of the flyback converter, that the output voltage is transmitted back to the primary winding and the bias winding when the power switch, e.g. MOSFET, is off and the secondary-side diode is on. By measuring either the primary winding voltage or the bias winding voltage during such an interval (switch off and secondary diode on) of each switching cycle, the output voltage can be fully tracked. The application of such a principle, typically termed magnetic sensing (MS), can help to eliminate opto-couplers and their associating circuits, reduce the system complexity, and provide a cheaper design with a higher efficiency. Since the feedback signal is obtained through the primary winding or the bias winding, which is purposely designed to be electrically isolated from the secondary side, the concern about the isolation for the feedback path can be relieved in the case of MS approaches.

Magnetic sensing control can be classified as (i) primary-side sensing (PSS) control [5, 21] and (ii) bias-side sensing (BSS) control [8, 20, 22–27] depending on which winding voltage is used to

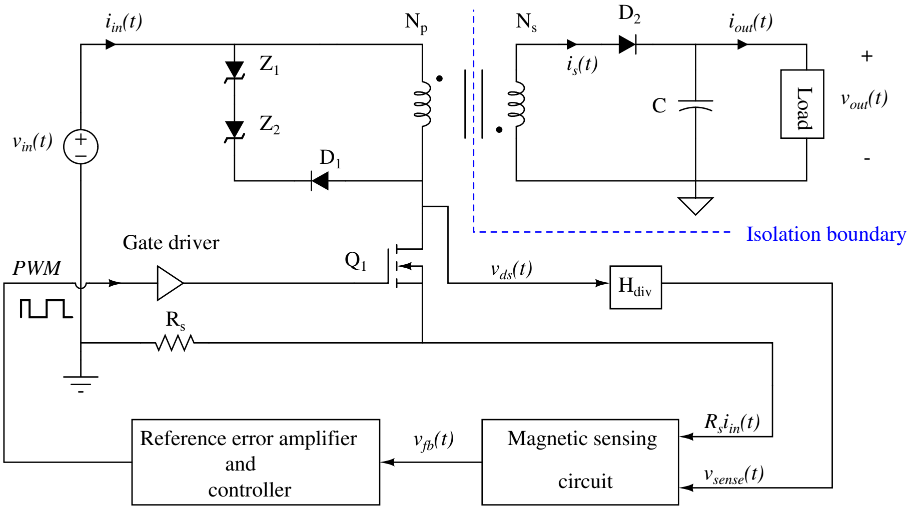

Figure 7.2: Primary-side sensing control for a flyback converter. The information about the output voltage is obtained from the primary winding voltage.

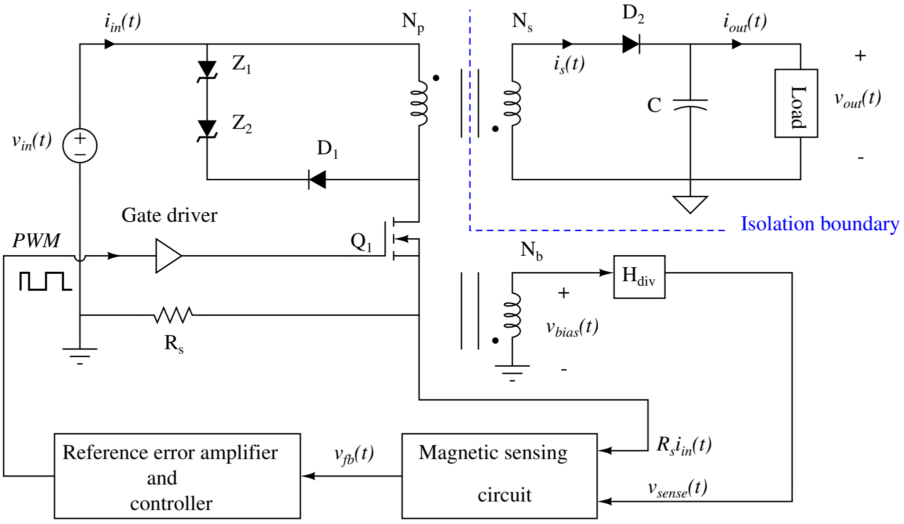

Figure 7.3: Bias-side sensing control for a flyback converter. The information about the output voltage is obtained from the bias winding voltage.

obtain the output voltage information. The PSS technique, as illustrated in Fig. 7.2, estimates the output voltage based on the MOSFET drain-source voltage $v_{ds}(t)$ and possibly the input current $i_{in}(t)$. Since all measurements are on the high voltage side, the implementation of PSS frequently requires a high voltage sensor. In order to provide an accurate estimation of the output voltage, the magnetic sensing circuit needs to consider the impairments occurring in the winding voltages due to the presence of the leakage inductance and parasitic resistance. Such an issue is discussed in detail in Section 7.2. The performance of primary-side sensing (PSS) control depends not only on the controller but also on the accuracy of the magnetic sensing circuit. For the BSS approach, as depicted in Fig. 7.3, the role of the magnetic sensing circuit is similar to that of the PSS case except that no high voltage sensor is required. Though both forms of MS-based control are different in the feedback signal, the same framework for designing the MS circuit and controller can be equally applied for each case. Hence, without a loss of generality, only the BSS method is considered in this chapter.

The remainder of this chapter is organized as follows. A detailed review of different magnetic sensing techniques is presented in Section 7.2. Based on the review, a unified MS method that can run seamlessly in both CCM and DCM is adopted in in Section 7.3. The accuracy and stability of the proposed sensing solution is analysed through simulation in Section 7.4. The conclusion is covered in Section 7.5.

7.2 Review of magnetic sensing techniques

The control-oriented model of an open-loop flyback converter, developed in Chapter 6, is used as a means to facilitate the study of MS methods in this section. For convenience, the converter model in Fig. 6.3 is adapted, which results in the modified model as shown in Fig. 7.4, where $v_{in}(t)$ and $v_{out}(t)$ are the converter input and output voltages, respectively. The flyback transformer is now described by a simple model consisting of the magnetizing inductance L_m, the leakage inductance L_{lk}, the winding resistance r_w and and an ideal transformer with the voltage transform ratios n_2 and n_3. Understanding the voltage and current waveforms corresponding to different operating points of the converter is useful for investigating MS techniques. Since the signal waveforms are quite similar when the converter does not change its operating mode, i.e. CCM or DCM, only two typical working points, one in CCM and another in DCM, are simulated. Figure 7.5 plots the simulated bias voltage $v_{bias}(t)$ and transformer currents $i_{in}(t)$, $i_m(t)$ and $i_s(t)$ over one switching cycle. For comparison, the secondary current $i_s(t)$ is referred to the primary side of the transformer.

As can be seen in Fig. 7.5, the bias winding voltage $v_{bias}(t)$ contains information about the output voltage during the Q-off and D-on subinterval, as well as information about the input voltage during the Q-on and D-off subinterval. Therefore, $v_{bias}(t)$ needs to be processed by some means in order to get useful input voltage and output voltage data out of it. One commonly used approach is to sample and process $v_{bias}(t)$ during the interval when Q is off and D is on, e.g. (t_2, t_3) in Fig. 7.5. If the sampling instant is chosen at $t = t_{s2}$, where $t_2 < t_{s2} < t_3$, the relation between the bias winding voltage $v_{bias}(t)$ and the output voltage $v_{out}(t)$ at the chosen sampling point is governed by

$$v_{bias}(t_{s2}) = \frac{n_3}{n_2}\big[v_{out}(t_{s2}) + v_{para}(t_{s2})\big], \tag{7.1}$$

where

$$v_{para}(t_{s2}) = r_{Don} i_s(t_{s2}) + V_f \tag{7.2}$$

denotes the cable voltage drop due to the forward-biased voltage V_f and the diode resistance r_{Don}. Equation (7.1) shows that the information of the output voltage contained inside the sampled bias

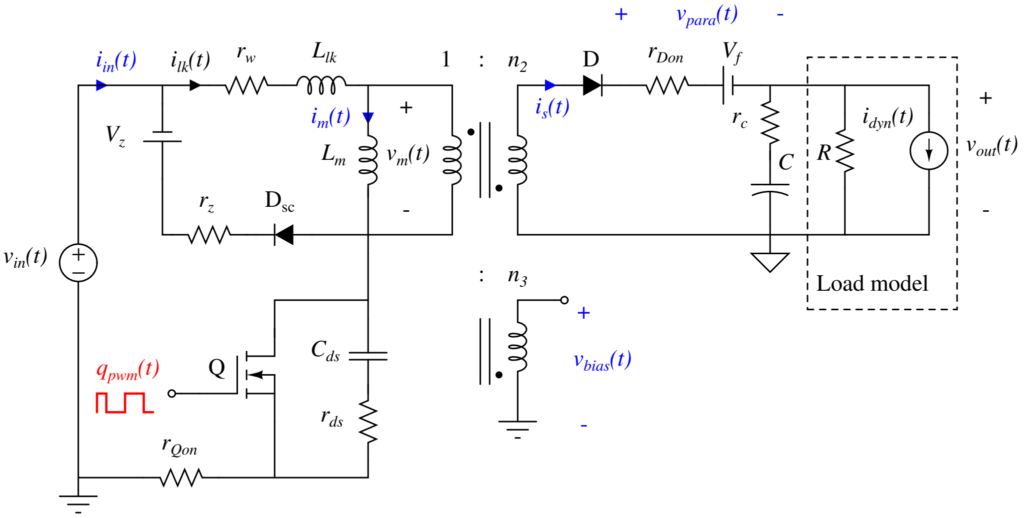

Figure 7.4: Flyback converter model for magnetic sensing analysis.

winding voltage is affected by the cable voltage drop. Fortunately, such an effect can be eliminated, if $v_{para}(t_{s2})$ is known. As can be seen in Eq. (7.2), the value of $v_{para}(t_{s2})$ depends only on the secondary current $i_s(t)$ and the sampling instant t_{s2} because the model parameters V_f and r_{Don} are constant and known. Unfortunately, $i_s(t)$ can not be measured by any means. The only options left are to find the sampling instant t_{s2} such that $i_s(t_{s2})$ is constant irrespective of variations in the waveforms of the secondary current, or to estimate $i_s(t_{s2})$ from cycle to cycle using dedicated analogue/digital circuitry [21].

The former option has been widely considered in recent investigations [20, 22–26], in which $v_{bias}(t)$ is proposed to be sampled at a time instant when the magnetic circuit is reset, or the current $i_m(t)$ is almost drained out of the magnetising inductor. Such an instant is highlighted by t_3 in Fig. 7.5(b). The point on the bias winding voltage $v_{bias}(t)$ at $t = t_3$ is typically called the knee point. The purpose of the knee-point sampling scheme is twofold: (i) to avoid the ringing occurring in $v_{bias}(t)$ after the MOSFET turn-on instant, i.e. t_2 in Fig. 7.5, and (ii) to minimize the effect of the cable voltage drop on the secondary side.

The knee point can be located by inspecting the bias winding voltage [22–25], or the magnetic flux [20, 26]. In the first philosophy, the bias winding voltage $v_{bias}(t)$ is processed directly by a state machine [22], or multiple samplers and a digital signal processor [23], or an envelop detector circuit [24], in order to determine the instant t_3. In the second philosophy, the magnetizing current $i_m(t)$, or the magnetic flux of the flyback transformer, is first computed from $v_{bias}(t)$ by a resetting integrator. The magnetizing current is then compared with zero to determine the knee point position [20, 26]. The second philosophy can be simply explained through the illustration in Fig. 7.5(b), where the knee point is coincided with the zero-crossing point of $i_m(t)$. Although sampling $v_{bias}(t)$ at the knee point can be advantageous in terms of output voltage regulation, a live determination of such a point in each cycle is not an easy task and most of the time requires high computational digital processors or dedicated analogue circuits. In addition, the definition of the knee point is not very useful in CCM because the inductor current $i_m(t)$ never goes to zero in

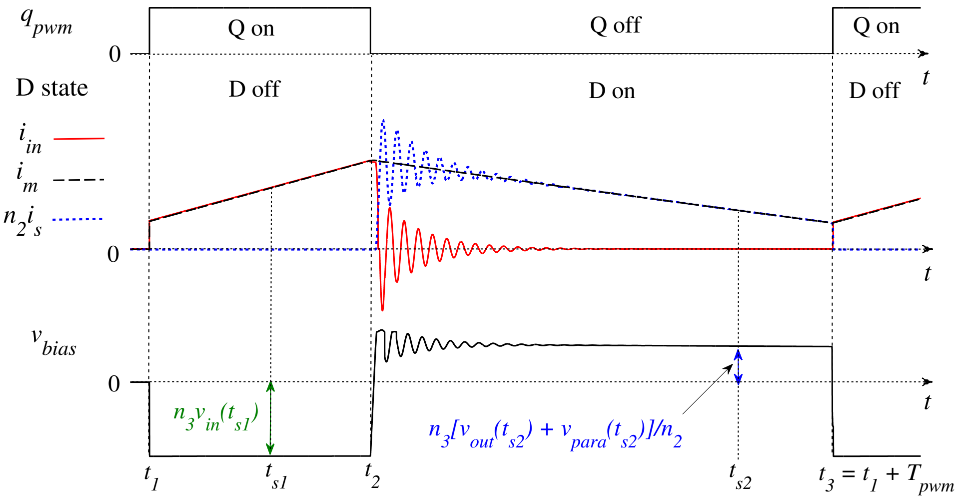

(a) Continuous conduction model

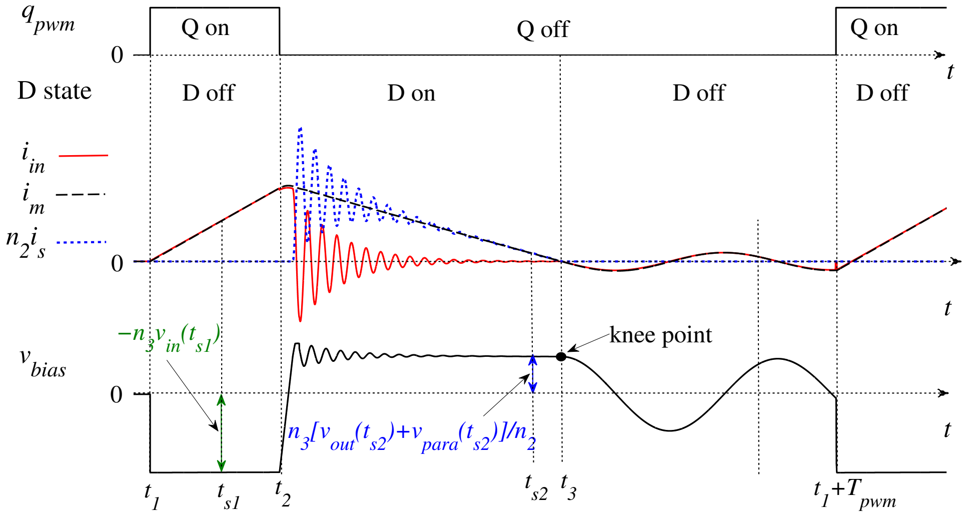

(b) Discontinuous conduction mode

Figure 7.5: Simulated waveform of the bias voltage and transformer currents at two different working conditions of the flyback converter: (a) continuous conduction mode, and (b) discontinuous conduction mode. T_{pwm} represents the switching period. The switch is on when $q_{pwm} = 1$ and is off when $q_{pwm} = 0$

such a mode. As a result, all knee-point detection techniques in both the philosophies are valid for DCM only.

Some authors [8, 21] claimed that their methods can operate in both CCM and DCM; however, they have not recommended any solution for compensating the cable voltage drop $v_{para}(t_{s2})$ in CCM. Therefore it is desirable to have a simple and reliable sensing strategy that can work accurately and smoothly in both CCM and DCM. Such is the objective of this chapter.

7.3 Unified CCM and DCM magnetic sensing solution

A unified MS technique is studied in this section, with the aim of providing an accurate sensing solution for both CCM and DCM flyback converters, but requiring only minimum computation. The technique does not try to sample at the knee point but rather at a point at which the secondary current $i_s(t)$ can be estimated by some means. The theory behind the unified sensing solution is described in Section 7.3.1, while the implementation of such a theory, using a simple analogue circuit and a low-cost digital microcontroller, is discussed in Sections 7.3.2 and 7.3.3, respectively.

7.3.1 Principle of operation

As reviewed in Section 7.2, most MS techniques either find the sampling instant t_{s2} such that $i_s(t_{s2})$ is constant, or firstly sample the bias winding voltage according to a pre-defined scheme and then try to compensate for the cable voltage drop. In this section, a different approach is proposed. In particular, the sampling instant t_{s2} for the bias winding voltage $v_{bias}(t)$ is chosen not at the knee point but at the point where the inductor current $i_s(t)$ is known. The procedure for determining t_{s2} and estimating the cable voltage drop $v_{para}(t)$ is summarized as follows:

Step 1: Sample the input current $i_{in}(t)$ and the bias winding voltage $v_{bias}(t)$ at $t = t_{s1}$, where t_{s1} should be defined in advance and stays well within the Q-on and D-off interval, i.e. $t_1 < t_{s1} < t_2$

Step 2: Search within the Q-off and D-on interval for the sampling instant t_{s2} satisfying the condition

$$i_s(t_{s2}) = \frac{1}{n_2} i_{in}(t_{s1}). \tag{7.3}$$

Step 3: Sample the bias winding voltage $v_{bias}(t)$ at $t = t_{s2}$.

Step 4 Calculate the voltage drop $v_{para}(t_{s2})$ based on the sampled input current $i_{in}(t_{s1})$ via

$$v_{para}(t_{s2}) = \frac{1}{n_2} r_{Don} i_{in}(t_{s1}) + V_f \tag{7.4}$$

Step 5: Compute the feedback voltage $v_{fb}(t_{s2})$, which is a scaled version of the estimated output voltage $\hat{v}_{out}(t)$, via

$$\begin{aligned} v_{fb}(t_{s2}) = \frac{n_3}{n_2}\hat{v}_{out}(t_{s2}) &= v_{bias}(t_{s2}) - \frac{n_3}{n_2} v_{para}(t_{s2}) \\ &= v_{bias}(t_{s2}) - \frac{n_3}{n_2^2} r_{Don} i_{in}(t_{s1}) - \frac{n_3}{n_2} V_f \end{aligned} \tag{7.5}$$

An application of the proposed MS procedure to a CCM flyback converter is demonstrated in Fig. 7.6. Most steps of the procedure above are relatively trivial and can be easily implemented except for Step 2, where the secondary current $i_s(t)$ cannot be measured by any means and, as a result, is not available for verifying Eq. (7.3). The determination of t_{s2} in Step 2 needs further

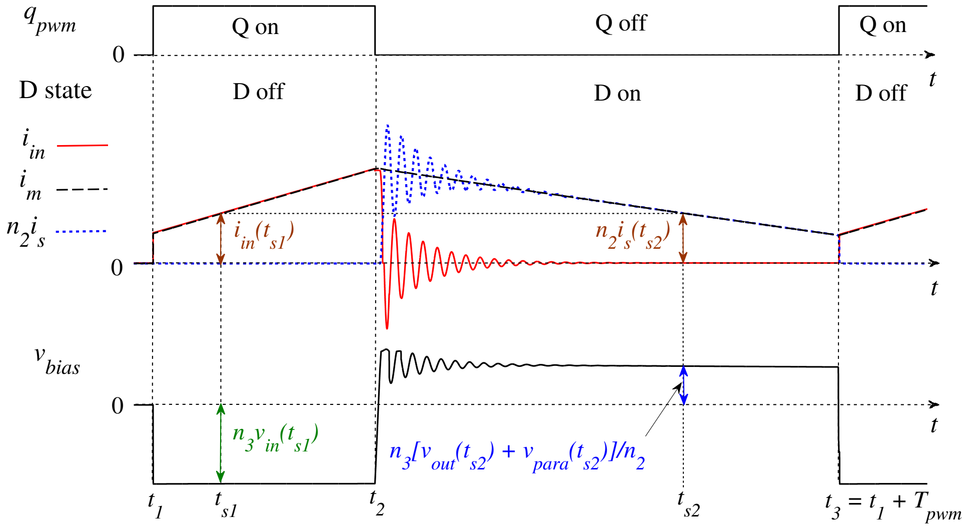

Figure 7.6: Operating principle of the unified CCM and DCM magnetic sensing technique.

elaboration. In order to clarify the determination of t_{s2}, the following observations, based on the waveforms of the transformer currents in Fig. 7.5, are made:

- The input current $i_{in}(t)$ and the magnetising current $i_m(t)$ are equal when Q is on and D is off. This statement can be mathematically expressed by

$$i_m(t) = i_{in}(t) \quad t_1 < t < t_2. \tag{7.6}$$

Since Eq. (7.6) holds for any instant within the interval (t_1, t_2), it also holds for $t = t_{s1}$, which means

$$i_m(t_{s1}) = i_{in}(t_{s1}). \tag{7.7}$$

- The referred secondary current $n_2 i_s(t)$, during the interval (t_2, t_3), can be considered as a sum of the magnetizing current $i_m(t)$ and a high-frequency oscillation component which typically dies out after a certain amount of time. If Δ_{osc} is assumed to be the duration from the instant t_2 to the point at which the ringing component in $i_s(t)$ becomes negligible, the value of the secondary current from $t_2 + \Delta_{osc}$ to t_3 can be well approximated by

$$i_s(t) \approx \frac{1}{n_2} i_m(t) \quad t_2 + \Delta_{osc} < t < t_3. \tag{7.8}$$

If t_{s2} satisfies $t_2 + \Delta_{osc} < t_{s2} < t_3$, the value of the secondary current at $t = t_{s2}$ can be computed via

$$i_s(t_{s2}) \approx \frac{1}{n_2} i_m(t_{s2}). \tag{7.9}$$

Notice that because of the lack of damping resistance in the converter model, the ringing component in the simulated waveform of $i_s(t)$, as shown in Fig. 7.5, decays slowly and lasts many cycles after Q turns off. In practice, such a ringing collapses much quicker than that obtained from simulation, and Δ_{osc} in Eq. (7.8) can be neglected.

A close examination of Eqs. (7.7) and (7.9) reveals that if t_{s2} is selected to be

$$i_m(t_{s2}) = i_m(t_{s1}), \tag{7.10}$$

the constraint in Eq. (7.3) is always satisfied. The problem now reduces to finding a t_{s2} which meets the condition given by Eq. (7.10).

7.3.2 Analogue circuit based realization

In this section, the implementation of the unified MS approach proposed in Section 7.3.1 is considered. The major focus is on designing an analogue circuit which can use Eq. (7.10) as a basis for the determination of t_{s2}.

Equation (7.10) reveals that if the magnetising current $i_m(t)$ and the sampling instant t_{s1} are known, t_{s2} can be easily obtained by a comparator. Unfortunately, $i_m(t)$ is not a physical quantity and cannot be measured directly. In theory, $i_m(t)$ can be formed from the bias winding voltage $v_{bias}(t)$ via

$$\begin{aligned} i_m(t) &= -\frac{1}{n_3 L_m}\int_{t_0}^{t} v_{bias}(\phi)\,d\phi + i_m(t_0) \\ &= -\frac{1}{\tau_m}\int_{t_0}^{t} v_{bias}(\phi)\,d\phi + i_m(t_0),\ \ t \geq t_0 \end{aligned} \tag{7.11}$$

where $\tau_m = n_3 L_m$ is the integrator constant, and $i_m(t_0)$ denotes the initial condition of $i_m(t)$. An accurate calculation of $i_m(t)$ in Eq. (7.11) requires an ideal integrator and a known value of τ_m. However, in practice, analogue integrators typically suffer from output voltage drift and saturation which can distort the calculation in Eq. (7.11). Therefore, trying to accurately reproduce $i_m(t)$ is not good practice [239].

Since Eq. (7.11) is valid for any time $t \geq t_0$, it can be applied to relate $i_m(t_{s1})$ and $i_m(t_{s2})$. More precisely, if t_0 and t in Eq. (7.11) are set to $t_0 = t_{s1}$ and $t = t_{s2}$, Eq. (7.11) becomes

$$i_m(t_{s2}) = -\frac{1}{\tau_m}\int_{t_{s1}}^{t_{s2}} v_{bias}(\phi)\,d\phi + i_m(t_{s1}). \tag{7.12}$$

If the condition in Eq. (7.11) is fulfilled, Eq. (7.12) can be simplified to

$$\frac{1}{\tau_m}\int_{t_{s1}}^{t_{s2}} v_{bias}(\phi)\,d\phi = 0. \tag{7.13}$$

Equation (7.13) provides a simple and effective way to locate t_{s2} using only information about t_{s1} and $v_{bias}(t)$ by integrating $v_{bias}(t)$ over time. If the output of an integrator is set to zero at $t = t_{s1}$, the sampling instant t_{s2} is the point at which the integrator output falls back to zero again. Since τ_m in Eq. (7.13) has the same role as a scaling factor and does not affect the validity of Eq. (7.13), the choice of the integrator constant depends on the implementation aspect only.

Figure 7.7 shows an analogue circuit-based realisation of the proposed MS approach which is designed using only two operational amplifiers (Op-amps), one comparator, three sample and hold (SH) devices, and some resistors and capacitors. The analogue MS circuit consists of two parts. In the first part, t_{s2} is determined based on $v_{bias}(t)$ and t_{s1}. Equation (7.13) is used as a basis for the implementation of such a function. The first part consists of an analogue integrator with a reset function, a comparator, and an SR latch. The role of the resetting integrator is to perform integration of $v_{bias}(t)$ with respect to time, and to guarantee that the integrator output $v_{int}(t)$ is zero at $t = t_{s1}$ while the comparator is for detecting the zero-crossing point of $v_{int}(t)$. The SR latch is inserted after the comparator to resolve a situation when $v_{int}(t)$ has multiple zero-crossing points. The integrator constant can be adjusted through selection of the values of R_{i1} and C_{i1} in the circuit of Fig. 7.7. The value of the integrator constant should be carefully designed to avoid the saturation of Op-amp 1. The value of R_{i2} should be small enough to ensure that the integrator is fully reset at $t = t_{s1}$.

The second part of the design in Fig. 7.7 has the following functions consisting of sampling $i_{in}(t)$ and $v_{bias}(t)$ at $t = t_{s1}$, sampling $v_{bias}(t)$ at $t = t_{s2}$ and calculating the feedback voltage $v_{fb}(t)$ according to Eq. (7.5). These functions can be implemented by SH devices and an Op-amp voltage subtractor. The values of the resistors R_{a1}, R_{a2}, R_{a3} and R_{a4} of the subtractor circuit need to satisfy the following relations

$$R_{a2} = \frac{n_2^2}{n_3 r_{Don}} R_{a1}, \quad R_{a3} = \frac{n_2}{n_3} R_{a1}, \quad R_{a4} = \frac{n_2^2}{n_2 n_3 + n_3 r_{Don}} R_{a1}. \tag{7.14}$$

The operation of the analogue MS circuit in Fig. 7.7 is best explained through its internal waveforms as exemplified in Fig. 7.8. The integration is periodically started at $t = t_{s1}$, which is a fixed delay after the MOSFET turn-on moment t_1, and stopped at the end of the switching cycle $t_1 + T_{pwm}$. The integrator reset action happens during the interval (t_1, t_{s1}) of each switching cycle. When the integrator output $v_{out}(t)$ crosses zero, the level of the zero crossing detection trigger S_{zcd} is raised from low to high. Whenever $q_{pwm}(t)$ is low and the SR latch sees a rising edge in S_{zcd}, the output of the SR latch S_{ts2} is immediately latched to high. The rising-edge in S_{ts2} will command SH2 to sample $v_{bias}(t)$. The role of the SR latch is to make sure that a maximum of one rising-edge can occur for each switching cycle. Once the values of $i_{in}(t_{s1})$ and $v_{bias}(t_{s2})$ are known, the feedback voltage $v_{fb}(t)$ is instantly updated by the subtractor circuit. Though only signal waveforms for DCM has been illustrated in Fig. 7.8, the performance of the MS circuit in CCM can be easily verified.

The starting time t_{s1} of the integrator should be properly chosen to guarantee that the integrator is entirely reset, and that the input current $i_{in}(t)$ is sampled after the fluctuations occurring in $i_{in}(t)$ due to switching actions have died out.

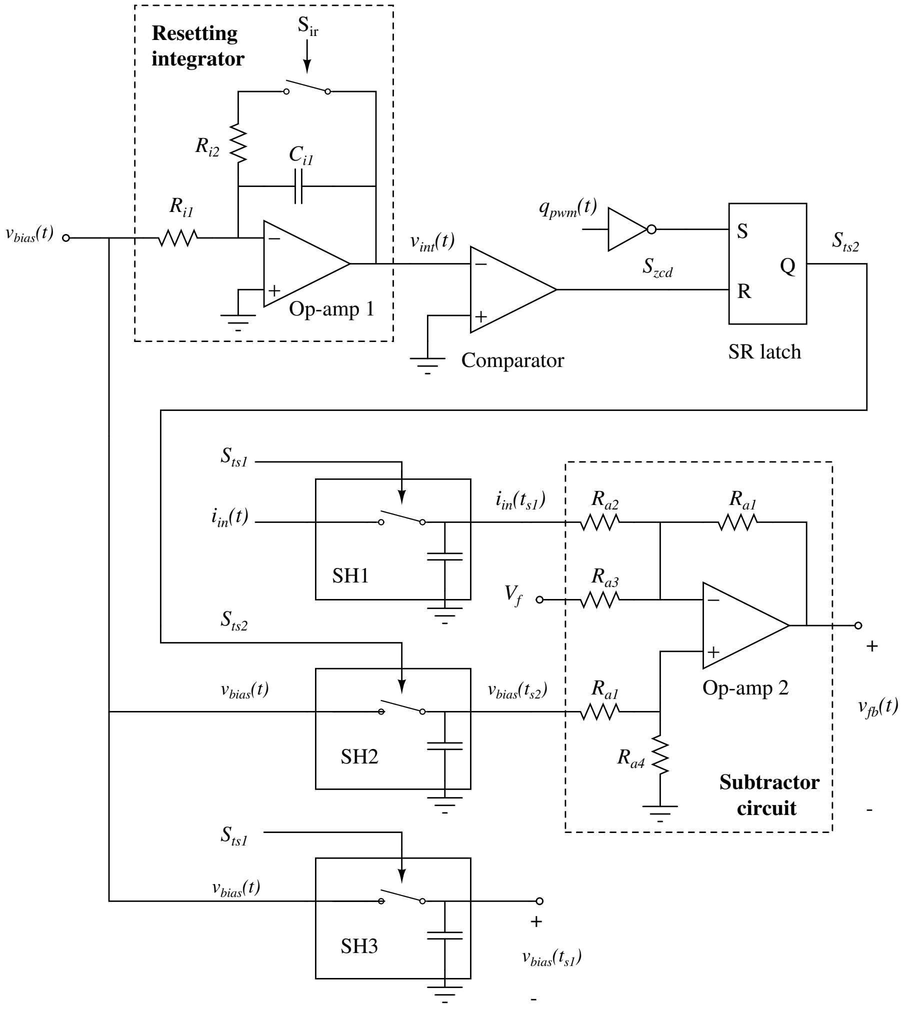

Figure 7.7: Realisation of the unified CCM and DCM magnetic sensing method using analogue circuit components.

7.3.3 Microcontroller based realization

In principle, the proposed MS technique in Section 7.3.1 can be implemented using microcontrollers by transforming the analogue circuit in Fig. 7.7 into an equivalent digital design. The transformation is quite simple and straightforward. For example, the analogue integrator in Fig. 7.7 can be replaced by its digital counterpart, while the subtractor circuit can be easily implemented by the digital functions of a microcontroller. In theory, the digital implementation, based on the transformation of the analogue design, can perform as well as the original analogue counterpart. However, in practice, the performance of such digital implementation largely depends on the accuracy of the digital integrator, which is influenced by the specifications of the microcontroller employed, particularly the sampling frequency, the resolution of each sample and the computation speed. For low-cost microcontrollers with low ADC specifications, the digital integrator is not adequate for integrating $v_{bias}(t)$ which contains many high frequency components. Such an issue

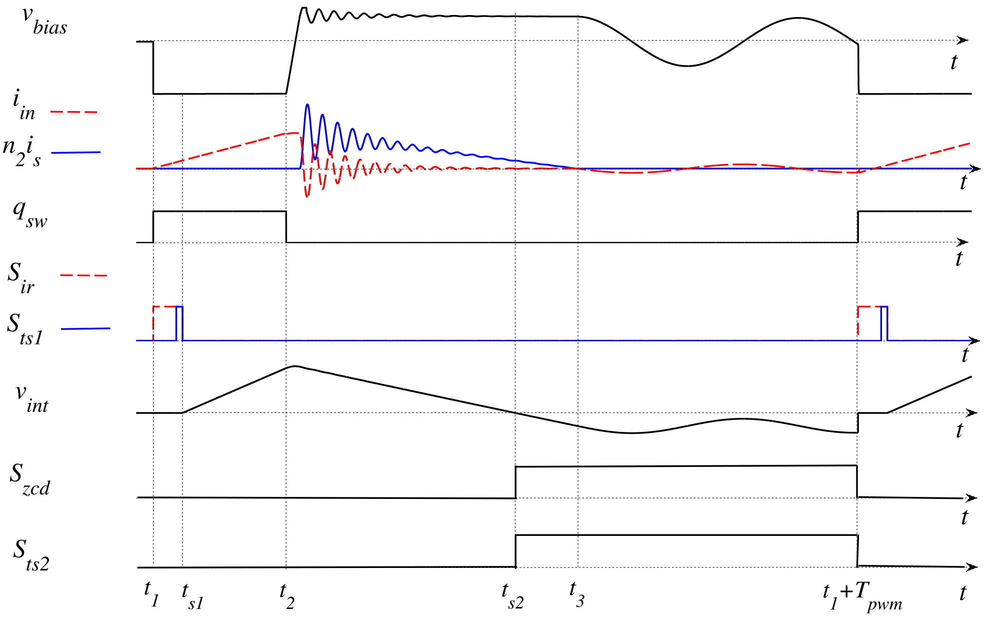

Figure 7.8: Internal signal waveforms of the unified analogue MS circuit in Fig. 7.7.

may lead to an incorrect sampling instant t_{s2}, compromising the sensing system. Therefore, a different method for implementing the proposed sensing solution needs to be considered.

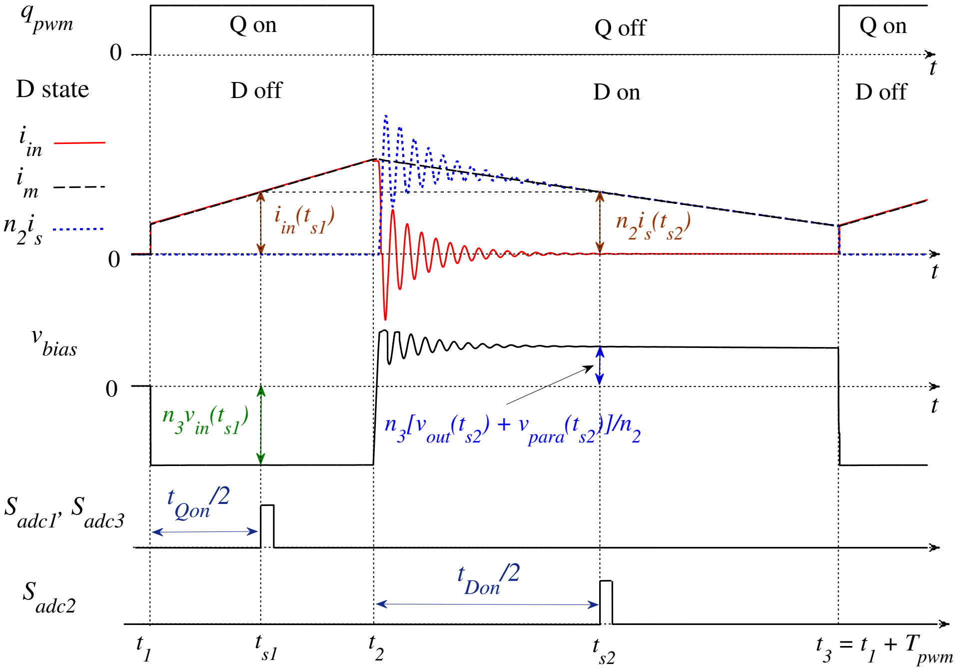

Figure 7.9: Timing diagram of the proposed digital MS technique for flyback converters.

The approach in Section 7.3.2 relies on an analogue integrator to obtain t_{s2} that satisfies

Eq. (7.10). However, such an integrator-based approach does not lend itself to microcontroller-based implementation. Fortunately, t_{s2} can still be determined without the need of an integrator. A close examination of the waveform of $i_m(t)$, as plotted in Fig. 7.5, reveals that the magnetising current $i_m(t)$ can be well approximated by a linear function of time during the intervals (t_1, t_2) and (t_2, t_3). If the sampling instants t_{s1} and t_{s2} are chosen to be

$$t_{s1} = \frac{t_1 + t_2}{2}, \tag{7.15}$$

$$t_{s2} = \frac{t_3 + t_2}{2}, \tag{7.16}$$

the values of $i_m(t_{s1})$ and $i_m(t_{s2})$ can be expressed as a function of $i_m(t_1)$, $i_m(t_2)$ and $i_m(t_3)$ via

$$i_m(t_{s1}) = \frac{i_m(t_1) + i_m(t_2)}{2}, \tag{7.17}$$

$$i_m(t_{s2}) = \frac{i_m(t_3) + i_m(t_2)}{2}. \tag{7.18}$$

When the flyback converter operates at steady state, the condition $i_m(t_1) = i_m(t_3)$ still holds. Combining such a condition with Eqs. (7.17) and (7.18) yields

$$i_m(t_{s2}) = i_m(t_{s1}). \tag{7.19}$$

Equations from (7.15) to (7.19) indicate that, by setting t_{s1} and t_{s2} to the mid-points of the Q-on duration t_{Qon} and D-on time t_{Don}, respectively, the constraint in Eq. (7.10) will be automatically satisfied at steady state. Such an observation suggests a simple way to implement the proposed MS technique with a microcontroller.

The proposed solution, whose timing diagram in CCM is sketched in Fig. 7.9, utilizes 3 analogue-to-digital converters (ADCs) to sample the input current at t_{s1}, and the bias winding voltage at t_{s1} and t_{s2}, whose values are set according to Eqs. (7.15) and (7.16). The results from ADC1 and ADC3 is for the input current and input voltage estimation, respectively, while the output from ADC2 is utilized to calculate the feedback signal according to Eq. (7.5).

One difficulty arising from this approach is how to identify the mid-points of t_{Qon} and t_{Don} whose information is not available in advance. Fortunately, the values of t_{Qon} and t_{Don} in the active cycle can be measured and employed to determine the sampling points in the next cycle. Voltage drop compensation may be not accurate during the transient state due to the cycle-by-cycle variation of t_{Qon} and t_{Don}; however, such an effect will disappear at steady state. Although only the timing diagram for a CCM flyback converter is provided, the validity of the method for a DCM flyback converter can be easily confirmed.

7.4 Accuracy and stability analysis

The best test for the proposed magnetic sensing method in Section 7.3 is to examine its performance under both the working modes, CCM and DCM, of a flyback converter. A wide variation load is usually a good choice to excite both operating conditions. Since the converter behaves differently, in terms of its dynamic response, in CCM and DCM, a simple PID controller finds itself hard to adapt to such variations in the system dynamics. Therefore, a switching current-mode controller, as given in Fig. 7.10, is suggested. The structure of the proposed controller is similar to a conventional peak current mode control, except that the voltage compensator can be switched according to the working mode.

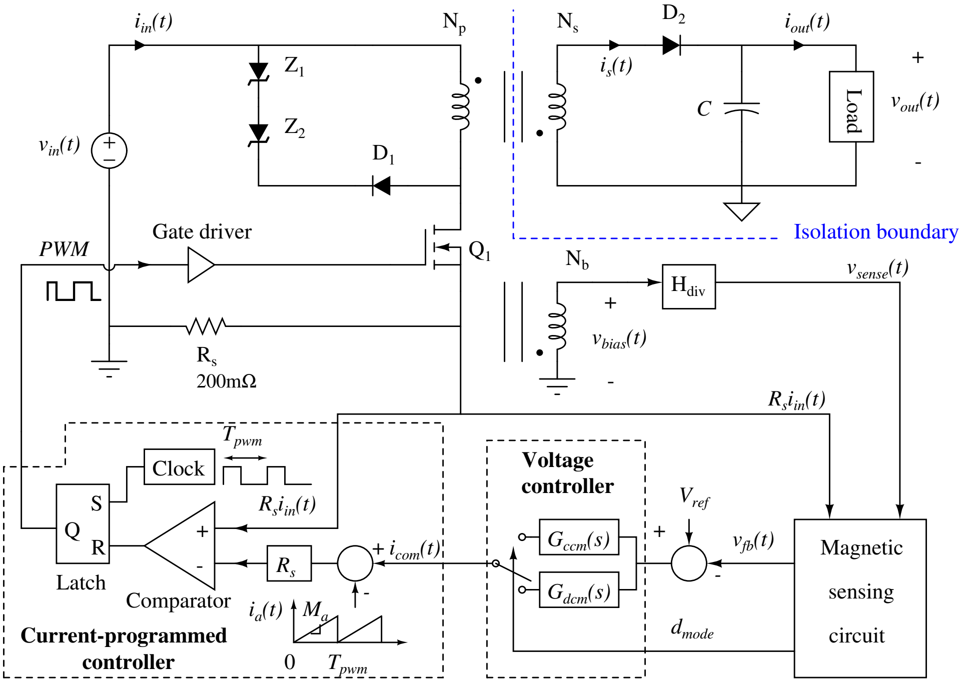

Figure 7.10: Block diagram of a flyback converter with magnetic sensing and gain scheduling current mode control.

7.4.1 Controller design

The operation of the controller in Fig. 7.10 can be summarized as follows. The current-programmed block operates like a peak-current regulator. It forces the peak value of the primary current $i_{in}(t)$ to follow the command level $i_{com}(t)$ by varying the duty ratio D of the PWM signal q_{pwm}. The artificial ramp $i_a(t)$ is required to stabilize the current-programmed controller when $D > 0.5$. The command signal $i_{com}(t)$ is set by the voltage controller in response to the difference between the feedback voltage $v_{fb}(t)$ and the reference V_{ref}. Notice that the feedback voltage $v_{fb}(t)$ is linearly proportional to the estimation of the output voltage $v_{out}(t)$, as described in Eq. (7.5). Two voltage controllers, $G_{ccm}(s)$ and $G_{dcm}(s)$, have been designed for two nominal operating points (one in CCM and one in DCM). Switching between these controllers is determined by the mode detection signal, d_{mode}, which is generated based on the waveform of the bias winding voltage $v_{bias}(t)$. In particular, if the value of $v_{bias}(t)$ drops to zero before the end of the switching cycle, the converter operates in DCM, otherwise operation is in CCM.

For simplicity, the output voltage $v_{out}(t)$ is assumed to be perfectly tracked by the magnetic sensing circuit. Given such an assumption, the transfer function from $v_{out}(t)$ to $v_{fb}(t)$ can be simplified to

$$H_{vs}(s) = \frac{\tilde{v}_{fb}(s)}{\tilde{v}_{out}(s)} = \frac{n_3}{n_2} H_{div}, \tag{7.20}$$

where $\tilde{v}_{out}(s)$ and $\tilde{v}_{fb}(s)$ denote the Laplace transformation of the small signal deviations of the output voltage and the feedback voltage, respectively. H_{div} is the gain of the voltage divider. The voltage compensator can now be synthesized using the typical design approach for current mode control. Firstly, the procedure outlined in Section 2.4.2 is applied to find the small singal model for the converter in Fig. 7.10. The transfer function relating the control signal $i_{com}(t)$ and the output voltage $v_{out}(t)$ in CCM is

$$G_{vc}^{ccm}(s) = \frac{\tilde{v}_{out}(s)}{\tilde{i}_{com}(s)} = \frac{F_m G_{vd}(s)}{1 + F_m G_{id}(s) + F_m F_v G_{vd}(s)}, \tag{7.21}$$

where

$$G_{vd}(s) = \left.\frac{\tilde{v}_{out}(s)}{\tilde{d}(s)}\right|_{\tilde{v}_{in}(s),\tilde{i}_{dyn}(s)=0} = \frac{\frac{V_{in}}{n_2 L_m C}\Big(- s\frac{n_2 L_m}{(1-D)V_{in}}\left(\frac{V_{out}}{R} + I_{dyn}\right) + 1\Big)}{s^2 + \frac{s}{RC} + \frac{(1-D)^2}{n_2^2 L_m C}},$$

$$G_{id}(s) = \left.\frac{\tilde{i}_m(s)}{\tilde{d}(s)}\right|_{\tilde{v}_{in}(s),\tilde{i}_{dyn}(s)=0} = \frac{s\frac{V_{in}}{(1-D)L_m} + \frac{(1+D)V_{in}}{(1-D)RL_m C} + \frac{I_{dyn}}{n_2 L_m C}}{s^2 + \frac{s}{RC} + \frac{(1-D)^2}{n_2^2 L_m C}},$$

$$F_m = \frac{1}{M_a T_{pwm}},\ F_v = \frac{\big(1-D\big)^2 T_{pwm}}{2n_2 L_m},\ \text{and}\ D = \frac{V_{out}}{V_{out+n_2 V_{in}}}.$$

Recall that $n_2 = \frac{N_s}{N_p}$ is the transformer turn ratio, M_a is the slope of the compensation ramp $i_a(t)$, and T_{pwm} indicates the period of the PWM signal. Capital letters V_{in}, V_{out} and D denote the steady state values of signals at an operating point, while lower case symbols with a tilde on them represent signal deviations from their operating point in either the time domain or the frequency domain depending on the letter that comes with these symbols. For example, $\tilde{i}_m(t)$ is the small signal deviation of the magnetising inductor current in the time domain while $\tilde{i}_m(s)$ indicates the frequency domain equivalent of $\tilde{i}_m(t)$. In the case of DCM, the control signal to output voltage transfer function is

$$G_{vc}^{dcm}(s) = \frac{\tilde{v}_{out}(s)}{\tilde{i}_{com}(s)} = F_m G_{vd}(s), \tag{7.22}$$

where

$$G_{vd}(s) = \left.\frac{\tilde{v}_{out}(s)}{\tilde{d}(s)}\right|_{\tilde{v}_{in}(s),\tilde{i}_{dyn}(s)=0} = \frac{\frac{2V_{in}}{nL_mC}\left(-s\frac{DT_{pwm}}{2}+1\right)}{s^2+s\left(\frac{2M}{DT_{pwm}}+\frac{1}{RC}\right)+\frac{4M}{DT_{pwm}RC}+\frac{2I_{dyn}}{nDT_{pwm}CV_{in}}},$$

$$F_m = \frac{1}{\left(M_a+\frac{V_{in}}{L_m}\right)T_{pwm}}, \quad D = \frac{V_{out}}{V_{in}}\sqrt{\frac{2L_m}{T_{pwm}R}\left(1+\frac{RI_{dyn}}{V_{out}}\right)}, \quad M = \frac{V_{out}}{nV_{in}}.$$

For numerical illustration, the converter specification and component values are chosen (based on the component datasheets of the reference design in Fig. 6.1) as follows: the input voltage V_{in} = 150V, nominal output voltage V_{out} = 32V, output capacitor C = 900μF, compensation slope $M_a = 10^5 A/s$, switching frequency $f_{pwm} = 80kHz$ and dynamic load $I_{dyn} = 0$. The transformer is constructed to have a magnetising inductance $L_m = 791.76\mu$H, and the winding turns $N_p = 46$, $N_s = 10$, and $N_b = 6$. These converter parameters are utilized in calculation for both operating modes, except for a value of $R = 10\Omega$ in CCM and $R = 100\Omega$ in DCM. Substituting these assigned parameters into Eqs. (7.21) and (7.22), the numerical values of $G_{vc}(s)$ in CCM and DCM are given by Eqs. (7.23) and (7.24), respectively,

$$G_{vc}^{ccm}(s) = \frac{5.636\cdot 10^3(-s+1.375\cdot 10^5)}{(s+3.001\cdot 10^5)(s+215.3)}, \tag{7.23}$$

$$G_{vc}^{dcm}(s) = \frac{803.25(-s+6.664\cdot 10^5)}{(s+22.22)(s+6.539\cdot 10^5)}. \tag{7.24}$$

A simple technique to design a compensator is to cancel the dominant poles and zeros in $G_{vc}(s)$. Unfortunately, the pole zero cancellation method typically suffers a slow response under a large load change. Therefore, loop shaping is utilized instead to widen the bandwidth of the closed-loop system, but still guarantee a phase margin of at least 50°. The compensators designed for the nominal operating points in CCM and DCM have the form of

$$G_{ccm}(s) = \frac{7\cdot 10^4(s+800)}{s(s+2.94\cdot 10^4)}, \tag{7.25}$$

$$G_{dcm}(s) = \frac{9\cdot 10^4(s+500)}{s(s+3\cdot 10^4)}. \tag{7.26}$$

7.4.2 A sample simulation result

Since the waveform of $v_{bias}(t)$ in a real circuit can be very different from that obtained from an ideal model, a detailed realistic simulation of a flyback converter is required for verifying the proposed sensing solution. The control-oriented model, as sketched in Fig. 7.4, is re-used for simulation purposes. The parameters of the converter model are chosen based on the component datasheets of the reference design in Fig. 6.1 and listed in Table 7.1. The simulation is implemented in the Matlab/Simulink environment.

Table 7.1: Parameter values of the control-oriented model

Input voltage $v_{in}(t)$	120V - 373V
Nominal output voltage V_{out}	32V
Dynamic load $i_{dyn}(t)$	0
Resistive load R	10 - 100Ω,
Magnetizing inductance L_m	791.76μH
Leakage inductance L_{lk}	8.03μH
Winding resistance r_w	0.3522Ω
Voltage transformation ratios n_2, n_3	0.2174, 0.1304
Output capacitor C	900μF
Output capacitor resistance r_c	10mΩ
Diode forward voltage drop V_f	0.45V
Resistances r_{Don}, r_{Qon}, r_{ds}	0.05Ω, 0.4Ω, 50Ω
Zener voltage V_z and resistance r_z	180V, 0.5Ω
MOSFET drain source capacitance C_{ds}	96.697pF

Three different scenarios are considered to study the tracking ability and stability of the analogue MS circuit proposed in Section 7.3.2. In the first scenario, a periodic step-load current from 3.2A to 1A is applied so that the converter stays in CCM. Fig. 7.11(a) plots the estimated voltage $\hat{v}_{out}(t)$ and the actual output voltage $v_{out}(t)$ on the same graph. As can be seen, the magnetic sensing circuit can fully track the variation of $v_{out}(t)$ and its response is instantaneous without any appreciable delay. For the second scenario, the converter runs in DCM only by enforcing another periodic step-load change from 0.32A to 0.64A at the converter output. The obtained result, which is depicted in Fig. 7.11(b), demonstrates that the proposed sensing solution can also work accurately in DCM. The final scenario involves a large load current perturbation from 3.2A to 0.32A in order to excite both operating modes of the converter. A good match between $\hat{v}_{out}(t)$ and $v_{out}(t)$, which is shown in Fig. 7.11(c), again supports the accuracy and robustness claims of the proposed observer. Notice that the performance of the digital MS circuit presented in Section 7.3.3 is not included in this chapter and will be examined together with the digital controller in Chapter 8.

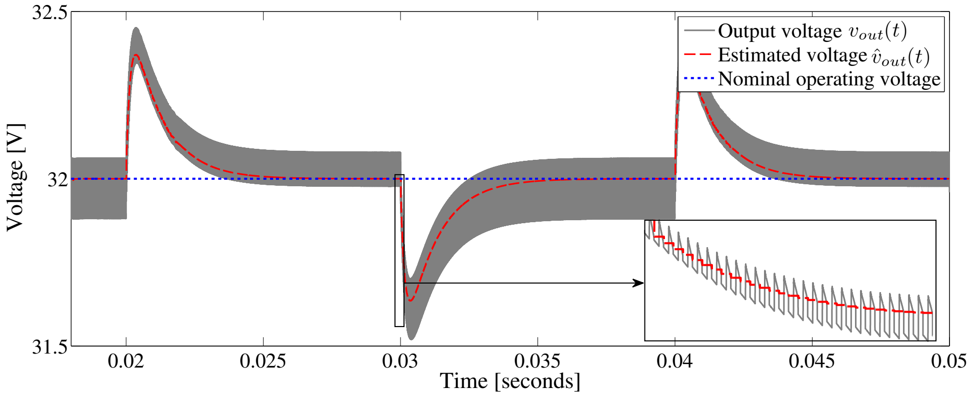

(a) Scenario 1: CCM only

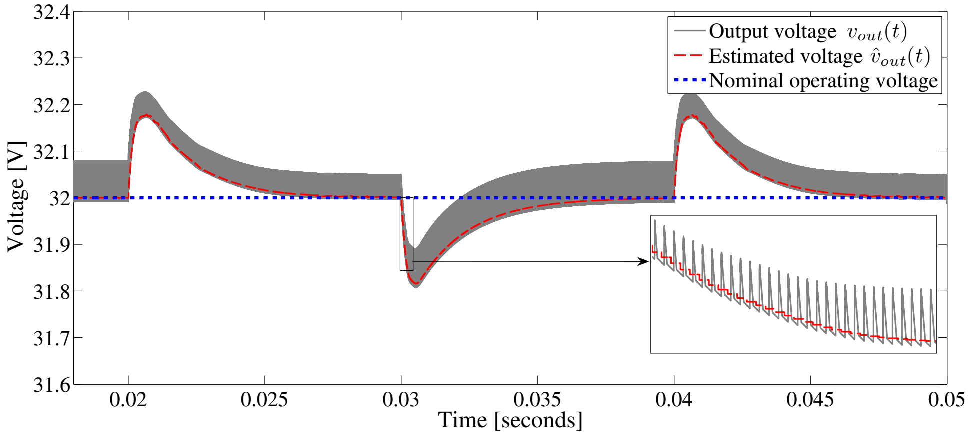

(b) Scenario 2: DCM only

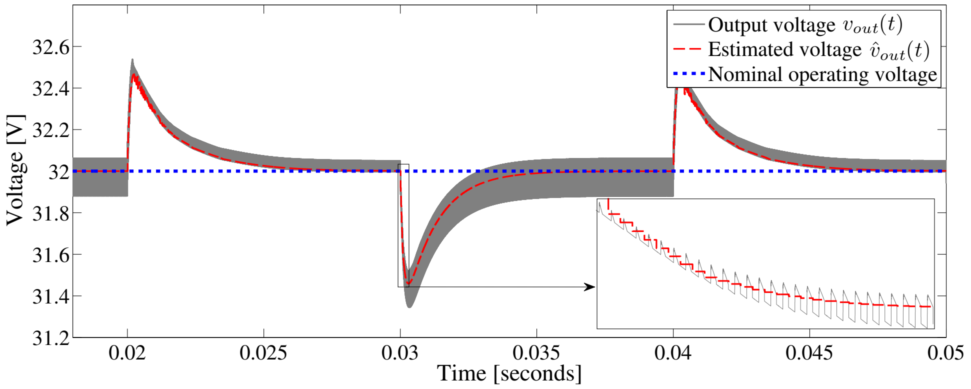

(c) Scenario 3: both CCM and DCM

Figure 7.11: Estimated voltage and output voltage response under different step-load scenarios: (a) 1A to 3.2A step-load, (b) 0.32A to 0.64A step-load, and (c) 0.32A to 3.2A step-load

7.5 Conclusion

A unified magnetic sensing technique has been developed in this chapter. Unlike existing magnetic sensing approaches, the proposed solution does not try to sample the bias winding voltage at the knee point but at the point where the secondary current is known. The proposed sensing technique can accurately compensate for the cable voltage drop and track the output voltage in both CCM and DCM.

The sensing algorithm is simple and can be achieved by an analogue circuit or a digital microcontroller. A simple implementation with stable performance and a universal working mode makes the proposed observer more attractive in the industrial field. In addition to output voltage estimation, the magnetizing current can also be used to predict the average input voltage and output current. This feature is very useful for applications where both output voltage regulation and output current regulation are required. Although only simulation have been used to verify the performance of the proposed sensing method in this chapter, experimental verification will be considered in Chapter 8.

Chapter 8

Optimum digital control design for flyback converters

8.1 Introduction

Traditionally, the regulation of switched-mode power supplies in general, and flyback converters in particular, has been handled by analogue controllers which provide good performance and adequate efficiency for most applications [240]. However, with the introduction of new energy regulations as well as an increasing demand for cost and size reduction, analogue control is not suitable for future applications, and is gradually being replaced by digital control, which allows implementation of sophisticated functions while keeping the system cost and complexity within an acceptable range. Although digital control is more advantageous than its analogue counterpart in terms of functionality, size, and power consumption, the application of digital control to flyback converters is not straightforward due to the low cost nature of flyback converters. In other words, the digital control solution is only valuable if its implementation costs less than or at worst equal to that of the analogue control.

The objective of this chapter is to design and implement digital optimum control for a flyback converter using a low-cost microcontroller. In addition to the main task, which is to regulate the converter output and offer fast and stable operation, the digital control solution is expected to perform other tasks including magnetic sensing, efficiency optimisation, and n$^{\text{th}}$ valley switching operation.

For the problem at hand, a PID controller is typically the first option that should be considered because of its simplicity and efficacy. In general, PID controllers can be easily tuned for one given operating point, corresponding to a load current and an input voltage, but provide zero robustness when the system deviates from the designed point. Although PID tuning capability is very important in terms of design flexibility and control performance, robustness is what we are looking for in the control design for flyback converters. Such a requirement is the main reason for the rejection of PID controllers and also the motivation for the study in this chapter.

Two major works, consisting of control architecture development, and compensator design and implementation, are carried out in sequence in this chapter. The first work focuses on integrating different control functions, e.g. efficiency optimization, and magnetic sensing (MS), into a single control architecture, as presented in Section 8.2. The compensator of the proposed control solution is synthesized and implemented using a TI C2000 microcontroller in the second work. Particularly, a study of a H_∞ robust controller is discussed in Section 8.3, while a gain-adaptive predictive functional controller (GAPFC) is presented in Section 8.4. Finally, a gain-adaptive robust compensator, which can achieve fast transient response and global stability, is proposed in Section 8.5.

8.2 Control architecture development

This section focuses on developing a digital control structure, which not only allows an integration of various state-of-the-art functions, but is also capable of being implemented with a low-cost microcontroller. The development of the control structure includes two steps which are: (i) specify all key objectives and constraints, e.g transient response, stability, efficiency, cost, technology, which are essential for the selection of control schemes, and (ii) propose a control solution which can fulfil all these given specifications. The detailed description of the work in steps (i) and (ii) is presented in Sections 8.2.1 and 8.2.2, respectively.

8.2.1 Control objectives and constraints

Table 8.1: Control specifications for a 65W flyback converter.

Input voltage $v_{in}(t)$	113V - 373V
Nominal output voltage V_{out}	19.5V
Output voltage ripple and noise ΔV_{ripple}	$1V_{\text{p-p}}$, max.
Output power P_{out}	0W - 65W
Output current $i_{out}(t)$	0A - 3.5A
Switching frequency f_{pwm}	1kHz - 120kHz
Operating mode	CCM and DCM
Feedback isolation	Magnetic sensing through bias winding
Steady state output voltage regulation $\left\lvert\frac{v_{out}(t)-V_{out}}{V_{out}}\right\rvert$	$\leq 1\%$
Line and load regulation $\lvert v_{out}(t) - V_{out}\rvert$	$\leq$ 1V
Averaged active mode efficiency η	$\geq 90\%$
Standby power loss	30mW, max.

The main control objective is to develop a digital control solution that is compatible with commercial products but also offers several distinctive features which are listed below.

- Maximise the efficiency of flyback converters for all operating points at steady state. The efficiency optimisation can be performed either in an online or offline manner, but should be simple to implement and not require much computation power.
- Offer fast transient responses over the range from light load, e.g. 5mW, to full load, e.g. 65W and, most importantly, is stable over the full operating range of consideration.
- Allow regulation of the output voltage through either the bias winding or primary winding.
- Facilitate valley switching operation which is the key factor in reducing electromagnetic interference (EMI) and improving the system efficiency.
- Facilitate low complexity design which can be implemented with a very low-cost microcontroller.

The control objectives, as described above, as well as the standard specifications for the input voltage, output load, switching frequency, line and load regulation, and no load power consumption, are quantified and summarized in Table 8.1, where the active mode efficiency is an average of the system efficiency measured at 25%, 50%, 75% and 100% of the nominal load.

8.2.2 Digital optimum control architecture

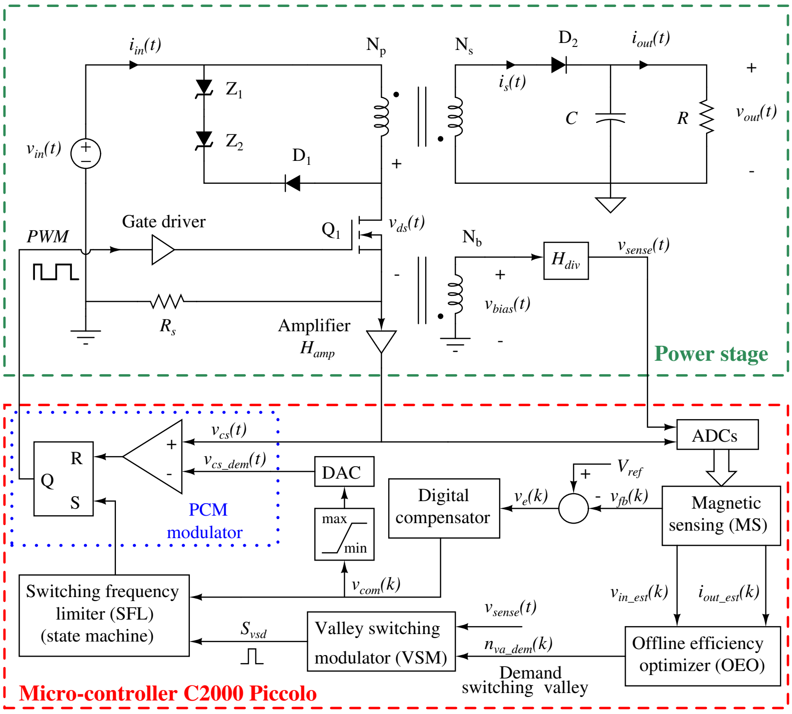

Figure 8.1: Functional diagram of the digital control architecture for a flyback converter application. For simplicity, the compensation ramp $i_a(t)$ for peak current mode control is not included in this figure.

Figure 8.1 shows the block diagram of a flyback converter along with the digital optimum control structure which is proposed to achieve all the specifications in Table 8.1. The operation of the proposed digital control solution can be outlined as follows. The magnetic sensing (MS) function derives the output voltage information from the sensed bias-winding voltage and uses it for regulation purposes. The use of MS allows not only elimination of the galvanic isolation in the feedback path, but also improvement of the output voltage regulation and converter efficiency. In addition to the feedback signal, the input voltage and load current can be also obtained from the MS circuit. The detailed description of the algorithm behind the MS function is presented in Chapter 7.

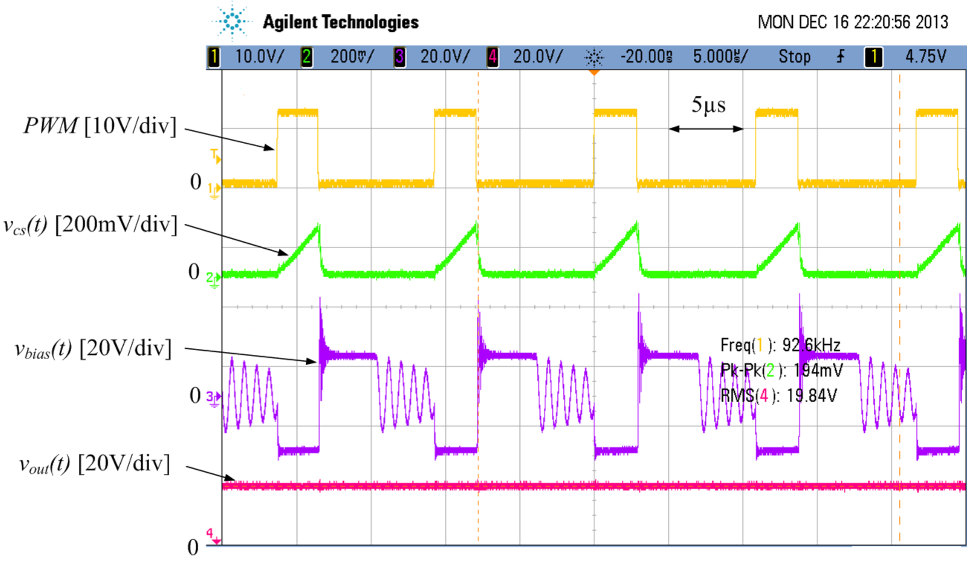

Figure 8.2: An example of a valley switching technique based on the bias winding voltage. The MOSFET is turned on at the valley of $v_{bias}(t)$.

Due to the fast response and high reliability, peak current modulation is adopted in the digital control design of Fig. 8.1. However, unlike traditional PCMC where the PWM frequency is fixed and decided by an internal oscillator, the proposed optimum control implements valley switching operation, also known as quasi-resonant control in [57], to improve system efficiency at the cost of a variable PWM frequency. In principle, the valley switching technique requires that the MOSFET should be turned on at the minimum value of the switching node voltage $v_{ds}(t)$, i.e. at the valley of $v_{ds}(t)$. However, due to some difficulties in handling the high voltage $v_{ds}(t)$, the sensed bias-winding voltage $v_{sense}(t)$ is used in the control design of Fig. 8.1 instead. Figure 8.2 shows an example of a valley switching technique based on the bias winding voltage.

In order to further improve the converter efficiency, a constrained optimization procedure, as described in Section 2.5.5.2, is applied offline to find the optimal switching frequency for each combination of input voltage and output load. The results obtained for V_{in} = 120V, 240V and 360V are plotted as a function of the load demand in Fig. 8.3. Owing to some implementation difficulties [7, 60], the optimal switching frequencies are transformed into equivalent switching valleys and saved into a look-up table, which is essentially the offline efficiency optimiser (OEO)

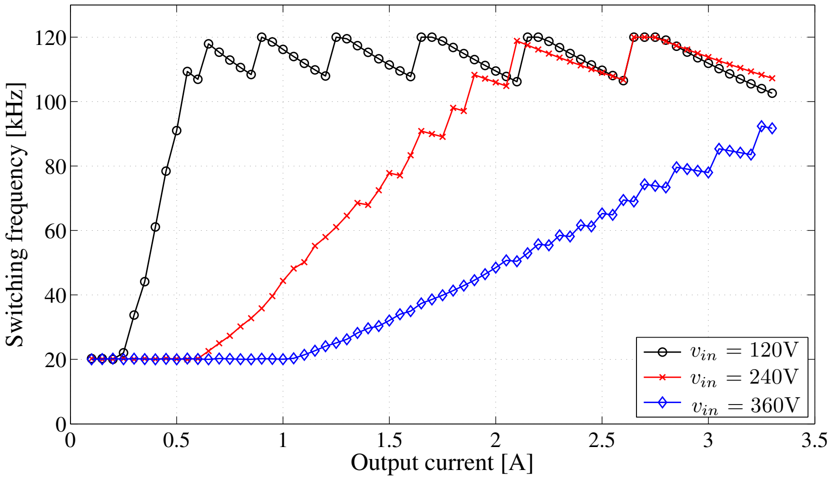

Figure 8.3: Optimum switching frequency at different working loads for a 65W flyback converter with $V_{in} = 120V, 240V$ and $360V$. The frequency range is limited to $20kHz - 120kHz$ which is required to minimize EMI and audible noise.

in Fig. 8.1.

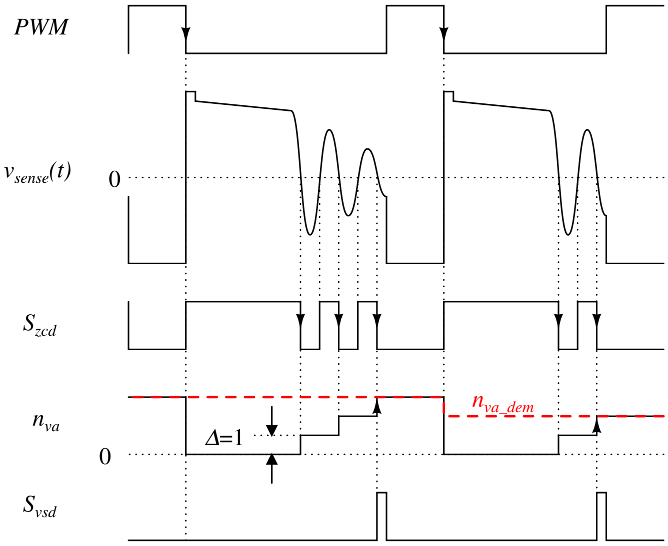

Figure 8.4: Timing diagram describing the relation between the inputs, output and internal states of the valley switching modulator.

The main function of the valley switching modulator (VSM) is to use the sensed bias-winding voltage as a reference signal, and set the SR latch to turn the MOSFET on at the demand valley which is output by the efficiency optimizer block. The operating principle of the VSM is best explained through the timing diagram, as depicted in Fig. 8.4, where the PWM signal, the sensed bias winding voltage $v_{sense}(t)$, and the demand switching valley n_{va_dem} are the inputs of the VSM while the valley switching detection signal S_{vsd} is its output. Comparing $v_{sense}(t)$ with zero results in the zero crossing detection signal S_{zcd}, based on which a pulse counter is employed to work out the number of valleys n_{va} which has occurred in $v_{sense}(t)$. The valley counter state n_{va} is reset by the falling edge of the PWM signal and is increased by 1 whenever it sees a falling edge in S_{zcd}. Once n_{va} reaches the value specified by the demand switching valley n_{va_dem}, a short pulse is immediately generated at the VSM output.

Due to the acoustic noise and EMI constraints, the pulse command S_{vsd} produced by the VSM cannot be used to control the SR latch immediately, but has to be checked by the switching frequency limiter (SFL) first to assure that the PWM frequency is within a pre-defined range. In particular, the SFL stores a set of upper and lower frequency thresholds as a function of the compensator output $v_c(k)$, and utilizes a simple state machine to force the converter operating within these stored boundaries. A typical design of these frequency constraints for a flyback converter is sketched in Fig. 8.5. The valley switching operation is achieved only if the PWM frequency lies between the upper and lower threshold levels; otherwise, it will be clamped by either one of these two limits, whichever is violated. When the upper and lower constraints coincide, as in the case of Fig. 8.5 with $v_c(k) \leq V_{th1}$ or $v_c(k) \geq V_{th2}$, the PWM frequency will equal the lower one and no valley switching operation is performed in this case. Though the OEO function suggests the frequency at which the converter should operate, the real working frequency is always decided by the SFL.

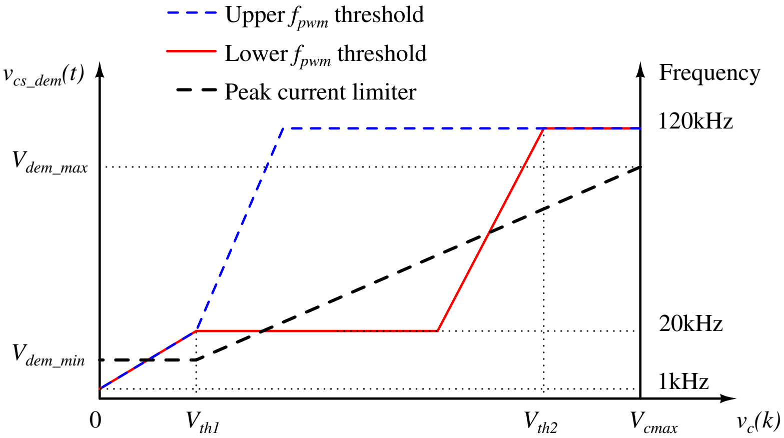

Figure 8.5: Typical design of the demand peak current limiter, and the upper and lower threshold levels of the switching frequency limiter. Optimum valley switching operation can be carried out when the compensator output satisfies $V_{th1} \leq v_c(k) \leq V_{th2}$ and the PWM frequency falls inside the area enclosed by these frequency constraints.

In addition to the PWM frequency, the restriction on the demand peak current, as sketched in Fig. 8.5, is also required to satisfy the minimum MOSFET on-time and protects the transformer from saturation. As can be seen from Fig. 8.5, the proposed control architecture utilizes two modulation schemes for different loading conditions. In particular, a constant peak current and variable frequency modulation is needed when $v_c(k) \leq V_{th1}$, i.e. at light and no load, while a peak current modulation is used for $v_c(k) \geq V_{th1}$, i.e. at average and full load. The transition between the constant peak current modulation and peak current modulation occurs smoothly at $v_c(k) = V_{th1}$ because of no abrupt change in either the demand peak current or the switching frequency. The smooth transition is a key technique that allows preservation of system stability across the whole operating range. When $v_c(k) \leq V_{th1}$, the compensator does not have any control over the peak current, or the MOSTFET on-time, but rather controls the switching frequency. A smaller value of $v_c(k)$ results in a smaller switching frequency. If no load exists at the converter output, $v_c(k)$ is expected to equal zero and the switching frequency will reach its lowest value, which is 1kHz in the case of the design in Fig. 8.5. The lowest switching frequency should be chosen to make sure that the standby power loss specification in Table 8.1 is met.

8.3 A feasibility study into the robust controller

Due to the nature of the efficiency optimisation, the closed-loop flyback converter in Fig. 8.1 usually exhibits multiple operating modes and a variable switching frequency, which poses considerable difficulties for robust control design. Dealing with variable frequency converters has been considered in various studies [7, 57, 58], whose authors rely heavily on trial and error expertise to design controllers that can satisfy certain given performance specifications. Although some researchers claim that their approaches allow achievement of both robust stability and robust performance across all operating points of the flyback converter [57], no theoretical proof has been provided so far. Hence, a systematic approach to the synthesis of a robust compensator for the variable frequency, wide operating range, flyback converter is of great interest.

As has been discussed in detail in Section 4.5.2, various applications of robust control theories to DC-to-DC converters and transformer-isolated converters, including mixed-sensitivity H_∞ control, have been reported in the literature with the main focus on fixed switching frequency schemes. Although the difference between fixed and variable frequency converters is merely the relation between the on- and off-time of each switching cycle, the control design procedure for these two applications is not the same. Therefore, the mixed-sensitivity H_∞ design framework is reconsidered in this section to synthesis a controller for the variable-frequency flyback converter in Fig. 8.1.

For control study purposes, this section is organised as follows: The small signal model of the digitally controlled converter in Fig. 8.1 is derived in Section 8.3.1, while the control design framework and its application to the flyback converter are presented in Section 8.3.2. Finally, the stability and performance of the obtained compensator are analysed in Section 8.3.3.

8.3.1 Converter model

Although the control scheme in Fig. 8.1 makes use of a variable switching frequency to regulate the output voltage, the control signal can still be classified as PWM. The reason is that the compensator can vary the on-time of the MOSFET but has no control over the length of the operational cycle. Moreover, the switching frequency can also be assumed to be quasi-static at steady state. Therefore, the small signal model of the flyback converter, which is developed in Chapter 2, is still valid for use in this case.

With broad external excitation and switching frequencies, the flyback converter, as shown in Fig. 8.1, will operate in both CCM and DCM, which requires different small signal models, one for each working scenario. Due to the similarity between the proposed control in Fig. 8.1 and PCM control, the small signal model derived in Section 2.4.2 can be reused, but needs some modifications. Figure 8.6 shows a complete block diagram of the small signal model of both CCM and DCM flyback converters, taking into account the effects of the MS function, voltage divider, current sense circuitry, analogue-to-digital converter (ADC) and digital-to-analogue converter (DAC) blocks. Designing the robust compensator $G_c(s)$ requires knowledge of all the transfer functions within the control loop, which can be derived based on the operating principle of each block in the proposed control structure in Fig. 8.1.

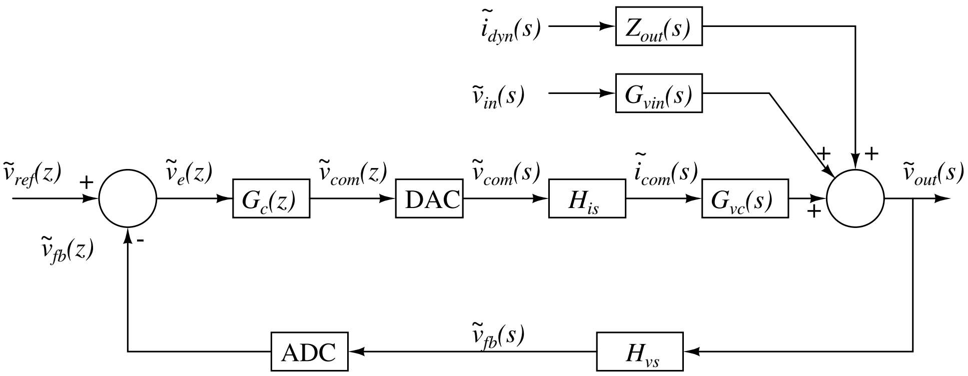

Figure 8.6: Block diagram of the small signal model of the digitally controlled flyback converter operating in both CCM and DCM. H_{vs} and H_{is} represents the output voltage and inductor current sensing gains, respectively. $G_c(z)$ is the digital compensator which needs to be designed.

If the magnetic sensing function is assumed to perform correctly and consistently regardless of the operating condition of the converter, the transfer function from the output voltage $v_{out}(t)$ to the sense voltage $v_{fb}(t)$ in Fig. 8.1 can be simply modelled by

$$H_{vs} = \frac{\tilde{v}_{fb}(s)}{\tilde{v}_{out}(s)} = \frac{N_b}{N_s} H_{div}, \tag{8.1}$$

where N_s and N_b are the number of turns in the secondary and bias windings respectively while H_{div} represents the voltage divider gain. The current sensing gain can be simply derived from the sense resistor R_s and amplifier gain H_{amp} via

$$H_{is} = \frac{1}{H_{amp} R_s}. \tag{8.2}$$

The conversion gains of the ADC and DAC blocks can be computed via

$$H_{adc} = \frac{2^{M_{adc}} - 1}{\Delta V_{adc}}, \qquad H_{dac} = \frac{\Delta V_{dac}}{2^{M_{dac}} - 1}, \tag{8.3}$$

where M_{adc} and M_{dac} are the number of ADC and DAC resolution bits, respectively, while ΔV_{adc} and ΔV_{dac} denote the dynamic range of ADC input and DAC output, respectively.

The transfer functions of the PCM controlled flyback converter $G_{vc}(s)$ for both CCM and DCM have been derived in Section 2.4.2 and can be found in Eqs. (2.51) and (2.57), respectively;

however, they will be reiterated here for convenience.

Converter in CCM: the transfer function of the PCM controlled flyback converter is

$$G_{vc}^{ccm}(s) = \frac{\tilde{v}_{out}(s)}{\tilde{i}_{com}(s)} = \frac{F_m G_{vd}(s)}{1 + F_m G_{id}(s) + F_m F_v G_{vd}(s)}, \tag{8.4}$$

where

$$G_{vd}(s) = \left.\frac{\tilde{v}_{out}(s)}{\tilde{d}(s)}\right|_{\tilde{v}_{in}(s),\tilde{i}_{dyn}(s)=0} = \frac{\frac{V_{in}}{n_2 L_m C}\Big(- s\frac{n_2 L_m}{(1-D)V_{in}}\left(\frac{V_{out}}{R} + I_{dyn}\right) + 1\Big)}{s^2 + \frac{s}{RC} + \frac{(1-D)^2}{n_2^2 L_m C}},$$

$$G_{id}(s) = \left.\frac{\tilde{i}_m(s)}{\tilde{d}(s)}\right|_{\tilde{v}_{in}(s),\tilde{i}_{dyn}(s)=0} = \frac{s\frac{V_{in}}{(1-D)L_m} + \frac{(1+D)V_{in}}{(1-D)RL_mC} + \frac{I_{dyn}}{n_2 L_m C}}{s^2 + \frac{s}{RC} + \frac{(1-D)^2}{n_2^2 L_m C}},$$

$$F_m = \frac{1}{M_a T_{pwm}}, \quad F_v = \frac{\big(1-D\big)^2 T_{pwm}}{2n_2 L_m}, \quad D = \frac{V_{out}}{V_{out+n_2V_{in}}}.$$

Converter in DCM: the control signal $\tilde{i}_{com}(t)$ to output voltage $\tilde{v}_{out}(t)$ transfer function is

$$G_{vc}^{dcm}(s) = \frac{\tilde{v}_{out}(s)}{\tilde{i}_{com}(s)} = F_m G_{vd}(s), \tag{8.5}$$

where

$$G_{vd}(s) = \left.\frac{\tilde{v}_{out}(s)}{\tilde{d}(s)}\right|_{\tilde{v}_{in}(s),\tilde{i}_{dyn}(s)=0} = \frac{\frac{2V_{in}}{nL_mC}\left(-s\frac{DT_{pwm}}{2} + 1\right)}{s^2 + s\left(\frac{2M}{DT_{pwm}} + \frac{1}{RC}\right) + \frac{4M}{DT_{pwm}RC} + \frac{2I_{dyn}}{nDT_{pwm}CV_{in}}},$$

$$F_m = \frac{1}{\left(M_a + \frac{V_{in}}{L_m}\right)T_{pwm}}, \quad D = \frac{V_{out}}{V_{in}}\sqrt{\frac{2L_m}{T_{pwm}R}\left(1 + \frac{RI_{dyn}}{V_{out}}\right)}, \quad M = \frac{V_{out}}{nV_{in}}.$$

8.3.2 Mixed sensitivity H_∞ controller design

The parameters and working range of the 65W converter design, which are based mainly on the control specifications in Table 8.1, are summarized in Table 8.2 for ease of control design. The tolerances of the magnetizing inductance and output capacitance are obtained from the manufacturer's data-sheets. The synthesis of an H_∞ controller for the converter under consideration is described step-by-step in Sections 8.3.2.1, 8.3.2.2 and 8.3.2.3.

Table 8.2: Component values and operating ranges of the 65W flyback converter.

Input voltage $v_{in}(t)$	120V - 373V
Nominal output voltage V_{out}	19.5V
Resistance load R	5.9Ω - 1950Ω
Dynamic load $i_{dyn}(t)$	0A
Switching frequency f_{pwm}	1kHz - 120kHz
Winding turns $N_p : N_s : N_b$	26:6:4
Magnetizing inductance L_m	$172\mu H\pm$ 20%
Output capacitance C	$1390\mu F\pm$ 10%
Current sense resistor R_s	200mΩ
Voltage divider gain H_{div}	0.165
Current amplifier gain H_{amp}	4
Dynamic range of ADC input ΔV_{adc} and DAC output ΔV_{dac}	3.3V, 3.3V
ADC resolution M_{adc} and DAC resolution M_{dac}	12 bits, 10 bits

8.3.2.1 Mixed-sensitivity $\mathbf{H}_\infty$ framework

The study of H_∞ optimization control was firstly introduced in the late 1970s by Zames [194] and subsequently caught the attention of many control theorists, see [195–197, 241, 242] and references cited therein. Basically, the method transforms the requirements of system performance and robustness into a constrained optimization problem whose cost function is evaluated using the ∞-norm of the Hardy spaces. By minimizing the cost function, a robust controller which satisfies the given specifications can be found. H_∞ control theory can be equally applied to both multiple-input-multiple-output (MIMO) and single-input-single-output (SISO) systems; however, for simplicity, this section only gives a brief sketch of the control design procedure for SISO systems and includes no theoretical and mathematical derivations. For a detailed proof of the H_∞ optimal solution, the books of Zhou [195, 242] and Skogestad [196] can serve as good references.

Conventional control methods make use of a fixed plant model in the design phase to tune the controller parameters. However, in practice, several existing elements, e.g. low-order approximations, unmodelled dynamics, and operating point movements, can cause plant/controller mismatches, usually referred to as model uncertainty, which greatly affects the stability and performance of closed-loop systems.

In contrast to conventional approaches, model uncertainty is used as a part of the system model in the synthesis of robust control. Model uncertainty can be represented in a structured or unstructured manner. This study focuses on multiplicative unstructured uncertainty of the form [196]

$$G_p(s) = G(s)\left(1 + W_I(s)\Delta_I(s)\right), \tag{8.6}$$

where $G(s)$ denotes the nominal plant model with no uncertainty while $G_p(s)$ indicates the perturbed model. Here, $\Delta_I(s)$ is any stable transfer function satisfying

$$|\Delta_I(j\omega)| \leq 1 \ \forall\omega, \tag{8.7}$$

and $W_I(s)$ is usually termed the multiplicative weight. In most applications, a set Π of possible plants, arising from parameter variations and operating point changes, rather than the nominal plant and the multiplicative weight, is given. Therefore, some extra processing steps, as described below, are required to convert this set of plants into a form given by Eq. (8.6).

1. Select a nominal model $G(s)$. The choice of the nominal model can be made in 3 ways: (a) any simplified model, e.g low-order, delay-free model, (b) a model obtained by averaging parameter values of all perturbed models in the set Π, or (c) a model which is at the middle of all perturbed plants in the Nyquist plot [196]. Each choice has its own advantages and disadvantages, so the best option certainly depends on the requirements of each problem.

2. For each perturbed plant $G_p(s) \in \Pi$, calculate the relative multiplicative uncertainty as

$$l_p(\omega) = \left|\frac{G_p(j\omega) - G(j\omega)}{G(j\omega)}\right| \tag{8.8}$$

3. Chose the rational weight $W_I(s)$ such that

$$|W_I(\omega)| \geq \max_{\forall l_p(\omega)} \left(l_p(\omega)\right), \ \forall\omega \tag{8.9}$$

Given a set of model perturbations in Eq. (8.6), the mixed-sensitivity H_∞ framework seeks a controller $G_c(s)$ which minimizes the cost function [196]

$$\parallel F_l(P, G_c) \parallel_\infty = \left\| \begin{matrix} W_1(s)S(s) \\ W_2(s)T(s) \end{matrix} \right\|_\infty, \tag{8.10}$$

where

$$S(s) = \frac{1}{1 + G(s)G_c(s)} \tag{8.11}$$

is the system sensitivity function, and

$$T(s) = \frac{G(s)G_c(s)}{1 + G(s)G_c(s)} \tag{8.12}$$

is the complementary sensitivity function. The weighting functions $W_1(s)$ and $W_2(s)$ in Eq. (8.10) are used as a means to specify the robustness and performance of the closed loop system. Particularly, $W_1(s)$ is chosen to reduce the sensitivity function $S(s)$ at low frequencies, which gives good disturbance rejection and good command following, i.e. maintains system performance regardless of parametric variations in the system model due to operating point changes and modelling errors. $W_2(s)$ is chosen to attenuate sensor noises and modelling errors through penalising the complementary sensitivity function $T(s)$ at high frequencies. Furthermore, $W_2(s)$ is also used to ensure robust stability by letting [196]

$$|W_2(j\omega)| \geq |W_I(j\omega)|, \qquad \forall\omega. \tag{8.13}$$

8.3.2.2 Model uncertainty

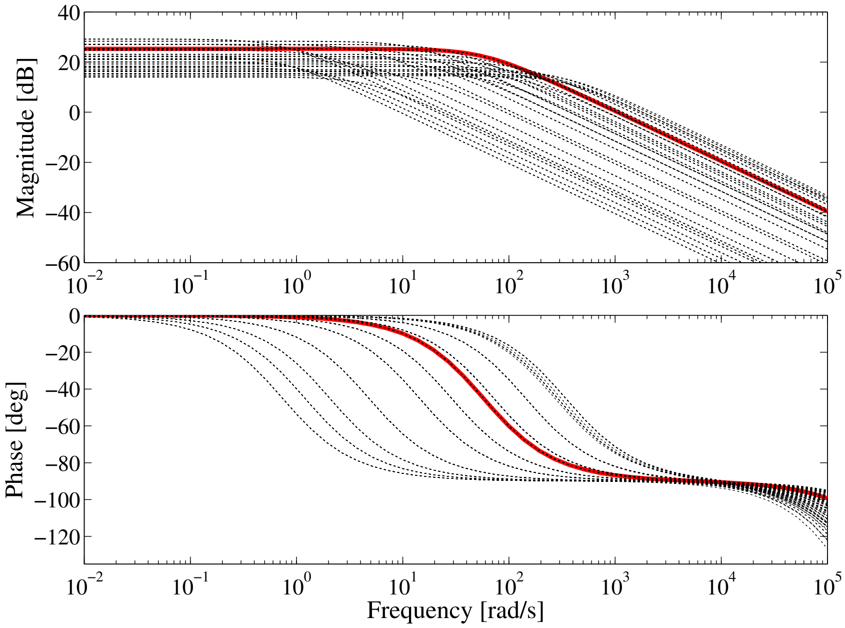

Figure 8.7: Frequency response of $G_{vcp}(s)$ at different operating points. The solid line is the nominal plant while the dotted lines represent perturbed plants

As can be observed in Fig. 8.1, the switching frequency f_{pwm} is decided by the external variables, i.e. the input voltage $v_{in}(t)$ and output current $i_{out}(t)$, rather than by the compensator. As a result, f_{pwm} can be considered as an independent variable in the derivation of model uncertainty.

Given the converter model parameters in Table 8.2, the perturbed plant transfer function $G_{vcp}(s)$ at different combinations of the input voltage, output load, and switching frequency can be calculated based on Eqs. (8.4) and (8.5). The frequency responses of the obtained perturbed plants $G_{vcp}(s)$ are illustrated in Fig. 8.7, based on which a nominal plant is selected to be at the middle of the variation range of perturbed plants and yield the smallest uncertainty region. The transfer function of such a nominal plant is given by

$$G_{vcn}(s) = \frac{-343.244\left(s - 2.49 \cdot 10^{6}\right)}{(s + 57.56)\left(s + 8.093 \cdot 10^{5}\right)}, \tag{8.14}$$

which is illustrated by the solid line in Fig. 8.7. Given the perturbed plants $G_{vcp}(s)$ and the nominal plant $G_{vcn}(s)$ as in Eq.(8.14), the magnitude of the relative multiplicative uncertainty $l_p(\omega)$ for each plant can be computed using Eq. (8.8) and is plotted in Fig. 8.8. In order to cover all the relative multiplicative uncertainties as represented by dotted lines in Fig. 8.8, the multiplicative weight

$$W_I(s) = \frac{1.239(s + 0.8929)(s + 1000)}{(s + 1.212)(s + 1250)} \tag{8.15}$$

is used, as also shown in Fig. 8.8.

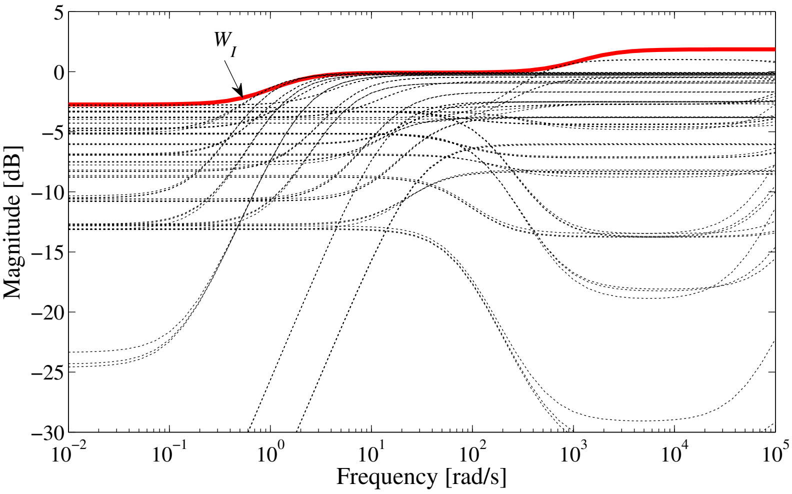

Figure 8.8: Magnitude of the multiplicative uncertainty (dotted lines) for different working points and the uncertainty weight $W_I(s)$ (solid line).

8.3.2.3 Weight selection

Some performance specifications, i.e. the tracking/regulation error and closed-loop bandwidth, can be achieved by means of the weight $W_1(s)$. In particular, the weight $W_1(s)$ must act like an integrator at low frequencies to achieve zero steady-state error, while moving the zero crossing point of $W_1(s)$ to higher frequencies can help to increase the bandwidth of the closed-loop system. Based on such an observation, $W_1(s)$ is chosen as

$$W_1(s) = 0.0185\frac{s + 4000}{s + 0.01}. \tag{8.16}$$

For simplicity, the weight $W_2(s)$ is chosen to be equal to $W_I(s)$, according to Eq. (8.13). The magnitudes of the weighting functions $W_1(s)$ and $W_2(s)$ are plotted as a function of frequency in Fig. 8.9.

Given the weights $W_1(s)$ and $W_2(s)$, the robust compensator can be found through minimization of the cost function, as given by Eq. (8.10). Such an optimisation problem can be solved using the MATLAB Robust Control Toolbox. A direct result from the MATLAB routine is a 5th-order controller which is

$$G_{c5th}(s) = \frac{9.4124 \cdot 10^6\,(s + 1.212)\,(s + 57.56)(s + 8.093 \cdot 10^5)}{(s + 3.42 \cdot 10^{-3})\,(s + 10.34)\,(s + 1239)\,(s^2 + 3.673 \cdot 10^6 + 4.668 \cdot 10^{12})}. \tag{8.17}$$

Applying model reduction through calculation of Hankel singular values of the transfer function

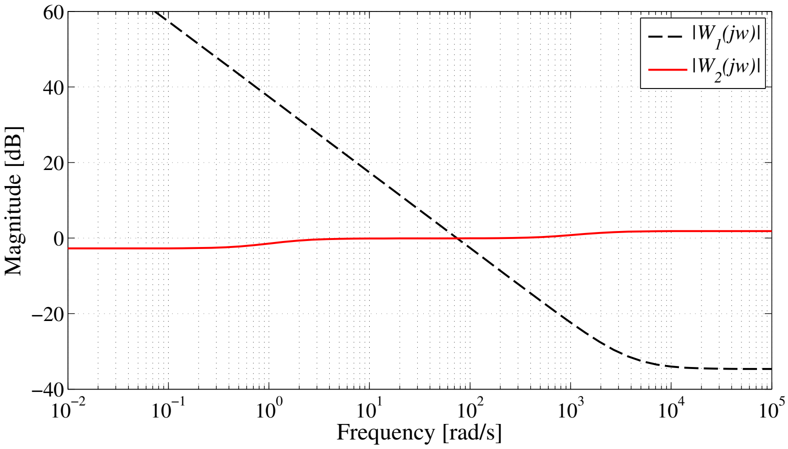

Figure 8.9: Magnitude of the weighting functions $W_1(s)$ and $W_2(s)$.

in Eq. (8.17) and elimination of low energy states [196], the 5th-order compensator is reduced to

$$G_{c3rd}(s) = \frac{2.364 \cdot 10^7\,(s+1.005)\,(s+27.22)}{(s+3.426\cdot 10^{-3})\,(s+7.225)\,(s+8.4172\cdot 10^6)}. \tag{8.18}$$

8.3.3 Controller performance and stability analysis

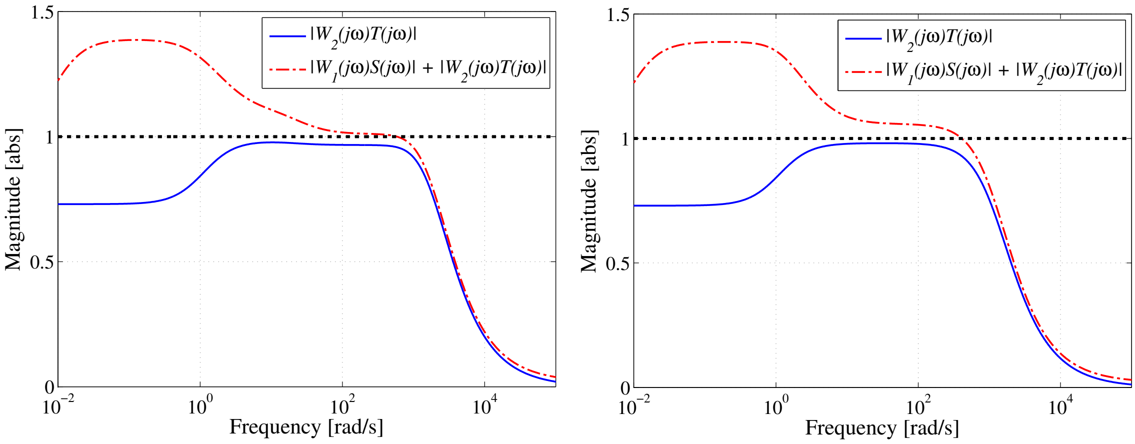

(a) 5rd order controller (b) 3rd order controller

Figure 8.10: Plots of $|W_2(j\omega)T(j\omega)|$ and $|W_1(j\omega)S(j\omega)| + |W_2(j\omega)T(j\omega)|$ for robust stability and performance assessment of: (a) 5rd order controller and (b) 3rd order controller. In both graphs, the upper bound on $|W_2(j\omega)T(j\omega)|$ and $|W_1(j\omega)S(j\omega)| + |W_2(j\omega)T(j\omega)|$ to guarantee the robustness is 1.

The stability and performance of the full 5th-order H_∞ controller, as given by Eq. (8.17), can be verified by examining the magnitude of $|W_2(j\omega)T(j\omega)|$ and $|W_1(j\omega)S(j\omega)| + |W_2(j\omega)T(j\omega)|$ versus frequency [196]. In particular, for systems with multiplicative uncertainty as described by

Eq. (8.6), the condition for robust stability [196] is

$$|W_2(j\omega)T(j\omega)| < 1, \quad \forall\omega, \tag{8.19}$$

while robust performance requires

$$|W_1(j\omega)S(j\omega)| + |W_2(j\omega)T(j\omega)| < 1, \quad \forall\omega. \tag{8.20}$$

The results, as illustrated in Fig. 8.10(a), show that $|W_2(j\omega)T(j\omega)|$ is always smaller than 1 over the frequency range of interest, while $|W_1(j\omega)S(j\omega)| + |W_2(j\omega)T(j\omega)|$ can remain below 1 at high frequency only, which means that the compensator $G_{c5th}(s)$ can ensure robust stability but fails to achieve robust performance. In other words, the performance specifications, i.e. the gain margin, phase margin, and bandwidth of the closed loop system given in term of $W_1(s)$, are not met for some plants in the perturbed set.

The assessment of the stability and performance for the reduced 3^{th}-order controller $G_{c3rd}(s)$, given by Eq. (8.18), are carried out in a similar way. The assessment results as shown in Fig. 8.10(b), which are similar to that of the full order controller, confirm that the reduced order compensator can guarantee robust stability but also fails in the robust performance test. The results from the stability and performance assessments for both the full and reduced order controllers reveal that both stability and performance properties are preserved after model reduction.

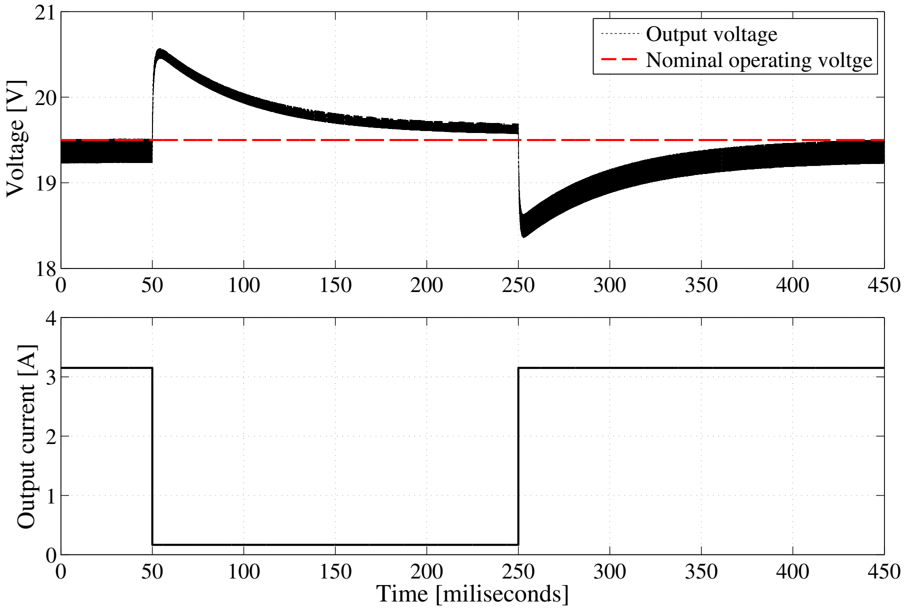

Figure 8.11: Variations of the converter output voltage $v_{out}(t)$ in response to a resistive load stepping between 0.165A and 3.15A every 200 milliseconds. The input voltage $v_{in}(t)$ is kept fixed at 150V.

Since both 5^{th}- and 3^{rd}-order compensators perform equally, the lower order solution, i.e. 3^{rd}-order, is of greater interest, and hence is mainly considered in the next study. A large-signal simulation of the system in Fig. 8.1 is employed to further assess the performance of the reduced order controller $G_{c3rd}(s)$. The simulation is developed based on the control-oriented model of the flyback converter in Chapter 6, and is implemented in the MATLAB/SIMULINK environment. Figure 8.11 shows the simulated transient response of the flyback converter for a 0.165A and 3.15A step current load and an input voltage $v_{in}(t) = 150$V. The variation step of the load current used in the test is selected based on the standard benchmark for measuring power supplies' performance.

The result, from Fig. 8.11, shows that the controller can bring the output voltage close to the reference level but cannot achieve zero steady error, which is due to the absent of the integral action in the compensator $G_c(s)$ as can be observed through examining Eq. (8.18).

The transient response of the output voltage, as illustrated in Fig. 8.11, is robustly stable but has a long settling time which does not meet the desired performance specified in Table 8.1. The long-settling-time result can be explained in the sense that, because of the huge variation in the model dynamics as shown in Fig. 8.7, some performance has been traded for robust stability.

8.4 Gain-adaptive fixed-parameter digital controller

As has been shown in Section 8.3.3, the wide variations of the input voltage and output load, in addition to the variable switching frequency, result in an impossible task for a 'traditional' robust H_∞ control approach. The poor performance is partly due to the act of considering f_{pwm} to be an independent source of variations in the control design process. In fact, f_{pwm} is not an independent variable but rather has an algebraic dependence on the input voltage $v_{in}(t)$ and output load $i_{load}(t)$. By including such a relation in the control synthesis framework proposed in Section 8.3, control performance can be improved. Unfortunately, the algebraic relation between f_{pwm}, $v_{in}(t)$, and $i_{load}(t)$ is rather complex and cannot be described by a simple analytical expression. One approach is to come up with a simple mechanism that can reduce, or ideally eliminate, model uncertainty before designing a robust controller.

In addition to the challenge of designing a globally stable controller with adequate performance, another difficulty is the requirement that the proposed control solution should be implemented in a low-cost microcontroller, which has very limited computational power, at a sampling frequency in the region of 100kHz. Such challenges are the main force driving the study in this section.

The remainder of this section is organized as follows. Firstly, the effect of a variable sampling frequency on the dynamics of a fixed-parameter digital compensator is addressed in Section 8.4.1. Given the knowledge about the origin of the parametric variations, Section 8.4.2 re-examines the converter model in DCM and represents it into a form which is most suitable for the synthesis of the digital controllers in Sections 8.4.4 and 8.5. Based on the resulting model, Section 8.4.3 proposes a simple gain-adaptive compensator which take its inspiration from predictive functional control theory. Finally, Section 8.4.4 presents the application of the proposed controller to the flyback converter and verifies its performance through both simulation and experiment.

8.4.1 Effect of a variable sampling rate on digital compensator

In the digital control of power converters, the sampling period can be chosen to be fixed or variable depending on the nature of the applications and algorithms used. With a variable-frequency PWM converter controlled by a low-cost microcontroller, a practical solution is to sample the feedback voltage and compute the control variable once per switching cycle. Such an implementation scheme, however, results in a variable sampling rate which varies the performance of the digital controller across the range of the operating frequency. The inconsistent performance is largely due to the movement of the equivalent continuous-time poles and zeros in response to the sampling period variation, given the fixed parameters of the digital compensator. In order to demonstrate such an effect, a simple example is considered here. Without loss of generality, the discrete-time compensator is assumed to have 2 poles and 2 zeros, with an effective sampling period of T_{pwm}, and is formulated as

$$G_{cz}(z) = G_{cz0}\frac{(1-z_1z^{-1})(1-z_2z^{-1})}{(1-z^{-1})(1-p_1z^{-1})}, \tag{8.21}$$

where G_{cz0} denotes the controller gain while z_1, z_2 and p_1 are the compensator zeros and pole, respectively. These zeros and pole are assumed to be inside the unit circle. In addition to these pole and zeros, $G_{cz}(z)$ has one predefined pole at $z = 1$ which is purposely selected to represent a class of practical controllers where integral action is typically required. The Tustin's transformation is commonly used in digital control due to its ability to preserve the bulk of the frequency response after transformation. For that reason, the Tustin's transformation is utilized to map $G_{cz}(z)$ to the continuous-time domain. The derivations for other discrete-to-continuous-time transformations are not included here but can be performed in a similar manner. The Tustin continuous-time equivalent of $G_{cz}(z)$ is given by

$$G_c(s) = G_{c0}\frac{\left(1-\frac{sT_{pwm}}{w_{z1}}\right)\left(1-\frac{sT_{pwm}}{w_{z2}}\right)}{sT_{pwm}\left(1-\frac{sT_{pwm}}{w_{p1}}\right)}, \tag{8.22}$$

where

$$G_{c0} = \frac{G_{c0z}(1-z_1)(1-z_2)}{(1-p_1)}, \qquad w_{p1} = 2\frac{p_1-1}{p_1+1},$$
$$w_{z1} = 2\frac{z_1-1}{z_1+1}, \qquad w_{z2} = 2\frac{z_2-1}{z_2+1}.$$

It can be seen from Eq. (8.22) that the poles and zeros of the continuous-time equivalent compensator, $G_c(s)$, *are directly proportional* to the sampling frequency while the integrator gain does not change, and is equal to that of $G_{cz}(z)$. This result can be explained in the sense that the values of poles/zeros of any discrete-time transfer function represent the position of their continuous-time equivalent, relative to the sampling frequency. Thus, keeping the values of these discrete-time poles/zeros fixed, and changing the sampling frequency will, in effect, force the continuous-time poles/zeros to vary. In other words, a fixed discrete-time transfer function with a variable sampling frequency is equivalent to a variable continuous-time transfer function.

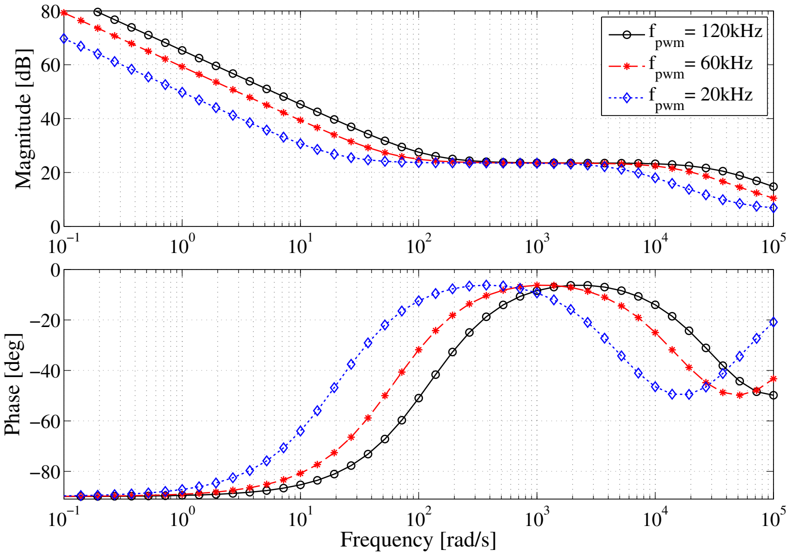

Figure 8.12: Frequency responses of the continuous-time equivalents of $G_{cz}(z)$ evaluated with three different sampling frequencies 120kHz, 60kHz, and 20kHz.

The effect of a variable sampling rate is graphically illustrated in Fig. 8.12, where the digital compensator under consideration is assigned a numerical value of

$$G_{cz}(z) = \frac{2.01\left(1-0.999z^{-1}\right)\left(1+0.946z^{-1}\right)}{\left(1-z^{-1}\right)\left(1-0.739z^{-1}\right)}, \tag{8.23}$$

and is examined with three sampling rates 120kHz, 60kHz and 20kHz. The results show that the frequency responses of the equivalent continuous-time transfer functions have the same shape and move closer to the origin when the sampling frequency is reduced, which agrees well with the observations from Eq. (8.22).

Although the sampling-rate-dependent dynamics generally makes the controller design and analysis harder to carry out, it can help to stabilize a system whose transfer function also depends on the switching frequency.

8.4.2 Converter transfer function re-examination

Due to constraints on the switching frequency, as well as the size of the transformer, the converter is forced to stay in discontinuous conduction mode (DCM) at most working points, except at maximum load and over load. Hence, variations in the converter model dynamics can be partly reduced by focusing on synthesizing a compensator for DCM only but verifying its stability and performance in both operating conditions.

Assuming the PCM controlled flyback converter is operating in DCM, and that the output load is purely resistive, the transfer function from the control signal $\tilde{i}_{com}$ to the output voltage $\tilde{v}_{out}$ in

Fig. 8.6 can be obtained by simplifying Eq. (8.5) to

$$G_{vc}(s) = \frac{2V_{in}}{nL_mCT_{pwm}\left(M_a + \frac{V_{in}}{L_m}\right)} \frac{\left(-s\frac{DT_{pwm}}{2} + 1\right)}{s^2 + s\left(\frac{2M}{DT_{pwm}} + \frac{1}{RC}\right) + \frac{4M}{DT_{pwm}RC}}, \tag{8.24}$$

where M_a is the slope of the compensation ramp $i_a(t)$, while D and T_{pwm} indicate the duty ratio and period of the PWM signal respectively. Now focus on the coefficient of s in the denominator of $G_{vc}(s)$ in Eq. (8.24). For small L_m design, the following relation holds

$$\frac{RC}{2} \gg \frac{DT_{pwm}}{4M}. \tag{8.25}$$

Therefore, $\left(\frac{RC}{2} + \frac{DT_{pwm}}{4M}\right)$ in Eq. (8.24) can be replaced with $\left(\frac{RC}{2} + \frac{DT_{pwm}}{2M}\right)$ and the resulting equation is factorized as

$$G_{vc}^{s1}(s) = \frac{V_{in}DR}{2nL_mM\left(M_a + \frac{V_{in}}{L_m}\right)} \frac{\left(1 - \frac{DT_{pwm}}{2}s\right)}{\left(1 + \frac{RC}{2}s\right)\left(1 + \frac{DT_{pwm}}{2M}s\right)}. \tag{8.26}$$

Equation (8.26) shows that the plant has two left-half poles and one right-half plane zero, but only one of them, i.e. the dominant pole $w_p = \frac{2}{RC}$, is located at a frequency less than half of the switching frequency. While the high frequency pole and zero is critical for predicting the intra-cycle phenomena in PCMC, their retention is not very useful for controller design which focuses on the inter-cycle behaviour only. For such reasons, the high frequency pole and zero Eq. (8.26) can be eliminated, which leads to

$$G_{vc}^{s2}(s) = \frac{V_{in}DR}{2nL_mM\left(M_a + \frac{V_{in}}{L_m}\right)} \frac{1}{\left(1 + \frac{RC}{2}s\right)}. \tag{8.27}$$

The simplified version of $G_{vc}(s)$ as given by Eq. (8.27) is consistent with the result reported in [3] which also relies on a small L_m assumption to simplify their model. Equation (8.27) does show the dependence of the converter gain and pole on the external excitation, i.e. the input voltage and output load. However, we want to express these parametric changes in a way which is tractable and intuitive for the control design step. For a DCM flyback converter with a resistive load, the following relations can be found

$$D = \frac{I_{pk}L_m}{V_{in}T_{pwm}}, \tag{8.28}$$

$$R = \frac{2V_{out}^2T_{pwm}}{L_mI_{pk}^2}, \tag{8.29}$$

$$I_{pk} = \frac{V_{in}I_{com}}{L_m\left(M_a + \frac{V_{in}}{L_m}\right)}, \tag{8.30}$$

where I_{pk} is the steady state peak current of the magnetizing inductor, while I_{com} indicates the steady state value of the command peak current which is proportional to the compensator output.

Substituting Eqs. (8.28), (8.29) and (8.30) into Eq. (8.27) yields

$$G_{vc}^{s2}(s) = \frac{V_{out}}{I_{com}} \frac{1}{1 + \frac{V_{out}^2 C T_{pwm}}{L_m I_{pk}^2} s}. \tag{8.31}$$

For some applications, if the compensation slope M_a is chosen such that $M_a \ll \frac{V_{in}}{L_m}$, Eq. (8.30) can be well approximated by $I_{pk} \approx I_{com}$ and Eq. (8.31) can be further simplified to

$$G_{vc}^{*}(s) = \frac{V_{out}}{I_{com}} \frac{1}{1 + \frac{V_{out}^2 C T_{pwm}}{L_m I_{com}^2} s}. \tag{8.32}$$

The accuracy of the modelling simplification process can be confirmed through comparing the frequency responses of the simplified transfer function $G_{vc}^{*}(s)$ in Eq. (8.32) with the original system $G_{vc}(s)$ given by Eq. (8.24), which is shown in Fig. 8.13. The results show that the differences between the frequency responses of the simplified and full model are negligible except for the phase in the vicinity of half the switching frequency and beyond that. The unmatched phase at high frequencies is definitely due to the cancellation of the high frequency pole and zero during the simplification step. All data in Fig. 8.13 is calculated based on the converter parameters in Table 8.2, with the input voltage $v_{in}(t) = 150$V, switching frequency $f_{pwm} = 110$kHz, compensation slope $M_a = 10^4$A/s, and 4 different values of the resistance load R = {5Ω, 100Ω, 500Ω, 2kΩ}.

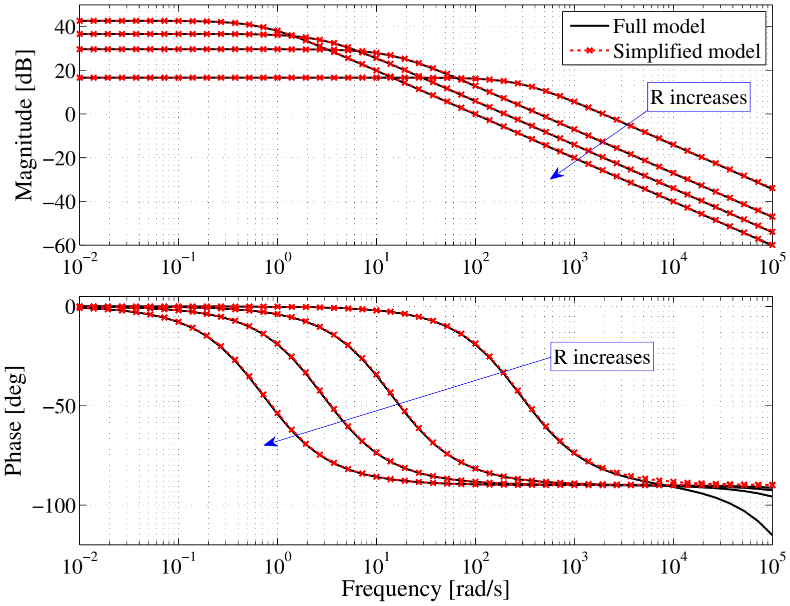

Figure 8.13: Frequency response of the open-loop PCM controlled flyback converter predicted by the full model $G_{vc}(s)$, as described by Eq. (8.24), and the simplified model $G_{vc}^{*}(s)$ in Eq. (8.32).

As implied in Eq. (8.32), the approximated gain of the converter is dependent on both the output voltage V_{out} and command inductor peak current I_{com}. Interestingly, V_{out} is a regulated variable and should be kept constant during the operation, so the gain of $G_{vc}(s)$ is essentially inversely proportional to I_{com}, which can help explain the high gain property of the DCM flyback converter.

The representation of the pole in Eq. (8.32) is somewhat complicated compared to that of Eq. (8.27); however, such a representation can help to explain the benefit of a fixed-parameter digital controller compared to its continuous-time counterpart. For example, if a continuous zero is employed to compensate for the plant pole in Eq. (8.32), this compensator zero will remain fixed irrespective of the movement of the converter pole due to the change of I_{com} and/or T_{pwm}, in response to a load variation. Unlike the continuous-time approach, a fixed discrete-time zero essentially behaves like a continuous-time counterpart, but varies correspondingly with the switching frequency. This effect can be exploited to compensate for the dependency of the flyback converter pole on T_{pwm}, as can be seen in Eq. (8.32).

8.4.3 Gain-adaptive predictive functional controller

8.4.3.1 Controller design

Since the converter model in Eq. (8.31) is simple and implementable, a model-based control method is a good choice for this application. Many techniques, such as Q-parameterization [243], predictive functional control (PFC) [244], etc., have been proposed to design a controller based on an internal model. In this work, PFC has been chosen because it allows a formulation of the control law directly in the z-domain.

PFC belongs to the family of model predictive controller; however, it makes use of an independent internal model and the measured process output to calculate the control action. The independent internal model means that the model output depends on the control variable only. In general, customizing the reference trajectory, i.e. the desired closed-loop time response, in PFC and adaptively deriving the control law are possible. However, for simplicity, the following settings are performed in this section:

- The reference trajectory is an exponential decay function $y(t) = e^{-\frac{t}{T_r}}$, where T_r is the time constant of the exponential decay.
- The coincidence point, i.e. the point where the future plant response should coincide with the reference trajectory, is set to 1 sample, i.e. $h = 1$.
- The internal model is based on the converter transfer function in Eq. (8.32).

According to the block diagram in Fig. 8.6, the internal model should be formed based on the transfer function from the compensator output $v_{com}(t)$ to the feedback signal $v_{fb}(t)$, which is

$$v_{mdl}(t) = \frac{K_{mdl}}{1 + \tau_{mdl} s} v_{com}(t), \tag{8.33}$$

where

$$K_{mdl} = \frac{H_{adc}H_{dac}H_{vs}H_{is}V_{out}}{I_{com}}, \tag{8.34}$$

$$\tau_{mdl} = \frac{V_{out}^2 C T_{pwm}}{L_m I_{com}^2}. \tag{8.35}$$

In order to represent the effect of the ADC and DAC in the plant, the zero-order-hold equivalent is employed to find the discrete-time equivalent of the internal model in Eq. (8.33), as given by

$$v_{mdl}(k) = \alpha v_{mdl}(k-1) + K_{mdl}(1-\alpha)v_{com}(k-1), \tag{8.36}$$

where $\alpha = e^{-(T_{pwm}/\tau_{mdl})}$. The expression of τ_{mdl} in Eq. (8.35) implies that α does not depend on the switching frequency. This result is consistent with the discussion in Section 8.4.2. Given the reference trajectory and the internal model, the control law can be formulated [244] as

$$v_c(k) = \frac{(V_{ref} - v_{fb}(k))(1-\lambda^h)}{K_{mdl}(1-\alpha^h)} + \frac{V_{mdk}(k)}{K_{mdl}}, \tag{8.37}$$

where $\lambda = e^{-\frac{3T_{pwm}}{T_r}}$. Since the desired response of the closed-loop system is specified through the reference trajectory, the controller can be tuned by varying the value of T_r and h. As a rule of thumb, the desired settling time of the closed-loop system is typically approximated by $3T_r$. Notice that if the parameter λ is kept fixed during the operation, the ratio T_{pwm}/T_r will be constant, which implies that the closed-loop response will be forced to follow the switching period.

8.4.3.2 Internal model update and implementation

When the converter moves away from the designed operating point, the internal model as given by Eq. (8.36) is less accurate. Fortunately, the model can be updated to cope with the new working condition. Let's revisit the model equations in Eqs. (8.36), (8.34) and (8.35). Since both the model gain and pole are dependent only on the steady state value of the command inductor peak current I_{com}, updating both of these internal model parameters is possible. However, recalculating K_{mdl} requires much less computational power than updating τ_{mdl}. As a result, only gain adaptation will be exploited in this study. Due to the availability of the compensator output V_{com} in the implementation, I_{com} will be replaced by $V_{com}H_{dac}H_{is}$ in the calculation of K_{mdl} in Eq. (8.34).

Due to the presence of the parameter K_{mdl} in both the internal model Eq. (8.36) and the control law Eq. (8.37), the gain adaptation process wastes a lot of computation power for only updating K_{mdl} and, as a result is, computationally inefficient. Fortunately, this issue can be handled by dividing the two sides of Eq. (8.36) by K_{mdl} and then replacing $v_{mdl}(k)/K_{mdl}$ with $v_{mds}(k)$. The resulting model and control law are given by

$$v_{mds}(k) = \alpha v_{mds}(k-1) + (1-\alpha)v_{com}(k-1), \tag{8.38}$$

$$v_{com}(k) = \frac{(V_{ref} - v_{fb}(k))(1-\lambda)}{K_{mdl}(1-\alpha)} + v_{mds}(k). \tag{8.39}$$

The complete structure of PFC with gain adaptation is illustrated in Fig. 8.14, where two first-order unity-DC-gain low-pass filters, named $G_{lp1}(z)$ and $G_{lp2}(z)$, are added to the compensator for the purpose of filtering high-frequency noise and supporting the gain-adaptation function. Since the main function of $G_{lp1}(s)$ is to eliminate the high-frequency noise, its cut-off frequency should be chosen to be close to half of the sampling frequency and away from the system loop-gain cross-over point. The low-pass filter $G_{lp2}(z)$ is employed to obtain a quasi-steady-state representation of the compensator output which is required to update the compensator gain K_{mdl} in Eq. (8.39). The cut-off frequency of $G_{lp2}(s)$ should be smaller than $T_{pwm}/20$.

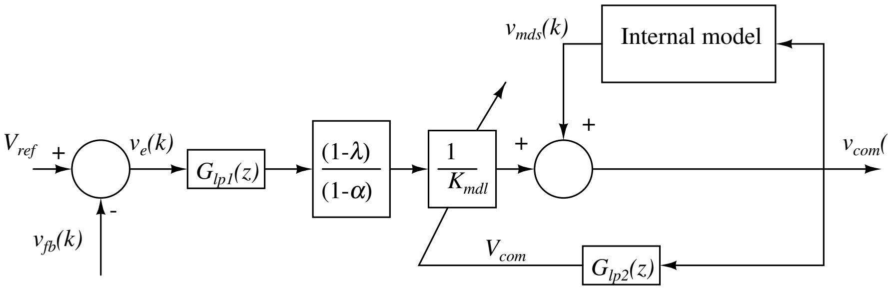

Figure 8.14: Block diagram of the adaptive predictive functional controller, where both $G_{lp1}(z)$ and $G_{lp2}(z)$ are digital low-pass filters. The use of $G_{lp1}(z)$ is to filter out all the high frequency noise invading the feedback signal through the sampling process, while $G_{lp2}(z)$ is required for the gain adaptation function.

8.4.4 Simulation and experimental evaluations

The gain-adaptive predictive functional controller (GAPFC) proposed in Section 8.4.3 is evaluated and implemented in this section. The 65W flyback converter, whose parameters are listed in Table 8.2, is reused for examining the proposed controller. The converter operates in DCM, and varies its operating point whenever it sees a fluctuation in either input voltage or load current.

Table 8.3: Parameters of the proposed GAPFC

K_{mdl}	4.316
α	0.998
λ	0.9048
Low-pass digital filter $G_{lp1}(z)$	$0.1515\frac{1+0.98z^{-1}}{1-0.7z^{-1}}$
Low-pass digital filter $G_{lp2}(z)$	$0.125\frac{z^{-1}}{1-0.875z^{-1}}$

Let's consider the nominal operating point with the input voltage $V_{in} = 150$V, the output load $R = 6.5\Omega$, the switching frequency $f_{pwm} = 110$kHz, and the compensation slope $M_a = 10^4$A/s. The converter is expected to have a critically damped response and settle after 90 switching cycles, i.e. $T_r = 30T_{pwm}$. The parameters of the gain-adaptive PFC are listed in Table 8.3.

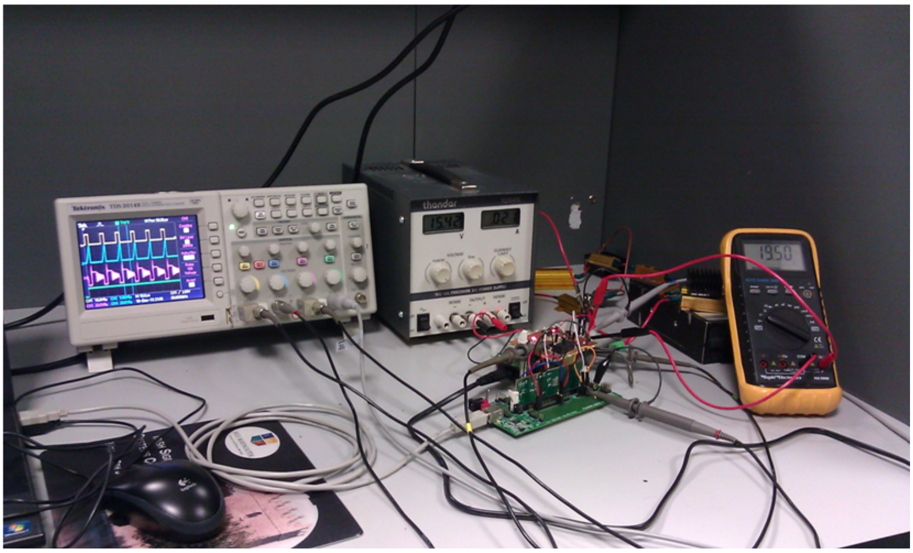

(a) Far view

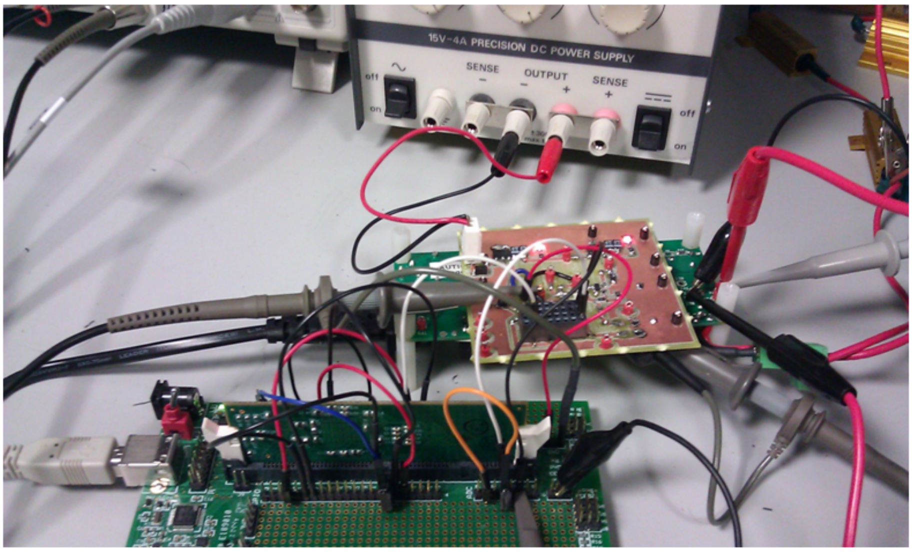

(b) Closed-up

Figure 8.15: Flyback power stage and a TI C2000 microcontroller assembly on the test bench.

Both simulation and experiment are employed to evaluate the stability and performance of the obtained controller. The simulation implemented in the MATLAB/SIMULINK environment is based on the control-oriented model of the flyback converter, as studied in Chapter 6, and the designed controller, while the experiment is set up with a flyback power stage interfaced with a TI C2000 microcontroller (F28069 Piccolo ControlSTICK) and an external gate drive circuit. The digital optimum control structure in Fig. 8.1 is implemented entirely in the C2000 microcontroller, which minimizes the use of the external hardware. The photos of the test bench used for experimental purposes are shown in Fig. 8.15.

A standard step-load test from 5% to 95% of the maximum load power is applied in the tests. The converter transient response over different working conditions from both simulation and

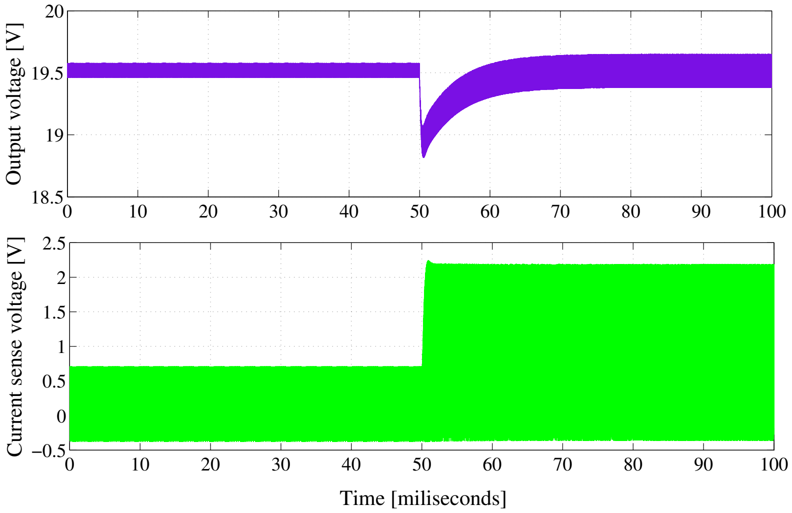

(a) Simulated results: $v_{out}(t)$ = upper curve, $v_{cs}(t) = R_s i_{in}(t)$ = lower curve

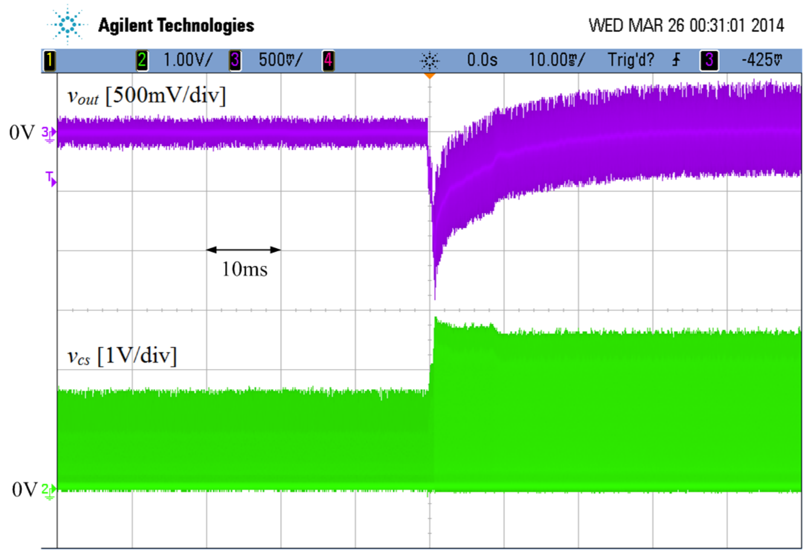

(b) Experimental results: $v_{out}(t)$ = Ch3 [500mV/div], $v_{cs}(t) = R_s i_{in}(t)$ = Ch2 [1V/div]

Figure 8.16: Transient responses of the converter output voltage and inductor current (through current sense voltage) when a 118.18Ω to 6.19Ω step load and an input voltage $v_{in}(t) = 150$V are used. The data is collected from (a) simulation and (b) experiment.

experiment are captured and plotted in Fig. 8.16 where the load is stepped from 118.18Ω to 6.19Ω, and in Fig. 8.17, where the load is stepped from 6.19Ω to 118.18Ω. In both test cases, the input voltage is set to $v_{in}(t) = 150$V. The simulated results from Figs. 8.16(a) and 8.17(a) confirm that the proposed controller can provide zero steady state errors, i.e. the output voltage is brought back to the nominal operating value after a transient time, and relatively fast transient responses which satisfy both requirements on the output voltage drop and settling time. Similar observations about the control performance can be drawn from the experimental data in Figs. 8.16(b) and 8.17(b) except that the zero steady-state error property cannot be verified because the output voltage is captured in the AC coupling mode of the oscilloscope which means that only variations around the

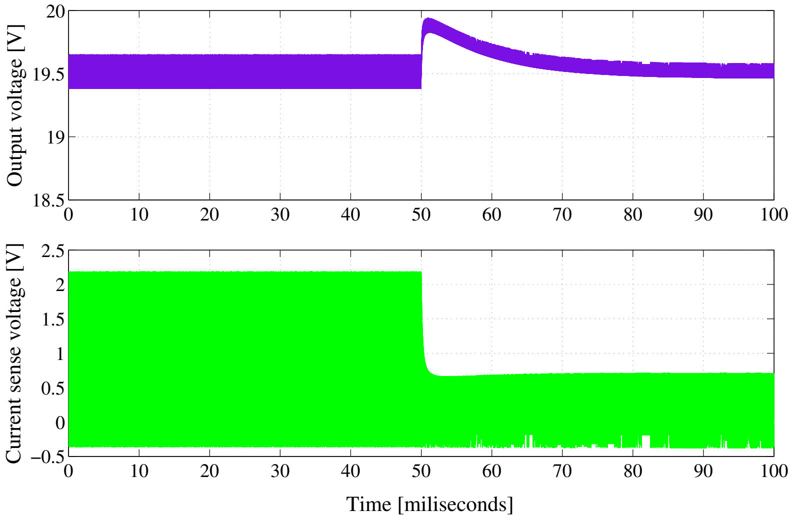

(a) Simulatied results: $v_{out}(t)$ = upper curve, $v_{cs}(t) = Ri_{in}(t)$ = lower curve

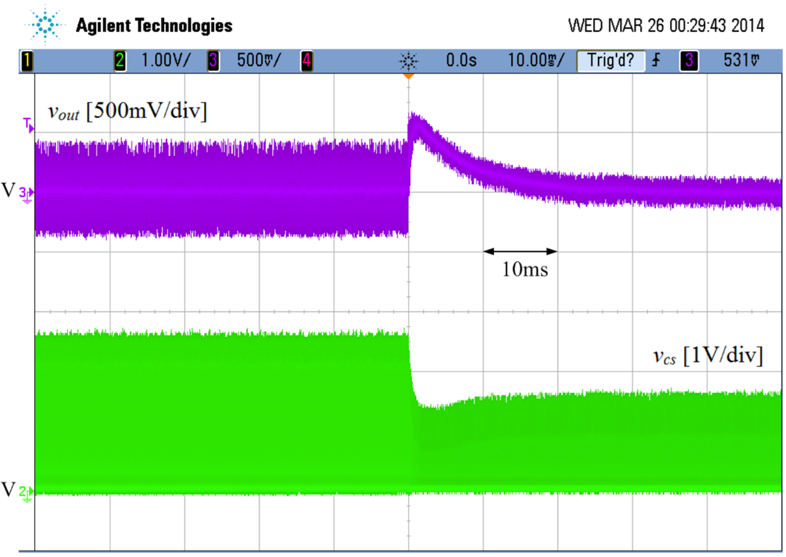

(b) Experimental results: $v_{out}(t)$ = Ch3 [500mV/div], $v_{cs}(t) = Ri_{in}(t)$ = Ch2 [1V/div]

Figure 8.17: Waveforms of the converter output voltage and inductor current (through current sense voltage) in response to a 6.19Ω to 118.18Ω step load with $v_{in}(t) = 150$V. The data is collected from (a) simulation and (b) experiment.

DC level are transmitted through and shown in the oscilloscope's screen. The reason for not using the DC coupling option is simply because of the large ratio between the DC value and variations in the output voltage.

As can also be seen from Figs. 8.16 and 8.17, the simulated results are consistent with the experimental ones, and can accurately predict the behaviour of the closed-loop system under different loading conditions. The only discrepancy that can be found is between the amplitudes of the simulated and experimental current sense voltages, which is probably due to the presence of the spike in the experiment inductor current waveform, which is typically ignored in the modelling process. The similarity between the simulated and experimental waveforms, in conjunction with the results presented in Section 6.4, further confirms the accuracy and usefulness of the control-oriented modelling method proposed in Chapter 6.

Due to some difficulties in measuring internal signals of the microcontroller, no specific test has been provided to evaluate the performance of the digital MS circuit in Fig. 8.1. Fortunately, the results in Figs. 8.16 and 8.17 can be used as an indirect means to validate the accuracy and robustness of the proposed MS solution. More precisely, the zero steady state error can only be achieved if the feedback signal from the MS block in Fig. 8.1 is accurate while the stability of the whole control solution is also influenced by the robustness of the sensing circuit.

Figures 8.16 and 8.17 also show that the proposed controller offers an acceptable recovery time and specifically a critically-damped closed-loop response which is an expected property when using an exponential decaying function as the reference trajectory, refer to Section 8.4.3.1 for more details.

8.5 Robust gain-adaptive digital controller

Although the controller designed using the predictive function control theory in Section 8.4 can achieve zero steady state errors and transient response performance compatible with the control specifications in Table 8.1, the stability of the closed-loop flyback converter is still an open question and needs further investigation.

With the aim of seeking a controller which can perform as well as that in Section 8.4 but also has the global stability property of the compensator synthesized in Section 8.3, this section proposes a robust gain-adaptive controller which is synthesized based on the results developed in Section 8.4, except that quantitative feedback theory (QFT) is used instead of predictive functional control theory.

8.5.1 Model uncertainty reduction through adaptation

Since both the gain and pole of the plant model in Eq. (8.32) vary according to the operating point, the behaviour of the converter over a working space, as specified in Table 8.2, can be described by a set of transfer functions, whose mathematical representation can be derived, with an assumption that only PCMC is used throughout the operation, as

$$G_{vcp}(s) = \frac{V_{out}}{I_{com}} \frac{1}{1 + \frac{V_{out}^2 C T_{pwm}}{L_m I_{com}^2} s}, \quad I_{com} \in [I_{cmin}, I_{cmax}], \quad T_{pwm} \in [T_{pmin}, T_{pmax}], \tag{8.40}$$

where I_{cmin}, I_{cmax}, T_{pmin} and T_{pmax} are the extreme values of the command peak current and PWM switching period, respectively. These extreme values can be calculated from the control specifications in Table 8.2 and the relations in Eqs. (8.28), (8.29) and (8.30). Notice that Eq. (8.40) is similar to Eq. (8.32), except that Eq. (8.40) represents a set of perturbed plants rather than a model at a single operating point.

In principal, the global stability of the converter can be achieved through finding the controller which can stabilize all the perturbed plants within the set in Eq. (8.40); however, a direct application of robust control theory to the system in Eq. (8.40) may result in a globally stable controller but with poor control performance, as highlighted in Section 8.3. Two possible solutions, which can be applied to enhance the converter performance, are (1) keeping the model perturbation set in Eq. (8.40) unchanged but giving up some stability, and (2) reducing the variation range of the perturbed set. The latter approach is considered in this section.

The gain of the converter model in Eq. (8.40) is inversely proportional to the command peak current I_{com}. This dependence can be eliminated by a simple gain-adaptive mechanism which utilizes a low-pass filter to obtain a quasi-steady-state version of I_{com} from the compensator output V_{com}, and a multiplication operator to eliminate the dependency on I_{com}. The functional diagram of the gain-adaptive function is shown in Fig. 8.18, where the digital low-pass filter $G_{lp}(z)$ is formulated by

$$G_{lp}(z) = \frac{1}{V_{sf}} \frac{kz^{-1}}{1-(1-k)z^{-1}}, \tag{8.41}$$

where V_{sf} is a scaling factor, while k is the filter parameter which should be chosen to ensure that the cut-off frequency of $G_{lp}(s)$ is smaller than $T_{pwm}/20$. The transfer function of the gain-adaptive block can be simply described by

$$G_{ga}(s) = \frac{V_{com}}{V_{sf}}. \tag{8.42}$$

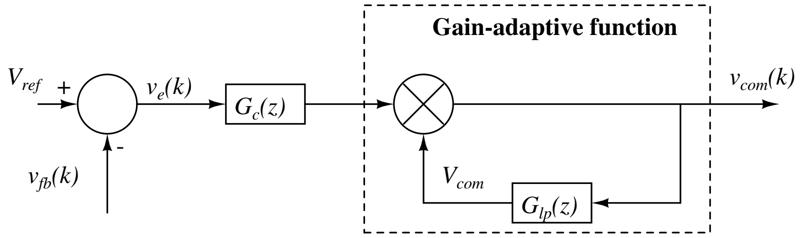

Figure 8.18: Realization of the gain-adaptive function in digital control, where $G_{lp}(z)$ is a first-order digital low-pass filter used to obtain the the steady state value of $v_{com}(k)$ while $G_c(z)$ denotes the robust compensator needs to be designed.

In addition to gain-variation elimination, the dependence of the model dynamics on the switching period T_{pwm} can be reduced by exploiting the variable sampling rate technique proposed in Section 8.4.1. If the parameters of $G_c(z)$ are chosen to be similar to that of the transfer function described by Eq. (8.21), its Tustin continuous-time equivalent will be

$$G_c(s) = G_{c0} \frac{\left(1 - \frac{sT_{pwm}}{w_{z1}}\right)\left(1 - \frac{sT_{pwm}}{w_{z2}}\right)}{sT_{pwm}\left(1 - \frac{sT_{pwm}}{w_{p1}}\right)}. \tag{8.43}$$

Given the compensator, gain adaptive function and plant model, the loop gain of the controlled flyback converter in Fig. 8.6 can be calculated via

$$\begin{aligned} L(s) &= G_c(s)G_{ga}(s)H_{dac}H_{is}G_{vcp}(s)H_{vs}H_{adc} \\ &= \frac{G_{c0}H_{adc}H_{vs}V_{out}}{V_{sf}} \frac{\left(1-\frac{sT_{pwm}}{w_{z1}}\right)\left(1-\frac{sT_{pwm}}{w_{z2}}\right)}{sT_{pwm}\left(1-\frac{sT_{pwm}}{w_{p1}}\right)\left(1+\frac{V_{out}^2 CsT_{pwm}}{L_m I_{com}^2}\right)}. \end{aligned} \tag{8.44}$$

Equation (8.44) implies that the use of a variable switching frequency results in a shift in the frequency response of the loop gain $L(s)$. In particular, the magnitude and phase responses of $L(s)$ are shifted to the left when the switching frequency f_{pwm} decreases and to the right when f_{pwm} increases, as demonstrated in Fig. 8.19. Since f_{pwm} does not affect the shape of the magnitude and phase responses of the loop gain $L(s)$ but only shifts them along the frequency axis, the stability of the closed-loop system, which can be determined from the frequency response of $L(s)$, is not influenced by variations of f_{pwm}. For such a reason, designing a robust controller for the perturbed plants in Eq. (8.40) can be simplified to designing a robust controller for a smaller set of plants, given by

$$G_{vcp}(s) = \frac{V_{out}}{I_{com}} \frac{1}{1+\frac{V_{out}^2 CT_{pwm0}}{L_m I_{com}^2}s}, \quad I_{com} \in [I_{cmin}, I_{cmax}], \tag{8.45}$$

where T_{pwm0} is any switching period satisfying $T_{pwm0} \in [T_{pmin}, T_{pmax}]$.

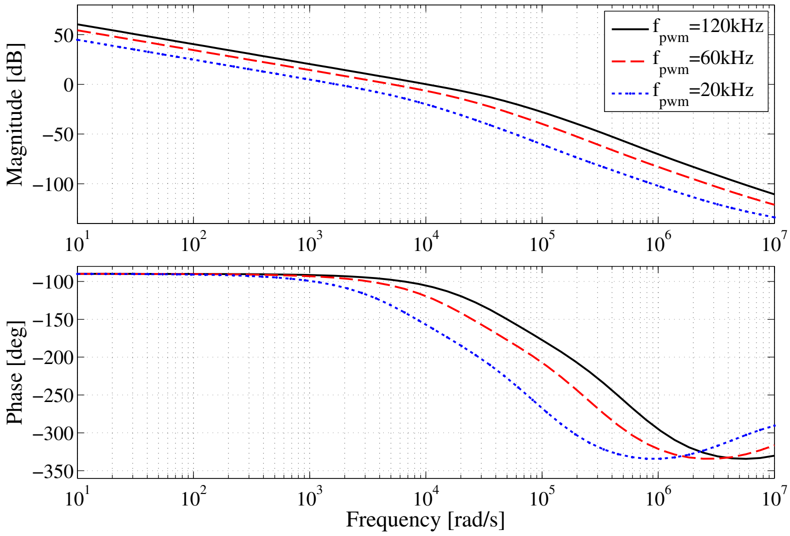

Figure 8.19: Numerical illustration of the frequency responses of the loop-gain $L(s)$ evaluated at three different switching frequencies 120kHz, 60kHz, and 20kHz.

To facilitate the control design step, the small signal model in Fig. 8.6 is reconstructed and simplified to the system as illustrated in Fig. 8.20, where $G_{rp}(s)$ is the residual plant transfer function which can be described by

$$G_{rp}(s) = \frac{H_{adc}H_{vs}V_{out}}{V_{sf}}\frac{1}{1+\frac{V_{out}^2 C T_{pwm0}}{L_m I_{com}^2}s}, \quad I_{com} \in [I_{cmin}, I_{cmax}]. \tag{8.46}$$

After the uncertainty inside the flyback converter has been minimized through the gain-adaptive function and the variable-sampling rate method, a robust controller is required to handle the leftover model uncertainty in $G_{rp}(s)$ of Eq. (8.46) which is not modelled or compensated. The robust controller design using, QFT, is discussed in Section 8.5.2.

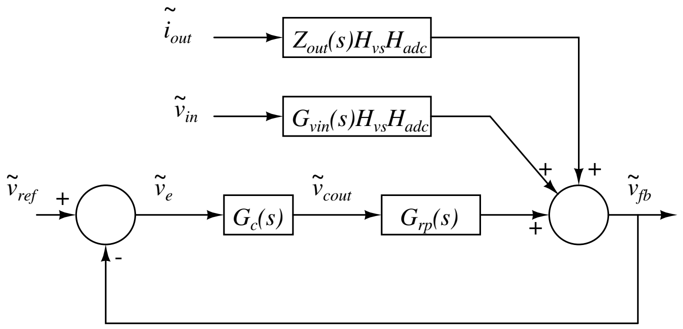

Figure 8.20: Functional diagram of the digitally controlled flyback converter after collecting the plant model $G_{vcp}(s)$ and the transfer functions of the voltage- and current-sense circuits, and gain-adaptive mechanism into a single transfer function $G_{rp}(s)$. $G_c(s)$ is the continuous-time equivalent of $G_c(z)$.

8.5.2 QFT robust compensator synthesis

Quantitative feedback theory (QFT) makes use of the Nichols chart to synthesize (loop-shape) a simple, low-order, robust controller for systems with uncertainty [245]. In particular, the robust stability condition and robust performance condition are specified in the time domain and equivalently represented by bounds (constraints) in the Nichols chart. Similarly, the variations in the magnitude and phase of the plant model are also mapped into the Nichols chart and surrounded by some closed curves called templates. Given the graphical representation of the system variations (templates), and stability and performance constraints (bounds), the loop-shaping technique is then applied to find the robust controller that satisfies all the desired specifications. In this section, QFT is applied to synthesize the robust controller for the system discussed in Section 8.5.1.

The 65W flyback converter, whose parameters are listed in Table 8.2, is reused for control design purposes. The converter is assumed to operate in DCM only. The switching frequency and the compensation slope are chosen to be $f_{pwm0} = \frac{1}{T_{pwm0}} = 100\text{kHz}$ and $M_a = 10^4\text{A/s}$. The digital low-pass filter $G_{lp}(z)$ in Eq. (8.41) is designed with the scaling factor $V_{sf} = 2^{10}$ and the filter parameter $k = 0.125$. Given the converter parameters, T_{pwm0}, and M_a, the numerical version of the residual plant transfer function $G_{rp}(s)$ in Eq. (8.46) can be computed as

$$G_{rp}(s) = \frac{2.602}{1 + \frac{s}{p}}, \quad p \in [12.06 \quad 769.67]\,. \tag{8.47}$$

As a part of the QFT design approach, a nominal plant is required and is typically chosen among the family of the perturbed plants in Eq. (8.47). One of the possibilities is

$$G_{rpn}(s) = \frac{2.602}{1 + \frac{s}{600}}. \tag{8.48}$$

8.5.2.1 Template generation

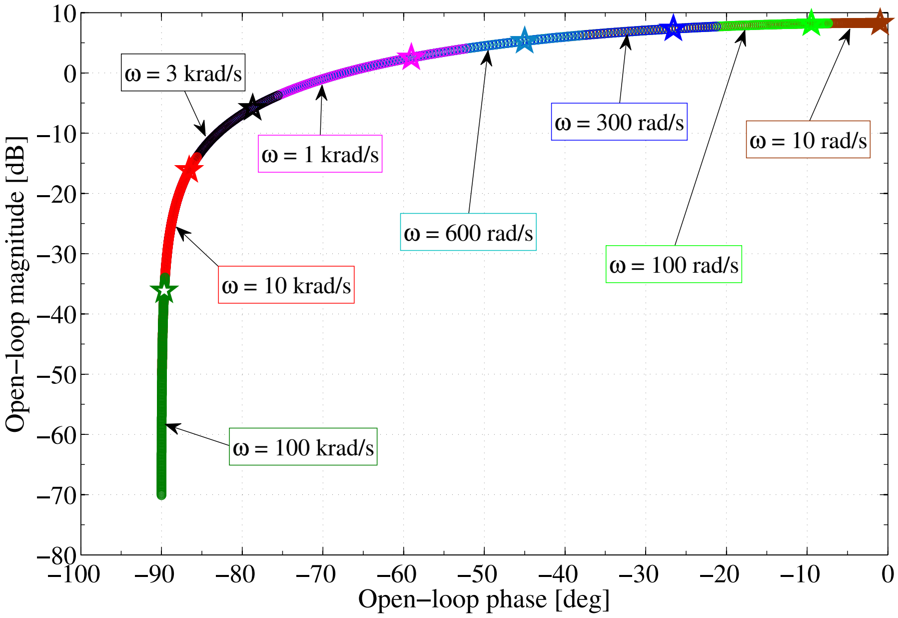

Figure 8.21: Frequency response of the residual plant transfer function $G_{rp}(s)$ at the quantized frequencies Ω_p. The nominal plant is indicated by star symbols in the templates.

The first step in designing a controller with QFT is to pictorially represent the uncertainty of the system under consideration in the Nichols chart. Essentially, for a fixed value of the parameter p in Eq. (8.47), the frequency response of $G_{rp}(s)$ at any frequency $\omega = \omega_1$ is a point in the Nichols chart. Due to the parametric uncertainty of p, the relation between the magnitude and phase responses of $G_{rp}(s)$, for the given frequency ω_1, can be described by a set of possible points, each point corresponds to a member of the family of the plant. Such a set of points defines a region in the Nichols chart known as a plant template [245]. Before plotting the plant templates, the frequency range of interest should be defined and quantized. For the flyback converter application, the following frequencies are considered

$$\Omega_q = \begin{bmatrix} 10 & 100 & 300 & 600 & 1000 & 3000 & 10^4 & 10^5 \end{bmatrix} \text{(rad/s)}. \tag{8.49}$$

The templates of the residual plant $G_{rp}(s)$ at the quantized frequencies Ω_q are plotted in Fig. 8.21, where the nominal plant is represented by star symbols.

8.5.2.2 Closed-loop performance specifications and QFT bounds

In QFT control, the stability of the closed-loop system can be defined in terms of minimum gain- and phase-margins while the closed performance, i.e. disturbance rejection, can be specified through upper bounds on the system sensitivity function. In addition to stability and disturbance rejection, other existing closed-loop specifications, such as reference tracking, noise rejection, and control effort, can be included in the synthesis of the controller. However, only conditions for robust stability and performance are considered, because they are the most demanding properties in flyback converter applications.

A. Robust stability: The stability of the closed-loop system in Fig. 8.20 can be achieved by imposing a constraint on the peak magnitude of the system complementary sensitivity $T(s)$ function via

$$|T(j\omega)| = \left|\frac{L(j\omega)}{1+L(j\omega)}\right| \leq \gamma, \quad \forall\omega > 0 \text{ and } \forall G_{rp}(s), \tag{8.50}$$

where $L(s) = G_{rp}(s)G_c(s)$ denotes the open loop gain, while γ is a constant bound which has a direct relation with the minimum phase margin (PM) and the minimum gain margin (GM) [245] via

$$PM = 2\arcsin(\frac{1}{2\gamma}) \text{ [deg]}, \quad GM = 20\log(\frac{\gamma+1}{\gamma}) \text{ [dB]}. \tag{8.51}$$

B. Robust performance : To fulfil the requirements of disturbance attenuation, the magnitude of the system sensitivity function $S(s)$ is forced to satisfy

$$|S(j\omega)| = \left|\frac{1}{1+L(j\omega)}\right| \leq |S_{bound}(j\omega)|, \quad \forall\omega > 0 \text{ and } \forall G_{rp}(s) \tag{8.52}$$

where $S_{bound}(s)$ is the desired system sensitivity function that is constructed based on the specifications for input and output disturbance rejection.

For the problem at hand, the minimum gain- and phase-margins are set to $PM = 45°$ and $GM = 4.95$dB, which results in a peak magnitude constraint of

$$\gamma = 1.3. \tag{8.53}$$

The upper boundary on the sensitivity function is chosen as,

$$S_{bound}(s) = \frac{s(s+65000)}{(s+600)(s+4000)}. \tag{8.54}$$

Given the nominal plant $G_{rpn}(s)$ in Eq. (8.48), the QFT methodology converts the closed-loop system specifications and model uncertainty at the quantized frequencies, as investigated in Section 8.5.2.1, to a set of constraints or bounds in the Nichols chart. Different procedures are required

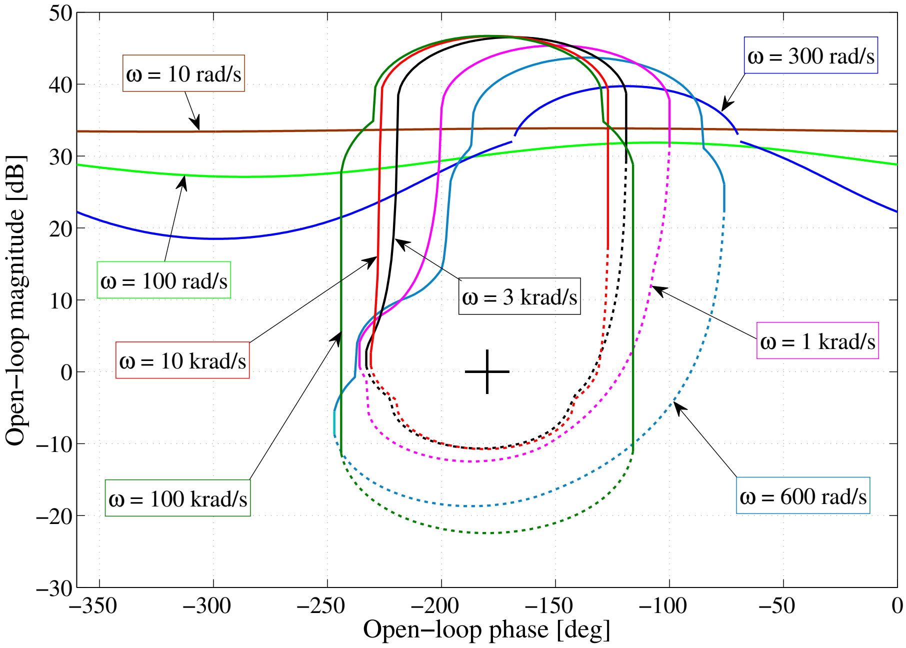

Figure 8.22: Composite bounds $B(\omega)$ computed at the quantized frequencies in the vector Ω_q based on the plant templates in Section 8.5.2.1 and the stability and performance specifications.

for the generation of bounds depending on the type of closed-loop specifications which needs to be mapped into the Nichols chart. The procedures for generating stability bounds and disturbance bounds are well documented in [245] and hence are not presented here. For the implementation of these procedures in MATLAB, one can refer to the QFT control toolbox [246].

For each quantized frequency in the vector Ω_q, multiple bounds, each of which corresponds to a closed-loop specification, can be found. For simplicity, the bounds at each frequency are combined together to form a composite bound covering all the worst-case scenarios of the bounds involved [245]. The composite bounds, termed $B(\omega)$, corresponding to the quantized frequency vector Ω_p, are shown in Fig. 8.22.

8.5.2.3 QFT loop-shaping controller

The task in this section involves synthesising the controller $G_c(s)$ using the Nichols chart and the classical loop-shaping approach. Given the control structure of $G_c(s)$, in Eq. (8.43), the objective is to adjust the compensator gain, poles and zeros until the nominal system loop-gain, defined as $L_{nom}(s) = G_c(s)G_{rpn}(s)$, lies near but outside the forbidden regions enclosed by the set of composite bounds obtained in Section 8.5.2.2. Since the bounds on the Nichols chart are combinations of the stability and performance specifications and model uncertainty, satisfying these bounds means that the obtained controller is able to achieve both robust stability and performance. One of the possible designs of the compensator obtained from the loop-shaping technique is

$$G_c(s) = \frac{2.013(s+295)(s+22.5\cdot 10^4)}{s(s+3.02\cdot 10^4)}. \tag{8.55}$$

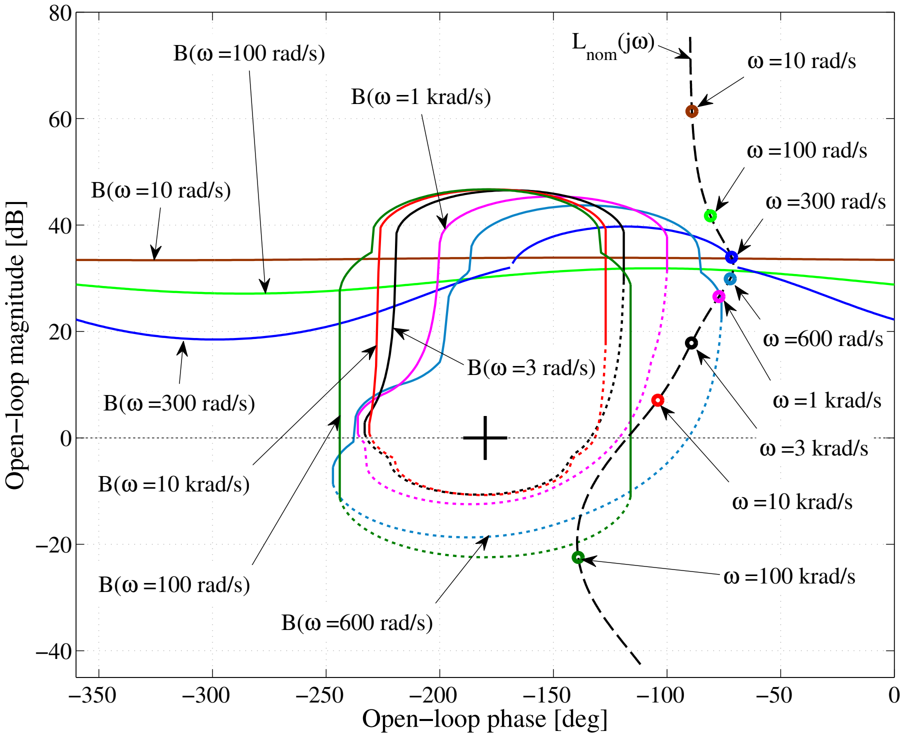

Figure 8.23: Graphical illustration of the controller synthesis procedure using the loop-shaping technique. The parameters of $G_c(s)$ are chosen such that the nominal loop gain $L_{nom}(s)$ meets the design criterion.

The nominal loop gain $L_{nom}(s)$, calculated from $G_c(s)$, is illustrated together with the composite bounds $B(\omega)$ in Fig. 8.23. The synthesis of $G_c(s)$ in Eq. (8.55) may require some iterations until both stability and performance constraints are satisfied; however, with the help of graphical design, the parameter tuning process can be achieved in a relatively short period of time.

8.5.3 Stability and performance validation

The QFT controller $G_c(s)$ in Eq. (8.55) has been loop-shaped to satisfy the closed-loop specifications for a finite set of frequencies, which does not mean that such a condition holds for any other frequency, inside or outside the considered range. For such a reason, a validation of $G_c(s)$ should be made.

The stability and performance of $G_c(s)$ in Eq. (8.55) can be theoretically verified using the conditions specified in Eqs. (8.50) and (8.52), which require calculation of the sensitivity function and complementary sensitivity function for all plants in the perturbed set, at all frequencies. Since the comparison in Eqs. (8.50) and (8.52) focuses on the peak values of the magnitude of $T(s)$ and $S(s)$, the envelopes of these magnitudes should be used instead. Figure 8.24 shows the magnitude envelopes of the complementary sensitivity functions for all perturbed plants along with the robust stability bound defined in Eq. (8.53), while the comparison between the performance bounds in Eq. (8.54) and the sensitivity functions are considered in Fig. 8.25. The results in Figs. 8.24 and 8.25 show that the magnitude envelopes of $T(s)$ and $S(s)$ are well below the robustness bounds, which confirms that $G_c(s)$ can meet all the specified robust stability and disturbance attenuation requirements and that the worst-case performance of $G_c(s)$ occurs at a frequency in the vicinity of 300 rad/s.

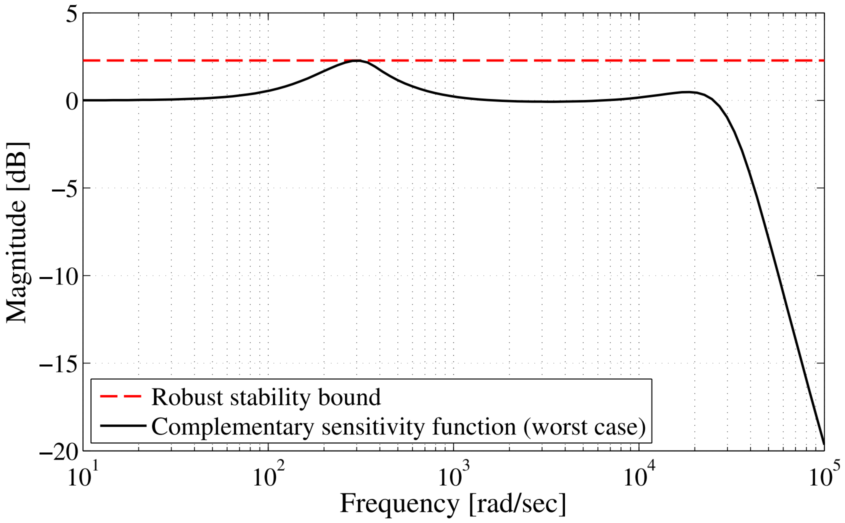

Figure 8.24: Magnitude envelope of the complementary sensitivity function of all plants in the perturbed set and the robust stability bound γ.

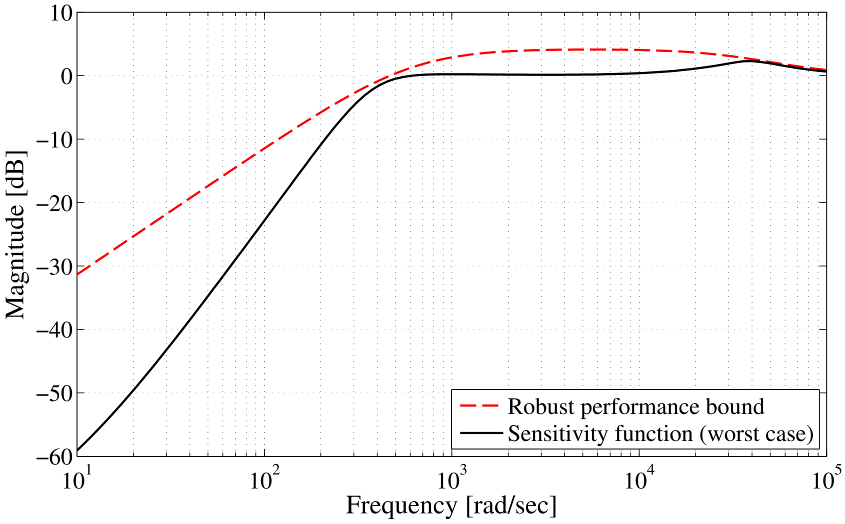

Figure 8.25: Magnitude envelope of the sensitivity function of all plants in the perturbed set and the robust performance bound $S_{bound}(s)$.

In addition to the theoretical validation, the obtained controller $G_c(s)$ is also experimentally tested by the 65W flyback converter prototype, whose design and parameters have been described in detail in Section 8.4.4. For implementation, $G_c(s)$ is discretized with a sampling period $T_{pwm0} =$

10μs, which results in

$$G_c(z) = \frac{2.013\left(1 - 0.9971z^{-1}\right)\left(1 + 0.9446z^{-1}\right)}{\left(1 - z^{-1}\right)\left(1 - 0.7393z^{-1}\right)}. \tag{8.56}$$

The proposed optimum control and digital QFT controller $G_c(z)$ can be implemented in a similar way as mentioned in Section 8.4.4. Two types of external source disturbances, including input voltage and output load, are typically employed in industry to examine the performance of switched-mode power supplies. However, only output load disturbances are considered in this study because they are the most demanding and important assessment for PCM controlled flyback converters. Four commonly used load schemes which are considered for the experiment are listed in the order of level of challenge for the controller below:

Load profile 1: Periodically varying load whose value steps back and forth between 1.65A to 3.33A every 50ms, or equivalently between 50% to 100% of the maximum output power.

Load profile 2: Periodically varying load whose value steps back and forth between 0.165A to 1.65A every 50ms, or equivalently between 5% to 50% of the maximum output power.

Load profile 3: Periodically varying load whose value steps back and forth between 0.165A to 3.15A every 50ms, or equivalently between 5% to 95% of the maximum output power.

Load profile 4: Periodically varying load who value steps back and forth between 1mA to 3.3A every 100ms, or equivalently between the minimum to maximum output power.

The experimental results corresponding to the load profiles 1, 2, 3 and 4 are collected by an oscilloscope and shown in Figs. 8.26(a), 8.26(b), 8.27(a), and 8.27(b), respectively. In these experiments, the input voltage is kept constant and set to a value of $v_{in}(t) = 150V$. The output voltage is measured with the AC coupling function of the oscilloscope, while the DC coupling option is used for other signals, including $i_{out}(t)$ and $v_{cs}(t)$.

The experimental data in Figs. 8.26 and 8.27 shows that the proposed controller can robustly and quickly regulate the output voltage, regardless of variations in the output load. In most case, the voltage drop due to load variations is small and falls within the tolerance range defined in Table 8.1, except for the most extreme test as shown in Fig. 8.27(b), which shows a significant voltage drop of around 3V. The failure in this test is due to the fact that the bandwidth of the closed-loop system, which depends on the switching frequency, is very low at light load and at no load, where the switching frequency is set to a value of around 1kHz or lower. A sudden change in the output load does not give enough time for the controller to react, which results in a large drop in the output voltage. In addition to the slow closed-loop responses at light and no load, the use of the magnetic sensing function, which introduces a delay into the feedback loop, also exacerbates the situation.

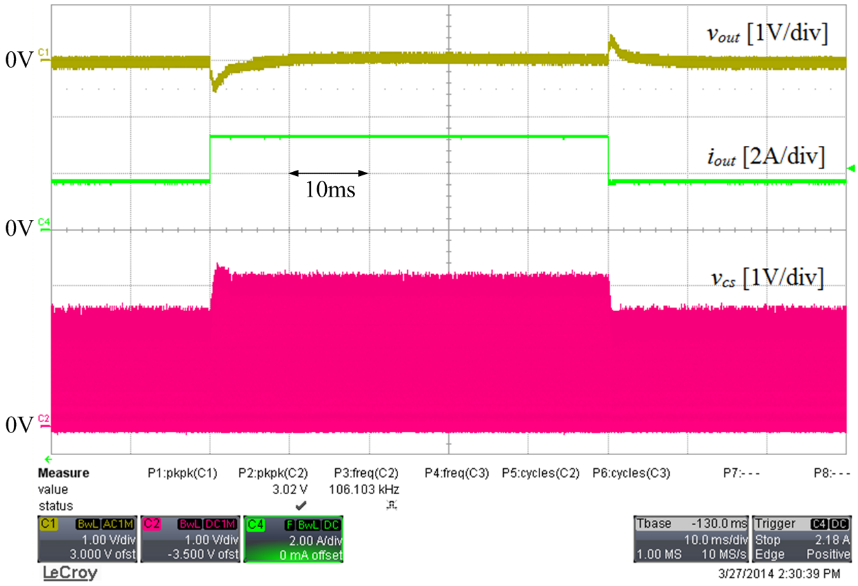

(a) Load profile 1

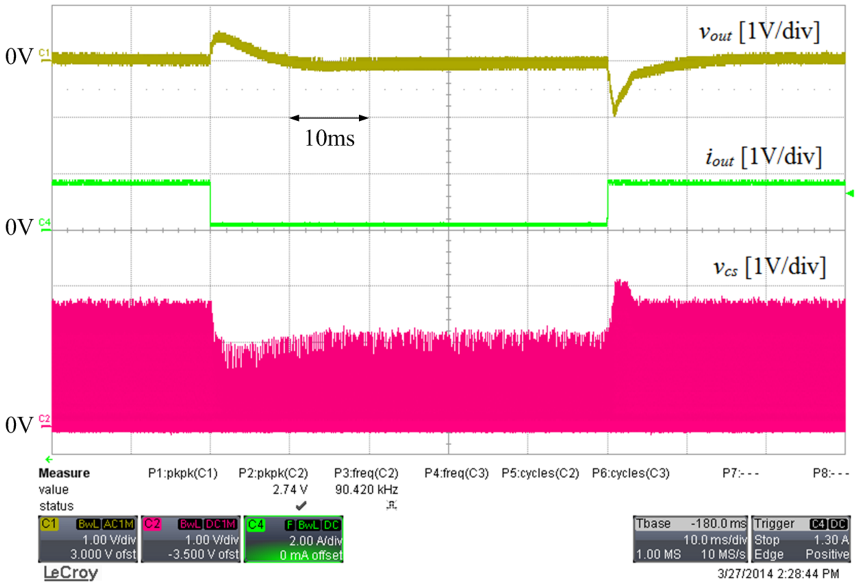

(b) Load profile 2

Figure 8.26: Dynamic responses of the converter output voltage $v_{out}(t)$ and input current (through current sense voltage $v_{cs}(t)$) against load disturbance: (a) stepping between 0.165A to 1.65A every 50ms and (b) stepping between 1.65A to 3.33A every 50ms. The input voltage is set to $v_{in}(t) = 150V$.

8.6 Conclusion

This chapter is aimed at designing and implementing digital optimum control for a variable-frequency wide-operating range flyback converter. The control solution can provide high energy conversion efficiency, global stability, high performance and, most importantly, can be implemented with a low-cost microcontroller.

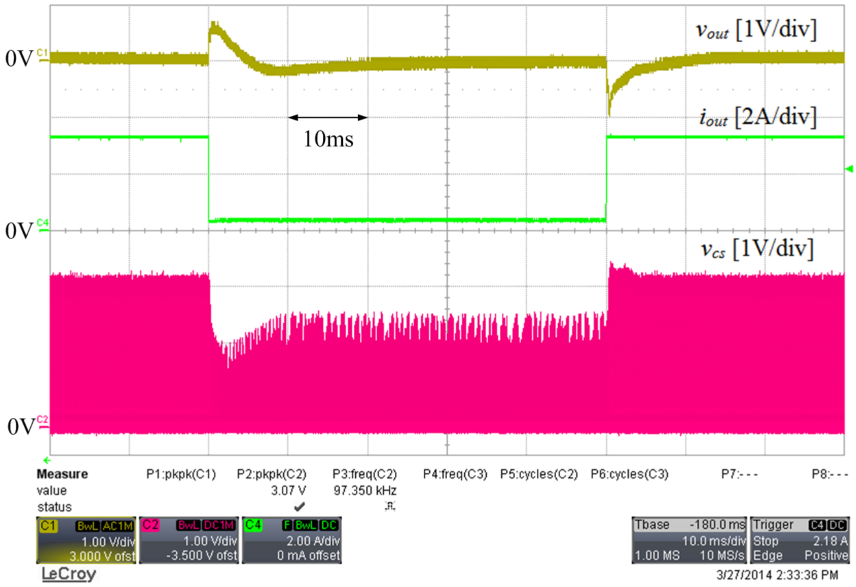

(a) Load profile 3

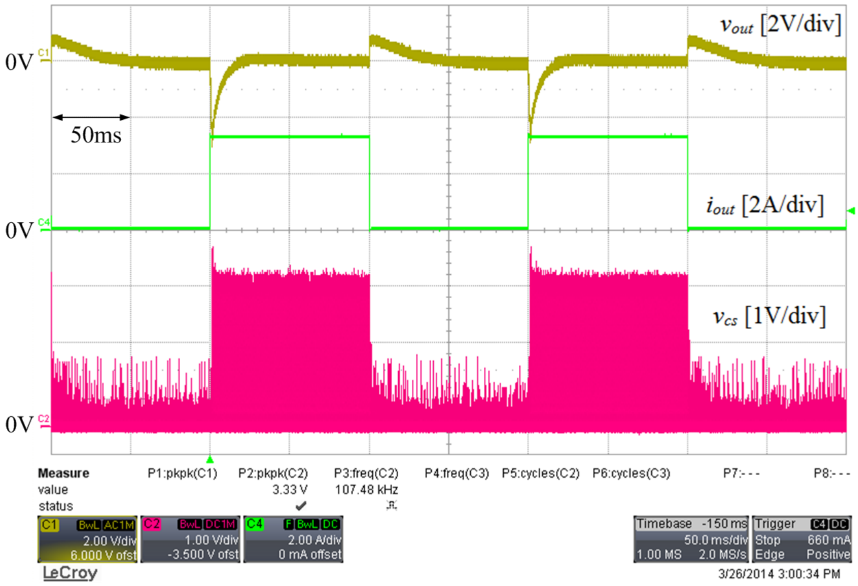

(b) Load profile 4

Figure 8.27: Dynamic responses of the converter output voltage $v_{out}(t)$ and input current (through current sense voltage $v_{cs}(t)$) against load disturbance: (a) stepping between 0.165A to 3.33A every 50ms and (b) stepping between 1mA to 3.33A every 100ms. The input voltage is set to $v_{in}(t) = 150V$.

Section 8.2 proposes a digital control architecture which allows integration of different state-of-the-art control functions including magnetic sensing, efficiency optimisation, valley switching operation, etc. and can be implemented within a low-cost microcontroller without the need of any external auxiliary circuit.

Section 8.3 focuses on synthesizing a robust compensator for a variable frequency flyback converter using the mixed-sensitivity H_∞ framework. The presence of the variable frequency, in addition to the broad external disturbances causing parametric variations, introduces another degree of variation into the plant and results in a very conservative uncertainty model. Such a model can easily fail the H_∞ synthesis procedure. The simulated results in Section 8.3.3 show that it is possible to design a single controller that can preserve robust stability over the whole working space of the flyback converter, but robust performance may be compromised.

Several interesting properties about the parametric variations in the converter model can be deduced from the study of Section 8.3. The wide variations in the converter model across the operating range are caused by the differences in the dynamics of the CCM and DCM converter. For example, an open-loop flyback converter in CCM possesses a fast dynamic response with a low gain, while it behaves inversely in DCM with a slow response but a high open-loop gain. The poles and zeros of the PCM controlled converter in DCM depend not only on the input voltage and output load but also on the switching frequency of the control signal, while the factor influencing the converter dynamics in CCM is the external excitation only.

Given knowledge about the parametric variations in the converter transfer function, Section 8.4 exploited the effect of a variable sampling frequency on the dynamics of a fixed-parameter digital compensator to reduce model uncertainty. The approach is based on the fact that a fixed-parameter digital compensator with a variable sampling rate is equivalent to a variable continuous time compensator. Such sampling rate dependent dynamics are useful in the case where the converter dynamics also vary correspondingly with the switching frequency. Although the approach has been demonstrated with the flyback converter in DCM only, it can possibly be extended to other systems where the sampling/switching frequency is variable. In addition to the study of a variable sampling rate, a new simple representation of the converter model, which is suitable for controller design, is also derived. Based on the resulting analysis, a gain-adaptive predictive functional controller, which can be easily implemented in a low-cost microcontroller, is proposed. The experimental and simulated results show that the gain-adaptive controller can achieve zero steady state error, fast transient response and, most importantly, is stable over the operating range of consideration.

Section 8.5 proposes a simple procedure, which combines the adaptive control approach in Section 8.4 and the robust control knowledge in Section 8.3, to synthesize a robust adaptive digital compensator. The theoretical and experimental validation in Section 8.5 confirms that the proposed QFT controller can achieve fast transient responses satisfying the desired specifications in Table 8.1 while preserving global stability over the whole operating range. As can be seen in Figs. 8.26 and 8.27, the QFT controller can retain robust performance over the wide range of excitation current load except for the most extreme test as illustrated in Fig. 8.27(b). However, such unsatisfactory results are unavoidable because the flyback converter has to lower the switching frequency, correspondingly reducing the system bandwidth, for higher efficiency at light and no load.

Section 8.5 also highlights the fact that, with the support of graphical design, QFT provides an intuitive and efficient approach to solving practical control problems where both system performance and stability are of interest.

Chapter 9

Conclusion

9.1 Overall conclusions

The overall conclusions to be drawn from the main research work in this thesis are reported in this section. With recent advances in semiconductor manufacturing and computational technology, digital control systems have grown to a relatively mature stage, and will soon become a viable replacement for their analogue counterparts in the design of isolated and non-isolated DC-to-DC converters in general, and flyback converters in particular.

The first-ever digital control design (in the literature) for a wide-operating range flyback converter, based on a low-cost microcontroller, is proposed in this thesis. The digital controller is fully implemented within the microcontroller, which minimizes the need of external sensing circuits and also the implementation cost. As demonstrated in Chapter 8, the digital control solution offers a variety of functions including output voltage regulation, magnetic sensing, efficiency optimisation, and n^{th} valley switching operation. The proposed controller can provide transient performance as fast as other existing control approaches in the field. At the same time, the following benefits are achieved:

- The digital compensator has a low order (second order), so it is simple to design, and does not require much computation power and, most importantly, can be implemented with a low-cost, low-performance microcontroller.
- The stability of the proposed controller can be theoretically verified.

Although the transient performance of the proposed controller does not fully satisfy all the design specifications, there is a high possibility that such an issue can be resolved in the near future when mixed-signal control technologies are permitted in low-cost microcontrollers.

As explained in Chapter 2, in practice the output load of the flyback converter can have the properties of a resistor, a current source, or both. Therefore, the use of the general load model in the derivation of the small signal models of open-loop and closed-loop flyback converters allows for a better understanding of system dynamics, better prediction of potential causes of instability, and a more realistic investigation into stability and performance of designed controllers when compared to existing approaches.

The formulae derived in Section 2.3.3 demonstrated that the poles of the transfer functions of open-loop continuous conduction mode (CCM) flyback converters are affected by the resistive part of the load only. These formulae further show that the converter transfer functions in discontinuous conduction mode (DCM) have two poles that depend on both resistive and current-source loads. One interesting fact which can be observed from the use of the general load model in DCM is that the current-source load can turn two real poles of DCM converters into two complex poles, which generally makes the system harder to control and stabilize. Though the converter model developed in Chapter 2 has not been fully exploited in the control design studies in Chapters 7 and 8 — where the focus was put on a load with resistive properties only — it can serve as a basis for future research, or as a cross reference for the study of flyback converters in general.

The reviews in Chapters 3 and 4 highlighted the fact that different investigations into modelling, controller synthesis, and simulation for DC-to-DC converter have been considered in the literature. However, several issues relating to the accuracy of existing transformer models, the execution time of simulation, and robust stability and robust performance of digital control, have not been fully addressed. Inspired by these issues, the author has conducted a thorough research work which covers all aspects of digital control design for the flyback converter including transformer modelling, converter modelling and simulation, isolated-feedback control, and controller synthesis and implementation, with this thesis. These research studies are separately documented in Chapters 5, 6, 7 and 8, respectively.

The starting point of the research work is in Chapter 5, where the focus is put on the development of a non-linear dynamic model for a 3-winding flyback transformer, and the identification of model parameters from time-domain data. The use of separate modules for representing linear and non-linear functions of the proposed transformer model allows for the separate determination of the parameters of the linear and non-linear parts. This, in turn, reduces the work involved in the identification step, and significantly improves the accuracy of the model. The results from the small and large signal tests presented in Chapter 5 confirmed that the obtained transformer model can fully reproduce both linear and non-linear dynamic characteristics of a practical transformer. It was found that identifying the transformer model based on time-domain data is more advantageous than that based on frequency-domain data, in terms of measurement device requirement, model accuracy, and complex model handling. However, the time-domain identification approach also has one drawback, which is the round-off error occurring in the collected data due to the finite resolution of the acquisition device. As demonstrated in Chapter 5, the round-off error can be effectively reduced by adjusting the value of the current sensing resistor in each experiment, although the selection and replacement of the sensing resistor may consume some extra work and time.

Chapter 5 showed that the direct approach (SRIVC algorithm) and indirect approach (IV algorithm) to the identification of continuous time models will yield consistent results if mapping between the parameters of a continuous-time model and its equivalent discrete-time counterparts, during a discrete-to-continuous (D2C) transformation, is unique. The condition for a unique D2C mapping, based on a pre-filter and a constraint on the discrete-time model, is also proposed. Although such a method has been demonstrated in the context of transformer model identification and two algorithms in particular, the SRIVC and IV, its principle can be generalized to a wider range of applications. It is also shown in Chapter 5 that the air gap length has a large contribution to the non-linearity of the transformer, and the inclusion of the gap length into the identification process significantly improves the accuracy of the obtained transformer model, particularly around the saturation region. As shown in Section 5.5.3, the full-order converter model, constructed from the non-linear dynamic transformer model and other component models, can produce very high fidelity results when compared with experimental data; however, the simulation is very time-consuming. For this reason, the full-order converter model lends itself to short-term simulation, for example device stress testing, but not long-term simulation, for example line or load transient response calculation.

Based on the full-order converter model, Chapter 6 demonstrated that the model simplification process allows for the development of a control-oriented model which is able to preserve the bulk of the full converter model fidelity, critical for a control design step, while at the same time requiring a significantly shorter execution time for simulation. The execution time is reduced by around 3 orders of magnitude, compared with that of the full-order model. The generality of the model reduction procedure is that different models can be derived from the full-order model depending on the amount of information required, and the model complexity requirement, i.e. execution speed of simulation. In addition to model complexity, it is also shown in Chapter 6 that algebraic loops and the large disparity in the different time constants of the flyback converter are the cause of a slow simulation execution speed. Such issues can be effectively handled by sequencing the equation-solving order and increasing the values of damping resistors.

A unified CCM and DCM magnetic sensing principle, which relies on sampling the bias winding voltage at the point where the secondary current is known, is developed in Chapter 7. The implementation of the proposed sensing technique, based on analogue circuitry and a microcontroller, is also studied in the same chapter. It is demonstrated that using the input current information to compensate for the cable voltage drop can help to improve the accuracy of the sensing network, and significantly reduce the computation involved. These result in a simplification of hardware and software implementation. The simulation results in Chapter 7 confirm that the unified sensing solution operates smoothly and accurately regardless of variations in operating modes of the flyback converter. Furthermore, it is shown in Section 8.4.3 that the proposed method is accurate and robustly stable not only in theory, but also in practice. Although the implementation of the unified sensing method based on a microcontroller does not perform as well as that based on an analogue circuit during transient phases, the simplicity of the microcontroller-based solution makes it much more attractive for modern power supply applications. Compared with other magnetic sensing methods, the proposed technique may not be the most optimized solution in terms of hardware requirements, but it allows the widest operation condition, including both CCM and DCM, with high accuracy.

The main focus of Chapter 8 is on the design and implementation of digital optimum control for a wide-operating range flyback converter, based on the research outcomes in Chapters 2, 6, and 7. The control architecture was purposely designed to perform a variety of tasks, including efficiency optimisation, magnetic sensing, and valley switching operation, in addition to the main task of regulating the output voltage. Three different methods for synthesizing optimum compensators, based on mixed-sensitivity H_∞ robust control theory, gain-adaptive predictive functional control (GAPFC) theory, and gain-adaptive quantitative feedback theory (GAQFT), were also proposed. All the three designed controllers show stable operation against variations in the external excitations, even though global stability of only the H_∞ controller and the GAQFT controller have been theoretically verified. The achieved performance of the three controllers, in terms of settling time and output voltage regulation ability, is much different. The H_∞ compensator has long transient time, unsatisfactory output voltage regulation, and non-zero steady state errors, while both the GAPFC and GAQFT compensators have fast transient responses which pass the desire specifications in Table 8.1. The compromise with the performance of the H_∞ controller is unavoidable, and highlights the fact that wide parametric variations in the system model are the main elements limiting the performance of robust controllers, and that the only possibility of achieving both fast transient responses and global stability is to minimize model uncertainty before applying any robust control techniques. Such a principle has been successfully applied to the synthesis of the GAQFT compensator, as detailed in Section 8.5.

One significant point in Chapter 8, which should be noted, is that the GAQFT compensator failed in the most extreme transient-load test, from very light load to full load, as did the GAPFC controller. The failure is due to the low bandwidth of these digital controllers at light load, where the sampling frequency is around 1kHz or even lower. The low-bandwidth issue can be handled by increasing the switching frequency; however, such an action will result in higher converter losses, or lower efficiency which may not meet the design target. Therefore, a compromise between converter performance and efficiency needs to be reached in this case.

9.2 Possible follow-on research

Several directions for future research, which emerged in the course of the reported research, are described as follows:

- In Chapter 7, the proposed magnetic sensing method, based on analogue circuitry, has been verified with simulation only, and as a result may not have much value in practice. Therefore, an experimental verification would prove the usefulness of such a design.
- The optimum digital control solution reported in Chapter 8 is derived for a DCM flyback converter with a resistive output load only. An extension to a flyback converter operating in both continuous and discontinuous conduction modes with a general load, including both resistive and current-source-type loads, would be of great interest.
- Further useful possible follow-on work could be to improve the performance of the proposed digital optimum controller at very light load or no load, but without compromising the converter efficiency.
- It would be interesting to extend the idea of variable sampling rate control discussed in Section 8.4.1 to other DC-to-DC converter topologies where the switching frequency is variable.
- Finally, a more intelligent approach to robust performance, where converter efficiency is considered as performance metric, could also be of interest.

Appendix A

State-space matrices for various switch configurations

The state-space matrices for the 5 switch configurations of the control-oriented model are derived in this Appendix. In brevity, the following definitions are used in the derivation, $r_{Qw} = r_{Qon} + r_w$, $n_2 = \frac{N_s}{N_p}$, $r_{Dcr} = r_{Don} + \frac{r_c R}{r_c + R}$, $r_{zds} = \frac{r_z r_{ds}}{r_z + r_{ds}}$.

Configuration 1: Q is on, D is off and $\mathbf{D_s}$ is off

$$\mathbf{A}_1 = \begin{bmatrix} 0 & -\frac{r_{Qw}}{L_{lk}+Lm} & 0 & 0 \\ 0 & -\frac{r_{Qw}}{L_{lk}+Lm} & 0 & 0 \\ 0 & \frac{1}{C_{ds}} & -\frac{1}{r_{ds}C_{ds}} & 0 \\ 0 & 0 & 0 & -\frac{1}{(r_c+R)C} \end{bmatrix}, \quad \mathbf{B}_1 = \begin{bmatrix} -\frac{1}{L_{lk}+Lm} & 0 & 0 & 0 \\ -\frac{1}{L_{lk}+Lm} & 0 & 0 & 0 \\ 0 & 0 & 0 & 0 \\ 0 & -\frac{R}{(r_c+R)C} & 0 & 0 \end{bmatrix},$$

$$\mathbf{C}_1 = \begin{bmatrix} 0 & 1 & 0 & 0 \\ 0 & -r_{Qw} & 0 & 0 \\ 0 & 0 & 0 & \frac{R}{r_c+R} \\ 0 & 0 & 0 & 0 \\ 0 & n_2 r_{Qw} & 0 & -\frac{R}{r_c+R} \\ 0 & 0 & 0 & 0 \\ 0 & r_{Qon} & 0 & 0 \end{bmatrix}, \quad \mathbf{E}_1 = \begin{bmatrix} 0 & 0 & 0 & 0 \\ 1 & 0 & 0 & 0 \\ 0 & -\frac{r_c R}{r_c+R} & 0 & 0 \\ 0 & 0 & 0 & 0 \\ -n_2 & \frac{r_c R}{r_c+R} & -1 & 0 \\ 0 & 0 & 0 & 0 \\ -1 & 0 & 0 & -1 \end{bmatrix}.$$

Configuration 2: Q is off, D is off and $\mathbf{D_s}$ is off

$$\mathbf{A}_2 = \begin{bmatrix} 0 & -\frac{r_{Qw}+r_{ds}}{L_{lk}+Lm} & -\frac{1}{L_{lk}+L_m} & 0 \\ 0 & -\frac{r_{Qw}+r_{ds}}{L_{lk}+Lm} & -\frac{1}{L_{lk}+L_m} & 0 \\ 0 & \frac{1}{C_{ds}} & 0 & 0 \\ 0 & 0 & 0 & -\frac{1}{(r_c+R)C} \end{bmatrix}, \quad \mathbf{B}_2 = \begin{bmatrix} -\frac{1}{L_{lk}+Lm} & 0 & 0 & 0 \\ -\frac{1}{L_{lk}+Lm} & 0 & 0 & 0 \\ 0 & 0 & 0 & 0 \\ 0 & -\frac{R}{(r_c+R)C} & 0 & 0 \end{bmatrix},$$

$$\mathbf{C}_2 = \begin{bmatrix} 0 & 1 & 0 & 0 \\ 0 & -(r_{Qw} + r_{ds}) & -1 & 0 \\ 0 & 0 & 0 & \frac{R}{r_c+R} \\ 0 & 0 & 0 & 0 \\ 0 & n_2(r_{Qw} + r_{ds}) & n_2 & -\frac{R}{r_c+R} \\ 0 & 0 & 0 & 0 \\ 0 & r_{Qon} + r_{ds} & 1 & 0 \end{bmatrix}, \quad \mathbf{E}_2 = \begin{bmatrix} 0 & 0 & 0 & 0 \\ 1 & 0 & 0 & 0 \\ 0 & -\frac{r_c R}{r_c+R} & 0 & 0 \\ 0 & 0 & 0 & 0 \\ -n_2 & \frac{r_c R}{r_c+R} & -1 & 0 \\ 0 & 0 & 0 & 0 \\ -1 & 0 & 0 & -1 \end{bmatrix}.$$

Configuration 3: Q is on, D is on and $\mathbf{D_s}$ is off

$$\mathbf{A}_3 = \begin{bmatrix} -\left(r_{Qw} + \frac{r_{Dcr}}{n_2^2}\right)\frac{1}{L_{lk}} & \frac{r_{Dcr}}{n_2^2 L_{lk}} & 0 & \frac{R}{n_2(r_c+R)L_{lk}} \\ \frac{r_{Dcr}}{n_2^2 L_m} & -\frac{r_{Dcr}}{n_2^2 L_m} & 0 & -\frac{1}{n_2 L_m} \\ 0 & 0 & -\frac{1}{r_{ds}C_{ds}} & 0 \\ -\frac{R}{n_2(r_c+R)C} & \frac{R}{n_2(r_c+R)C} & 0 & -\frac{1}{(r_c+R)C} \end{bmatrix},$$

$$\mathbf{B}_3 = \begin{bmatrix} \frac{1}{L_{lk}} & -\frac{r_c R}{n_2(r_c+R)L_{lk}} & \frac{1}{n_2 L_{lk}} & 0 \\ 0 & \frac{r_c R}{n_2(r_c+R)L_m} & -\frac{1}{n_2 L_m} & 0 \\ 0 & 0 & 0 & 0 \\ 0 & -\frac{R}{(r_c+R)C} & 0 & 0 \end{bmatrix},$$

$$\mathbf{C}_3 = \begin{bmatrix} 1 & 0 & 0 & 0 \\ \frac{r_{Dcr}}{n_2^2} & -\frac{r_{Dcr}}{n_2^2} & 0 & -\frac{1}{n_2} \\ -\frac{r_c R}{n_2(r_c+R)} & \frac{r_c R}{n_2(r_c+R)} & 0 & 1 \\ -\frac{1}{n_2} & \frac{1}{n_2} & 0 & 0 \\ 0 & 0 & 0 & 0 \\ 0 & 0 & 0 & 0 \\ 0 & r_{Qon} & 0 & 0 \end{bmatrix}, \quad \mathbf{E}_3 = \begin{bmatrix} 0 & 0 & 0 & 0 \\ 0 & \frac{r_c R}{n_2(r_c+R)} & -\frac{1}{n_2} & 0 \\ 0 & -\frac{r_c R}{r_c+R} & 0 & 0 \\ 0 & 0 & 0 & 0 \\ 0 & 0 & 0 & 0 \\ 0 & 0 & 0 & 0 \\ -1 & 0 & 0 & -1 \end{bmatrix}.$$

Configuration 4: Q is off, D is on and $\mathbf{D_s}$ is off

$$\mathbf{A}_4 = \begin{bmatrix} -\left(r_{Qw} + r_{ds} + \frac{r_{Dcr}}{n_2^2}\right)\frac{1}{L_{lk}} & \frac{r_{Dcr}}{n_2^2 L_{lk}} & -\frac{1}{L_{lk}} & \frac{R}{n_2(r_c+R)L_{lk}} \\ \frac{r_{Dcr}}{n_2^2 L_m} & -\frac{r_{Dcr}}{n_2^2 L_m} & 0 & -\frac{R}{n_2(r_c+R)L_m} \\ \frac{1}{C_{ds}} & 0 & 0 & 0 \\ -\frac{R}{n_2(r_c+R)C} & \frac{R}{n_2(r_c+R)C} & 0 & -\frac{1}{(r_c+R)C} \end{bmatrix},$$

$$\mathbf{B}_4 = \begin{bmatrix} \frac{1}{L_{lk}} & -\frac{r_c R}{n_2(r_c+R)L_{lk}} & \frac{1}{n_2 L_{lk}} & 0 \\ 0 & \frac{r_c R}{n_2(r_c+R)L_m} & -\frac{1}{n_2 L_m} & 0 \\ 0 & 0 & 0 & 0 \\ 0 & -\frac{R}{(r_c+R)C} & 0 & 0 \end{bmatrix},$$

$$\mathbf{C}_4 = \begin{bmatrix} 1 & 0 & 0 & 0 \\ \frac{r_{Dcr}}{n_2^2} & -\frac{r_{Dcr}}{n_2^2} & 0 & -\frac{R}{n_2(r_c+R)} \\ -\frac{r_c R}{n_2(r_c+R)} & \frac{r_c R}{n_2(r_c+R)} & 0 & \frac{R}{r_c+R} \\ -\frac{1}{n_2} & \frac{1}{n_2} & 0 & 0 \\ 0 & 0 & 0 & 0 \\ 0 & 0 & 0 & 0 \\ 0 & r_{Qon} + r_{ds} & 1 & 0 \end{bmatrix}, \quad \mathbf{E}_4 = \begin{bmatrix} 0 & 0 & 0 & 0 \\ 0 & \frac{r_c R}{n_2(r_c+R)} & -\frac{1}{n_2} & 0 \\ 0 & -\frac{r_c R}{r_c+R} & 0 & 0 \\ 0 & 0 & 0 & 0 \\ 0 & 0 & 0 & 0 \\ 0 & 0 & 0 & 0 \\ -1 & 0 & 0 & -1 \end{bmatrix}.$$

Configuration 5: Q is off, D is on and $\mathbf{D_s}$ is on

$$\mathbf{A}_5 = \begin{bmatrix} -\left(r_{Qw} + \frac{r_z r_{ds}}{r_z+r_{ds}} + \frac{r_{Dcr}}{n_2^2}\right)\frac{1}{L_{lk}} & \frac{r_{Dcr}}{n_2^2 L_{lk}} & -\frac{r_z}{(r_z+r_{ds})L_{lk}} & \frac{R}{n_2(r_c+R)L_{lk}} \\ \frac{r_{Dcr}}{n_2^2 L_m} & -\frac{r_{Dcr}}{n_2^2 L_m} & 0 & -\frac{R}{n_2(r_c+R)L_m} \\ \frac{r_z}{(r_z+r_{ds})C_{ds}} & 0 & -\frac{1}{(r_z+r_{ds})C_{ds}} & 0 \\ -\frac{R}{n_2(r_c+R)C} & \frac{R}{n_2(r_c+R)C} & 0 & -\frac{1}{(r_c+R)C} \end{bmatrix},$$

$$\mathbf{B}_5 = \begin{bmatrix} \frac{r_z}{(r_z+r_{ds})L_{lk}} & -\frac{r_c R}{n_2(r_c+R)L_{lk}} & \frac{1}{n_2 L_{lk}} & -\frac{r_{ds}}{(r_z+r_{ds})L_{lk}} \\ 0 & \frac{r_c R}{n_2(r_c+R)L_m} & -\frac{1}{n_2 L_m} & 0 \\ \frac{1}{(r_z+r_{ds})C_{ds}} & 0 & 0 & \frac{1}{(r_z+r_{ds})C_{ds}} \\ 0 & -\frac{R}{(r_c+R)C} & 0 & 0 \end{bmatrix},$$

$$\mathbf{C}_5 = \begin{bmatrix} \frac{r_z}{r_z+r_{ds}} & 0 & -\frac{1}{r_z+r_{ds}} & 0 \\ \frac{r_{Dcr}}{n_2^2} & -\frac{r_{Dcr}}{n_2^2} & 0 & -\frac{R}{n_2(r_c+R)} \\ -\frac{r_c R}{n_2(r_c+R)} & \frac{r_c R}{n_2(r_c+R)} & 0 & \frac{R}{r_c+R} \\ -\frac{1}{n_2} & \frac{1}{n_2} & 0 & 0 \\ 0 & 0 & 0 & 0 \\ \frac{r_{ds}}{r_z+r_{ds}} & 0 & \frac{1}{r_z+r_{ds}} & 0 \\ 0 & 0 & 0 & 0 \end{bmatrix},$$

$$\mathbf{E}_5 = \begin{bmatrix} \frac{1}{r_z+r_{ds}} & 0 & 0 & \frac{1}{r_z+r_{ds}} \\ 0 & \frac{r_c R}{n_2(r_c+R)} & -\frac{1}{n_2} & 0 \\ 0 & -\frac{r_c R}{r_c+R} & 0 & 0 \\ 0 & 0 & 0 & 0 \\ 0 & 0 & 0 & 0 \\ -\frac{1}{r_z+r_{ds}} & 0 & 0 & -\frac{1}{r_z+r_{ds}} \\ 0 & 0 & 0 & 0 \end{bmatrix}.$$

References

[1] P. Semiconductors, "Chapter 2: Switched mode power supplies," Power Semiconductor Application Laboratory, Philips Semiconductors, Tech. Rep., 1994. [Online]. Available: http://www.nxp.com/documents/application_note/APPCHP2.pdf

[2] O. Semiconductor, "Switchmode power supplies: Reference manual and design guide," ON Semiconductor, Tech. Rep., July 2002.

[3] R. W. Erickson and D. Maksimovic, *Fundamental of Power Electronics*, 2nd ed. Kluwer Academic Publishers, 2004.

[4] D. G. Inc., "External ac-dc power supplies: Economic factors, application drivers, architecture/packaging trends, technology and regulatory developments," Darnell Group Inc., Tech. Rep., Feb. 2011.

[5] R. Nalepa, N. Barry, and P. Meaney, "Primary side control circuit of a flyback converter," in *16th Annu. IEEE Applied Power Electronics Conf. and Expo. (APEC)*, 2001, pp. 542–547.

[6] C. W. Chang, Y. T. Lin, and Y. T. Tzou, "Digital primary-side sensing control for flyback converters," in *Int. Conf. on Power Electronics and Drive Systems (PEDS)*, Nov. 2009, pp. 689–694.

[7] S. H. Kang, D. Maksimovic, and I. Cohen, "Efficiency optimization in digitally controlled flyback DC-DC converters over wide ranges of operating conditions," *IEEE Trans. Power Electron.*, vol. 27, no. 8, pp. 3734–3748, Aug. 2012.

[8] S. H. Kang and D. Maksimovic, "Simplified sensing and A/D conversion for digitally controlled flyback DC-DC converters with on-line efficiency optimization," in *27th Annu. IEEE Applied Power Electron. Conf. and Expo. (APEC)*, Feb. 2012, pp. 1075–1082.

[9] A. A. Dauhajre, "Modelling and estimation of leakage phenomena in magnetic circuits," Ph.D. dissertation, California Institude of Technology, Pasadena, CA, Apr. 1986.

[10] V. A. Niemela, J. Owen, H. A., and T. G. Wilson, "Cross-coupled-secondaries model for multiwinding transformers with parameter values calculated from short-circuit impedances," in *21st Ann. IEEE Power Electronics Specialists Conf. (PESC)*, 1990, pp. 822–830.

[11] G. Ludwig and S. El-Hamamsy, "Coupled inductance and reluctance models of magnetic components," *IEEE Trans. Power Electron.*, vol. 6, no. 2, pp. 240–250, Apr. 1991.

[12] R. W. Erickson and D. Maksimovic, “A multiple-winding magnetics model having directly measurable parameters,” in *29th Ann. IEEE Power Electronics Specialists Conf. (PESC)*, vol. 2, May 1998, pp. 1472–1478.

[13] M. Shah and K. Ngo, “Parameter extraction for the extended cantilever model of magnetic component windings,” *IEEE Trans. Aerosp. Electron. Syst.*, vol. 36, no. 1, pp. 260–266, Jan. 2000.

[14] K. Ngo, S. Srinivas, and P. Nakmahachalasint, “Broadband extended cantilever model for magnetic component windings,” *IEEE Trans. Power Electron.*, vol. 16, no. 4, pp. 551–557, July 2001.

[15] J. H. Chan, A. Vladimirescu, X. C. Gao, P. Liebmann, and J. Valainis, “Nonlinear transformer model for circuit simulation,” *IEEE Trans. Comput.-Aided Des. Integr. Circuits Syst.*, vol. 10, no. 4, pp. 476–482, Apr. 1991.

[16] F. D. Leon and A. Semlyen, “A simple representation of dynamic hysteresis losses in power transformers,” *IEEE Trans. Power Del.*, vol. 10, no. 1, pp. 315–321, Jan. 1995.

[17] S. Casoria, G. Sybille, and P. Brunelle, “Hysteresis modeling itheoryMATLAB/Power System Blockset ,” *Mathematics and Computers in Simulation*, vol. 63, no. 35, pp. 237–248, 2003, modelling and Simulation of Electric Machines, Converters and Systems. [Online]. Available: http://www.sciencedirect.com/science/article/pii/S0378475403000703

[18] D. C. Jiles and D. Atherton, “Theory of ferromagnetic hysteresis,” *Journal of Magnetism and Magnetic Materials*, vol. 61, pp. 48–60, 1986.

[19] M. L. Hodgdon, “Applications of a theory of ferromagnetic hysteresis,” *IEEE Trans. Magn.*, vol. 24, no. 1, pp. 218–221, Jan. 1988.

[20] M. D. I. D. Silva, J. Kumar, and V. A. Lalithambika, “Switch mode power supply controllers,” US Patent 7,248,487 B1, Jul. 24, 2007.

[21] J. Xiao, J. Wu, W. Li, and X. He, “Primary-side controlled flyback converter with current compensation in micro-power applications,” in *IEEE 6th Int. Power Electronics and Motion Control Conf. (IPEMC)*, May 2009, pp. 1361–1366.

[22] M. R. Muegge, M. Eason, and M. D. Telefus, “PWM power converter controlled by transition detection of a comparator error signal,” US Patent 6,900,995 B2, May, 2005.

[23] P. Konecny and Y. Yedevelly, “Primary side sensing for isolated flyback converters,” US Patent 2011/0 157 922 A1, Jun. 30, 2011.

[24] D. R. Coulson, J. Piper, and D. M. Garner, “Switch mode power supply controlled with feedback signal decay sensing,” US Patent 7,944,722 B2, May 17, 2011.

[25] S. Huynh, M. Chen, C. Xiao, and M. Yu, “Primary side contant output voltage controller,” US Patent 7,307,390 B2, Dec. 11, 2007.

[26] A. Mednik, D. S. Schie, J. H. Nguyen, and W. Gu, “Switching power converter and method of controlling output voltage there of using preductive sensing of magnetic flux,” US Patent 6,958,920 B2, Oct. 25, 2005.

[27] C. W. Chang and Y. Y. Tzou, “Primary-side sensing error analysis for flyback converters,” in *Proc. IEEE 6th Int. Conf. on Power Electronics and Motion Control*, May 2009, pp. 524–528.

[28] *Limits for Harmonic Current Emissions (Equipment Input Current < 16A per Phase)*, IEC Std. 61 000-3-2.

[29] R. D. Middlebrook and S. Cuk, “A general unified approach to modelling switching-converter power stages,” in *Proc. IEEE Power Electronics Specialists Conf.*, 1976, pp. 73–86.

[30] S. Cuk and R. D. Middlebrook, “A general unified approach to modelling switching DC-to-DC converters in discontinuous conduction mode,” in *Proc. IEEE Power Electronics Specialists Conf.*, 1977, pp. 36–57.

[31] J. Sun, D. M. Mitchell, M. F. Greuel, P. T. Krein, and R. M. Bass, “Averaged modeling of PWM converters operating in discontinuous conduction mode,” *IEEE Trans. Power Electron.*, vol. 16, no. 4, pp. 482–492, July 2001.

[32] C. W. Deisch, “Simple switching control method changes power converter into a current source,” in *IEEE Power Electronics Specialists Conf. (PESC)*, 1978, pp. 300–306.

[33] R. D. Middlebrook, “Topics in multiple-loop regulators and current-mode programming,” *IEEE Trans. Power Electron.*, vol. PE-2, no. 2, pp. 109–124, Apr. 1987.

[34] G. Verghese, C. Bruzos, and K. Mahabir, “Averaged and sampled-data models for current mode control: a re-examination,” in *20th Annu. IEEE Power Electronics Specialists Conf. (PESC)*, vol. 1, June 1989, pp. 484–491.

[35] L. Dixon, “Average current mode control of switching power supplies,” Unitrode Corporation, Tech. Rep., 1990.

[36] R. Ridley, “A new, continuous-time model for current-mode control,” *IEEE Trans. Power Electron.*, vol. 6, no. 2, pp. 271–280, Apr. 1991.

[37] F. Tan and R. Middlebrook, “A unified model for current-programmed converters,” *IEEE Trans. Power Electron.*, vol. 10, no. 4, pp. 397–408, July 1995.

[38] D. Perreault and G. Verghese, “Time-varying effects and averaging issues in models for current-mode control,” *IEEE Trans. Power Electron.*, vol. 12, no. 3, pp. 453–461, May 1997.

[39] K. Wan, L. Jingsheng, and M. Ferdowsi, “Control methods in DC-DC power conversion - a comparative study,” in *IEEE Power Electrononic Specialists Conf. (PESC)*, June 2007, pp. 921–926.

[40] F. Azcondo, C. Bracas, R. Casanueva, and D. Maksimovic, “Approaches to modeling converters with current programmed control,” in *IEEE Workshop Power Electronics Education*, June 2005, pp. 98–104.

[41] J. Sun and B. Choi, "Averaged modeling and switching instability prediction for peak current control," in *36th IEEE Power Electronics Specialists Conf.*, June 2005, pp. 2764–2770.

[42] *ENERGY STAR Program Requirements for single voltage external AC-DC and AC-AC power supply*, Energy Star Partner Std., Rev. 2.0.

[43] B. Arbetter, R. Erickson, and D. Maksimovic, "DC-DC converter design for battery-operated systems," in *26th Annu. IEEE Power Electronics Specialists Conf. (PESC)*, vol. 1, June 1995, pp. 103–109.

[44] S. H. Kang, H. Nguyen, D. Maksimovic, and I. Cohen, "Efficiency characterization and optimization in flyback DC-DC converters," in *IEEE Energy Conversion Congr. and Expo. (ECCE)*, Sept. 2010, pp. 527–534.

[45] M. Gildersleeve, H. P. Forghani-zadeh, and G. A. Rincon-Mora, "A comprehensive power analysis and a highly efficient, mode-hopping DC-DC converter," in *IEEE Asia-Pacific Conf. ASIC*, Nov. 2002, pp. 153–156.

[46] X. Zhou, T. G. Wang, and F. C. Lee, "Optimizing design for low voltage DC-DC converters," in *12th Annu. Applied Power Electronics Conf. and Expo. (APEC)*, vol. 2, Feb. 1997, pp. 612–616.

[47] J. A. A. Qahouq, O. Abdel-Rahman, L. Huang, and I. Batarseh, "On load adaptive control of voltage regulators for power managed loads: Control schemes to improve converter efficiency and performance," *IEEE Trans. Power Electron.*, vol. 22, no. 5, pp. 1806–1819, Sept. 2007.

[48] J.-P. Vandelac and P. Ziogas, "A novel approach for minimizing high-frequency transformer copper losses," *IEEE Trans. Power Electron.*, vol. 3, no. 3, pp. 266–277, July 1988.

[49] K. Venkatachalam, C. Sullivan, T. Abdallah, and H. Tacca, "Accurate prediction of ferrite core loss with nonsinusoidal waveforms using only Steinmetz parameters," in *Proc. IEEE Workshop Computers in Power Electronics*, June 2002, pp. 36–41.

[50] B. Arbetter and D. Maksimovic, "Control method for low-voltage DC power supply in battery-powered systems with power management," in *28th Annu. IEEE Power Electron. Specialists Conf.*, vol. 2, Jun. 1997, pp. 1198–1204.

[51] T. Wang, X. Zhou, and F. Lee, "A low voltage high efficiency and high power density DC/DC converter," in *28th Annu. IEEE Power Electron. Specialists Conf.*, vol. 1, Jun. 1997, pp. 240–245.

[52] J. Xiao, A. Peterchev, J. Zhang, and S. Sanders, "A 4-μA quiescent-current dual-mode digitally controlled buck converter ic for cellular phone applications," *IEEE J. of Solid-State Circuits*, vol. 39, no. 12, pp. 2342–2348, Dec. 2004.

[53] N. Rahman, K. Wang, and A. Prodic, "Digital pulse-frequency/pulse-amplitude modulator for improving efficiency of SMPS operating under light loads," in *IEEE Workshops on Computers in Power Electron.*, Jul. 2006, pp. 149–153.

[54] D. M. Dwellry, “Voltage mode feedback burst mode circuit,” US Patent 6 307 356 B1, Oct., 2001.

[55] Y. Jang and M. M. Jovanovic, “Light-load efficiency optimization method,” *IEEE Trans. Power Electron.*, vol. 25, no. 1, pp. 67–74, Jan. 2010.

[56] H. S. Choi and D. Huh, “Techniques to minimize power consumption of SMPS in standby mode,” in *36th IEEE Power Electron. Specialists Conf.*, Jun 2005, pp. 2817–2822.

[57] Y. Panov and M. Jovanovic, “Adaptive off-time control for variable-frequency, soft-switched flyback converter at light loads,” *IEEE Trans. Power Electron.*, vol. 17, no. 4, pp. 596–603, Jul. 2002.

[58] Y. Li and J. Zheng, “A low-cost adaptive multi-mode digital control solution maximizing AC/DC power supply efficiency,” in *25th Ann. IEEE Applied Power Electronics Conf. and Expo.*, Feb. 2010, pp. 349–354.

[59] X. Zhang and D. Maksimovic, “Multimode digital controller for synchronous buck converters operating over wide ranges of input voltages and load currents,” *IEEE Trans. Power Electron.*, vol. 25, no. 8, pp. 1958–1965, Aug. 2010.

[60] S. H. Kang, D. Maksimovic, and I. Cohen, “On-line efficiency optimization in flyback DC-DC converters over wide ranges of operating conditions,” in *26th Annu. IEEE Applied Power Electron. Conf. and Expo. (APEC)*, Mar. 2011, pp. 1417–1424.

[61] N. Mohan, W. Robbins, T. Undeland, R. Nilssen, and O. Mo, “Simulation of power electronic and motion control systems-an overview,” *Proc. IEEE*, vol. 82, no. 8, pp. 1287–1302, Aug. 1994.

[62] D. Maksimovic, A. Stankovic, V. Thottuvelil, and G. Verghese, “Modeling and simulation of power electronic converters,” *Proc. IEEE*, vol. 89, no. 6, pp. 898–912, Jun. 2001.

[63] G. F. Franklin, J. D. Powell, and M. L. Workman, *Digital Control of Dynamic Systems*, 3rd ed. Addison-Wesley, 1998.

[64] S. Kelkar, R. Wunderlich, and L. Hitchcock, “Device level simulation for power converters,” in *4th Annu. IEEE Applied Power Electronics Conf. and Expo. (APEC)*, Mar. 1989, pp. 335–343.

[65] G. Franz, “Multilevel simulation tools for power converters,” in *5th Annu. Applied Power Electronics Conf. and Expo. (APEC)*, Mar. 1990, pp. 629–633.

[66] S. S. Kelkar and F. C. Y. Lee, “A fast time domain digital simulation technique for power converters: Application to a buck converter with feedforward compensation,” *IEEE Trans. Power Electron.*, vol. PE-1, no. 1, pp. 21–31, Jan. 1986.

[67] A. Luciano and A. Strollo, “A fast time-domain algorithm for the simulation of switching power converters,” *IEEE Trans. Power Electron.*, vol. 5, no. 3, pp. 363–370, July 1990.

[68] A. Massarini, U. Reggiani, and M. Kazimierczuk, “Analysis of networks with ideal switches by state equations,” *IEEE Trans. Circuits Syst. I, Fundam.l Theory Appl.*, vol. 44, no. 8, pp. 692–697, Aug. 1997.

[69] D. Bedrosian and J. Vlach, “Time-domain analysis of networks with internally controlled switches,” *IEEE Trans. Circuits Syst. I, Fundam. Theory Appl.*, vol. 39, no. 3, pp. 199–212, Mar. 1992.

[70] R. C. Wong, J. Owen, H.A., and T. Wilson, “An efficient algorithm for the time-domain simulation of regulated energy-storage DC-to-DC converters,” *IEEE Trans. Power Electron.*, vol. PE-2, no. 2, pp. 154–168, Apr. 1987.

[71] C. C. Fang and E. Abed, “Sampled-data modeling and analysis of closed-loop pwm DC-DC converters,” in *Proc. IEEE Int. Symp. on Circuits and Systems (ISCAS)*, vol. 5, 1999, pp. 110–115.

[72] D. Maksimovic and R. Zane, “Small-signal discrete-time modeling of digitally controlled DC-DC converters,” in *IEEE Workshops Computers in Power Electronics (COMPEL)*, July 2006, pp. 231–235.

[73] R. D. Middlebrook, “A general unified approach to modelling switching-converter power stages,” *Int. J. of Electron.*, vol. 42, pp. 18–34, 1977.

[74] F. Guinjoan, J. Calvente, A. Poveda, and L. Martinez, “Large-signal modeling and simulation of switching dc-dc converters,” *IEEE Trans. Power Electron.*, vol. 12, no. 3, pp. 485 –494, May 1997.

[75] A. Witulski and R. Erickson, “Extension of state space averaging to resonant switches-and beyond,” in *Power Electron. Specialists Conf., 1989. PESC ’89 Record., 20th Annu. IEEE*, Jun. 1989, pp. 476 –483 vol.1.

[76] V. Thottuvelil, D. Chin, and G. Verghese, “Hierarchical approaches to modeling high-power-factor AC-DC converters,” *IEEE Trans. Power Electron.*, vol. 6, no. 2, pp. 179–187, Apr. 1991.

[77] R. Ridley, “New simulation techniques for PWM converters,” in *8th Annu. Applied Power Electronics Conf. and Expo. (APEC)*, Mar. 1993, pp. 517–526.

[78] P. R. K. Chetty, “Current injected equivalent circuit approach to modeling switching DC-DC converters,” *IEEE Trans. Aerosp. Electron. Syst.*, vol. AES-17, no. 6, pp. 802–808, Nov. 1981.

[79] J. Sun and H. Grotstollen, “Averaged modelling of switching power converters: reformulation and theoretical basis,” in *23rd Annu. IEEE Power Electronics Specialists Conf. (PESC)*, vol. 2, June 1992, pp. 1165–1172.

[80] G. Wester and R. Middlebrook, “Low-frequency characterization of switched DC-DC converters,” *IEEE Trans. Aerosp. Electron. Syst.*, vol. AES-9, no. 3, pp. 376–385, May 1973.

[81] W. Tang, F. Lee, and R. Ridley, “Small-signal modeling of average current-mode control,” in *7th Annu. Applied Power Electronics Conf. and Expo. (APEC)*, Feb. 1992, pp. 747–755.

[82] S. Ben-Yaakov, "Average simulation of PWM converters by direct implementation of behavioral relationships," in *8th Annu. Applied Power Electronics Conf. and Expo.*, Mar. 1993, pp. 510–516.

[83] G. C. Verghese, M. E. Elbuluk, and J. G. Kassakian, "A general approach to sampled-data modeling for power electronic circuits," *IEEE Trans. Power Electron.*, vol. PE-1, no. 2, pp. 76–89, Apr. 1986.

[84] J. Burdio and A. Martinez, "A unified discrete-time state-space model for switching converters," *IEEE Trans. Power Electron.*, vol. 10, no. 6, pp. 694–707, Nov. 1995.

[85] F. Huliehel and S. Ben-Yaakov, "Low-frequency sampled-data models of switched mode DC-DC converters," *IEEE Trans. Power Electron.*, vol. 6, no. 1, pp. 55–61, Jan. 1991.

[86] I. Zafrany and S. Sam Ben-Yaakov, "Generalized switched inductor model (GSIM): accounting for conduction losses," *IEEE Trans. Aerosp. Electron. Syst.*, vol. 38, no. 2, pp. 681–687, Apr. 2002.

[87] A. Davoudi and J. Jatskevich, "Parasitics realization in state-space average-value modeling of pwm dc-dc converters using an equal area method," *IEEE Trans. Circuits and Syst. I, Reg. Papers*, vol. 54, no. 9, pp. 1960–1967, Sept. 2007.

[88] M. E. Staff, *Magnetic Circuits and Transformers.* Principles of Electrical Engineering Series, The Technology Press, MIT, 1943.

[89] L. W. Matsch, *Capacitor, Magnetic Circuits, and Transformers*, ser. Electrical Engineering. Prentice Hall, Inc., Englewood Cliffs, N. J., 1964.

[90] J. Martinez and B. Mork, "Transformer modeling for low- and mid-frequency transients - a review," *IEEE Trans. Power Del.*, vol. 20, no. 2, pp. 1625–1632, Apr. 2005.

[91] D. Hamill, "Lumped equivalent circuits of magnetic components: the gyrator-capacitor approach," *IEEE Trans. Power Electron.*, vol. 8, no. 2, pp. 97–103, Apr. 1993.

[92] E. C. Cherry, "The duality between interlinked electric and magnetic circuits and the formation of transformer equivalent," *Proc. Physical Society B*, vol. 62, pp. 101–111, 1949.

[93] J. Hayes, N. O'Donovan, and M. Egan, "The extended T model of the multiwinding transformer," in *35th Ann. IEEE Power Electronics Specialists Conf. (PESC)*, vol. 3, June 2004, pp. 1812–1817.

[94] V. Niemela, "Leakage-impedance model for multiple-winding transformers," in *31st Ann. IEEE Power Electronics Specialists Conf. (PESC)*, vol. 1, June 2000, pp. 264–269.

[95] K. Changtong, R. Erickson, and D. Maksimovic, "A comparison of the ladder and full-order magnetic models," in *32nd Ann. IEEE Power Electronics Specialists Conf. (PESC)*, vol. 4, June 2001, pp. 2067–2071.

[96] X. Margueron and J. Keradec, "Identifying the magnetic part of the equivalent circuit of n -winding transformers," *IEEE Trans. Instrum. Meas.*, vol. 56, no. 1, pp. 146–152, Feb. 2007.

[97] R. Asensi, J. Cobos, O. Garcia, R. Prieto, and J. Uceda, “A full procedure to model high frequency transformer windings,” in *25th Annu. IEEE Power Electronics Specialists Conf. (PESC)*, vol. 2, June 1994, pp. 856–863.

[98] D. Maksimovic and R. Erickson, “Modeling of cross-regulation in multiple-output flyback converters,” in *14th Ann. Applied Power Electronics Conf. and Expo. (APEC)*, vol. 2, Mar. 1999, pp. 1066–1072.

[99] F. D. Leon and A. Semlyen, “Time domain modeling of eddy current effects for transformer transients,” *IEEE Trans. Power Del.*, vol. 8, no. 1, pp. 271–280, Jan. 1993.

[100] J. M. Lopera, M. J. Prieto, A. M. Pernia, and F. Nuno, “A multiwinding modeling method for high frequency transformers and inductors,” *IEEE Trans. Power Electron.*, vol. 18, no. 3, pp. 896–906, May 2003.

[101] H. Y. Lu, J. G. Zhu, and S. Y. R. Hui, “Experimental determination of stray capacitances in high frequency transformers,” *IEEE Trans. Power Electron.*, vol. 18, no. 5, pp. 1105–1112, Sept. 2003.

[102] D. Wilcox, W. Hurley, and M. Conlon, “Calculation of self and mutual impedances between sections of transformer windings,” *IEE Proc. C Generation, Transmission and Distribution,*, vol. 136, no. 5, pp. 308–314, Sept. 1989.

[103] W. Hurley and D. Wilcox, “Calculation of leakage inductance in transformer windings,” *IEEE Trans. Power Electron.*, vol. 9, no. 1, pp. 121–126, Jan. 1994.

[104] J. Pleite, R. Prieto, R. Asensi, J. A. Cobos, and E. Olias, “Obtaining a frequency-dependent and distributed-effects model of magnetic components from actual measurements,” *IEEE Trans. Magn.*, vol. 35, no. 6, pp. 4490–4502, Nov. 1999.

[105] A. Keyhani, H. Tsai, and S. Sebo, “Modelling and parameter estimation of power transformers for the study of high frequency system transients,” in *Proc. 32nd Midwest Symp. Circuits and Systems*, vol. 1, Aug. 1989, pp. 258–264.

[106] J. Bak-Jenson, B. Bak-Jenson, S. D. Mikkelsen, and C. G. Jensen, “Parametric identification in potential transformer modelling,” *IEEE Trans. Power Del.*, vol. 7, no. 1, pp. 70–76, Jan. 1992.

[107] S. M. Islam, K. M. Coates, and G. Ledwich, “Identification of high frequency transformer equivalent circuit using matlab from frequency domain data,” in *32nd IEEE Industry Applications Conf.*, vol. 1, Oct. 1997, pp. 357–364.

[108] E. D. Torre, “Modeling of magnetizing processes,” *Proc. IEEE*, vol. 78, no. 6, pp. 1017–1026, June 1990.

[109] P. Andrei, O. Caltun, and A. Stancu, “Differential phenomenological models for the magnetization processes in soft MnZn ferrites,” *IEEE Trans. Mag.*, vol. 34, no. 1, pp. 231–241, Jan. 1998.

[110] D. C. Jiles, J. B. Thoelke, and M. K. Devine, "Numerical determination of hysteresis parameters for the modeling of magnetic properties using the theory of ferromagnetic hysteresis," *IEEE Trans. Magn.*, vol. 28, no. 1, pp. 27–35, Jan. 1992.

[111] C. D. Boley and M. L. Hodgdon, "Model and simulations of hysteresis in magnetic cores," *IEEE Trans. Magn.*, vol. 25, no. 5, pp. 3922–3924, Sept. 1989.

[112] S. R. Naidu, "Simulation of the hysteresis phenomenon using preisach's theory," *Proc. IEE A*, vol. 137, no. 2, pp. 73–79, Mar. 1990.

[113] G. Bertotti, F. Fiorillo, and M. Pasquale, "Measurement and prediction of dynamic loop shapes and power losses in soft magnetic materials," *IEEE Trans. Magn.*, vol. 29, no. 6, pp. 3496–3498, Nov. 1993.

[114] F. Ossart and G. Meunier, "Comparison between various hysteresis models and experimental data," *IEEE Trans. Magn.*, vol. 26, no. 5, pp. 2837–2839, Sept. 1990.

[115] I. Mayergoyz, *Mathematical Models of Hysteresis and Their Applications*, 1st ed., ser. Elsevier Series in Electromagnetism. Elsevier Science Inc., 2003.

[116] J. H. B. Deane, "Modeling the dynamics of nonlinear inductor circuits," *IEEE Trans. Magn.*, vol. 30, no. 5, pp. 2795–2801, Sept. 1994.

[117] P. L. Chapman and S. D. Sudhoff, "Dynamic lossy inductor model for power converter simulation," in *17th Ann. IEEE Applied Power Electronics Conf. and Expo. (APEC)*, vol. 1, 2002, pp. 137–143.

[118] X. Wang, D. W. P. Thomas, M. Sumner, J. Paul, and S. H. L. Cabral, "Characteristics of Jiles-Atherton model parameters and their application to transformer inrush current simulation," *IEEE Trans. Magn.*, vol. 44, no. 3, pp. 340–345, Mar. 2008.

[119] J. V. Leite, N. Sadowski, P. Kuo-Peng, N. J. Batistela, and J. P. A. Bastos, "The inverse jiles-atherton model parameters identification," *IEEE Trans. Magn.*, vol. 39, no. 3, pp. 1397–1400, May 2003.

[120] P. Nakmahachalasint, K. D. T. Ngo, and L. Vu-Quoc, "A static hysteresis model for power ferrites," *IEEE Trans. Power Electron.*, vol. 17, no. 4, pp. 453–460, July 2002.

[121] E. Dallago, G. Sassone, and G. Venchi, "High-frequency power transformer model for circuit simulation," *IEEE Trans. Power Electron.*, vol. 12, no. 4, pp. 664–670, Jul. 1997.

[122] R. Prieto, R. Asensi, C. Fernandez, J. Oliver, and J. Cobos, "Bridging the gap between FEA field solution and the magnetic component model," *IEEE Trans. Power Electron.*, vol. 22, no. 3, pp. 943–951, May 2007.

[123] S. Voss, "Equivalent circuit modelling for wire-wound coils and transformers in power electronics," Ph.D. dissertation, Faculty of Engi., University of Erlangen-Nuremberg, 2006. [Online]. Available: http://www.opus.ub.uni-erlangen.de/opus/volltexte/2006/402/pdf/StephanVossDissertation.pdf

[124] R. W. Erickson and D. Maksimovic, “High efficiency DC-DC converter for battery-operated system with energy management,” University of Colorado, Boulder, Tech. Rep., 1995.

[125] L. Calderone, L. Pinola, and V. Varoli, “Optimal feed-forward compensation for PWM DC/DC converters with ‘linear’ and ‘quadratic’ conversion ratio,” *IEEE Trans. Power Electron.*, vol. 7, no. 2, pp. 349–355, Apr. 1992.

[126] B. Arbetter and D. Maksimovic, “Feedforward pulse width modulators for switching power converters,” *IEEE Trans. Power Electron.*, vol. 12, no. 2, pp. 361–368, Mar. 1997.

[127] T. B. Petrovic and A. Z. Rakic, “Linear robust approach to DC/DC converter modelling - i: Deterministic switching,” *Electrical Engineering*, vol. 86, pp. 267–273, 2004, 10.1007/s00202-003-0210-6. [Online]. Available: http://dx.doi.org/10.1007/s00202-003-0210-6

[128] H. Bevrani, M. Abrishamchian, and N. Safari-Shad, “Nonlinear and linear robust control of switching power converters,” in *IEEE Int. Conf. on Contr. Appl.*, vol. 1, 1999, pp. 808–813.

[129] T. W. Martin and S. S. Ang, “Digital control for switching converters,” in *IEEE Int. Symp. on Industrial Electronic (ISIE)*, vol. 2, 10-14 1995, pp. 480–484.

[130] S. Chattopadhyay and S. Das, “A digital current-mode control technique for DC-DC converters,” *IEEE Trans. Power Electron.*, vol. 21, no. 6, pp. 1718–1726, Nov. 2006.

[131] D. He and R. Nelms, “Average current-mode control for a boost converter using an 8-bit microcontroller,” in *IEEE Int. Symp. on Industrial Electron.*, vol. 2, May 2004, pp. 1185–1190.

[132] K. M. Smedley and S. Cuk, “One-cycle control of switching converters,” *IEEE Trans. Power Electron.*, vol. 10, no. 6, pp. 625–633, Nov. 1995.

[133] M. T. Zhang, M. M. Jovanovic, and F. C. Lee, “Design considerations for low-voltage on-board DC/DC modules for next generations of data processing circuits,” in *IEEE Int. Conf. on Power Electronics and Drive Systems*, vol. 1, Feb. 1995, pp. 385–394.

[134] C. Song, “Accuracy analysis of constant-on current-mode DC-DC converters for powering microprocessors,” in *24th Annu. IEEE Applied Power Electronics Conf. and Expo.*, Feb. 2009, pp. 97–101.

[135] R. Redl and J. Sun, “Ripple-based control of switching regulators - an overview,” *IEEE Trans. Power Electron.*, vol. 24, no. 12, pp. 2669–2680, Dec. 2009.

[136] J. Sun, “Characterization and performance comparison of ripple-based control for voltage regulator modules,” *IEEE Trans. Power Electron.*, vol. 21, no. 2, pp. 346–353, Mar. 2006.

[137] C. Song and J. L. Nilles, “Accuracy analysis of hysteretic current-mode voltage regulator,” in *20th Annu. IEEE Applied Power Electronics Conf. and Expo. (APEC)*, vol. 1, Mar. 2005, pp. 276–280.

[138] R. Miftakhutdinov, “An analytical comparision of alternative control techniques for powering next generation microprocessors,” Texas Instruments, Tech. Rep., 2002.

[139] D. Liberzon, *Switching in Systems and Control*, T. Basar, Ed. Birkhauser Boston, 2003.

[140] H. Sira-Ramirez, “Sliding motions in bilinear switched networks,” *IEEE Trans. Circuits and Syst.*, vol. 34, no. 8, pp. 919–933, Aug. 1987.

[141] V. Ramanarayanan, A. Sabanovic, and S. Cuk, “Sliding-mode control of power converter,” in *J. Indian Inst. Sci.* Indian Institude of Science, May 1989, pp. 193–211.

[142] W. Burns and T. Wilson, “A state-trajectory control law for DC-to-DC converters,” *IEEE Trans. Aerosp. Electron. Syst.*, vol. AES-14, no. 1, pp. 2–20, Jan. 1978.

[143] S. C. Tan, Y. M. Lai, C. K. Tse, and M. K. H. Cheung, “Adaptive feedforward and feedback control schemes for sliding mode controlled power converters,” *IEEE Trans. Power Electron.*, vol. 21, pp. 182–192, Jan. 2006. [Online]. Available: http://ieeexplore.ieee.org/stamp/stamp.jsp?tp=&arnumber=1566704&isnumber=33234

[144] R. Munzert and P. Krein, “Issues in boundary control,” in *27th Annu. IEEE Power Electronics Specialists Conf. (PESC)*, vol. 1, June 1996, pp. 810–816.

[145] R. Bass and P. Krein, “State-plane animation of power electronic systems: a tool for understanding feedback control and stability,” in *5th Ann. IEEE Applied Power Electronics Conf. and Expo. (APEC) Proc.*, Mar. 1990, pp. 641–648.

[146] M. Greuel, R. Muyshondt, and P. Krein, “Design approaches to boundary controllers,” in *28th Annu. IEEE Power Electronics Specialists Conf. (PESC)*, vol. 1, June 1997, pp. 672–678.

[147] P. T. Krien, *Elements of Power Electronics*, ser. Electrical and Computer Engineering. New York, Oxford: Oxford University Press, 1998.

[148] P. Y. Wu and P. K. T. Mok, “Comparative studies of common fix-frequency controls for reference tracking and enhancement by end-point prediction,” *IEEE Trans. Circuits and Syst. I, Reg. Papers*, vol. 57, no. 11, pp. 3023 –3034, Nov. 2010.

[149] J. Calvente, F. Guinjoan, L. Martinez, and A. Poveda, “Subharmonics, bifurcations and chaos in a sliding-mode controlled boost switching regulator,” in *IEEE Int. Symp. Circuits and Systems (ISCAS) 'Connecting the World'., 1996*, vol. 1, May 1996, pp. 573 –576 vol.1.

[150] R. Venkataramana, “Sliding mode control of power converters,” Ph.D. dissertation, California Institude of Technology, Pasadena, CA, 1986.

[151] S. C. Tan, Y. M. Lai, and C. K. Tse, “A unified approach to the design of PWM-based sliding-mode voltage controllers for basic DC-DC converters in continuous conduction mode,” *IEEE Trans. Circuits and Syst. I, Reg. Papers*, vol. 53, no. 8, pp. 1816–1827, Aug. 2006.

[152] H. Sira-Ramirez and M. Rios-Bolivar, “Sliding mode control of DC-to-DC power converters via extended linearization,” *IEEE Trans. Circuits Syst. I, Fundam. Theory Appl.*, vol. 41, no. 10, pp. 652 –661, Oct. 1994.

[153] B. P. Schweitzer and A. B. Rosenstein, “Free running-switching mode power regulator: Analysis and design,” *IEEE Trans. Aerosp.*, vol. 2, no. 4, pp. 1171–1180, Oct. 1964.

[154] I. Babaa, T. Wilson, and Y. Yu, “Analytic solutions of limit cycles in a feedback-regulated converter system with hysteresis,” *IEEE Trans. Automat. Contr.*, vol. 13, no. 5, pp. 524–531, Oct. 1968.

[155] L. Malesani, R. G. Spiazzi, and P. Tenti, “Performance optimization of Cuk converters by sliding-mode control,” *IEEE Trans. Power Electron.*, vol. 10, no. 3, pp. 302–309, May 1995.

[156] S. K. Mazumder, A. H. Nayfeh, and A. Borojevic, “Robust control of parallel DC-DC buck converters by combining integral-variable-structure and multiple-sliding-surface control schemes,” *IEEE Trans. Power Electron.*, vol. 17, no. 3, pp. 428–437, May 2002.

[157] E. Alarcon, A. Romero, A. Poveda, S. Porta, and L. Martinez-Salamero, “Sliding-mode control analog integrated circuit for switching DC-DC power converters,” in *IEEE Int. Symp. Circuits and Systems*, vol. 1, May 2001, pp. 500–503.

[158] M. Ahmed, M. Kuisma, K. Tolsa, and P. Silventoinen, “Implementing sliding mode control for buck converter,” in *IEEE 34th Ann. Power Electronics Specialist Conf. (PESC)*, vol. 2, June 2003, pp. 634–637.

[159] L. Iannelli and F. Vasca, “Dithering for sliding mode control of DC/DC converters,” in *IEEE 35th Ann. Power Electronics Specialists Conf. (PESC)*, vol. 2, June 2004, pp. 1616–1620.

[160] V. Nguyen and C. Q. Lee, “Indirect implementations of sliding-mode control law in buck-type converters,” in *11th IEEE Ann. Applied Power Electronics Conf. and Expo. (APEC) Proc.*, vol. 1, Mar. 1996, pp. 111–115.

[161] S. C. Tan, Y. M. Lai, and C. K. Tse, “An evaluation of the practicality of sliding mode controllers in dc-dc converters and their general design issues,” in *37th IEEE Power Electronics Specialists Conf. (PESC)*, June 2006, pp. 1–7.

[162] L. Malesani, P. Mattavelli, and P. Tomasin, “Improved constant-frequency hysteresis current control of vsi inverters with simple feedforward bandwidth prediction,” *IEEE Trans. Ind. Appl.*, vol. 33, no. 5, pp. 1194–1202, Sept. 1997.

[163] G. C. Verghese, *The Control Handbook.* CRC Press - IEEE Press, 1996, vol. I, ch. 78, pp. 1413–1424.

[164] V. Vorperian, “Simplified analysis of PWM converters using model of PWM switch part I: Continuous conduction mode,” *IEEE Trans. Aerosp. Electron. Syst.*, vol. 26, no. 3, pp. 490–496, May 1990.

[165] ——, “Simplified analysis of PWM converters using model of PWM switch part II: Discontinuous conduction mode,” *IEEE Trans. Aerosp. Electron. Syst.*, vol. 26, no. 3, pp. 497–505, May 1990.

[166] L. Iannelli, K. H. Johansson, U. T. Jonsson, and F. Vasca, "Averaging of nonsmooth systems using dither," *Automatica*, vol. 42, no. 4, pp. 669–676, Apr. 2006. [Online]. Available: http://www.sciencedirect.com/science/article/B6V21-4J8JVS1-2/2/6426f28fbd54eba9ec1829c5f9807caf

[167] A. Davoudi, J. Jatskevich, and P. L. Chapman, "Averaged modelling of switched-inductor cells considering conduction losses in discontinuous mode," *IET Electric Power Appl.*, vol. 1, no. 3, pp. 402–406, May 2007.

[168] S. R. Sanders, J. M. Noworolski, X. Z. Liu, and G. C. Verghese, "Generalized averaging method for power conversion circuits," in *21st Annu. IEEE Power Electronics Specialists Conf. (PESC) Rec.*, June 1990, pp. 333–340.

[169] P. T. Krein, J. Bentsman, R. M. Bass, and B. C. Lesieutre, "On the use of averaging for the analysis of power electronic systems," in *20th Annu. IEEE Power Electronics Specialists Conf.*, vol. 1, June 1989, pp. 463–467.

[170] J. M. Noworolski and S. R. Sanders, "Generalized in-place circuit averaging," in *6th Annu. Applied Power Electronics Conf. and Expo. (APEC) Proc.*, Mar. 1991, pp. 445–451.

[171] Y. Lee, "Modelling and analysis of d.c.-d.c. converter using y-parameters," *Radio and Electronic Engineer*, vol. 54, no. 3, pp. 129–136, Mar. 1984.

[172] R. Tymerski and V. Vorperian, "Generation, classification and analysis of switched-mode DC-to-DC converters by the use of converter cells," in *Int. Telecommunications Energy Conf. (INTELEC)*, Oct. 1986, pp. 181–195.

[173] R. Tymerski, V. Vorperian, F. C. Y. Lee, and W. T. Baumann, "Nonlinear modeling of the PWM switch," *IEEE Trans. Power Electron.*, vol. 4, no. 2, pp. 225 –233, Apr. 1989.

[174] E. Van Dijk, J. N. Spruijt, D. M. O'Sullivan, and J. B. Klaassens, "PWM-switch modeling of DC-DC converters," *IEEE Trans. Power Electron.*, vol. 10, no. 6, pp. 659–665, Nov. 1995.

[175] F. C. Y. Lee, R. P. Iwens, Y. Yu, and J. E. Triner, "Generalized computer-aided discrete time-domain modeling and analysis of DC-DC converters," *IEEE Trans. Ind. Electron. Contr. Instrum.*, vol. IECI-26, no. 2, pp. 58–69, May 1979.

[176] D. J. Shortt and F. C. Lee, "Improved switching converter model using discrete and averaging techniques," *IEEE Trans. Aerosp. Electron. Syst.*, vol. AES-19, no. 2, pp. 190–202, Mar. 1983.

[177] R. Tymerski, "Sampled-data modelling of switched circuits, revisited," in *24th Annu. IEEE Power Electronics Specialists Conf. (PESC) Rec.*, June 1993, pp. 395–401.

[178] V. Rajasekaran, S. Jian, and B. S. Heck, "Bilinear discrete-time modeling for enhanced stability prediction and digital control design," *IEEE Trans. Power Electron.*, vol. 18, no. 1, pp. 381–389, Jan. 2003.

[179] M. S. Al-Numay, "Discrete-time model for PWM converters in discontinuous conduction mode," in *12th Int. Power Electroninics and Motion Control Conf. (EPE-PEMC)*, Sept. 2006, pp. 800–804.

[180] L. Iannelli, K. H. Johansson, U. T. Jonsson, and F. Vasca, "Subtleties in the averaging of a class of hybrid systems with applications to power converters," *Control Engineering Practice*, vol. 16, no. 8, pp. 961–975, June 2008. [Online]. Available: http://www.sciencedirect.com/science/article/B6V2H-4R71DM9-1/2/a5d3a08f59f5737ebbcc8d1becb00bce

[181] D. Czarkowski and M. K. Kazimierczuk, "Energy-conservation approach to modeling PWM DC-DC converters," *IEEE Trans. Aerosp. Electron. Syst.*, vol. 29, no. 3, pp. 1059–1063, July 1993.

[182] A. Reatti and M. K. Kazimierczuk, "Small-signal model of PWM converters for discontinuous conduction mode and its application for boost converter," *IEEE Trans. Circuits Syst. I, Fundam.l Theory Appl.*, vol. 50, no. 1, pp. 65–73, Jan. 2003.

[183] A. Davoudi, J. Jatskevich, and P. L. Chapman, "Simple method of including conduction losses for average modelling of switched-inductor cells," *Electron. Lett.*, vol. 42, no. 21, pp. 1246–1247, Oct. 2006.

[184] A. Davoudi and J. Jatskevich, "Realization of parasitics in state-space average-value modeling of PWM DC-DC converters," *IEEE Trans. Power Electron.*, vol. 21, no. 4, pp. 1142–1147, July 2006.

[185] R. W. Erickson, S. Cuk, and R. D. Middlebrook, "Large-signal modelling and analysis of switching regulators," in *13th Annu. Power Electronics Specialists Conf.*, 1982, pp. 240–250.

[186] R. M. Bass and P. T. Krein, "Large signal design alternatives for switching power converter control," in *22nd Annu. IEEE Power Electronics Specialists Conf.*, June 1991, pp. 882–887.

[187] P. T. Krein and R. M. Bass, "Geometric formulation, classification and methods for power electronic systems," in *21st Annu. IEEE Power Electronics Specialists Conf. (PESC) Rec.*, June 1990, pp. 499–505.

[188] R. Leyva, L. Martinez-Salamero, H. Valderrama-Blavi, J. Maixe, R. Giral, and F. Guinjoan, "Linear state-feedback control of a boost converter for large-signal stability," *IEEE Trans. Circuits Syst. I, Fundam.l Theory Appl.*, vol. 48, no. 4, pp. 418–424, Apr. 2001.

[189] F. Chen and X. S. Cai, "Design of feedback control laws for switching regulators based on the bilinear large signal model," *IEEE Trans. Power Electron.*, vol. 5, no. 2, pp. 236–240, Apr. 1990.

[190] S. R. Sanders and G. C. Verghese, "Lyapunov-based control for switched power converters," *IEEE Trans. Power Electron.*, vol. 7, no. 1, pp. 17–24, Jan. 1992.

[191] J. G. Kassakian, M. F. Schlecht, and V. G. C., *Principle of Power Electronics.* Addition-Wesley Publishing Company, 1991.

[192] A. Kelly and K. Rinne, "Control of DC-DC converters by direct pole placement and adaptive feedforward gain adjustment," in *20th Ann. IEEE Applied Power Electronics Conf. and Expo. (APEC)*, vol. 3, Mar. 2005, pp. 1970–1975.

[193] G. Bocchetti, N. De Angelis, and A. De Carli, “Advanced digital control strategies for power DC/DC converters,” in *Int. Conf. on Industrial Electronics, Control and Instrumentation*, vol. 1, Oct. 1991, pp. 411–416.

[194] G. Zames, “Feedback and optimal sensitivity: Model reference transformations, multiplicative seminorms, and approximate inverses,” *IEEE Trans. Automat. Contr.*, vol. 26, no. 2, pp. 301–320, Apr. 1981.

[195] K. Zhou, J. C. Doyle, and K. Glover, *Robust and Optimal Control.* Englewood Cliffs, New Jersey: Prentice Hall, 1996.

[196] S. Skogestad and I. Postlethwaite, *Multivariable Feedback Control - Analysis and Design.* John Wiley & Sons, 2001.

[197] R. Y. Chiang and M. G. Safonov, *Robust Control Toolbox User’s Guide.* Natic, MA: The Mathworks, Jun. 2001.

[198] R. Naim, G. Weiss, and S. Ben-Yaakov, “H_∞ control applied to boost power converters,” *IEEE Trans. Power Electron.*, vol. 12, no. 4, pp. 677–683, Jul. 1997.

[199] A. Kugi and K. Schlacher, “Nonlinear H_∞ controller design for a DC-to-DC power converter,” *IEEE Trans. Contr. Syst. Technol.*, vol. 7, no. 2, pp. 230–237, Mar. 1999.

[200] E. Vidal-Idiarte, L. Martinez-Salamero, H. Valderrama-Blavi, F. Guinjoan, and J. Maixe, “Analysis and design of H_∞ control of nonminimum phase-switching converters,” *IEEE Trans. Circuits Syst. I, Fundam. Theory Appl.*, vol. 50, no. 10, pp. 1316–1323, Oct. 2003.

[201] Z. Q. Wang, M. Sznaier, I. Batarseh, and J. Bu, “Robust controller design for a series resonant converter,” *IEEE Trans. Aerosp. Electron. Syst.*, vol. 32, no. 1, pp. 221–233, Jan. 1996.

[202] J. Bu, M. Sznaier, Z. Wang, and I. Baterseh, “Robust controller design for a parallel resonant converter using μ-synthesis,” *IEEE Trans. Power Electron.*, vol. 12, no. 5, pp. 837–853, Sep. 1997.

[203] S. Buso, “Design of a robust voltage controller for a buck-boost converter using μ-synthesis,” *IEEE Trans. Contr. Syst. Technol.*, vol. 7, no. 2, pp. 222–229, Mar. 1999.

[204] R. Tymerski, “Worst case stability analysis of switching regulators using the structured singular value,” in *25th Annu. IEEE Power Electron. Specialists Conf.*, vol. 1, Jun. 1994, pp. 281–288.

[205] G. Wallis and R. Tymerski, “Generalized approach for μ-synthesis of robust switching regulators,” *IEEE Trans. Aerosp. Electron. Syst.*, vol. 36, no. 2, pp. 422–431, Apr. 2000.

[206] C. Olalla, R. Leyva, A. El Aroudi, and P. Garc?s, “QFT robust control of current-mode converters: application to power conditioning regulators,” *Int. J. of Electron.*, vol. 96, no. 5, pp. 503–520, 2009.

[207] O. Ojo, "Robust control of series parallel resonant converters," *IEE Proc. Contr. Theory Appl.*, vol. 142, no. 5, pp. 401–410, Sep. 1995.

[208] G. Ioannidis and S. Manias, "H_∞ loop-shaping control schemes for the buck converter and their evaluation using μ-analysis," *IEE Proc. Electric Power Appl.*, vol. 146, no. 2, pp. 237–246, Mar. 1999.

[209] C. Jacobson, A. Stankovic, and G. Tadmor, "Design of robust controllers for resonant DC/DC converters," in *4th IEEE Conf. on Contr. Appl.*, Sep. 1995, pp. 360–365.

[210] A. Altowati, K. Zenger, and T. Suntiof, "Analysis and design of QFT-based robust control of a boost power converter," in *4th IET Conf. on Power Electron., Machines and Drives*, Apr. 2008, pp. 537–542.

[211] C. Olalla, R. Leyva, A. El Aroudi, P. Garces, and I. Queinnec, "LMI robust control design for boost PWM converters," *IET Power Electron.*, vol. 3, no. 1, pp. 75–85, Jan. 2010.

[212] C. Olalla, I. Queinnec, R. Leyva, and A. El Aroudi, "Optimal state-feedback control of bilinear DC-DC converters with guaranteed regions of stability," *IEEE Trans. Ind. Electron.*, vol. 59, no. 10, pp. 3868–3880, Oct. 2012.

[213] C. Olalla, R. Leyva, I. Queinnec, and D. Maksimovic, "Robust gain-scheduled control of switched-mode DC-DC converters," *IEEE Trans. Power Electron.*, vol. 27, no. 6, pp. 3006–3019, June 2012.

[214] S. Hiti and D. Boroyevich, "Control of boost converter with adjustable output voltage and unknown resistive load," in *25th Ann. IEEE Power Electronics Specialists Conf. (PESC) Rec.*, vol. 1, June 1994, pp. 294–300.

[215] J. T. Su, C. W. Liu, and D. M. Liu, "Adaptive control scheme for interleaved DC/DC power converters," in *Int. Power Electronics Conference (IPEC)*, June 2010, pp. 3105–3111.

[216] L. Corradini, P. Mattavelli, W. Stefanutti, and S. Saggini, "Simplified model reference-based autotuningfor digitally controlled SMPS," *IEEE Trans. Power Electron.*, vol. 23, no. 4, pp. 1956–1963, July 2008.

[217] J. Morroni, L. Corradini, R. Zane, and D. Maksimovic, "Robust adaptive tuning of digitally controlled switched-mode power supplies," in *24th Ann. IEEE Applied Power Electronics Conf. and Expo. (APEC)*, Feb. 2009, pp. 240–246.

[218] A. Kelly and K. Rinne, "A self-compensating adaptive digital regulator for switching converters based on linear prediction," in *21st Annu. IEEE Applied Power Electron. Conf. and Expo.*, Mar. 2006, pp. 712–718.

[219] S. J. Jeong and S. H. Song, "Improvement of predictive current control performance using online parameter estimation in phase controlled rectifier," *IEEE Trans. Power Electron.*, vol. 22, no. 5, pp. 1820–1825, Sept. 2007.

[220] S. C. Tan, Y. M. Lai, and C. K. Tse, "Implementation of pulse-width-modulation based sliding mode controller for boost converters," *IEEE Power Electron. Lett.*, vol. 3, no. 4, pp. 130–135, Dec. 2005.

[221] ——, "Design of PWM based sliding mode voltage controller for DC-DC converters operating in continuous conduction mode," in *European Conf. on Power Electronics and Applications*, 2005, pp. P.1–P.10.

[222] D. C. Jiles, "Frequency dependence of hysteresis curves in 'non-conducting' magnetic materials," *IEEE Trans. Magn.*, vol. 29, no. 6, pp. 3490–3492, Nov. 1993.

[223] L. Ljung, *System Identification - Theory For the User*, 2nd ed. Prentice Hall PRT, Upper Saddle River, New York, 1999.

[224] G. P. Rao and H. Unbehauen, "Identification of continuous-time systems," *IEE Proc. Control Theory Applications*, vol. 153, no. 2, pp. 185–220, Mar. 2006. [Online]. Available: http://link.aip.org/link/?ICT/153/185/1

[225] P. Young, J. W., H. Garnier, and M. Gilson, "An optimal instrumental variable approach for identifying hybrid continuous-time box-jenkins models," in *14th IFAC Symp. on System Identification (SYSID)*, Mar. 2006, pp. 225–230. [Online]. Available: http://hal.archives-ouvertes.fr/hal-00090647/en/

[226] P. C. Young, *Recursive Estimation and Time-Series Analysis: An Introduction for The Student and Practioner*, 2nd ed. Springer-Verlag Berlin Heidelberg, 2011.

[227] H. Garnier, M. Gilson, and V. Laurain. (2009, Nov.) Contsid toolbox for matlab (version 5.0). CRAN, Nancy Univesity. [Online]. Available: http://www.iris.cran.uhp-nancy.fr/contsid/

[228] A. Keyhani, S. M. Miri, and S. Hao, "Parameter estimation for power transformer models from time-domain data," *IEEE Trans. Power Del.*, vol. 1, no. 3, pp. 140–146, July 1986.

[229] R. E. Araujo, A. V. Leite, and D. S. Freitas, "Indirect parameter estimation of continuous-time systems using discrete time," in *29th Ann. IEEE Industrial Electronics Society Conf. (IECON)*, vol. 1, Nov. 2003, pp. 600–605.

[230] C. D. Motchenbacher and J. A. Connelly, *Low-Noise Electronic System Design.* John Wiley & Sons, Inc., 1993.

[231] A. Technologies. (2009, Jun.) Agilent impedance measurement handbook. [Online]. Available: http://cp.literature.agilent.com/litweb/pdf/5950-3000.pdf

[232] K. V. Price, S. R. M., and J. A. Lampinen, *Differential Evolution: A Practical Approach to Global Optimization.* Springer, NewYork, 2005.

[233] J. Nocedal and S. Wright, *Numerical Optimisation.* Springer, NewYork, 2000, ch. 9, pp. 238–240.

[234] N. Schmidt and H. Guldner, "A simple method to determine dynamic hysteresis loops of soft magnetic materials," *IEEE Trans. Magn.*, vol. 32, no. 2, pp. 489–496, Mar. 1996.

[235] P. R. Wilson and J. N. Ross, "Definition and application of magnetic material metrics in modeling and optimization," *IEEE Trans. Magn.*, vol. 37, no. 5, pp. 3774–3780, Sept. 2001.

[236] W. H. Press, S. A. Teukolsky, W. T. Vetterling, and B. P. Flannery, *Numerical Recipes in C: The Art of Scientific Computing.* Cambridge University Press, 1992.

[237] M. P. Sayani, R. V. White, D. G. Nason, and W. A. Taylor, "Isolated feedback for off-line switching power supplies with primary-side control," in *3rd Annu. IEEE Applied Power Electronics Conf. and Expo. (APEC)*, Feb. 1988, pp. 203–211.

[238] R. Mammano, "Isolating the control loop," Unitrode Corporation, Tech. Rep., 1990.

[239] T. T. Vu, S. O'Driscoll, and J. V. Ringwood, "Primary-side sensing for a flyback converter in both continuous and discontinuous conduction modes," in *Proc. Irish Signal and System Conf.*, 2012.

[240] L. Balogh, "A practical introduction to digital power supply control," Texas Instrument Inc., Tech. Rep., 2005.

[241] H. Kwakernaak, "Robust control and H_∞-optimization - tutorial paper," *Automatica*, vol. 29, no. 2, pp. 255–273, 1993. [Online]. Available: http://doc.utwente.nl/29962/

[242] K. Zhou and J. Doyle, *Essential of Robust Control.* Englewood Cliffs, New Jersey: Prentice Hall, 1999.

[243] J. Doyle, B. Francis, and Tannenbaum, *Feedback Control Theory.* Macmillan, 1990.

[244] J. Richalet and D. O. Donovan, *Predictive Functional Control.* Springer Verlag London, 2009.

[245] C. H. Houpis and S. J. Rasmussen, *Quantitative Feedback Theory: Fundamentals and Applications*, N. Munro, Ed. Marcel Dekker, Inc., 1999.

[246] A. M. Mario Garcia-Sanz and C. Philippe. (2014, Aug.) The qft control toolbox (qftct) for matlab (version 5.02). CWRU, UPNA and ESA-ESTEC. [Online]. Available: http://cesc.case.edu